

**Synthesis of well-defined sub-10 nm coin metal
nanoparticles
and the electrochemical application for the
carbon dioxide reduction reaction**

Dissertation

zur Erlangung des Doktorgrades der Naturwissenschaften
(Dr. rer. nat.)

der
Naturwissenschaftlichen Fakultät II
Chemie, Physik und Mathematik
der Martin-Luther-Universität
Halle-Wittenberg

von
Emil Robin Dieterich

Gutachter:

Prof. Dr. Michael Bron
Prof. Dr. Christina Roth

Verteidigung: 14.03.2024

Danksagung

*Ich danke **Prof. Dr. Michael Bron** für das Überlassen des spannenden Themas, das in mich gesetzte Vertrauen, die Möglichkeiten viele eigene Ideen frei umzusetzen, der Unterstützung bei diesem Vorgehen und den wertvollen und kritischen wissenschaftlichen Diskussionen.*

*Des Weiteren möchte ich mich bei allen Mitgliedern und ehemaligen Mitgliedern der Arbeitsgruppe bedanken, die bei der Umsetzung und dem Gelingen meiner Arbeit eine wichtige Rolle gespielt haben. Besonderer Dank gilt **Dr. Matthias Steimecke** für seinen tiefgehenden wissenschaftlichen Input, die Diskussionen und die Durchführung bzw. Anleitung der Charakterisierung mittels elektrochemischer Rastermikroskopie. Auch **Simon-Johannes Kinkelin** gilt mein Dank für die Durchführung von Raman Messungen von Kohlenstoffen in verschiedensten Schritten meiner Arbeit, deren intensiver Auswertung und der wissenschaftlichen Diskussion. **Dr. Alice Schätz** möchte ich für die gute Zusammenarbeit danken. Bei **Annett Quetschke** möchte ich mich für die Vielzahl der TEM, SEM und TG-MS Messungen und die Offenheit der Anpassung genannter Methoden bedanken. **Eik Koslowski** möchte ich meinen Dank für die XRD und XPS Messungen aussprechen und die gute Zusammenarbeit mit der wir XPS als standard Analysetechnik für die Arbeitsgruppe gemeinsam betrieben haben. **Dr. Sabine Schimpf** gebührt mein Dank für weitere TEM Messungen. Auch bedanken möchte ich mich bei **Julian Radicke, Lukas Herrmann, Kai Hetze, Olga Dzhyginas** und **Lukas Binnenböse** für ihre Arbeit, die im Umfang ihrer Abschlussarbeiten stattgefunden hat. **Anke Hassi** gilt mein Dank für die schnelle und zuverlässige Unterstützung bei allen administrativen Angelegenheiten. Der gesamten Arbeitsgruppe möchte ich weiterhin für die sehr angenehme Arbeitsatmosphäre danken.*

*Auch möchte ich mich bei **Dr. Jonas Jacobs** und **Dr. Florian Oehler** der Arbeitsgruppe von **Prof. Dr. Stefan Ebbinghaus** für die XRD Messungen und Analysen sowie den wissenschaftlichen Diskurs bedanken. Bei **Jenny Bienias Dragon** aus der Arbeitsgruppe von **Prof. Dr.-Ing. Thomas Hahn** für die Durchführung der Stickstoffadsorptions Messungen mit BET Auswertung. Sowie bei **Frank Syrowatka** vom Interdisziplinären Zentrum für Materialwissenschaften für die STEM Messungen. Nicht zuletzt möchte ich mich bei meinen Freunden, meiner Familie und Steffie bedanken die mich alle immer sehr unterstützt haben.*

Eigenständigkeitserklärung

Ich bestätige, dass ich die vorliegende Arbeit selbstständig und ohne fremde Hilfe verfasst und sie nur unter Verwendung der angegebenen Quellen und Hilfsmittel angefertigt habe. Wörtliche oder inhaltliche Übernahmen aus den benutzten Werken sind als solche kenntlich gemacht. Diese Arbeit wurde bisher an keiner anderen Universität vorgelegt.

Halle (Saale), den 07.11.2023

Lebenslauf

Emil Robin Dieterich

Berufserfahrung

- 06.2023 - heute Wissenschaftlicher Mitarbeiter
Umweltbundesamt Dessau-Roßlau
- 08.2018 - 10.2022 Wissenschaftlicher Mitarbeiter
Martin-Luther-Universität Halle-Wittenberg
Naturwissenschaftliche Fakultät II – Chemie, Physik und
Mathematik
Institut für Chemie - Technische Chemie und
Makromolekulare Chemie
Technische Chemie erneuerbarer Energien (AK Prof. Bron)

Ausbildung

- 08.2018 - 03.2024 Promotionsstudent
Technische Chemie erneuerbarer Energien (AK Prof. Bron)
Martin-Luther-Universität Halle-Wittenberg
Naturwissenschaftliche Fakultät II – Chemie, Physik und
Mathematik
Institut für Chemie - Technische Chemie und
Makromolekulare Chemie
- 10.2015 - 06.2018 Master of Science *Erneuerbare Energien*
Martin-Luther-Universität Halle-Wittenberg
Naturwissenschaftliche Fakultät II – Chemie, Physik und
Mathematik
Masterarbeit: **Synthese von Goldnanopartikeln und ihre
elektrokatalytischen Eigenschaften** (AK Prof. Bron)
- 10.2010 - 06.2014 Bachelor of Science *Angewandte Naturwissenschaften*
TU Bergakademie Freiberg
Naturwissenschaftliche Fakultät II – Chemie, Physik und
Mathematik
Bachelorarbeit: **Synthese und Charakterisierung von
Übergangsmetallverbindungen der Zusammensetzung
 $Ni_xB_yH_z$** (Physikalische Chemie I)

Publikationen

Multimethod Approach to the Low-Overpotential Region of Micro- to Macro-Scale Working Electrodes of Sub-10 nm Gold Nanoparticles in the CO_2 Reduction Reaction

E. Dieterich, L. Herrmann, O. Dzhyginas, L. Binnenböse, M. Steimecke, S.-J. Kinkelin and M. Bron, *Analytical Chemistry* 2023, DOI: 10.1021/acs.analchem.3c02338

Structural, morphological and electrochemical characterization of the degradation processes during the oxygen reduction reaction of iron(II) phthalocyanine supported on carbon nanotubes

S.-J. Kinkelin, M. Steimecke, E. Dieterich, M. Bron, *Electrochimica Acta* 2023, 142060, DOI: 10.1016/j.electacta.2023.142060

Quantifying the removal of stabilizing thiolates from gold nanoparticles on different carbon supports and the effect on their electrochemical properties

E. Dieterich, S.-J. Kinkelin, M. Steimecke, M. Bron, *Nanoscale Adv.* 2022, DOI: 10.1039/d2na00561a

Comparative study of the synthesis of sub-10 nm carbon supported gold nanoparticles and their suitability for the methanol electrooxidation in alkaline media

E. Dieterich, S.-J. Kinkelin and M. Bron, *ChemNanoMat* 2022, DOI: 10.1002/cnma.202200098R1

Probing Individual Cuprous Oxide Microcrystals towards Carbon Dioxide Reduction by in situ Raman-coupled Scanning Electrochemical Microscopy

M. Steimecke, A. M. Araújo-Cordero, E. Dieterich, M. Bron, *ChemElectroChem* 2022, 9, DOI: 10.1002/celec.202101221

Structure, Magnetism, and Thermal Stability of $La_2NiO_{2.5}F_3$: A Ruddersden-Popper Oxyfluoride Crystallizing in Space Group $P4_2/nmm$

J. Jacobs, M. A. L. Marques, H.-C. Wang, E. Dieterich, S. G. Ebbinghaus, *Inorganic Chemistry* 2021, 60, 13646, DOI: 10.1021/acs.inorgchem.1c01957

Konferenz

Electrochemistry 2022

09.2022, GDCH, Berlin

Poster: **Impact of carbon support for the CO_2 reduction reaction on gold nanoparticles at low overpotentials**

Vorbemerkung

Die vorliegende Arbeit wurde in der Arbeitsgruppe der Technischen Chemie erneuerbarer Energien, des Instituts für Chemie der Martin-Luther-Universität Halle-Wittenberg angefertigt. Es handelt sich um eine kumulative Dissertationsschrift und beinhaltet drei erschienene Zeitschriftenartikel. Zu Beginn wird eine Einführung in die elektrochemische CO_2 Reduktion gegeben. Die spezifischen Eigenschaften von Nanomaterialien, die Synthese von Münzmetallnanopartikeln und deren Anwendung wird im Weiteren erläutert. An diese Einführung schließt sich die Zielstellung dieser Arbeit an. Gefolgt von einem Kapitel, welches die Kurzfassungen der für diese Arbeit relevanten Zeitschriftenartikel von mir aufführt und nicht veröffentlichten Ergebnissen zeigt und Diskutiert. Abschließend werden alle Ergebnisse zusammengefasst und ein Ausblick gegeben. Im Anhang folgen die Volltexte der Zeitschriftenartikel. Diese geben ein geschlossenes Bild, beginnend mit verschiedenen Synthesen von Goldnanopartikeln (**Comparative study of the synthesis of sub-10 nm carbon supported gold nanoparticles and their suitability for the methanol electrooxidation in alkaline media**) dem Trägern dieser und der Entfernung des Stabilisators (**Quantifying the removal of stabilizing thiolates from gold nanoparticles on different carbon supports and the effect on their electrochemical properties**). Folgend wird der Einsatz der geträgerten Goldnanopartikel für die elektrochemische CO_2 Reduktion untersucht (**Multimethod Approach to the Low-Overpotential Region of Micro- to Macro-Scale Working Electrodes of Sub-10 nm Gold Nanoparticles in the CO_2 Reduction Reaction**).

Alle Abkürzungen werde an erster Stelle aufgeführt, in einigen Fällen auch ein weiteres Mal und sie sind im Abkürzungsverzeichnis (S. 36) aufgeführt. Eine Auflistung aller Abbildungen ist auf S. 37 im Abbildungsverzeichnis und eine Auflistung aller Tabellen im Tabellenverzeichnis S. 37 zu finden.

Preliminary note

This thesis was prepared in the working group of the Technical Chemistry of Renewable Energies, Institute of Chemistry, Martin-Luther-University Halle-Wittenberg. It is a cumulative dissertation thesis and includes three published peer-reviewed articles. At the beginning, an introduction to electrochemical CO_2 reduction is given. The specific properties of nanomaterials, the synthesis of coin metal nanoparticles and their applications are further explained. This introduction is followed by the scope of this thesis, which is followed by the abstracts of the three published peer-reviewed articles and a chapter on unpublished results. The summary of all results and an outlook is given. Then the full text of the three journal articles is attached. These give a closed picture, starting with different syntheses of gold nanoparticles (**"Comparative study of the synthesis of sub-10 nm carbon supported gold nanoparticles and their suitability for the methanol electrooxidation in alkaline media"**) the support of these and the removal of the stabilizer (**"Quantifying the removal of stabilizing thiolates from gold nanoparticles on different carbon supports and the effect on their electrochemical properties"**). Subsequently, the use of supported gold nanoparticles for electrochemical CO_2 reduction is investigated (**"Multimethod Approach to the Low-Overpotential Region of Micro- to Macro-Scale Working Electrodes of Sub-10 nm Gold Nanoparticles in the CO_2 Reduction Reaction"**).

All abbreviations are explained first, in some cases a second time, and they are listed in the Table of Abbreviations (p. 36). A list of all figures can be found on p. 37 in the List of Figures and a list of all tables on p. 37.

Kurzdarstellung

Der stark ansteigende Energiebedarf der Menschheit und damit einhergehende Bedarf an fossilen Energieträgern erhöht den Ausstoß an CO_2 . Die daraus resultierende Klimaerwärmung ist eine der großen Herausforderungen der Menschheit. Um der Klimaerwärmung entgegen zu wirken, benötigen wir eine nachhaltige Energieversorgung und Produktionsprozesse. Ein großes Problem der Energieversorgung mit erneuerbaren Energien ist die wetterbedingte Fluktuation dieser, weshalb Kurzzeit- und Langzeitenergiespeicher eine essentielle Rolle spielen. Hier bietet sich die CO_2 Reduktionsreaktion (CO₂RR) als möglicher Langzeitspeicher in Form von Energieträgern und Chemikalien an, welche auch die CO_2 Emissionen reduziert. Im Weiteren könnte so ein geschlossener Kohlenstoffkreislauf entwickelt werden, welcher die CO_2 Emission für Produkte der CO₂RR idealerweise komplett verhindert und den Bedarf an fossilen Ressourcen deutlich senkt.

Um dies umzusetzen, müssen die CO₂RR Elektrokatalysatoren weiterentwickelt werden, um eine wirtschaftliche Lösung zu ermöglichen. Hierbei sind sub-10 nm Münzmetall Nanopartikel von großem Interesse. Ziel dieser Arbeit ist es hier einen Beitrag zu leisten, was in drei Teilschritten erfolgte. Der erste Teil befasst sich mit der Synthese von Münzmetallnanopartikeln kleiner 10 nm. Diese sind von großem Interesse, da ihre Eigenschaften vom bulk Material und vom Material in atomarer/molekularer Größe abweichen.

Im zweiten Teil wurden diese Nanopartikel auf Industrieruß und Kohlenstoffnanoröhren (CNT) geträgert und nachbehandelt. Die Nachbehandlung dient der Entfernung des Stabilisators, welcher synthesebedingt auf der Metalloberfläche vorliegt. Aufgrund der Einflüsse des Stabilisators auf die Materialeigenschaften ist seine Entfernung essentiell, um die katalytischen Eigenschaften des Metall-Träger Systems zu charakterisieren. Dabei zeigte sich, dass eine weit verbreitete Methode bestehend aus zwei Behandlungsschritten mit unterschiedlicher Atmosphäre und Temperatur weniger gut geeignet war, als die Behandlungsschritte separat. Je nach Metall und Trägermaterial konnten mindestens 89 % des Stabilisators aus dem bulk Material entfernt werden. Für Goldnanopartikel (AuNP) auf denselben Trägermaterialien wurde spezifisch die Oberflächenentfernung untersucht, die eine komplette Stabilisatorentfernung für AuNP auf CNT zeigte, während für AuNP auf Industrieruß ähnliche Werte ermittelt wurden, wie für das bulk Material. Die AuNP zeigten während der Behandlung Oberflächenmobilität und insbesondere kleinere Partikel gingen verloren.

Im dritten Teil werden die AuNP auf drei verschiedenen Kohlenstoffträgern hinsichtlich ihrer Eigenschaften für die elektrochemische CO₂RR im Bereich geringer Überpotentiale untersucht. Dafür wurden unterschiedliche Halb- und Voll-Zell Experimente mit Elektrodengrößen von Mikropunkten bis 6,5 cm² genutzt, welche mit unterschiedlicher *in situ*, on line oder nachgeschalteter Analytik verbunden waren. Hervorzuheben ist, dass die AuNP auf CNT in dem spezifischen Potentialbereich von -0.25 V bis -0.4 V als Produkt Formaldehyd bildeten, während die AuNP auf den Industrierußen CO bildeten. Bei allen Katalysatoren kam es auch zur parasitären Wasserstoffentwicklung. Besonders hervorzuheben ist hier, dass Formaldehyd als Endprodukt der CO₂RR an Katalysatoren mit Gold als Aktivkomponente bisher nicht bekannt war. Dieses Ergebnis fand sich in allen angewendeten elektrochemischen Experimenten reproduzierbar wieder. Speziell das Auftreten im Bereich

niedriger Überpotentiale, welche bisher selten tiefergehend untersucht wurden, zeigt, wie wichtig es ist, diesen Potentialbereich genauer zu untersuchen und gut charakterisierte Katalysatoren zu nutzen.

Abstract

The growing energy demand of mankind and increased consumption of fossil fuels have caused an increase in CO_2 emissions, leading to the global warming crisis we face today. To oppose climate change, renewable energies and sustainable production are needed. However, renewable energies have the disadvantage of being weather-dependent and therefore the need for short-term and long-term energy storage systems. One possibility is the CO_2 reduction reaction (CO2RR) for long-term energy storage as fuels, chemicals and also the reduction of CO_2 emission. This could be further developed into a closed carbon cycle, which could reduce the emissions for the products of the CO2RR down to zero and reduce the need for fossil fuels.

For this, the CO2RR electrocatalysts need to be further developed for an economically feasible application. Sub-10 nm coin metal nanoparticles, with properties lying between bulk and atom/ molecular size structures, are of great interest for this purpose. The aim of this work is to make a contribution in three parts, with the first part focused on the synthesis of sub-10 nm coin metal nanoparticles.

In the second part, the post-treatment of the nanoparticles supported onto common industrial carbon materials and carbon nanotubes (CNTs) was conducted to remove the stabilizer and increase the stability of the particle support interaction. The individual steps of a two-step procedure, which is usually done in two different atmospheres and temperatures, were evaluated and found to be more effective than the combined steps. Depending on the metal and supporting material, different amounts of stabilizer were removed; the single-step treatment achieved a minimum removal of 89 %. The surface removal was also assessed for the Gold nanoparticles (AuNPs) on carbon support, revealing a complete removal of the stabilizer from AuNPs on CNT, while for the AuNPs on industrial carbon materials the removal of the surface and bulk were in the same range. Moreover, the AuNPs exhibited surface mobility and a loss of smaller particles during the treatments.

In the third part, the low overpotential region was investigated for the CO2RR capability of AuNPs supported on three different common carbon supports. Half-cell and full-cell experiments were conducted with electrodes ranging from micro size up to 6.5 cm^2 , with *in situ* or on line or following electrolyte analysis. The results demonstrated that only AuNPs on CNTs produced Formaldehyde in the low overpotential region (-0.25 V to -0.4 V), while AuNPs on industrial carbon materials yielded Carbon monoxide as a product. Furthermore, all three samples showed parasitic Hydrogen evolution. Notably, this is the first time that Formaldehyde has been reported as a CO2RR product on Gold, highlighting the significance of investigations of the low overpotential region and the need for in-depth characterization. Reproducible results were obtained from all four electrochemical experiments.

Table of Contents

Danksagung	II
Eigenständigkeitserklärung	III
Lebenslauf	IV
Publikationen	V
Konferenz	V
Vorbemerkung	VI
Preliminary note	VII
Kurzdarstellung	VIII
Abstract	IX
1 Introduction and basic concept	3
1.1 Carbon dioxide recycle	4
1.2 Nanomaterials	10
1.2.1 Properties of nanomaterials	10
1.2.2 Synthesis and supporting of nanoparticles	11
1.2.3 Degradation mechanisms of nanoparticles	13
1.3 Challenges of using coinage metals in the CO_2 reduction	14
2 Scope of the thesis	15
3 Published and unpublished research	16
3.1 Introduction of relevant publications	16
3.2 Unpublished research	17
3.2.1 Synthesis of Silver nanoparticles	17
3.2.2 Synthesis of Copper nanoparticles	22
3.2.3 Instruments and measurements	25
4 Summary and Outlook	26
References	30
Table of Abbreviations	36
List of Figures	37
List of Tables	38
Appendices	39
A :Comparative Study of the Synthesis of sub-10 nm Carbon-Supported Gold Nanoparticles and their Suitability for Methanol Electrooxidation in Alkaline Media	39

A.1	:Supporting informations - Comparative Study of the Synthesis of sub-10 nm Carbon-Supported Gold Nanoparticles and their Suitability for Methanol Electrooxidation in Alkaline Media	46
B	:Quantifying the removal of stabilizing thiolates from gold nanoparticles on different carbon supports and the effect on their electrochemical properties	58
B.1	:Supporting informations - Quantifying the removal of stabilizing thiolates from gold nanoparticles on different carbon supports and the effect on their electrochemical properties	68
C	:Reprinted with permission from American Chemical Society, Analytical Chemistry: Multimethod Approach to the Low-Overpotential Region of Micro- to Macro-Scale Working Electrodes of Sub-10 nm Gold Nanoparticles in the CO_2 Reduction Reaction, Dieterich E., Herrmann L., Dzhyginas O. et al. (2023)	81
C.1	:Reprinted with permission from American Chemical Society, Analytical Chemistry: Supporting informations - Multimethod Approach to the Low-Overpotential Region of Micro- to Macro-Scale Working Electrodes of Sub-10 nm Gold Nanoparticles in the CO_2 Reduction Reaction, Dieterich E., Herrmann L., Dzhyginas O. et al. (2023) . . .	90

1 Introduction and basic concept

The rapidly increasing energy demand that is still mostly satisfied by fossil fuels causes the constant rise of the atmospheric CO_2 concentration which accelerates global warming.^{1,2} The climate crisis requires rethinking the established systems of energy supply and the use of fossil fuels. Despite the great efforts in developing and establishing carbon neutral, renewable energy sources, fossil fuels are today the main energy carriers and their consumption still increases.² To reduce the CO_2 emission into the atmosphere, different strategies have been proposed. The capture and storage of CO_2 , for example pressurized in caves, in the deep sea, or by biosequestration in plants (e.g. algae) are strategies for long-term storage. The geological and deep-sea storage would allow for some continuous CO_2 emission, while capturing would protect the atmosphere from rising CO_2 levels; both entails great uncertainties and costs for sequestration, transport and the storage itself.³ Huge amounts of space would be needed and the long-term impact on the geologic and deep sea environment is not foreseeable, especially in the case of leakage.⁴ Due to these challenges and uncertainties, the recycling of CO_2 by usage as a carbon source is of great interest. By recycling, an artificial carbon cycle can be created. An outline is sketched in Fig. 1, exemplary for the electrochemical CO_2RR .

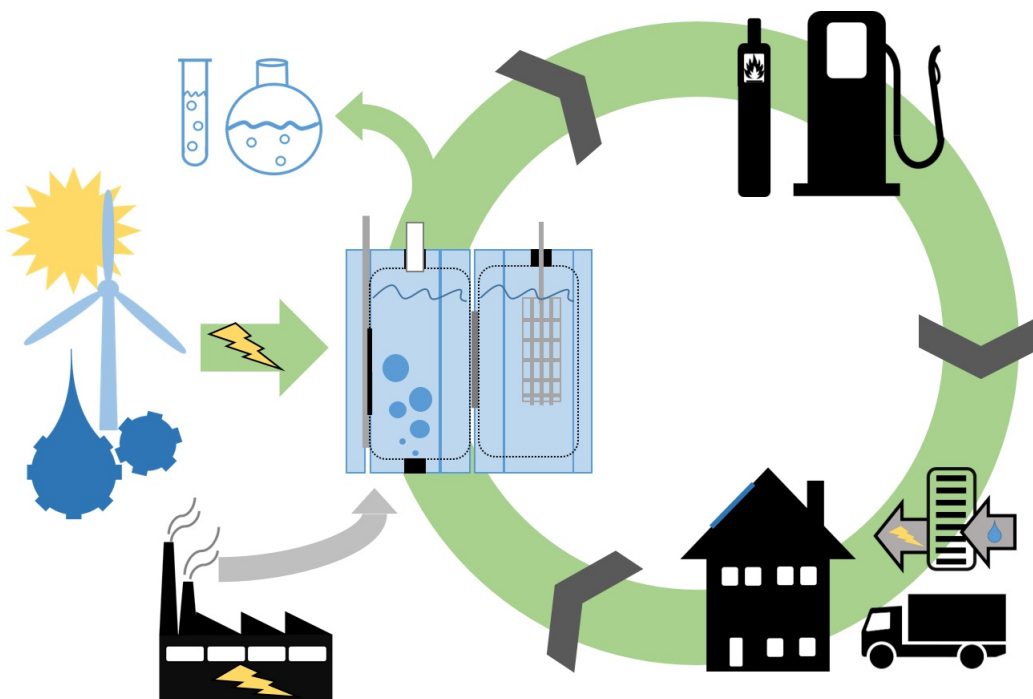


Figure 1: Outline of an artificial carbon cycle by the (electrochemical) CO_2RR for the production of fuels and chemicals by CO_2 and renewable energies. Energy is supplied by renewable energy sources to reduce CO_2 , to either produce fuels for further usage as energy carrier or in transport, or essential chemicals. The usage of these fuels produces CO_2 which can be captured and re-introduced into the CO_2RR . This would create a closed Carbon cycle. Also industrial CO_2 emissions can be introduced into the CO_2RR .

The recycling of CO_2 and further usage as a carbon source offers a promising alternative to reduce the CO_2 level in the atmosphere, and also to achieve sustainable production of essential chemicals. Different methods of the utilization of CO_2 are based on thermochemical, photochemical or electrochemically processes.^{3,5} All of these recycle processes rely on catalysts for an energetically efficient utilization.

The thermochemical conversion is a thermally activated hydrogenation of CO_2 with H_2 as reducing agent, which can reduce CO_2 to CO , by the reverse water–gas shift reaction.³ For this, an excess amount of H_2 is needed which, to produce sustainable chemicals, needs to be from “green” sources. Sustainable hydrogen usually comes from water electrolysis, powered by renewable energies, but most of today’s hydrogen still relies on steam reforming of natural gas, which is not sustainable. The product of the reverse water–gas shift reaction is a combination of CO and H_2O , which can be used further, by H_2 addition, for the Fischer–Tropsch reaction, the Methane synthesis or the Methanol synthesis. These reactions are exothermic, still run on high pressure and therefore have a high energy demand.⁵

The photochemical conversion offers great opportunities by being relatively independent from external energy sources. The photochemical conversion can be operated at room temperature and ambient pressure and therefore require less energy than the thermochemical and electrochemical CO2RR.^{6,7} Unfortunately until now the activity and selectivity is comparable low to the thermochemical and electrochemical conversion. Therefore, novel catalysts and new reactor designs are needed to improve the photochemical CO2RR.⁸

The electrochemical CO2RR offers a broad variety of possible products as up to 8 electrons can be transferred during the reduction process of one CO_2 molecule. Possible products are Carbon monoxide, Formate, Oxalate, Methanol, Methane, Formaldehyde, Ethanol, Ethylene etc..^{9,10} Advantages of the electrochemical CO2RR are controllable reactions steered by the applied potential and temperature, the possibility to recycle the electrolyte and therefore a minimal consumption of chemicals, and the simple, modular and compact design. These advantages make the electrochemical CO2RR suitable for large scale use.^{11,12,13,14} Drawbacks are the low energy efficiency, slow kinetics and problematic selectivity. Therefore, highly active and selective electrocatalysts are needed.^{13,15} Various materials have been tested. Bulk metals could be categorized for different main products, which will be discussed in chapter 1.1 in more detail. Further investigations showed that the size of nanoparticles as catalysts play an important role for the activity and selectivity.^{14,16,17}

Beside the already described problematic implementation of renewable energies over conventional ones, next to the exceeding energy demand, the fluctuation of the supply by renewable energies is problematic due to the permanently changing weather conditions. To enforce a structural change of the energy grid to renewable energies, there is a great need in energy storage systems. Energy storage systems, such as compressed air, batteries, redox flow batteries, pumped hydro and flywheels, are working well for short-term energy shortages but have a limited scalability, versatility and a maximum storage time.^{18,19} CO2RR could represent a long-term storage system of energy in chemicals and fuels which could close this gap in the energy supply chain of renewable energies. In order to make the CO2RR economically feasible, catalysts with high activity and selectivity at low overpotentials are needed.¹⁵

1.1 Carbon dioxide recycle

One of the challenges to use Carbon dioxide as a Carbon source is the great stability of the Carbon dioxide molecule; the Carbon is in the most oxidized form (oxidation state +4). As previously mentioned, typical approaches for the CO2RR to valuable chemicals and fuels use thermo-, photo- and electrochemical pathways.^{5,20} Electro-

chemical CO_2 reduction provides a way to create an artificial Carbon cycle and the typical cell design can be relatively easy up scaled, however, selectivity, activity, stability and the high overpotentials remain problematic.²¹ These issues can be addressed by manipulating the catalyst. Therefore, a closer look to the electrochemical CO2RR will be given.

Fig. 2 presents a model of a full-cell setup for the electrochemical CO2RR (further CO2RR addresses the electrochemical CO2RR) using an aqueous electrolyte with the principal reactions of the CO2RR, the competitive Hydrogen evolution reaction (HER) and the anode reaction (Oxygen evolution reaction, OER). Studies have shown that the reactions and products of the CO2RR are highly dependent on the catalysts, electrolyte, pH, temperature, and competing reactions (e.g. HER).^{22,23,24,25} A selection of products and their associated equilibrium potentials are given in Tab. 1. The potentials are referenced to the pH-independent reversible Hydrogen electrode (RHE). Notably, the direct reduction of CO_2 to CO_2^* by one electron, to form a CO_2 anion radical, has a highly negative potential and therefore no CO2RR should appear before -1.9 V vs. SHE (standard hydrogen electrode). To bypass this direct reduction and reduce the potential, an alternative mechanism has been proposed.⁹ This will be discussed in further detail later. Except for the direct reduction of CO_2 , all the potentials of the CO2RR and HER reactions occur in a relatively narrow potential region. The narrow potential region for the different possible CO2RR products, the HER and the experimental and material specific overpotentials are challenging for the selectivity.

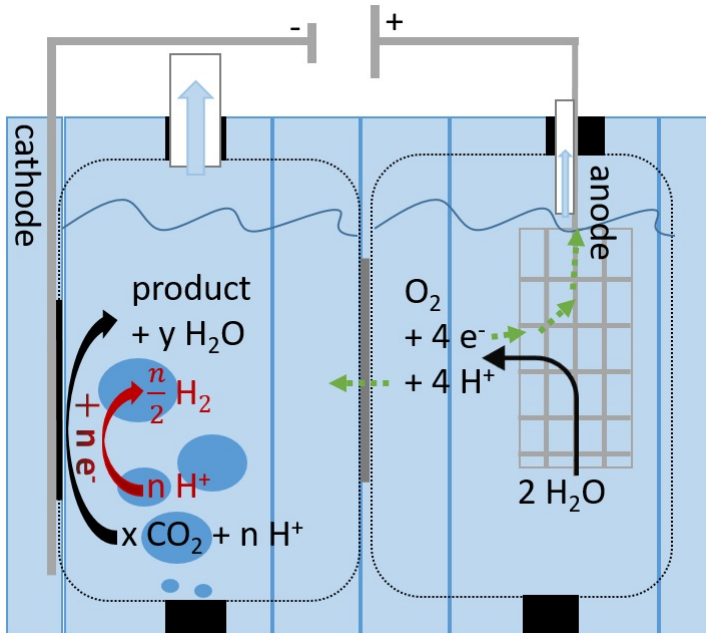


Figure 2: Full cell setup for the CO2RR in an Aqueous electrolyte, with the reaction (black) $x CO_2 + y H_2O \rightarrow product + z O_2$ separated in the half-cell reactions of the OER at the anode $2 H_2O \rightarrow O_2 + 4 H^+ + 4 e^-$ and the CO2RR at the cathode $x CO_2 + n H^+ + n e^- \rightarrow product + y H_2O$ and the competitive HER (red) $n H^+ + n e^- \rightarrow n/2 H_2$, whereby the anode and cathode sides are separated by a cation exchange membrane. As the electrolyte typical buffers (e.g. $KHCO_3$ Aqueous solutions) are used to improve the solubility of CO_2

These overpotentials are the difference between the thermodynamically calculated potential of the half-cell reaction and the experimentally measured potential. The overpotentials differ in each reaction and experimental setup (catalyst, elec-

Table 1: The thermodynamic equilibrium potentials for exemplary products, the reaction and the number of transferred electrons. The potentials are given vs. RHE.

Product	Reaction	Number of transferred electrons	E^0 vs. RHE in V
	$CO_2 + e^- \rightarrow CO_2^*$	1	-1.9(vs. SHE) ⁹
Formic acid	$CO_2 + 2 H^+ + 2e^- \rightarrow HCOOH_{(aq)}$	2	-0.12 ²⁶
Carbon monoxide	$CO_2 + 2 H^+ + 2 e^- \rightarrow CO_{(g)} + H_2O$	2	-0.10 ²⁶
Formaldehyde	$CO_2 + 4 H^+ + 4 e^- \rightarrow HCHO$	4	-0.07 ²⁷
Methanol	$CO_2 + 6 H^+ + 6 e^- \rightarrow CH_3OH_{(aq)} + H_2O$	6	0.03 ²⁶
Ethylene	$2 CO_2 + 12 H^+ + 12 e^- \rightarrow C_2H_4(aq) + 4 H_2O$	6/ CO_2	0.08 ²⁶
Methane	$CO_2 + 8 H^+ + 8 e^- \rightarrow CH_4(g) + 2 H_2O$	8	0.17 ²⁶
Hydrogen	$2 H^+ + 2 e^- \rightarrow H_2$	2	0.00 ²⁶
Oxygen	$2 H_2O \rightarrow O_2 + 4 H^+ + 4 e^-$	2	1.23 ²⁶

trolyte, temperature, pressure etc.). Careful selection of catalyst and experimental conditions can therefore be used to manipulate the selectivity, with superior catalysts displaying high selectivity for a single CO₂RR product and suppressing the HER relatively effectively. This emphasizes the importance of developing catalysts with high selectivity, efficiency and long-term stability, as a crucial step towards industrialization.

In first studies bulk metals have been investigated for the CO₂RR by Hori et al.²⁸ 1985, towards their selectivity for a specific main product. Four groups have been identified for the main product of CO (Au, Ag, Zn), $HCOO^-$ (Cd, In, Sn, Pb), H_2 (Fe, Ni, Ga, Pd, Pt, Ti) and beyond CO (Cu).^{28,29} Copper was the only bulk metal which produced significant amounts of higher reduced CO₂RR products, like Methane. For better knowledge of the CO₂RR mechanism and improving the catalytic activity and product selectivity, research has intensified over time. Understanding catalytic activity and selectivity, exploring the activity and selectivity of certain sites and structures is of great interest. Therefore, various strategies of changing morphologies, altering crystal facets, modifying the surface structure and the oxidation state are investigated. In the following, some of these approaches are summarized. With regard to the effects of catalyst modification by downsizing to nano-size, different structures/ shapes, surface adsorbates or non-metal catalysts, exemplary results are summarized in Tab. 2. Reske et al.¹⁷ synthesized polyvinylpyrrolidone-stabilized Copper nanoparticles (CuNP) in the range of 1.9 nm to 15.1 nm and investigated these for the CO₂RR, as well as Copper foil. They showed, that downsizing could increase the overall activity 1.5 times, while the selectivity changed strongly. The Copper foil produced the highest amount of CH_4 and C_2H_4 , these products decreased close to zero with particle sizes of 2.3 nm and smaller, while the HER and the CO selectivity increased greatly with particle downsizing. Based on the density functional theory (DFT), they calculated the coordination number of spherical particles in the size range of 2.2 nm to 6.9 nm. The calculations showed that atoms of edges and kinks are increasing strongly by a decrease in size. Reske et al.¹⁷ postulated that these facets have a different binding energy to CO ,

which inhibits further CO hydrogenation. Also Silver³⁰ and Gold¹⁶ nanoparticles (AgNP, AuNP) were investigated for the particle size effect. Testing AgNP of 2 nm to 6 nm, a maximum faradaic efficiency ($FE_{product}$) for CO was found for particle sizes of 3.7 nm, while for smaller particle sizes the FE_{H_2} increased strongly. Using larger AgNP, the FE_{CO} decreased slightly with no increase of FE_{H_2} . The DFT supports these findings and showed that the edges are mainly active for the HER, while the Ag(100) is mainly active for the CO2RR. For corners and Ag(111), the binding energies are nearly equal. Examining AuNP particles of 4 nm to 10 nm, particles of 8 nm demonstrated the highest activity for CO , whereas 10 nm showed the lowest. Applying DFT, the particle size-depending distribution of edges, corners and planes was calculated and demonstrated that corners favor the HER, while edges favor the CO2RR to CO . The calculations estimate for Au(211) a selectivity for the CO2RR to CO and for Au(111) an increased selectivity towards H_2 at the expense of the CO selectivity. Liu et al.³¹ investigated the effect of the shape of Gold (nano)structures using Gold needles, rods and particles with diameters up to 400 nm. The tips of the rods and the needles were of much smaller size. They found FE_{CO} between 90 % (needle), 35 % (rod) and 10 % (particle) (-0.35 V vs. RHE) and a shape-depending decrease of the CO onset potential. Also, they calculated by DFT that the K^+ (of the $KHCO_3$ electrolyte solution) adsorbed on the Au-surface lowered the CO_2 adsorption, as $COOH^*$ species, for Au(111), (100), (110) and (211) to less than half of the energy needed in pure H_2O . The impact of surface adsorbates, like stabilizers for the synthesis of nanostructures was investigated by Wakerley et al.³². Thiolate surfactant on Copper dendrites influenced the activity and selectivity strongly. By the Thiolate surfactant the surface gets a hydrophobic character, for which the CH_4 , CO , C_2H_4 and C_2H_5OH selectivity was strongly increased, while the HER was decreased. Contrary to the selectivity increase towards CH_4 , CO , C_2H_4 and C_2H_5OH , the overall activity was strongly decreased by the Thiolate surfactant. Recently, the addition of cationic Ammonium based surfactants showed to improve the CO2RR, mainly by suppressing the competitive HER.^{33,34} Ag , Au and Zn disc electrodes were investigated for the effects of cationic Ammonium surfactants. For Ag , the current density was increased ~ 12 fold by the addition and the HER was suppressed. The same effect was observed for Zn , but with less increasing current densities. For Au , the opposite effect was ascertained, the current density decreased with the addition of cationic Ammonium based surfactants.³³ Also non metal catalysts for the CO2RR to C_{2+} products are reported.³⁵ N -doped Carbon with faradaic efficiencies of ~ 77 % for Ethanol at -0.56 V vs. RHE was stable for around 6 h. While the energy density of non-metal catalysts is comparable low compared to metal catalysts, but also the costs for the non-metal material are relatively low. Further results for various catalysts and modifications are summarized in several reviews.^{17,36,37,38} It is noticeable that typical potentials of product investigations are between -0.5 V to -1.3 V vs. RHE. Rarely, the product investigation starts around -0.35 V vs. RHE. As already mentioned, catalysts for the low overpotential region are of great interest, therefore an investigation of smaller overpotentials would be desired.

The great variety of different products by the CO2RR can be explained by the binding energies of the adsorbates and intermediates, as well as the consecutive reactions of the products. Often, one of the first intermediates is CO . The transferred electrons, overall reactions and standard potentials for different products are listed in Tab. 1. For instance, if CO is bound weakly, it desorbs quickly and no further

Table 2: Summarizing results from literature of the investigation of different catalysts for the CO2RR to their products, and the energy density respectively faradaic efficiency at the investigated potential.

Material	Potential vs. RHE in V	Current density in $ mAcm^{-2} $	Products
^{17}Cu foil, CuNP 15.1 to 1.9 nm	-1.1	20 (foil to 4.8 nm), 40 (2.3 nm), 50 (1.9 nm)	CO, CH_4, C_2H_4, H_2
^{30}Ag NP 2 to 6 nm	-1.2	Only FE given, 60% H_2 and 10% CO for 1.9 nm, max. FE_{CO} at 3.7 nm of 98% CO , 2% H_2	CO, H_2
^{16}Au NP 4 to 10 nm	-0.35 to -0.9	Analyzed only for CO in Ag^{-1} at -0.37 V vs. RHE 0.2 (10 nm), 0.8 (8 nm), 0.6 (6 nm), 0.4 (4 nm)	CO, H_2
^{31}Au needles, rods and particles (~ 100 nm \emptyset)	-0.35	15 (needle), 0.7 (rod), 0.1 (particle), (average of 8 h),	CO, H_2
$^{32}Copper$ den- drimers with and without oc- tadecanethiol surfactant	-1.1 to -1.5	30 (-1.1 V vs. RHE, without surfac- tant), 30 (-1.5 V vs. RHE, with sur- factant)	$H_2, CO, HCOOH,$ $CH_4, CH_3OOH, C_2H_4,$ C_2H_5OH, C_2H_6
^{33}Ag -disc electrode with and without cationic ammonium surfactant	-0.9 to -1.2	with 0.47 CO , 0.02 $HCOO^-$, $\sim 0.6_{total}$ without 5.5 CO , 0.38 $HCOO^-$, $\sim 6.0_{total}$	$CO, HCOO^-, H_2$
^{35}N -doped carbon	-0.4 to -1.5	~ 0.15 (-0.56 V vs. RHE), 10 (-1.5 V vs. RHE)	C_2H_5OH, H_2

reduction can take place, as it is seen in bulk Au and Ag . Conversely, when the CO is adsorbed too strongly, the CO poisons the metal surface and no further reaction is possible, as it is the case with Pt .^{12,27,39} Fig. 3 presents proposed binding types of CO_2 to the catalyst surface. The types of adsorption that take place during the CO2RR include direct binding of an CO_2 anion radical (Fig. 3 a and b) and concerted proton-electron transfer (CPET, Fig. 3 c to g) - where CO_2 binds to a proton, or an adsorbed Hydrogen ($*H$)²². The CPET adsorption mechanism is the previously mentioned bypass for the direct CO_2 -anion radical adsorption.^{9,20,23,24,40} These types of adsorption are the first step of the CO2RR and important with regard to the final product. The binding energies of the adsorbates and intermediates depend on the base material and its crystal structure, as planes, edges and corners have different selectivities and activities. Therefore, the properties can be manipulated well by changing the crystal facets, oxidation state, structure and surface morphology.

In addition to the many advantages of nanoparticles in comparison to bulk metal in catalysis, it is well known, that they may have different properties depending on the particle size. The advantages and properties of nanoparticles are discussed in more detail in chapter 1.2. The surface morphology, in particular the ratio of planes, edges and corners, depends strongly on the particle size.^{16,17,30} Also the ratio of bulk to surface atoms is changing, which has a direct influence on the bind-

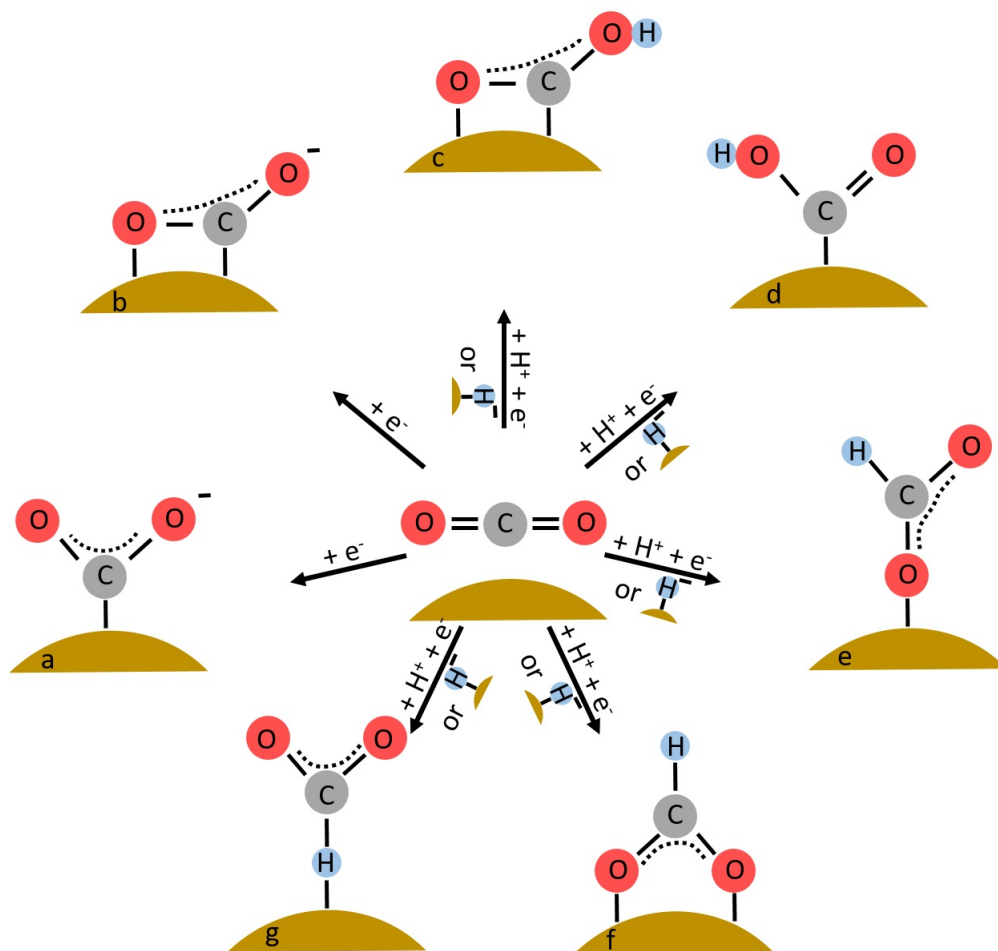


Figure 3: Mechanisms for the adsorption of CO_2 by a) and b) direct adsorption of a CO_2 —anion-radical and c) to g) by converted proton – electron transfer.^{9,23,24}

ing energies. In the literature, various intermediates and pathways for different products by specific catalysts are predicted. For some products different paths are postulated.^{9,20,22,40,41,42,43,44,45,46} Based on the experimental product and the catalyst (material, shape, structure, morphology and surfactants), it is possible to draw conclusions about the adsorption mechanism for CO_2 of the tested catalyst. Therefore, metallic nanoparticles and their size and potential-depending catalytic properties are of great interest for investigation of the CO_2RR mechanism. CO is the main product, for Au catalysts in various sizes, forms and shapes. Also $HCOOH$ and CH_3OH as products are found for some meso/ nano-porous structures, with low selectivity ($< 1\%$).²⁴ Calculations predict, that the final products often depend on the first intermediate, as $*COOH$ leads to CO , while $*OCOH$ leads to $HCOO^-$. Due to its oxophobic character, $*OCOH$ is unlikely to form on the Au surface (e.g. Fig. 3 f and e).⁴⁷ Also the pH has a strong influence, as a $pH < 6.8$ promotes CO , whereas a pH above 8 promotes Formate.^{48,49} Formaldehyde is seldom found as product of the CO_2RR , but often proposed as intermediate for other products, such as Methanol, Methane or C_2+ products. This relies on the energetically favorable self-condensation of Formaldehyde, where it reacts further to a great variety of possible products.²² Also important to note is, that Formaldehyde is energetically favored unbound to the metal surfaces, compared to the adsorbed $*CHOH$, according to DFT calculations.²⁰ Formaldehyde as intermediate is proposed for dif-

ferent mechanisms on different metal catalysts. The assumed first intermediates are *OCOH , *COOH and *OOCH , which are shown in Fig. 3 c, d and f. For *Au* nanocluster, the proposed mechanism to CH_4 , CH_2OH^* , Ethanol or Formate were calculated by DFT. However, there are some unlikely aspects in these calculations. Formaldehyde and CO are assumed to stay adsorbed as intermediates or there are oxygen-bound adsorbed intermediates. These aspects are unlikely because, as previously mentioned, *CO is usually not stable at *Au*-surfaces, the oxophobic character of *Au* and the calculated energetic favorability of desorbed Formaldehyde compared to the adsorbed *CHOH . Still, DFT calculations of desorbed Formaldehyde as product show an energetic favorability compared to CO .^{9,20,38,44,50} For Methanol as product catalyzed by *Au*, *CO is a proposed intermediate. This is contradictory, as *CO has generally a low binding energy to *Au* surfaces. This explains the low selectivity for Methanol that has been reported in literature.²⁴ Cave et al.⁴¹ proposed that undercoordinated *Au* atoms should promote the *CO binding and the reaction mechanism to Methanol, with Formaldehyde as desorbed intermediate. This promotes further the importance of the removal of Thiolates, as they are presumably bond stronger to the undercoordinated sides of AuNP.⁵¹ Thus, a broad range of possible products can be obtained by Gold as catalyst, depending on its shape, structure, morphology and surfactants. This great variability of CO2RR products by manipulating the catalyst, for example by adsorbed surface species is shown in our work “Multimethod Approach to the Low-Overpotential Region of Micro- to Macro-Scale Working Electrodes of Sub-10 nm Gold Nanoparticles in the CO_2 Reduction Reaction”⁵², which shows the crucial role of smallest remaining entities of stabilizer.

1.2 Nanomaterials

Nanomaterials are objects of a scale below 100 nm in at least one dimension. Nanoparticles are particles in the size range of 1 nm to 100 nm. Below 1 nm, particles usually are named nanocluster and above 100 nm microparticles are meant. Further this work will be focused on metal nanoparticles, which hold great promises in various disciplines. Just to name a few, there is heterogeneous catalysis, drug delivery and the usage as sensors in various applications.^{53,54}

1.2.1 Properties of nanomaterials

By downsizing bulk material to nanometer size, properties change, which implies great opportunities to tune materials for specific applications. The surface-to-volume ratio of the atoms of particles are greatly increasing with decreasing sizes. Surface atoms of particles behave differently than the bulk atoms due to their different electron density.⁵³ By the asymmetrical force of the outside atoms, the surface density is changed because the force acts towards the inside creating a surface tension, which is shortening the bonds of the surface atom layer.⁵⁴ For AuNP, AgNP and CuNP, the bond length is contracted between 4 % to 30 % depending on the size.⁵⁵ The shorter bond increases the stiffness and the stability of the nanoparticles. It also affects the mechanical, electrical and thermal properties.⁵⁴ The bandgap structure is also influenced strongly, if the *de Broglie* wavelength of the charge carrier, in case of the nanoparticles–electrons, is greater than the size of the nanoparticle, because of the limitation of the wave function (e.g. 7.6 nm for electrons in vacuum).

The bandgap increases with decreasing particle size, and therefore the conductivity and the density of states decrease too. Accordingly, the optical properties are changed, as the absorbed and emitted photons depend on the energy difference between the states among the bands.^{54,56} The bulk material is always energetically favored compared to the nanoparticles; therefore, in an infinite amount of time, the nanoparticles will age and agglomerate to bulk material. To overcome this effect, an energetic barrier is introduced, for example a surface charge, surface adsorbates (e.g. surfactant or stabilizer) or immobilization on supporting material. The higher energy level of the nanostructure compared to the bulk also affects the nanoparticle properties by changing the energy density. The quantum-size-effect describes the hybrid electronic structure of nanoparticles. They have discrete energy levels of atoms or molecules and the band structure of metals. The quantum-size-effect is increasing with decreasing particle size. For metallic nanoparticles below 2 nm, the behavior of the electronic band structure diminishes and mainly the behavior of discrete energy levels is observed.⁵⁴ A further size-dependent effect is the surface-plasmon-resonance (SPR). There, the nanoparticles/ structure interact with an electromagnetic radiation of an appropriate wavelength, which excites the conducting electrons near the metal dielectric (e.g. metal-electrolyte) interface. This excitation leads to collective oscillation, depending on the surface morphology of the nanostructure.⁵⁷ Whereby a momentary electric field is generated, which can extend into the dielectric, changing the absorbance depending on size and morphology. This was first described by Mie⁵⁸ for spherical particles and then further devolved for different shapes by Gans⁵⁹. The effect depends on the size, shape, environment, dielectric function, effective mass and electron density. Through the SPR, the local electronic field around nanostructures can be increased hugely, which for example can be used for surface enhanced Raman spectroscopy, which offers an increase of the Raman signal by over a million in intensity and can enable single molecule spectroscopy.^{60,61} The strong property dependence of nanostructures in terms of size, shape, morphology and surfactants emphasizes the importance of the chosen synthesis method. The size dependent properties of coin metals as catalysts for the CO₂RR are strong. This is already shown by the results in Tab. 2, where the current density is greatly influenced by the shape of a Gold structure or by the particle size of AuNP, AgNP and CuNP.

1.2.2 Synthesis and supporting of nanoparticles

The synthesis of nanoparticles can be achieved using a top-down or a bottom-up approach. For the top-down process, bulk materials are downsized by different methods, such as mechanical milling, laser ablation or sputtering. In the bottom-up process nanomaterials are derived from smaller molecules, atoms or ions as precursors that assemble into the final nanostructure. Typical representatives of a bottom-up approach are solid state methods (e.g. physical and chemical vapor deposition), liquid state methods (e.g. sol gel, chemical reduction, hydrothermal and solvothermal), gas phase methods (e.g. spray, laser and flame pyrolysis) biological (also often named “green synthesis”) methods (e.g. bio reduction, by bacteria, by fungi and by plant/plant products) and other methods (e.g. electrochemical deposition). Several publications report the typical advantages and disadvantages of each approach.^{62,63}

To synthesize small metallic nanoparticles precisely, bottom-up methods are preferred. They usually enable the production of smaller particle distributions

and sizes. The liquid chemical reduction method is a well-known method for preparing nanoparticles below 10 nm. In the chemical reduction method commonly the metal is prepared as ion in solution and then reduced by a reducing agent. Typical reducing agents are Sodium Borohydride or Trisodium Citrate. To prevent the colloids from agglomeration, different methods may be used. One method is to add surfactants as stabilizer. The surfactants protect the nanoparticles from agglomeration by steric, electrostatic or electro-steric hindering. The stabilizers (e.g. Thiulates, Polyvinylpyrrolidone (PVP), Polyvinyl alcohol (PVA), Trisodium Citrate) are added to the synthesis and bind or adsorb to the nanoparticle surface. They generate a repulsive surface charge or build a spatial demarcation (or both) which prevents convergence. Another method is to induce a surface charge to the nanoparticle itself. The charge must be strong enough for repulsive forces to prevent the particles from agglomeration. Another method is to synthesize the nanoparticles directly on a supporting material, where they are adsorbed or bound and thus prevent agglomeration. Problematic for the reduction method is that the ions of the metal salt and the reducing agent often promote aging effects of the colloids. Therefore, it is advantageous to minimize this effect, for example by synthesizing the particles in two phases, that do not mix well. A phase transfer agent is applied to transfer the freshly prepared nanoparticles, or the metal ion precursor is transferred beforehand, often as metal-complex. Then the metal ion is reduced to the particle at the phase boundary. The ions that promote particle aging are remaining in the Aqueous solution and can be removed afterwards. This method enables the synthesis with increased stable colloidal suspension. An exemplary process for the 2-phase synthesis of AuNP⁶⁴, where the Gold-ion is phase-transferred, is shown in Fig. 4.⁶⁵ The synthesis of AuNP is the focus of our work “Comparative Study of the Synthesis sub-10 nm Carbon-Supported Gold Nanoparticles and their Suitability for the Methanol Electrooxidation in Alkaline Media”⁶⁶. This publication provides a more detailed overview about five different synthesis procedures and their results. Different published methods of synthesis were tested using a liquid reducing synthesis in one phase synthesis, in a 2-phase synthesis, in a synthesis in which the AuNP were prepared directly on supporting material and in a colloidal synthesis without stabilizer. For the 2-phase synthesis of AgNP and for the synthesis of CuNP see chapter 3.2.1 and 3.2.2.

Metal nanoparticles as colloids are impractical for the application as (electro)catalyst. Therefore, they are often immobilized on supporting material. Typical supporting materials are metal oxides like TiO_2 ⁶⁷, ZnO ⁶⁸ or SiO_2 ⁶⁸ or Carbon-based materials like Carbon nanotubes (CNT)⁶⁹, multiwalled Carbon nanotubes (MWCNT)⁶⁹ or Carbon blacks⁷⁰. Supporting is increasing the stability and the applicability. The supporting material also can have synergetic effects, influence the activity and selectivity of the catalyst. This is well-studied for example for polymer electrolyte membrane fuel cells (PEM-FC). The support needs to have (I) good electric conductivity, (II) large surface area, (III) high electrochemical stability and should allow (IV) easy recovery of the metals.^{71,72} For the PEM-FC, it was found that Platinum nanoparticles on MWCNT have an improved stability over Platinum nanoparticles on Vulcan XC72.⁷³ The activity can be influenced strongly, as for $Pt - Ru$ nanoparticles during the Methanol oxidation the current density is strongly increased, if Carbon nanofibers are used as support, compared to Vulcan XC72.⁷⁴ This enhances the importance of investigating the effects of different supporting materials. Depending on the colloidal synthesis,

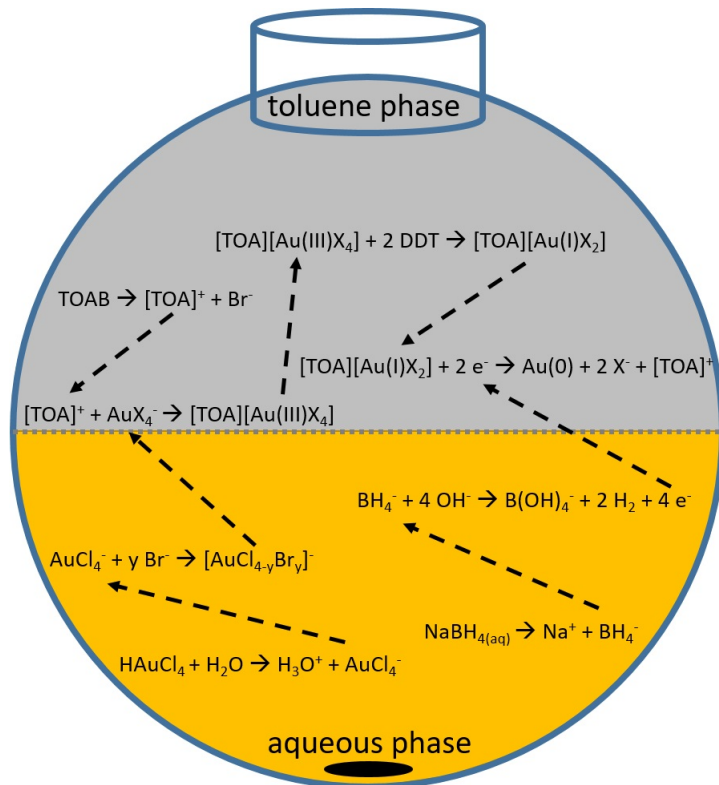


Figure 4: The 2-phase synthesis of AuNP, with Tetraoctylammoniumbromide (TOAB) as phase transfer agent, NaBH_4 as reducing agent, HAuCl_4 as Gold source, 1-dodecanethiolate (1-DDT) as stabilizer and 2-phases, Water and Toluene, visualization based on Goulet et al.⁶⁵

the supported nanoparticles are covered by the stabilizer. The stabilizer modifies the electronic structure and the accessibility and manipulates the activity and selectivity. Also, the stabilizer may react during the catalytic reaction, which would impact the catalyst and the catalytic reaction. Therefore, the removal of the stabilizer is of great interest. Even if the stabilizer is completely removed, the metal surface will be covered, partly being bound to the support and partly by smaller molecules as adsorbates. Our work “Quantifying the removal of stabilizing thiolates from Gold nanoparticles on different carbon supports and the effect on their electrochemical properties”⁷⁵ provides a deeper insight into exemplary effects of stabilizers to AuNP and experimental processes to remove the stabilizer. As already mentioned before, the traces of remaining stabilizer have crucial role for the CO₂RR on AuNP, which is emphasized in our work “Multimethod Approach to the Low-Overpotential Region of Micro- to Macro-Scale Working Electrodes of Sub-10 nm Gold Nanoparticles in the CO₂ Reduction Reaction”⁵².

1.2.3 Degradation mechanisms of nanoparticles

For the applicability of nanostructured catalysts, next to activity and selectivity the stability is of great interest, as it is substantial for an industrial usage. Typical degradation mechanisms of metallic nanostructured electrocatalysts are the (I) Ostwald-ripening, (II) dissolution, (III) agglomeration, (IV) detachment, (V) poisoning, (VI) reshaping and (VII) fragmentation. Ostwald-ripening is dissolution of metal ions from smaller particles, diffusion of these, followed by re-deposition to larger particles. For the dissolution mechanism, metal ions are dissolving into the

electrolyte, but are not re-deposited. Agglomeration describes the process of particles enclose together, for example by surface mobility and form larger particles. Detachment is the loss of particles in the electrolyte, by losing the contact to the electrode/ support. Poisoning is the strong adsorption of species to the metal surface, blocking the site for educts. Reshaping is the reformation of nanostructures by surface mobility or dissolving and re-depositing of atoms and/ or of particles and thereby build a new shape. Fragmentation is the process, where parts of bigger particles detach and are lost as active surface.^{76,77,78} The processes of degradation can be monitored *in situ* by electrochemical methods well, however these methods offer little mechanistic insights. A strong method for the observation of even single particles and their behavior before and after an electrochemical process is the identical-location transmission electron microscopy.^{78,79}

1.3 Challenges of using coinage metals in the CO_2 reduction

Coinage metals are of great interest as nano-catalyst. All three, Copper, Silver and Gold, have their own challenges. CuNP are oxidizing in air and building an oxide layer, and if brought into aqueous electrolyte, they dissolve further by oxidizing. If they are used for the CO2RR, the oxide layer is reduced with lowering the potential. Still the time period between the immersion of the electrode to applying the negative potential needs to be as short as possible, to impede Copper loss and prevent significant changes of the Copper catalyst. Therefore, the characterization of the CuNP before the reaction is only in partial agreement with the actual state of the catalyst during the reaction. The degree of agreement depends on the experimental setup and the handling during the experiment. The impact of solute Copper species in the electrolyte is unforeseeable. These uncertainties make the handling of CuNP difficult for the electrocatalysis. Still Copper is one of the most investigated CO2RR catalysts, because of its unique role as the only bulk metal producing significant amounts of hydrocarbons, such as Methane or C_{2+} products.^{26,80} (see chapter 1.1). Because of its inert behavior, Gold as bulk material has been of little interest for the catalysis, until Haruta et al.⁸¹ discovered the high activity of AuNP supported on metal oxides for the CO oxidation. Since then, Gold nanostructures in various shapes and sizes received increasing attention for the heterogeneous catalysis. Gold is one of the most stable catalysts with very high selectivity and some of the lowest observed overpotentials for the CO2RR towards CO .²⁶ The high selectivity at low overpotentials designates an extraordinary capability of AuNP for the CO2RR. Therefore, modifying Gold catalyst for further understanding of the mechanism of the CO2RR is of great interest.

Silver would be more economic feasible than Gold, with a comparable high selectivity towards CO . Increasing effort is taken to understand the catalytic mechanism of the CO2RR on Silver.⁸² Problematic for AgNP in comparison to AuNP is the lower stability to oxidative stress and the surface reformation of the surface oxide layer after electrochemical reduction by the low working potentials of the CO2RR. This makes the understanding more difficult as the catalyst changes in the beginning of the process. Therefore, *in situ* characterization is required to understand surface behaviors.^{83,84} The Oxygen affinity of Silver also offers interesting possibilities by introducing a specific amount of Oxygen to the Silver lattice, to modify the material and therefore tune the catalytic properties further.^{85,86}

2 Scope of the thesis

The importance of coin metal nanoparticles as catalysts in various fields, specifically the electrocatalysis, is well known. For the improvement and economic feasibility of catalyst development, the understanding of the catalytic processes on metallic nanoparticles is indispensable. The particle size, supporting material and stabilizer play a crucial role. As the properties of the nanoparticles change with the surface morphology, shape, particle size, supporting material and stabilizer, it is important to have a well-controlled synthesis and in depth characterization of the nanoparticles itself and supported. Furthermore, for the understanding of their catalytic behavior, the use of supported nanoparticles without any remaining stabilizer is essential, as stabilizer introduce complexity into the system. Additionally, the electrochemical stability of the nanoparticles in different pH environments is necessary for their application as a catalyst. The human world is in desperate need of renewable energy sources to reduce its Carbon dioxide footprint and mitigate global warming. Therefore, the CO₂RR is of great interest. A renewable Carbon source, at best in a closed cycle, would be a great improvement to mitigate ecological damage by the usage of fossil fuels.

This thesis seeks to deepen understanding of the CO₂RR mechanism at sub-10 nm Carbon-supported Gold metal nanoparticles. This particle size range is especially intriguing because the properties of the particles alter drastically from those of a bulk metal to those of molecules/ atoms. For this reason, the size controlled synthesis of coin metal nanoparticles was investigated thoroughly. A special emphasis was placed on the removal of stabilizer from the Carbon supported coin metal nanoparticles, as even the smallest remaining amounts of Stabilizer can profoundly affect the CO₂RR mechanism by binding specifically to certain sites on the nanoparticle surface. Gold is widely renowned for its selectivity towards *CO* and its low activity for the competing HER at low overpotentials. Selectivities of $< 1\%$ for MeOH is known. Therefore, the understanding of the mechanism depending on the particles size, stabilizer and support of *Au – C* for the CO₂RR is highly desirable. Special attention is given to the low overpotential region, as it is often overlooked in literature. To shed some light on this process, the *Au – C* catalysts were investigated by half-cell experiments, full-cell experiments and scanning electrochemical microscopy, which provides additional insights into the behavior of electrode upscaling.

3 Published and unpublished research

This chapters introduce our relevant publications regarding this thesis and present unpublished results of interest. For the publications title, author and abstracts are given, while the full text is shown in the appendix. The unpublished results are divided into two main sections, regarding the synthesis of Silver and Copper nanoparticles.

3.1 Introduction of relevant publications

“Comparative Study of the Synthesis of sub-10 nm Carbon-Supported Gold Nanoparticles and their Suitability for Methanol Electrooxidation in Alkaline Media”

Authors: Emil Dieterich, Simon-Johannes Kinkelin, and Michael Bron

Abstract: “Gold nanoparticles where synthesized and supported on carbon, or directly synthesized on carbon according to five different methods reported in literature, aiming at particles < 10 nm. Characterization was done with transmission electron microscopy and thermogravimetric analysis. Although all syntheses yielded particles with an average diameter < 10 nm, the formation of few very large particles, where a relatively large amount of *Au* is buried, as well as loss during the supporting procedure led to the exclusion of four of the five tested methods for further studies. The most promising AuNPs supported on carbon where tested for the methanol electrooxidation (MEO) in alkaline media. Four different *Au*-loadings where realized, and supporting led to moderate particle growth depending on the loading. To compare MEO activity of the samples with different *Au*-loadings a conversion factor was developed where the MEO activity can be compared in terms of NP size and *Au*-loading.”⁶⁶

Full text starts on p. 39

“Quantifying the removal of stabilizing thiolates from gold nanoparticles on different carbon supports and the effect on their electrochemical properties”

Authors: Emil Dieterich, Simon-Johannes Kinkelin, Matthias Steimecke and Michael Bron

Abstract: “Gold nanoparticles < 10 nm in size are typically prepared using stabilizing agents, e.g. thiolates. Often standard recipes from literature are used to presumably remove these stabilisers to liberate the surface, e.g. for catalytic or electrocatalytic applications, however the success of these procedures is often not verified. In this work, thiolate-stabilised AuNPs of ca. 2 nm in size were synthesized and supported onto three different carbon supports, resulting in loadings from 15 to 25 wt% *Au*. These materials were post treated using three different methods in varying gas atmospheres to remove the stabilizing agent and to liberate the surface for electrochemical applications. Using thermogravimetry – mass spectroscopy (TG-MS), the amount of removed stabilizer was determined to be up to 95 %. Identical location scanning transmission electron microscopy (il-(S)TEM) measurments revealed moderate particle growth but a stable support during the treatments, the latter was also confirmed by Raman spectroscopy. All treatments significantly improved the electrochemically accessible gold surface. In general, the results presented here point out the importance of quantitatively

verifying the success of any catalyst post treatment with the aim of stabilizer removal.”⁷⁵

Full text starts on p. 59.

“Multimethod Approach to the Low-Overpotential Region of Micro- to Macro-Scale Working Electrodes of Sub-10 nm Gold Nanoparticles in the CO_2 Reduction Reaction”

Authors: Emil Dieterich, Lukas Herrmann, Olga Dzhyginas, Lukas Binnenböse, Matthias Steimecke, Simon-Johannes Kinkelin and Micheal Bron

Abstract: “The electrochemical carbon dioxide reduction reaction (CO2RR) over carbon-supported gold nanoparticles (AuNP) was investigated using a broad variety of (electro)analytical methods, including linear sweep voltammetry with a rotating disk electrode (LSV-RDE), sample-generation tip-collection mode of scanning electrochemical microscopy (SG/TC-SECM), as well as full cell tests with highly sensitive online gas chromatography (GC). In contrast to most other studies, this work focuses on the low-overpotential region (0 to $-0.4 V$ vs RHE) where initial product formation is already detected and addresses micro- to macro-sized electrodes. The sub-10 nm AuNPs supported on three different carbon supports (CNTs and carbon blacks) were pretreated in H_2/Ar to remove the stabilizer used during AuNP synthesis. LSV-RDE points toward different CO2RR mechanisms at the samples, additionally confirmed by the SG/TC-SECM and full cell tests with online GC. Besides H_2 and CO , the AuNP supported on carbon nanotubes showed significant evolution of H_2CO in contrast to the other two samples, which was additionally confirmed by accumulating the product during chronoamperometric RDE experiments followed by mass spectroscopic analysis. Surface analysis indicated a complete removal of residual thiolate stabilizer molecules exclusively at the AuNPs supported on carbon nanotubes, which may result in a change in the adsorption geometry or reaction mechanism at this sample. The results demonstrate the effectiveness of the combination of these multiple methods to investigate the CO2RR in the low-overpotential region.”⁵²

Full text starts on p. 81.

3.2 Unpublished research

As described for the CO2RR, (bulk)materials are often classified according to their main product. Coin metals are highly interesting as Gold and Silver presents a high selectivity for CO . Copper is the only metal, where higher reduced species are found, such as Methane or C_{2+} . As already discussed, particle size has a great influence on the CO2RR. Therefore, we present here synthesis methods for AgNP and CuNP.

3.2.1 Synthesis of Silver nanoparticles

Results and discussion The synthesis route for AgNP is adapted to the AuNP synthesis process modified by us⁶⁶ developed by Brust et al.⁶⁴ Using a 2-phase synthesis route, but differently for AgNP not the metal ions, instead the particles are phase transferred, which needs an increased phase transfer time of 40 h.

To evaluate the particle size of the AgNP, TEM images were prepared. For the metal

loading and the amount of removed stabilizer from the supported samples, depending on the applied post-treatment TG-MS measurements have been performed.⁷⁵ Fig. 5 presents TEM images of AgNP, while Fig. 6 presents TEM images of AgNP supported on Vulcan and post-treated. The AgNP-ODT have an average size of 2.4 nm, AgNP-DDT 3.1 nm and AgNP-PET 7.3 nm. The supported and post-treated particles are larger (H_2 - 14.0 nm, O_2 - 16.7 nm) and got an Ag loading of 15.9 wt.%. The stabilizer was completely removed by the H_2 -post-treatment. The results of TEM and TG-MS are summarized in Tab. 3 and Fig. 7, which presents the particle size distribution. Above 98 % of the AgNP-DDT were below 10 nm in size. Due to the particle range up to 27.1 nm, around 4.5 % of the mass was in particles > 10 nm. The particle size distribution of the unsupported particles was narrow compared to that reported in the literature.^{87,88,89,90}

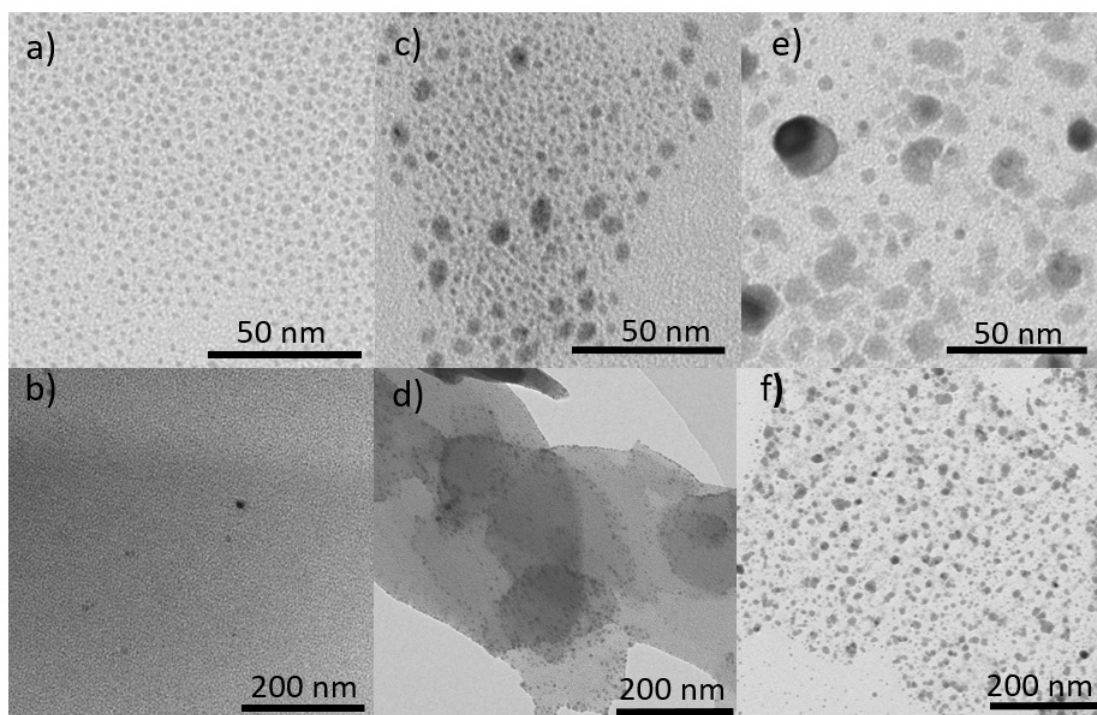


Figure 5: TEM images of a), b) AgNP stabilized with 1-ODT, c), d) stabilized with 1-DDT and e), f) stabilized with 1-PET.

Fig. 5 and 7 reveal the particle size distribution of AgNP stabilized with 1-ODT and 1-DDT which was generally below 5 nm, while for 1-PET a wide particle size distribution appears. The larger particle size of AgNP compared to AuNP was attributed to the difference in the phase-transfer condition during the 2-phase synthesis (Fig. 4); AuNP was phase-transferred from the aqueous phase to the organic phase as an *Au*-complex and then reduced at the phase boundary, while AgNP were reduced in the aqueous phase to form the AgNP before phase-transfer.⁹¹ Therefore, the benefits of the 2-phase synthesis are reduced for the AgNP synthesis, as the potential degradation promoters in the aqueous phase are affecting the AgNP during the reducing step. Another difference between AgNP and AuNP, the Thiolates behave different when binding.⁹² This are reasons for the different results of the AgNP and AuNP synthesis.

For the synthesis of AgNP, different synthesis parameters and procedures have been

Table 3: Particle size, standard deviation, particle size range, metal loading, metal transfer rate (calculated *Ag* loading of 20 wt.%) and the amount of removed stabilizer of the synthesized AgNP with three different stabilizers, 1-ODT, 1-DDT and 1-PET, and for the AgNP-DDT supported and post-treated on Vulcan. In brackets ($\pm \dots$) the standard deviation is given.

Sample	Size nm	in Size range in nm	Particles mea- sured	<i>Ag</i> load- ing wt.%	<i>Ag</i> trans- fer rate in %	Removed stabilizer in %
<i>AgNP</i> _{ODT}	2.4 (\pm 2.4)	0.6 - 70.6	1800	-	-	-
<i>AgNP</i> _{DDT}	3.1 (\pm 1.9)	0.8 - 27.1	2936	-	-	-
<i>AgNP</i> _{PET}	7.3 (\pm 5.7)	1.1 - 135.0	2471	-	-	-
<i>Ag - Vulcan - H₂</i>	14.0 (\pm 4.2)	5.1 - 41.1	1800	15.9 (\pm 2.4)	79.5	100
<i>Ag - Vulcan - O₂</i>	16.7 (\pm 6.7)	4.4 - 51.1	1800	15.9 (\pm 2.4)	79.5	74.7

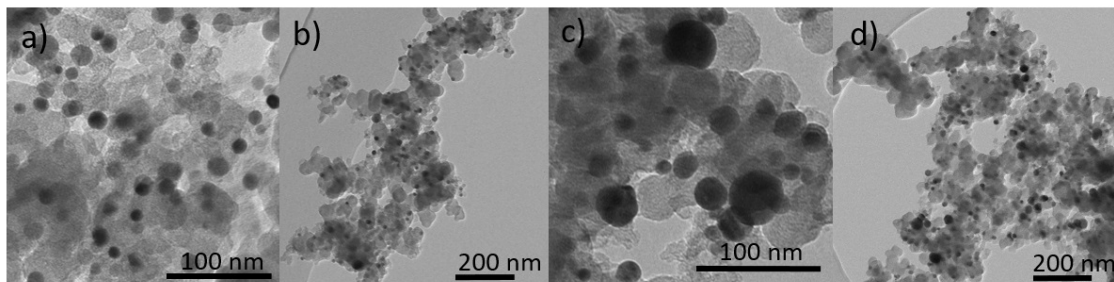


Figure 6: TEM images of a), b) *Ag - DDT - Vulcan - H₂* and c), d) *Ag - DDT - Vulcan - O₂*, the different magnifications to show the inhomogeneous particle distribution on Vulcan.

tested, which are summarized in Tab. 4. Compared with the here presented syntheses, the synthesis of Kang et al.⁹³ showed also small particles, but with a loss of *Ag* during the phase transfer and a in comparison much greater distribution of particle sizes.

The post-treatment of *Ag-Vulcan* samples was modified from a published procedure⁷⁰, which consisted of heat treatment in *O₂* followed by an *H₂* atmosphere. This method was previously studied in our work “Quantifying the removal of stabilizing thiolates from Gold nanoparticles on different Carbon supports and the effect on their electrochemical properties”⁷⁵ and demonstrated the superiority of a single *H₂* or *O₂* post-treatment over the combined post-treatments. The post-treated specific results of *Ag-Vulcan* samples show that the *O₂* post-treatment yielded a broader particle size, size distribution and size range, and removed less stabilizer compared to the *H₂* post-treatment. However, the average particle size of *Ag - Vulcan - H₂* was above 10 nm and 89 % of the AgNP were > 10 nm (\sim 90 % for *Ag - Vulcan - O₂*). Considering the greater increase in particle size with the *O₂* post-treatment, the combined method was not investigated. The theoretical *Ag* loading of 20 wt.% was calculated for the *Ag-Vulcan* synthesis, yet around 20.5 % of the Silver was lost during the process, according to the thermogravimetric analysis, with no difference between post-treatments.

To conclude, AgNPs with average particle sizes of 2.4 and 3.1 nm and a narrow size distribution were synthesized. AgNPs with an average size of 7.3 nm were also synthesized but with a wider size distribution, which limits their potential use. Changing the Thiolate stabilizer allowed for size variation, comparable with the observations for the AuNP synthesis.⁶⁶ Subsequent post-treatment with Oxygen and

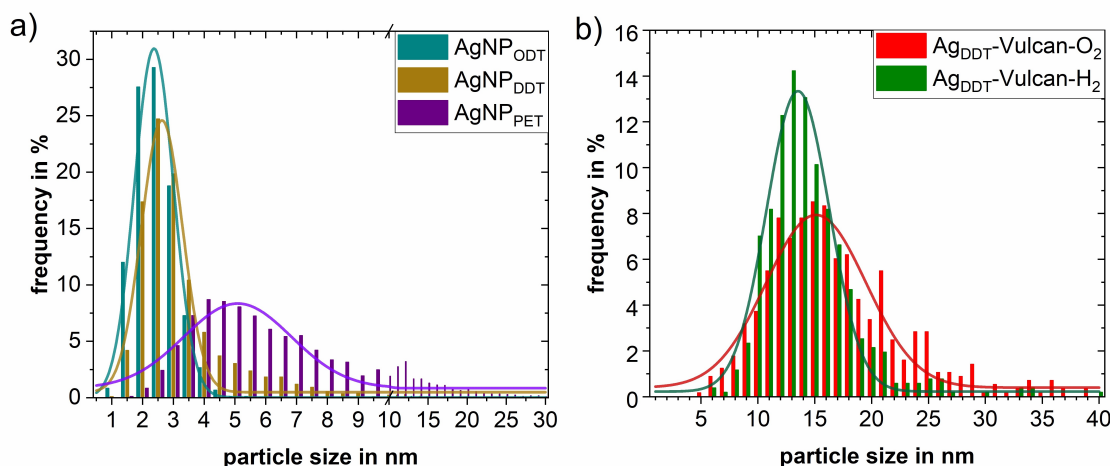


Figure 7: Particle size distribution of a) AgNP synthesized with different stabilizers and b) AgNP – O₂ and –H₂ post treated on Vulcan support.

Hydrogen removed the stabilizer by 75 % or 100 % and increased the average particle size to 16.7 and 14.0 nm, respectively. However, 20.5 % Silver was lost during the synthesis of AgNP, the supporting and post-treatment.

Experimental For the AgNP synthesis, 984.22 mg of Tetraoctylammoniumbromide (TOAB) dissolved in 36 ml Toluene (50 mM) and 20 ml of 30 mM AgNO₃ (aq) was added, then stirred for 25 min (300 rpm) and 431 ml 1-DDT was added. Following, 15 ml of 0.4 M NaBH₄ (aq) freshly prepared solution was added dropwise. For the synthesis, the molar ratio of metal precursor/ stabilizer/ phase transfer agent/ reducing agent was 1/3/3/10, respectively. Afterwards, the emulsion was stirred (300 rpm) for 40 h followed by decanting the aqueous phase. The Toluene suspension was reduced to a tenth of its volume by use of a rotary evaporator (55 °C, 125-115 mbar). Then 90 ml of abs. EtOH were added and the suspension is stored at 4 °C for at least 16 h. After the storage at 4 °C, the precipitate was separated by centrifugation (5000 rpm, 30 min), washed twice with abs. EtOH and once with Acetone (each 40 ml). The product was dispersed in 3 ml Toluene, 7 ml of abs. EtOH were added, and the dispersion was stored at 4 °C.

The supporting of the AgNP on Vulcan was prepared by the same method like as used for AuNP and has been described earlier⁷⁵. Vulcan was dispersed by sonication in n-hexane (20 ml/ 100 mg n-hexane/ Vulcan) for 6 h. The AgNP suspension was shaken twice, followed by sonication for 30 min. The AgNP suspension was added to the Vulcan suspension and sonicated further 30 min, followed by stirring (300 rpm) overnight. Afterwards, the suspension was separated by centrifugation (5000 rpm, 30 min) and washed twice with abs. EtOH. The suspending agent was removed by decantation. The precipitate was dried at room temperature at ~ 500 mbar. The black powder like product was stored in brown glass vials to decrease the possible impact of UV-light. The calculated theoretical Ag loading was 20 wt.%.

Different post-treatments for the removal of the stabilizer have been described in the literature⁷⁰ and are already well-discussed in our work⁷⁵. Shortly, the Ag-Vulcan sample was placed in a quartz glass vessel (15 * 50 * 10 mm, w * l * h) in a quartz glass tube (Ø 35 mm) in a tube furnace. The tube was flushed with Ar (6 l * h⁻¹)

Table 4: AgNP synthesis modified according to published procedures, reported resulting particle size, specifically altered synthesis parameters and the experimentally resulting particle sizes and size ranges.

Literature	Literature reported particle size in nm	Particle size (stdv.) in nm	Particle size range in nm	Comments
Oliveira et al. ⁹⁰	3.8	4.2 - 8.2 ($\pm 5.2 - 8.7$)	0.5 - 220	Large agglomeration of NP, 2-phase synthesis Toluene/ Water
He et al. ⁹⁴	4	1.6 - 2 (± 6)	0.5 - 63.3	High Ag loss during synthesis, 1-phase synthesis in Water, Sodium Citrate as stabilizer
Kang et al. ⁹³	7.7 - 7.9	4.2 - 4.6 ($\pm 1.6 - 2.7$)	1.9 - 18.3	2-phase synthesis Toluene/ Water, 1-hexadecane-sulfonic acid as phase transfer agent, particle distribution not distinct, very wide, high FWHM of Gaussian distribution, loss of Ag in aqueous phase
Modified from Brust et al. ⁶⁴	-	5.0 (± 5.6)	0.5 - 88.3	2-phase synthesis Toluene/ Water, phase transfer time 3 h, molar ratio (Ag/1-DDT/TOAB/ $NaBH_4$) 1/0.8/4.4/11.1, more precise particle distribution compared to ⁹³
		4.2 (± 0.7)	0.6 - 48.5	Molar ratio 1/3/3/10, 3 h phase transfer time
		3.5 (± 9.2)	1 - 325	Molar ratio 1/3/3/10, 20 min phase transfer time
		4.7 (± 3.7)	1 - 39	Molar ratio 1/3/3/10, 16 h phase transfer time

for 30 min, followed by starting the gas mixtures of 20 % O_2/Ar (total $6 l * h^{-1}$) or 15 % H_2/Ar (total $6 l * h^{-1}$). Then the temperature was raised by $10 K * min^{-1}$ to the aimed temperature of 300 °C for 20 % O_2/Ar or 400 °C for 15 % H_2/Ar . This ambient was kept for 1 h. After 1 h the atmosphere was changed to Ar for cooling down. The samples were extracted between 40-20 °C.

For the synthesis of the AgNP, the TOAB Toluene solution was clear, while the aqueous $AgNO_3$ solution was white cloudy. After mixing them, white drops can be observed in the clear Toluene phase. After the insertion of 1-DDT, the aqueous phase started being slightly white-cloudy. During the addition of the reducing agent, first a yellow coloring followed by a reddish coloring is observed. After the complete addition, the color is dark brown-black. After 40 h of stirring, the aqueous phase was clear, the Toluene phase was black. Following centrifugation, the Toluene phase was grayish with a black sediment. During the washing procedure, the liquids were clear after centrifugation. The redispersed product is black. For the supporting process, the n-hexane suspension is black with easily recognizable agglomerates. The suspension of the AgNP got a sediment on the bottom, which is suspended well after being shaken twice and sonication. The precipitate was a black powder. During the post-treatments, no visible changes of the samples were observed.

3.2.2 Synthesis of Copper nanoparticles

Results and discussion The synthesis of CuNP was conducted according to Ang et al.⁹⁵ in an inert atmosphere. A challenge in the synthesis of CuNP are the Oxygen free synthesis conditions, as otherwise the Cu-oxide (nano)particles are formed. Fig. 8 presents TEM images used for evaluating the particle size. Tab. 5 summarizes the parameters of the synthesized samples. The impact of changing the stabilizer was studied for 1-ODT and 1-DDT. 1-PET was not investigated due to the wide particle size distribution showed for AuNP and AgNP. The average particle size was 1.9 nm for CuNP-ODT and for CuNP-DDT 2.3 nm, with no particles larger than 12.3 nm. The *C*-chain length of the Thiolates employed in the synthesis of CuNP supported the finding that longer *C*-chains produce smaller particles, as observed with AuNP and AgNP. Raman spectroscopy was employed to investigate the oxidation states of the CuNP (Fig. 9 c and d), showing a small amount of Cu_2O and indicating mostly Cu^0 , by the steady intensity increase with increasing cm^{-1} .⁹⁶ It is likely that the slight oxidation of the CuNP is due to impurities in the atmosphere, such as traces of Oxygen and Water, as well as of the crystals of Copper(II)nitrate*hemipenthydrate used during the synthesis. The oxidation state of the CuNP is of great interest as Copper oxide dissolves into the electrolyte when it is electrochemically reduced.⁹⁷

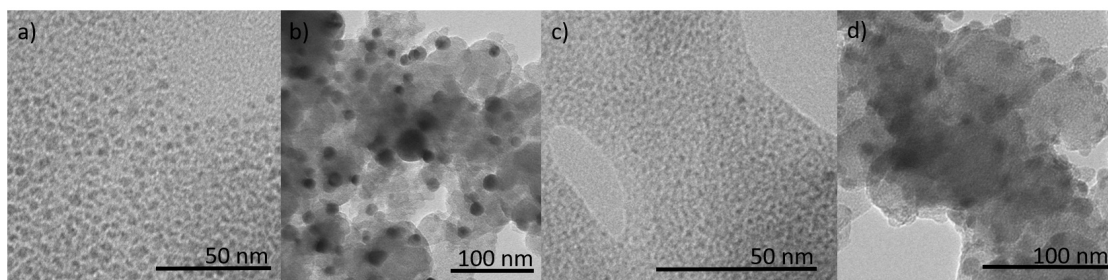


Figure 8: TEM images of a) CuNP-DDT, b) Cu-Vulcan-DDT- H_2 , c) CuNP-ODT and d) Cu-Vulcan-ODT- H_2 for the evaluation of particle size.

Table 5: Particle size, standard deviation, particle size range, metal loading, metal transfer rate (calculated Cu loading of 20 wt.%), the amount of removed stabilizer of the synthesized CuNP with two stabilizers, 1-ODT and 1-DDT, and these supported and post-treated on Vulcan. The standard deviation is given in brackets ($\pm \dots$).

Sample	Size nm	Size range in nm	Particles mea- sured	Ag load- ing in wt. %	Ag transfer rate in %	Removed stabi- lizer in %
$CuNP_{DDT}$	2.3 (± 0.9)	0.6 - 7.4	1729	-	-	-
$CuNP_{ODT}$	1.9 (± 1.0)	0.5 - 12.3	1639	-	-	-
$Cu_{DDT} - Vulcan - H_2$	8.9 (± 6.3)	0.6 - 48.4	2340	17.6	88.0	94
$Cu_{ODT} - Vulcan - H_2$	8.0 (± 3.7)	0.7 - 49.4	2637	18.9	94.5	94

Additionally, a synthesis similar to those used for AgNP and AuNP was investigated. Here Ethylene glycol was used instead the aqueous phase and all

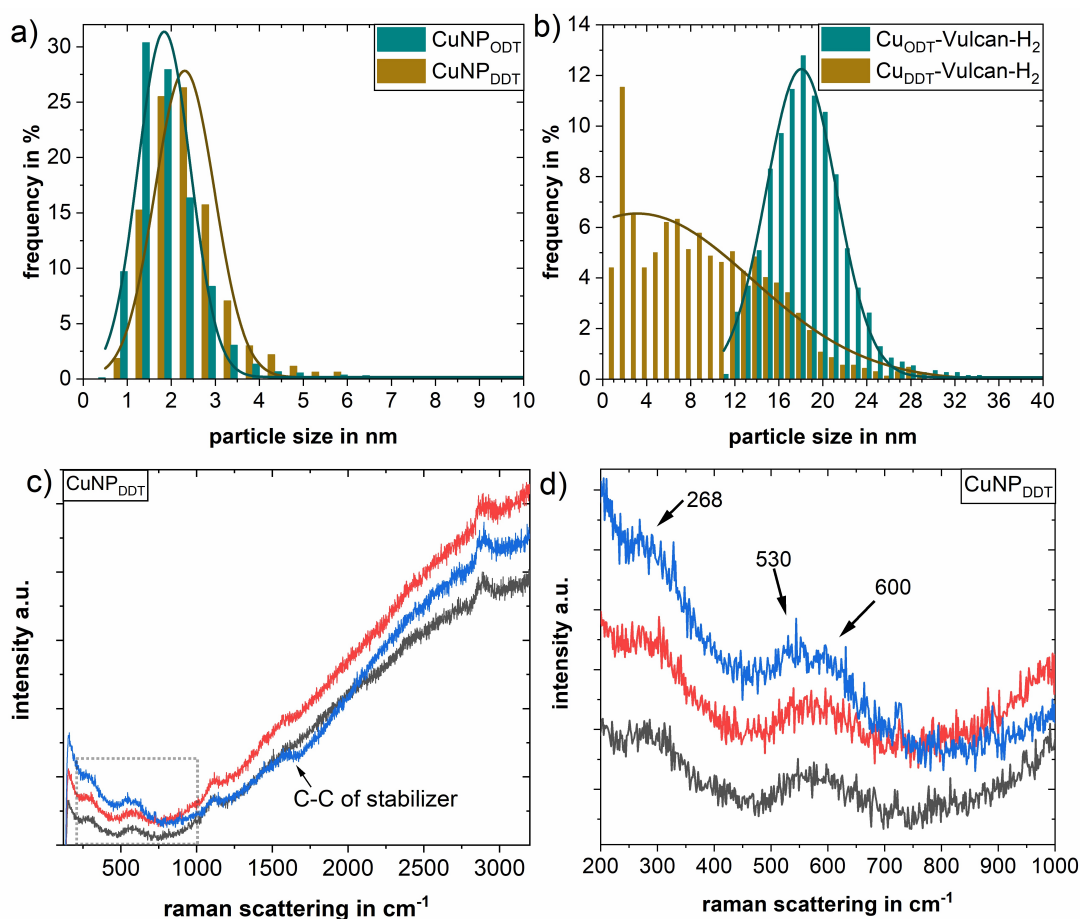


Figure 9: Particle size distribution of a) CuNP stabilized by either 1-DDT or 1-ODT, b) Cu-Vulcan- H_2 where the nanoparticles were either-synthesized with 1-DDT or 1-ODT and c) exemplary Raman measurements of CuNP-DDT to examine the composition of the CuNP with d) an enlargement of the Cu specific region, where the arrows are marking peaks at $\sim 268\text{ cm}^{-1}$, $\sim 530\text{ cm}^{-1}$ and $\sim 600\text{ cm}^{-1}$ of $C-C$ from the Thiolates.

solvents and suspension agents were flushed with Argon for at least 20 minutes, working in an Argon atmosphere, with a molar ratio of 1/3/3/10 (metal/ stabilizer/ phase transfer agent/ reducing agent). This synthesis yielded black particles with an average size of 2.8 nm (± 1.2 nm) and a size range of 0.9–19.8 nm. same supporting and post-treatment procedures applied for AuNP and AgNP were used for CuNP. The TEM images are shown in Fig. 8 b, d (Cu-Vulcan- H_2) and Fig. 10 (Cu-Vulcan- O_2). After performing the O_2 post-treatment, most of the sample was oxidized and a macroscopic change was observed, in parts with metallic-copper colored gloss and partly dark black precipitate (Fig. 11). Nanoparticles on Carbon support were observed but also micrometer large agglomerates were present.

Due to the Cu intake of the large agglomerations, the amount of Cu in nanoparticles was presumably minor. Therefore, the O_2 post-treatment was not investigated further. The H_2 post-treatment of the samples resulted in an average particle size of 8.9 nm (Cu-DDT-Vulcan- H_2) or. 8.0 nm (Cu-ODT-Vulcan- H_2). To mention is, the particle size distribution is wide and only for Cu-ODT-Vulcan- H_2 a Gaussian distribution fit worked well. With a metal loading of 17.6 wt.% to 18.9 wt.% (Cu-DDT-Vulcan- H_2 or. Cu-ODT-Vulcan- H_2) the metal loss was 5 to 12 %. According to the subsequent TG-MS analysis⁷⁵, the amount of removed

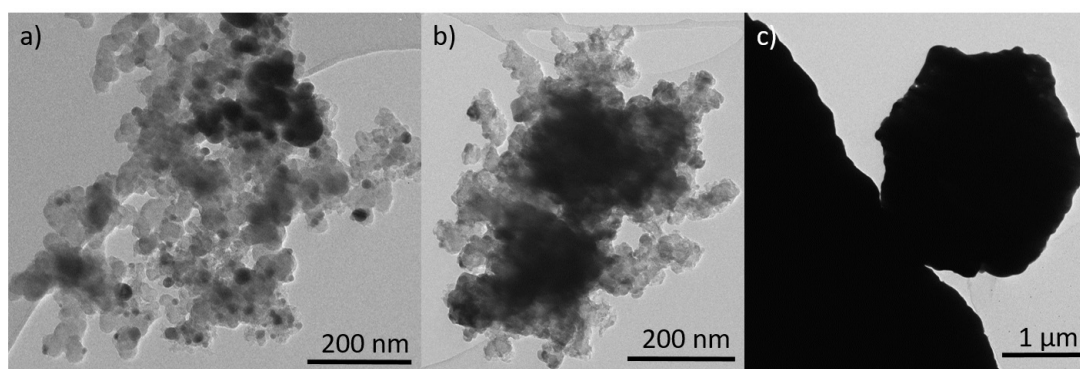


Figure 10: TEM images of Cu-Vulcan- O_2 where different areas of the product are presented. In a) nanoparticles are observed on the Carbon support, b) the dark area could be agglomeration of Copper species and c) is a Copper agglomeration

stabilizer by the H_2 post-treatment was 94 %.

In summary, CuNPs with average sizes of 1.9 nm and 2.3 nm and a narrow particle size distribution ranging from 0.6 nm to 12.3 nm were successfully synthesized. The size variation was achieved by altering the stabilizer. The CuNPs were primarily composed of Cu^0 with a small amount of Cu_2O . The O_2 post-treatment results were unsatisfactory due to heavy oxidation and inhomogeneity of the product. By contrast, the H_2 post-treatment had particle sizes of 8.0 nm for Cu-ODT-Vulcan- H_2 and 8.9 nm for Cu-DDT-Vulcan- H_2 . For Cu-DDT-Vulcan- H_2 , the particle size distribution did not fit a Gaussian distribution well, yet for Cu-ODT-Vulcan- H_2 , a Gaussian distribution was fitted well. The Cu loading of 17.6 to 18.9 wt.%, indicating Cu loss of 5 to 12 %. The H_2 post-treatment eliminated 94 % of the stabilizer from the bulk samples.

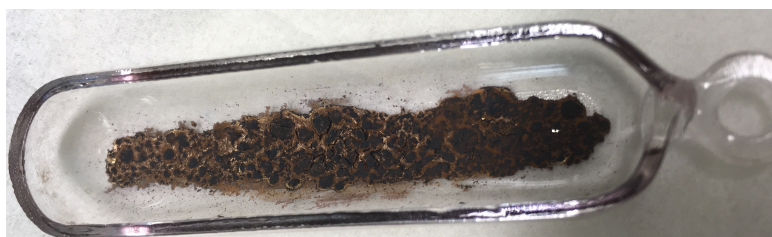


Figure 11: CuNP supported on Vulcan and post treated with 20 % O_2/Ar at 300 °C.

Experimental For starting the CuNP synthesis, 225 mg $Cu(NO_3)_2 \cdot 2.5H_2O$ was dissolved in 60 ml abs. EtOH. The solution was flushed with Ar for 20 min. Simultaneously, 40 ml abs. EtOH was flushed with Ar for 20 min. The required amount (232 μ l 1-DDT) of stabilizer was added to the $Cu(NO_3)_2$ solution (molar ratio Cu/reducing agent/ stabilizer, 1/6/1). After addition of the stabilizer, the solution was stirred for 15 min (300 rpm). The required amount (219.6 mg) of $NaBH_4$ (reducing agent) was added to the 40 ml Ar flushed abs. EtOH. The flask is sealed and placed in the ultrasonic bath for 15 min. Afterwards, the $NaBH_4$ suspension was stirred and added to the Copper containing solution. Both flasks were used with an Ar counter-stream to reduce the Air contamination during the addition. The $NaBH_4$ suspension was added in 1 ml steps over 30 min. Then, the flask was sealed and stirred for 2 h (300 rpm). The suspension was separated by centrifugation

(5000 rpm, 10 min), the solvent was removed by decantation. The precipitate was washed with Acetone, EtOH and a mixture of Toluene/ EtOH (3/47 volume parts). The resulting sample was dried under vacuum.

For the supporting on Vulcan and the post-treatment, the procedure was equal to the procedure described for AgNP and AuNP.⁷⁵

The Copper Nitrate solution was lightly blue and clear. Adding the drops of stabilizer, a slight cloudiness appeared and the color changed to a light blue-greenish, slightly cloudy appearance. The suspension of the reducing agent was observed as well-dispersed fine white particles. At the drip point of the addition of the reducing agent, the solution appeared brown-black. Initially, the dark color dissolved quickly; with further addition the color was getting intense. During the 2 h stirring, the suspension was coloring completely black-brown. After centrifugation the sediment was black with white remains on top; the dispersion agent was clear.

For the supporting process, the Vulcan and n-hexane suspension were black with easily recognizable particles. The addition of the required amount of CuNP does not change the appearance. After drying, the sample was a black powder.

During the O_2 post-treatment, the sample volume was reduced to around a third of its volume and parts with metallic-copper colored gloss and partly dark black precipitate were observed. An image is presented in Fig. 11. The appearance of the H_2 post treatment samples does not change.

3.2.3 Instruments and measurements

Chemicals. The following chemicals were used as received. HCl (37 %, ROTH), HNO_3 (65 %, ROTH), Ethanol (abs. HPLC, Th Geyer), DI H_2O (SG water Ultra Clear UV ultrapure water, $0.055 S * cm^{-1}$), $NaBH_4$ (99 %, Acros Organics), 1-dodencanethiol (> 98 %, Sigma Aldrich), 1-pentethiol (98 %, TCI), 1-octadecanethiol (> 97 %, TCI), Toluene (> 99.5 % for synthesis, ROTH, Acetone (99.5 % for synthesis, ROTH), n-hexane (> 99 % p.a. ACS, ROTH), Tetra-n-octylammonium Bromide (98+ %, Alfa Aesar), Vulcan XC72 (Carbon black, Cabot), Ar (99.999 %, Alphagaz), O_2 (99.998 %, Alphagaz), H_2 (99.999 %, Alphagaz), $AgNO_3$ (99.999 %, ROTH), $Cu(NO_3)_2 * 2.5H_2O$ (> 99.99 % trace metal basis, Alrdich) Instruments, measurements and preparations. Raman spectroscopy was performed with an InVia Raman spectrometer setup (Renishaw), which is equipped with a microscope with a 100x objective (both Leica), a Cobolt CW DPSS laser (532 nm excitation wavelength), a 1800 lmm^{-1} grating and a Peltier cooled charge coupled device camera detecting the Raman scattering. The Raman spectrometer was calibrated to a silicon reference peak and the signal was adjusted to $520.4 cm^{-1}$ before the measurements. At least three spots on the sample film were measured for each sample. The spectra were recorded between 100-3200 cm^{-1} with 1.0 % laser intensity. Glassware preparation, TEM and TG-MS instruments, preparations, measurements procedures and parameters are described in “Quantifying the removal of stabilizing thiolates from gold nanoparticles on different carbon supports and the effect on their electrochemical properties”⁷⁵

4 Summary and Outlook

Towards industrial usage of the CO₂RR, to reduce the Carbon footprint and to develop a new sustainable Carbon source, novel catalysts with high activity, selectivity and stability at low overpotentials are needed. Achieving this goal requires a thorough understanding of the CO₂RR mechanism for bulk and nanostructures of promising materials. Well-characterized catalysts are a key component to shed some light on experimental findings and combine these with theoretical considerations from existing literature. This thesis seeks to deepen the understanding of the CO₂RR of sub-10 nm gold nanoparticles, supported on different Carbon materials. To this end, three objectives are pursued: (1) to study the synthesis of AuNP, AgNP, and CuNP including their long term stability while tuning their size; (2) to investigate quantitatively the post-treatment procedure for stabilizer removal, the degradation of particle size, and the stability towards electrochemical stress of AuNP on Carbon support; and (3) to test the AuNP supported on three Carbon supports for the CO₂RR at low overpotentials, from microscopic investigations with scanning electrochemical microscopy (SECM) to half-cell experiments with rotating disc electrodes and full-cell experiments with constant online gas chromatography (GC) analysis and working electrodes of 6.5 cm².

In the first part, five different methods of AuNP synthesis and different synthesis/synthesis-parameters for AgNP and CuNP have been tested. The AuNP syntheses included 2-phase synthesis routes with Gold phase-transferred particles and complexes, direct synthesis onto a Carbon support and direct precipitation of stabilized AuNP on the Carbon support during the synthesis procedure. All of these yielded particles with an average size below 10 nm. Four procedures were excluded from further investigations due to particles of greater size or high losses during the transfer to the Carbon support. The remaining 2-phase synthesis produced colloids stabilized with 1-dodecanethiol (1-DDT) (see Fig. 4) of 2.3 nm (\pm 0.6 nm) in the size range of 0.6 to 7.5 nm. The colloids were stable for at least 8 months with only negligible particle growth. AgNP were prepared, by modifying the AuNP synthesis, but instead of a Silver complex, AgNP were phase-transferred, which led to an increasing phase transfer time. The resulting AgNP (1-DDT) had a size of 3.1 nm (\pm 1.9 nm) and a size range of 0.8 nm to 27.1 nm. A one-phase synthesis for CuNP under an *Ar* atmosphere in Ethanol produced CuNP (1-DDT) of 2.3 nm (\pm 0.9 nm). Copper particles in a metallic state are challenging, as they tend to oxidize during the synthesis. Therefore, an Oxygen and Air-free setting is needed. The synthesized CuNP did show slight contributions of Cu_2O , but mainly Cu^0 . By changing the Thiolate stabilizer to one with a different carbon-chain length, a reciprocal dependence of the particle size on the Carbon-chain length of the Thiolate stabilizer was found, for AuNP, AgNP and CuNP. To use nanoparticles as electrocatalysts, they are usually supported on high-surface materials with high electrical conductivity and high chemical, physical and electrochemical stability. Common supporting materials of commercial materials are industrial Carbons like Vulcan XC72 (Vulcan) and Black Pearls 2000 (BP2000), while industrial Carbon nanotubes as Baytubes (CNT) are common for research purposes. These three supporting materials are of special interest, as they are commonly used and offer certain similarities and differences. For example, Vulcan and BP2000 offer a similar share of disordered and graphitic structured Carbon but have a different specific surface area (SSA). CNTs have a similar SSA to Vulcan (\sim 200 m² g⁻¹) but a

greater share of graphitic Carbon structures, albeit with defects. There was no change in the particle size and shape of the nanoparticles during the supporting procedure, but the particle distribution was not homogeneous. The metal transfer rate was 76 % for AuNP, 80 % for AgNP, and 91 % for CuNP.

In conclusion, AuNP, AgNP and CuNP with average sizes ranging from 1.8 nm to 7.4 nm were successfully synthesized and size-manipulated by changing the stabilizer. When transferred to three different carbon supports, the metal experienced small losses of up to 24 % and was found to be highly stable over time.

The post-treatment process of removing the stabilizer bound to nanoparticle surfaces is a crucial objective, as it reduces the complexity of the catalyst. To investigate this, a combined treatment of 20 % O_2/Ar at 300 °C followed by a treatment of 15 % H_2/Ar at 400 °C was conducted.⁷⁰ The extent of stabilizer removal, changes in the nanoparticle size and shape, and the impact on the support and the electrochemical stability by the treatment were determined. The separate treatments of 20 % O_2/Ar at 300 °C or 15 % H_2/Ar at 400 °C (denoted as O_2 or H_2 post-treatment) were both found to remove the stabilizer more effectively than the combination of treatments. The H_2 post-treatment removed 91-97 % of the stabilizer while the O_2 post-treatment removed 73-91 %. The combined post-treatment removed 77-89 %. The specific analysis of the removal of the stabilizer from the surface indicated that the H_2 post-treatment removed stabilizer species of the surface of Au-CNT completely, while traces were still found on Au-BP2000 and Au-Vulcan. The H_2 post-treatment also led to less particle growth with an average size of 2.4 nm for Au-BP2000 and 3.4-3.7 nm for Au-CNT and Au-Vulcan. The O_2 post-treatment showed a broad variation in particle growth, depending on the support material. A particle surface mobility and a loss of specifically smaller particles during all three treatments were found. The particle growth during the treatment assumingly depend on the particle-to-particle distances, which would also explain less growth in the Au-BP2000 sample. No major changes of the support were observed. The electrochemical investigations revealed improved stability against electrochemical stress and an increase in the electrochemical active surface area. During electrochemical stress, predominantly a loss of smaller particles and a growth of bigger particles in areas of high particle density were observed. For AgNP on Vulcan, the single treatments demonstrated significant differences; the O_2 post-treatment removed 75 % of the stabilizer, while the H_2 post-treatment achieved a complete removal. By the H_2 post-treatment, the particle growth was smaller compared to the O_2 post-treatment, but still, the average particle size was 14 nm. For CuNP on the Vulcan, the H_2 post-treatment removed 94 % of the stabilizer, with an average particle size of 8.9 nm. Using the O_2 post-treatment, the CuNP were not stable. They agglomerated partly and particles in micrometer size were found.

In conclusion, a single treatment of AuNP, AgNP and CuNP supported on Carbon was found to be significantly more effective in removing the stabilizer, exhibiting high removal rates of up to 100 %. Additionally, the single treatments were advantageous for less particle growth. The particle growth by the treatments assumingly depends on the particle-to-particle distance on the supporting material. Particle surface mobility and a loss of smaller particles were found. However, all treated AuNP samples did show a significantly higher electrochemical available surface area and improved stability against electrochemical stress. During electrochemical stress, a growth of bigger particles in areas of high particle density and a loss of

smaller particles was observed.

In the third part, the CO₂RR over AuNPs on three different Carbon supports was investigated in the low overpotential region (0 V to -0.4 V vs. RHE, all further potentials are given vs. RHE), using a broad variety of (electro)analytical methods, including linear sweep voltammetry with a rotating disk electrode (LSV-RDE), sample generation-tip collection mode of scanning electrochemical microscopy (SECM), as well as full cell tests with highly sensitive on-line GC. These methods applied electrodes from micro to macro scale and showed comparable results, regardless of the electrode size. LSV-RDE revealed a steady increasing of the specific reduction current with a more negative potential for Au-Vulcan and Au-BP2000, with a slightly more negative reduction current for CO₂-saturated electrolytes than Ar-saturated electrolytes specifically for Au-BP2000. Au-CNT did show a unique behavior with a local current maximum at -0.32 V, which may indicate a change in the reaction/ adsorption mechanism. SECM showed HER onset potentials of -0.004 V. Using Au-Vulcan and Au-BP2000, a CO₂RR onset of -0.2 V was determined and by reference measurements a mixture of CO and H₂ as products were established. In contrast, Au-CNT presented a unique behavior with CH₂O and H₂ as products in the potential region of -0.25 V to -0.40 V. Further decreasing to a more negative potential led to the disappearance of CH₂O, and CO evolved. Mass spectroscopy of the electrolyte of chronoamperometry-RDE measurements upheld the CH₂O finding for Au-CNT, while no CH₂O was found using Au-Vulcan and Au-BP2000. No Methanol has been found for any sample. The full-cell test stands with on line GC found H₂ and CO for the same potential range as measured by LSV-RDE and SECM. Remarkably, the H₂ product flow rate for Au-CNT decreased strongly in the same potential region, where CH₂O was found by SECM, suggesting a change in the reaction path with the consumption of H₂ or the suppression of the HER. A strong local pH effect for the CH₂O formation could be ruled out because the SECM gives a good insight into local pH effects, as the HER onset potential, the PtO/ Pt reduction potential and the CO-oxidation potential all are strongly pH-dependent, but no shifts of these potentials have been observed.^{98,99} The absence of strong pH effects is supported by the chronoamperometry-RDE experiment, in which CH₂O has been found, even if an RDE was applied. This could be attributed to the fact that the Au-CNT surface was free of Thiolate stabilizer and had a less diversified surface structure, allowing for free undercoordinated sites. These free uncoordinated sites are reported in the literature to promote the production of Methanol with CH₂O as a desorbed intermediate because of a changed adsorption mechanism of H₂/CO, which also inhibits the desorption of CO.⁴¹ This would explain that the smallest remaining amounts of stabilizer impede the selectivity towards CH₂O. Therefore, for the Thiolate free Au-CNT assumingly CH₂O was found because of the free undercoordinated sites, which are blocked for Au-BP2000 and Au-Vulcan, by the remaining traces of stabilizer. No MeOH was found, as the local pH has not changed strongly and no self-condensation of CH₂O appeared. This emphasizes the importance of knowledge of the local pH.^{22,38,44}

Concluding, a HER onset of -0.004 V across all catalysts, and a CO onset of -0.2 V or -0.3 V on Au-Vulcan and Au-BP2000, respectively Au-CNT was identified. A unique behavior of Au-CNT was observed, producing CH₂O as a product in the potential region of -0.25 V to -0.4 V, likely due to its Thiolate-free, undercoordinated surface sites and less diverse surface structure. Furthermore, no significant

pH effects were observed.

All these results may suggest further experiments. It would be interesting to further explore treatment conditions that may yield high removal rates of stabilizer with minimal particle growth, especially for AgNP and CuNP. As Silver has been less investigated in the literature for the CO₂RR but shows a strong CO selectivity, comparable to Gold, Thiolate-free sub-10 nm AgNP may be very interesting for further investigations. Additionally, further exploration of the treatment conditions for Au-Vulcan and Au-BP2000 catalysts to achieve a Thiolate-free surface may provide insights into the selectivity of Gold towards CH₂O. More detailed investigations of the low overpotential region are promising, as it is not well-characterized in the literature. Furthermore, SECM using an Au UME or a double-junction Pt-Au UME could be employed to investigate *in situ*, for other products in potential regions of CO evolution. Lastly, a more stable electrode material than ITO could greatly expand the potential range for SECM investigations. Summing up, the influence of remaining traces of stabilizer or other impurities likely play a crucial role for the CO₂RR selectivity. Therefore, well-defined catalysts are needed. Furthermore, the low overpotential region should be studied in greater detail as it could offer great possibilities.

References

- [1] S. Yu, S. Louisia, P. Yang. The Interactive Dynamics of Nanocatalyst Structure and Microenvironment during Electrochemical CO_2 Conversion. *JACS Au* **2022**, *2*, 562–572.
- [2] IEA, *World Energy Outlook 2022 – Analysis - IEA*, **2022**. <https://www.iea.org/reports/world-energy-outlook-2022>.
- [3] W. Gao, S. Liang, R. Wang, Q. Jiang, Y. Zhang, Q. Zheng, B. Xie, C. Y. Toe, X. Zhu, J. Wang, L. Huang, Y. Gao, Z. Wang, C. Jo, Q. Wang, L. Wang, Y. Liu, B. Louis, J. Scott, A.-C. Roger, R. Amal, H. He, S.-E. Park. Industrial carbon dioxide capture and utilization: state of the art and future challenges. *Chemical Society reviews* **2020**, *49*, 8584–8686.
- [4] E. S. Rubin, J. E. Davison, H. J. Herzog. The cost of CO_2 capture and storage. *International Journal of Greenhouse Gas Control* **2015**, *40*, 378–400.
- [5] E. V. Kondratenko, G. Mul, J. Baltrusaitis, G. O. Larrazábal, J. Pérez-Ramírez. Status and perspectives of CO_2 conversion into fuels and chemicals by catalytic, photocatalytic and electrocatalytic processes. *Energy & Environmental Science* **2013**, *6*, 3112.
- [6] M. Tahir, N. S. Amin. Recycling of carbon dioxide to renewable fuels by photocatalysis: Prospects and challenges. *Renewable & Sustainable Energy Reviews* **2013**, *25*, 560–579.
- [7] W. Tu, Y. Zhou, Z. Zou. Photocatalytic conversion of CO_2 into renewable hydrocarbon fuels: state-of-the-art accomplishment, challenges, and prospects. *Advanced Materials* **2014**, *26*, 4607–4626.
- [8] M. Tahir, N. A. S. Amin. Photo-induced CO_2 reduction by hydrogen by selective CO evolution in a dynamic monolith photoreactor loaded with Ag-modified TiO_2 nanocatalyst. *International Journal of Hydrogen Energy* **2017**, *42*, 15507–15522.
- [9] Z. Sun, T. Ma, H. Tao, Q. Fan, B. Han. Fundamentals and Challenges of Electrochemical CO_2 Reduction Using Two-Dimensional Materials. *Chem* **2017**, *3*, 560–587.
- [10] F. Zhang, H. Zhang, Z. Liu. Recent advances in electrochemical reduction of CO_2 . *Current Opinion in Green and Sustainable Chemistry* **2019**, *16*, 77–84.
- [11] Y. Zhai, L. Chiachiarelli, N. Sridhar. Effect of Gaseous Impurities on the Electrochemical Reduction of CO_2 on Copper Electrodes. *ECS Transactions* **2009**, *19*, 1–13.
- [12] B. Kumar, J. P. Brian, V. Atla, S. Kumari, K. A. Bertram, R. T. White, J. M. Spurgeon. New trends in the development of heterogeneous catalysts for electrochemical CO_2 reduction. *Catalysis Today* **2016**, *270*, 19–30.
- [13] P. R. Yaashikaa, P. Senthil Kumar, S. J. Varjani, A. Saravanan. A review on photochemical, biochemical and electrochemical transformation of CO_2 into value-added products. *Journal of CO2 Utilization* **2019**, *33*, 131–147.
- [14] B. C. Marepally, C. Ampelli, C. Genovese, F. Tavella, L. Veyre, E. A. Quadrelli, S. Perathoner, G. Centi. Role of small Cu nanoparticles in the behaviour of nanocarbon-based electrodes for the electrocatalytic reduction of CO_2 . *Journal of CO2 Utilization* **2017**, *21*, 534–542.
- [15] X. Liu, J. Xiao, H. Peng, X. Hong, K. Chan, J. K. Nørskov. Understanding trends in electrochemical carbon dioxide reduction rates. *Nature communications* **2017**, *8*, 15438.
- [16] W. Zhu, R. Michalsky, Ö. Metin, H. Lv, S. Guo, C. J. Wright, X. Sun, A. A. Peterson, S. Sun. Monodisperse Au nanoparticles for selective electrocatalytic reduction of CO_2 to CO. *Journal of the American Chemical Society* **2013**, *135*, 16833–16836.
- [17] R. Reske, H. Mistry, F. Behafarid, B. Roldan Cuenya, P. Strasser. Particle size effects in the catalytic electroreduction of CO_2 on Cu nanoparticles. *Journal of the American Chemical Society* **2014**, *136*, 6978–6986.

-
- [18] Z. Yang, J. Zhang, M. C. W. Kintner-Meyer, X. Lu, D. Choi, J. P. Lemmon, J. Liu. Electrochemical energy storage for green grid. *Chemical Reviews (Washington, DC, United States)* **2011**, *111*, 3577–3613.
- [19] B. W. D’Andrade (Ed.), *The power grid: Smart, secure, green and reliable*, Elsevier Academic Press, London, **2017**.
- [20] Y. Y. Birdja, E. Pérez-Gallent, M. C. Figueiredo, A. J. Göttle, F. Calle-Vallejo, M. T. M. Koper. Advances and challenges in understanding the electrocatalytic conversion of carbon dioxide to fuels. *Nature Energy* **2019**, *4*, 732–745.
- [21] R. A. Tufa, D. Chanda, M. Ma, D. Aili, T. B. Demissie, J. Vaes, Q. Li, S. Liu, D. Pant. Towards highly efficient electrochemical CO_2 reduction: Cell designs, membranes and electrocatalysts. *Applied Energy* **2020**, *277*, 115557.
- [22] Y. Y. Birdja, M. T. M. Koper. The Importance of Cannizzaro-Type Reactions during Electrocatalytic Reduction of Carbon Dioxide. *Journal of the American Chemical Society* **2017**, *139*, 2030–2034.
- [23] F. Zhang, A. C. Co. Direct Evidence of Local pH Change and the Role of Alkali Cation during CO_2 Electroreduction in Aqueous Media. *Angewandte Chemie, International Edition* **2020**, *59*, 1674–1681.
- [24] S. Narayanaru, J. Chinnaiah, K. L. Phani, F. Scholz. pH dependent CO adsorption and roughness-induced selectivity of CO_2 electroreduction on gold surfaces. *Electrochimica Acta* **2018**, *264*, 269–274.
- [25] G. Marcandalli, M. C. O. Monteiro, A. Goyal, M. T. M. Koper. Electrolyte Effects on CO_2 Electrochemical Reduction to CO. *Accounts of chemical research* **2022**, *55*, 1900–1911.
- [26] S. Nitopi, E. Bertheussen, S. B. Scott, X. Liu, A. K. Engstfeld, S. Horch, B. Seger, I. E. L. Stephens, K. Chan, C. Hahn, J. K. Nørskov, T. F. Jaramillo, I. Chorkendorff. Progress and Perspectives of Electrochemical CO_2 Reduction on Copper in Aqueous Electrolyte. *Chemical Reviews (Washington, DC, United States)* **2019**, *119*, 7610–7672.
- [27] Y. Wang, C. Niu, D. Wang. Metallic nanocatalysts for electrochemical CO_2 reduction in aqueous solutions. *Journal of colloid and interface science* **2018**, *527*, 95–106.
- [28] Y. Hori, K. Kikuchi, S. Suzuki. Production of CO and CH_4 in Electrochemical Reduction of CO_2 at Metal Electrodes in Aqueous Hydrogencarbonate Solution. *Chemistry Letters* **1985**, *14*, 1695–1698.
- [29] A. Bagger, W. Ju, A. S. Varela, P. Strasser, J. Rossmeisl. Electrochemical CO_2 Reduction: A Classification Problem. *ChemPhysChem* **2017**, *18*, 3266–3273.
- [30] X. Deng, D. Alfonso, T.-D. Nguyen-Phan, D. R. Kauffman. Resolving the Size-Dependent Transition between CO_2 Reduction Reaction and H_2 Evolution Reaction Selectivity in Sub-5 nm Silver Nanoparticle Electrocatalysts. *ACS Catalysis* **2022**, 5921–5929.
- [31] M. Liu, Y. Pang, B. Zhang, P. de Luna, O. Voznyy, J. Xu, X. Zheng, C. T. Dinh, F. Fan, C. Cao, F. P. G. de Arquer, T. S. Safaei, A. Mepham, A. Klinkova, E. Kumacheva, T. Filleter, D. Sinton, S. O. Kelley, E. H. Sargent. Enhanced electrocatalytic CO_2 reduction via field-induced reagent concentration. *Nature* **2016**, *537*, 382–386.
- [32] D. Wakerley, S. Lamaison, F. Ozanam, N. Menguy, D. Mercier, P. Marcus, M. Fontecave, V. Mougel. Bio-inspired hydrophobicity promotes CO_2 reduction on a Cu surface. *Nature materials* **2019**, *18*, 1222–1227.
- [33] W. J. Teh, M. J. Kolb, F. Calle-Vallejo, B. S. Yeo. Enhanced Charge Transfer Kinetics for the Electroreduction of Carbon Dioxide on Silver Electrodes Functionalized with Cationic Surfactants. *Advanced Functional Materials* **2022**, 2210617.
-

- [34] O. Gutiérrez-Sánchez, N. Daems, M. Bulut, D. Pant, T. Breugelmans. Effects of Benzyl-Functionalized Cationic Surfactants on the Inhibition of the Hydrogen Evolution Reaction in CO_2 Reduction Systems. *ACS applied materials & interfaces* **2021**, *13*, 56205–56216.
- [35] Y. Song, W. Chen, C. Zhao, S. Li, W. Wei, Y. Sun. Metal-Free Nitrogen-Doped Mesoporous Carbon for Electroreduction of CO_2 to Ethanol. *Angewandte Chemie, International Edition* **2017**, *56*, 10840–10844.
- [36] C. van Hoang, V. G. Gomes, N. Kornienko. Metal-based nanomaterials for efficient CO_2 electroreduction: Recent advances in mechanism, material design and selectivity. *Nano Energy* **2020**, *78*, 105311.
- [37] Y. Ma, J. Wang, J. Yu, J. Zhou, X. Zhou, H. Li, Z. He, H. Long, Y. Wang, P. Lu, J. Yin, H. Sun, Z. Zhang, Z. Fan. Surface modification of metal materials for high-performance electrocatalytic carbon dioxide reduction. *Matter* **2021**, *4*, 888–926.
- [38] Y. Zhou, B. S. Yeo. Formation of C-C bonds during electrocatalytic CO_2 reduction on non-copper electrodes. *Journal of Materials Chemistry A* **2020**, *8*, 23162–23186.
- [39] M. Umeda, Y. Niitsuma, T. Horikawa, S. Matsuda, M. Osawa. Electrochemical Reduction of CO_2 to Methane on Platinum Catalysts without Overpotentials: Strategies for Improving Conversion Efficiency. *ACS Applied Energy Materials* **2020**, *3*, 1119–1127.
- [40] D. Yang, W. Pei, S. Zhou, J. Zhao, W. Ding, Y. Zhu. Controllable Conversion of CO_2 on Non-Metallic Gold Clusters. *Angewandte Chemie, International Edition* **2020**, *59*, 1919–1924.
- [41] E. R. Cave, J. H. Montoya, K. P. Kuhl, D. N. Abram, T. Hatsukade, C. Shi, C. Hahn, J. K. Nørskov, T. F. Jaramillo. Electrochemical CO_2 reduction on Au surfaces: mechanistic aspects regarding the formation of major and minor products. *Physical chemistry chemical physics* **2017**, *19*, 15856–15863.
- [42] M. S. Inkpen, Z.-F. Liu, H. Li, L. M. Campos, J. B. Neaton, L. Venkataraman. Non-chemisorbed gold-sulfur binding prevails in self-assembled monolayers. *Nature chemistry* **2019**, *11*, 351–358.
- [43] B. Kim, H. Seong, J. T. Song, K. Kwak, H. Song, Y. C. Tan, G. Park, D. Lee, J. Oh. Over a 15.9 % Solar-to-CO Conversion from Dilute CO_2 Streams Catalyzed by Gold Nanoclusters Exhibiting a High CO_2 Binding Affinity. *ACS Energy Letters* **2020**, *5*, 749–757.
- [44] K. U. D. Calvino, A. W. Alherz, K. M. K. Yap, A. B. Laursen, S. Hwang, Z. J. L. Bare, Z. Clifford, C. B. Musgrave, G. C. Dismukes. Surface Hydrides on Fe_2P Electrocatalyst Reduce CO_2 at Low Overpotential: Steering Selectivity to Ethylene Glycol. *Journal of the American Chemical Society* **2021**, *143*, 21275–21285.
- [45] M. Rybacki, A. V. Nagarajan, G. Mpourmpakis. Ligand removal energetics control CO_2 electroreduction selectivity on atomically precise, ligated alloy nanoclusters. *Environmental Science: Nano* **2022**, *9*, 2032–2040.
- [46] D. R. Alfonso, D. Kauffman, C. Matranga. Active sites of ligand-protected Au_{25} nanoparticle catalysts for CO_2 electroreduction to CO. *The Journal of chemical physics* **2016**, *144*, 184705.
- [47] K. J. P. Schouten, Z. Qin, E. Pérez Gallent, M. T. M. Koper. Two pathways for the formation of ethylene in CO reduction on single-crystal copper electrodes. *Journal of the American Chemical Society* **2012**, *134*, 9864–9867.
- [48] J. T. Feaster, C. Shi, E. R. Cave, T. Hatsukade, D. N. Abram, K. P. Kuhl, C. Hahn, J. K. Nørskov, T. F. Jaramillo. Understanding Selectivity for the Electrochemical Reduction of Carbon Dioxide to Formic Acid and Carbon Monoxide on Metal Electrodes. *ACS Catalysis* **2019**, *9*, 9411–9417.
- [49] N. Srekanth, K. L. Phani. Selective reduction of CO_2 to formate through bicarbonate reduction on metal electrodes: new insights gained from SG/TC mode of SECM. *Chemical communications (Cambridge, England)* **2014**, *50*, 11143–11146.

-
- [50] M.-J. Cheng, E. L. Clark, H. H. Pham, A. T. Bell, M. Head-Gordon. Quantum Mechanical Screening of Single-Atom Bimetallic Alloys for the Selective Reduction of CO_2 to C_1 Hydrocarbons. *ACS Catalysis* **2016**, *6*, 7769–7777.
- [51] A. S. Barnard. Modeling the Impact of Alkanethiol SAMs on the Morphology of Gold Nanocrystals. *Crystal Growth & Design* **2013**, *13*, 5433–5441.
- [52] E. Dieterich, L. Herrmann, O. Dzhyginas, L. Binnenböse, M. Steimecke, S.-J. Kinkelin, M. Bron. Multimethod Approach to the Low-Overpotential Region of Micro- to Macro-Scale Working Electrodes of Sub-10 nm Gold Nanoparticles in the CO_2 Reduction Reaction. *Analytical chemistry* **2023**.
- [53] C. Gao, F. Lyu, Y. Yin. Encapsulated Metal Nanoparticles for Catalysis. *Chemical Reviews (Washington, DC, United States)* **2021**, *121*, 834–881.
- [54] R. Vajtai (Ed.), *Springer Handbook of Nanomaterials // Science and Engineering of Nanomaterials 1st ed.*, of *Springer Handbooks*, Springer, Heidelberg, **2013**.
- [55] H. Haspel, R. Ionescu, P. Heszler, Á. Kukovecz, Z. Kónya, Z. Gingl, J. Mäklin, T. Mustonen, K. Kordás, R. Vajtai, P. M. Ajayan. Fluctuation enhanced gas sensing on functionalized carbon nanotube thin films. *Physica Status Solidi B: Basic Solid State Physics* **2008**, *245*, 2339–2342.
- [56] D. Guo, G. Xie, J. Luo. Mechanical properties of nanoparticles: basics and applications. *Journal of Physics D: Applied Physics* **2014**, *47*, 013001.
- [57] X. Lu, M. Rycenga, S. E. Skrabalak, B. Wiley, Y. Xia. Chemical synthesis of novel plasmonic nanoparticles. *Annual review of physical chemistry* **2009**, *60*, 167–192.
- [58] G. Mie. Beiträge zur Optik trüber Medien, speziell kolloidaler Metallösungen. *Annalen der Physik (Berlin, Germany)* **1908**, *330*, 377–445.
- [59] R. Gans. Über die Form ultramikroskopischer Goldteilchen. *Annalen der Physik (Berlin, Germany)* **1912**, *342*, 881–900.
- [60] M. Cyrankiewicz, T. Wybranowski, S. Kruszewski. Study of SERS efficiency of metallic colloidal systems. *Journal of Physics: Conference Series* **2007**, *79*, 012013.
- [61] S. Hong, X. Li. Optimal Size of Gold Nanoparticles for Surface-Enhanced Raman Spectroscopy under Different Conditions. *Journal of Nanomaterials* **2013**, *2013*, 1–9.
- [62] P. G. Jamkhande, N. W. Ghule, A. H. Bamer, M. G. Kalaskar. Metal nanoparticles synthesis: An overview on methods of preparation, advantages and disadvantages, and applications. *Journal of Drug Delivery Science and Technology* **2019**, *53*, 101174.
- [63] R. Luque, P. Prinsen (Eds.), *Nanoparticle design and characterization for catalytic applications in sustainable chemistry*, Vol. 38 of *Catalysis series*, Royal Society of Chemistry, Cambridge, **2019**.
- [64] M. Brust, M. Walker, D. Bethell, D. J. Schiffrin, R. Whyman. Synthesis of thiol-derivatised gold nanoparticles in a two-phase Liquid-Liquid system. *Journal of the Chemical Society, Chemical Communications* **1994**, *0*, 801–802.
- [65] P. J. G. Goulet, R. B. Lennox. New insights into Brust-Schiffrin metal nanoparticle synthesis. *Journal of the American Chemical Society* **2010**, *132*, 9582–9584.
- [66] E. Dieterich, S.-J. Kinkelin, M. Bron. Comparative Study of the Synthesis of sub-10 nm Carbon-Supported Gold Nanoparticles and their Suitability for Methanol Electrooxidation in Alkaline Media. *ChemNanoMat* **2022**, *8*.
- [67] A. Primo, A. Corma, H. García. Titania supported gold nanoparticles as photocatalyst. *Physical chemistry chemical physics* **2011**, *13*, 886–910.
-

- [68] G. Li, D.-e. Jiang, C. Liu, C. Yu, R. Jin. Oxide-supported atomically precise gold nanocluster for catalyzing Sonogashira cross-coupling. *Journal of Catalysis* **2013**, *306*, 177–183.
- [69] K. Zhang, W. Wang, W. Cheng, X. Xing, G. Mo, Q. Cai, Z. Chen, Z. Wu. Temperature-Induced Interfacial Change in $Au@SiO_2$ Core-Shell Nanoparticles Detected by Extended X-ray Absorption Fine Structure. *Journal of Physical Chemistry C* **2009**, *114*, 41–49.
- [70] J. Luo, M. M. Maye, N. N. Kariuki, L. Wang, P. Njoki, Y. Lin, M. Schadt, H. R. Naslund, C.-J. Zhong. Electrocatalytic oxidation of methanol: Carbon-supported gold–platinum nanoparticle catalysts prepared by two-phase protocol. *Catalysis Today* **2005**, *99*, 291–297.
- [71] Y. Shao, J. Liu, Y. Wang, Y. Lin. Novel catalyst support materials for PEM fuel cells: current status and future prospects. *Journal of Materials Chemistry* **2009**, *19*, 46–59.
- [72] S. Sharma, B. G. Pollet. Support materials for PEMFC and DMFC electrocatalysts—A review. *Journal of Power Sources* **2012**, *208*, 96–119.
- [73] Y. Shao, G. Yin, Y. Gao, P. Shi. Durability Study of Pt/C and Pt/CNTs Catalysts under Simulated PEM Fuel Cell Conditions. *Journal of the Electrochemical Society* **2006**, *153*, A1093.
- [74] T. Maiyalagan. Pt–Ru nanoparticles supported PAMAM dendrimer functionalized carbon nanofiber composite catalysts and their application to methanol oxidation. *Journal of Solid State Electrochemistry* **2009**, *13*, 1561–1566.
- [75] E. Dieterich, S.-J. Kinkelin, M. Steimecke, M. Bron. Quantifying the removal of stabilizing thiolates from gold nanoparticles on different carbon supports and the effect on their electrochemical properties. *Nanoscale advances* **2022**.
- [76] S. Popović, M. Smiljanić, P. Jovanović, J. Vavra, R. Buonsanti, N. Hodnik. Stability and Degradation Mechanisms of Copper-Based Catalysts for Electrochemical CO_2 Reduction. *Angewandte Chemie* **2020**, *132*, 14844–14854.
- [77] X. Yu, S. Ye. Recent advances in activity and durability enhancement of Pt/C catalytic cathode in PEMFC. *Journal of Power Sources* **2007**, *172*, 145–154.
- [78] F. J. Perez-Alonso, C. F. Elkjær, S. S. Shim, B. L. Abrams, I. E. Stephens, I. Chorkendorff. Identical locations transmission electron microscopy study of Pt/C electrocatalyst degradation during oxygen reduction reaction. *Journal of Power Sources* **2011**, *196*, 6085–6091.
- [79] K. J. Mayrhofer, J. C. Meier, S. J. Ashton, G. K. Wiberg, F. Kraus, M. Hanzlik, M. Arenz. Fuel cell catalyst degradation on the nanoscale. *Electrochemistry Communications* **2008**, *10*, 1144–1147.
- [80] M. Steimecke, A. M. Araújo-Cordero, E. Dieterich, M. Bron. Probing Individual Cuprous Oxide Microcrystals towards Carbon Dioxide Reduction by using In Situ Raman-coupled Scanning Electrochemical Microscopy. *ChemElectroChem* **2022**, *9*.
- [81] M. Haruta. Gold Catalysts Prepared by Coprecipitation for Low-Temperature Oxidation of Hydrogen and of Carbon Monoxide. *Journal of Catalysis* **1989**, 301–309.
- [82] A. Salehi-Khojin, H.-R. M. Jhong, B. A. Rosen, W. Zhu, S. Ma, P. J. A. Kenis, R. I. Masel. Nanoparticle Silver Catalysts That Show Enhanced Activity for Carbon Dioxide Electrolysis. *Journal of Physical Chemistry C* **2013**, *117*, 1627–1632.
- [83] C. Kim, H. S. Jeon, T. Eom, M. S. Jee, H. Kim, C. M. Friend, B. K. Min, Y. J. Hwang. Achieving Selective and Efficient Electrocatalytic Activity for CO_2 Reduction Using Immobilized Silver Nanoparticles. *Journal of the American Chemical Society* **2015**, *137*, 13844–13850.
- [84] C. G. Vayenas (Ed.), *Modern aspects of electrochemistry, Vol. 42*, Springer, New York, **2008**.
- [85] H. Mistry, Y.-W. Choi, A. Bagger, F. Scholten, C. S. Bonifacio, I. Sinev, N. J. Divins, I. Zegkinoglou, H. S. Jeon, K. Kisslinger, E. A. Stach, J. C. Yang, J. Rossmeisl, B. Roldan Cuenya. Enhanced Carbon Dioxide Electroreduction to Carbon Monoxide over Defect-Rich Plasma-Activated Silver Catalysts. *Angewandte Chemie* **2017**, *129*, 11552–11556.

- [86] N. J. Firet, M. A. Blommaert, T. Burdyny, A. Venugopal, D. Bohra, A. Longo, W. A. Smith. Operando EXAFS study reveals presence of oxygen in oxide-derived silver catalysts for electrochemical CO_2 reduction. *Journal of Materials Chemistry A* **2019**, *7*, 2597–2607.
- [87] K.-S. Chou, C.-Y. Ren. Synthesis of nanosized silver particles by chemical reduction method. *Materials Chemistry and Physics* **2000**, *64*, 241–246.
- [88] L. Mulfinger, S. D. Solomon, M. Bahadory, A. V. Jeyarajasingam, S. A. Rutkowsky, C. Boritz. Synthesis and Study of Silver Nanoparticles. *Journal of Chemical Education* **2007**, *84*, 322.
- [89] S. Agnihotri, S. Mukherji, S. Mukherji. Size-controlled silver nanoparticles synthesized over the range 5–100 nm using the same protocol and their antibacterial efficacy. *RSC Advances* **2014**, *4*, 3974–3983.
- [90] M. M. Oliveira, D. Ugarte, D. Zanchet, A. J. G. Zarbin. Influence of synthetic parameters on the size, structure, and stability of dodecanethiol-stabilized silver nanoparticles. *Journal of colloid and interface science* **2005**, *292*, 429–435.
- [91] P. J. G. Goulet, G. R. Bourret, R. B. Lennox. Facile phase transfer of large, water-soluble metal nanoparticles to nonpolar solvents. *Langmuir* **2012**, *28*, 2909–2913.
- [92] H. Sellers, A. Ulman, Y. Shnidman, J. E. Eilers. Structure and binding of alkanethiolates on gold and silver surfaces: implications for self-assembled monolayers. *Journal of the American Chemical Society* **1993**, *115*, 9389–9401.
- [93] S. Y. Kang, K. Kim. Comparative Study of Dodecanethiol-Derivatized Silver Nanoparticles Prepared in One-Phase and Two-Phase Systems. *Langmuir* **1998**, *14*, 226–230.
- [94] R. X. He, R. Liang, P. Peng, Y. Norman Zhou. Effect of the size of silver nanoparticles on SERS signal enhancement. *Journal of Nanoparticle Research* **2017**, *19*, 1394.
- [95] T. P. Ang, T. S. A. Wee, W. S. Chin. Three-Dimensional Self-Assembled Monolayer (3D SAM) of n -Alkanethiols on Copper Nanoclusters. *Journal of Physical Chemistry B* **2004**, *108*, 11001–11010.
- [96] Y. Deng, A. D. Handoko, Y. Du, S. Xi, B. S. Yeo. In Situ Raman Spectroscopy of Copper and Copper Oxide Surfaces during Electrochemical Oxygen Evolution Reaction: Identification of Cu^{III} Oxides as Catalytically Active Species. *ACS Catalysis* **2016**, *6*, 2473–2481.
- [97] F. D. Speck, S. Cherevko. Electrochemical copper dissolution: A benchmark for stable CO_2 reduction on copper electrocatalysts. *Electrochemistry Communications* **2020**, *115*, 106739.
- [98] S. Dieckhöfer, D. Öhl, J. R. C. Junqueira, T. Quast, T. Turek, W. Schuhmann. Probing the Local Reaction Environment During High Turnover Carbon Dioxide Reduction with Ag-Based Gas Diffusion Electrodes. *Chemistry - A European Journal* **2021**, *27*, 5906–5912.
- [99] M. C. O. Monteiro, A. Mirabal, L. Jacobse, K. Doblhoff-Dier, S. C. Barton, M. T. M. Koper. Time-Resolved Local pH Measurements during CO_2 Reduction Using Scanning Electrochemical Microscopy: Buffering and Tip Effects. *JACS Au* **2021**, *1*, 1915–1924.

Table of Abbreviations

1-DDT	1-dodecanethiolate
1-ODT	1-octadecanethiolate
1-PET	1-pentethiolate
AgNP	Silver nanoparticles
Ag-C	AgNP - supported onto Carbon
Ag-Vulcan	AgNP - supported onto Vulcan
AuNP	Gold nanoparticles
Au-C	AuNP - supported onto Carbon
BP2000	BlackPearls 2000
CNT	Carbon nanotubes
CO ₂ RR	CO ₂ reduction reaction
CPET	concerted proton electron transfer
CuNP	Copper nanoparticles
Cu-Vulcan	CuNP - supported onto Vulcan
$FE_{Product}$	<i>Faradaic</i> efficiency of a certain product
GC	gas chromatograph
HER	Hydrogen evolution reaction
LSV-RDE	linear sweep voltammetry with rotating disc electrode
MWCNT	multiwalled Carbon nanotubes
OER	Oxygen evolution reaction
PEM-FC	polymer electrolyte membrane - fuel cell
RHE	reversible Hydrogen electrode
SECM	scanning electrochemical microscopy
SHE	standard Hydrogen electrode
SPR	surface plasmon resonance
SSA	specific surface area
TEM	transmission electron microscopy
TG-MS	thermogravimetric - mass spectroscopy
TOAB	Tetraoctylammoniumbromide
Vulcan	Vulcan XC 72

List of Figures

1	Outline of an artificial carbon cycle by the (electrochemical) CO ₂ RR for the production of fuels and chemicals by CO_2 and renewable energies. Energy is supplied by renewable energy sources to reduce CO_2 , to either produce fuels for further usage as energy carrier or in transport, or essential chemicals. The usage of these fuels produces CO_2 which can be captured and re-introduced into the CO ₂ RR. This would create a closed Carbon cycle. Also industrial CO_2 emissions can be introduced into the CO ₂ RR.	3
2	Full cell setup for the CO ₂ RR in an Aqueous electrolyte, with the reaction (black) $x CO_2 + y H_2O \rightarrow product + z O_2$ separated in the half-cell reactions of the OER at the anode $2 H_2O \rightarrow O_2 + 4 H^+ + 4 e^-$ and the CO ₂ RR at the cathode $x CO_2 + n H^+ + n e^- \rightarrow product + y H_2O$ and the competitive HER (red) $n H^+ + n e^- \rightarrow n/2 H_2$, whereby the anode and cathode sides are separated by a cation exchange membrane. As the electrolyte typical buffers (e.g. $KHCO_3$ Aqueous solutions) are used to improve the solubility of CO_2	5
3	Mechanisms for the adsorption of CO_2 by a) and b) direct adsorption of an CO_2 -anion-radical and c) to g) by converted proton - electron transfer. ^{9,23,24}	9
4	The 2-phase synthesis of AuNP, with Tetraoctylammoniumbromide (TOAB) as phase transfer agent, $NaBH_4$ as reducing agent, $HAuCl_4$ as Gold source, 1-dodecanethiolate (1-DDT) as stabilizer and 2-phases, Water and Toluene, visualization based on Goulet et al. ⁶⁵	13
5	TEM images of a), b) AgNP stabilized with 1-ODT, c), d) stabilized with 1-DDT and e), f) stabilized with 1-PET.	18
6	TEM images of a), b) $Ag - DDT - Vulcan - H_2$ and c), d) $Ag - DDT - Vulcan - O_2$, the different magnifications to show the inhomogeneous particle distribution on Vulcan.	19
7	Particle size distribution of a) AgNP synthesized with different stabilizers and b) $AgNP - O_2$ and $-H_2$ post treated on Vulcan support.	20
8	TEM images of a) CuNP-DDT, b) Cu-Vulcan-DDT- H_2 , c) CuNP-ODT and d) Cu-Vulcan-ODT- H_2 for the evaluation of particle size.	22
9	Particle size distribution of a) CuNP stabilized by either 1-DDT or 1-ODT, b) Cu-Vulcan- H_2 where the nanoparticles were either-synthesized with 1-DDT or 1-ODT and c) exemplary Raman measurements of CuNP-DDT to examine the composition of the CuNP with d) an enlargement of the Cu specific region, where the arrows are marking peaks at $\sim 268 cm^{-1}$, $\sim 530 cm^{-1}$ and $\sim 600 cm^{-1}$ of $C - C$ from the Thiolates.	23
10	TEM images of Cu-Vulcan- O_2 where different areas of the product are presented. In a) nanoparticles are observed on the Carbon support, b) the dark area could be agglomeration of Copper species and c) is a Copper agglomeration	24
11	CuNP supported on Vulcan and post treated with 20 % O_2/Ar at 300 °C.	24

List of Tables

1	The thermodynamic equilibrium potentials for exemplary products, the reaction and the number of transferred electrons. The potentials are given vs. RHE.	6
2	Summarizing results from literature of the investigation of different catalysts for the CO ₂ RR to their products, and the energy density respectively faradaic efficiency at the investigated potential.	8
3	Particle size, standard deviation, particle size range, metal loading, metal transfer rate (calculated Ag loading of 20 wt.%) and the amount of removed stabilizer of the synthesized AgNP with three different stabilizers, 1-ODT, 1-DDT and 1-PET, and for the AgNP-DDT supported and post-treated on Vulcan. In brackets ($\pm \dots$) the standard deviation is given.	19
4	AgNP synthesis modified according to published procedures, reported resulting particle size, specifically altered synthesis parameters and the experimentally resulting particle sizes and size ranges.	21
5	Particle size, standard deviation, particle size range, metal loading, metal transfer rate (calculated Cu loading of 20 wt.%), the amount of removed stabilizer of the synthesized CuNP with two stabilizers, 1-ODT and 1-DDT, and these supported and post-treated on Vulcan. The standard deviation is given in brackets ($\pm \dots$).	22

Comparative Study of the Synthesis of sub-10 nm Carbon-Supported Gold Nanoparticles and their Suitability for Methanol Electrooxidation in Alkaline Media

Emil Dieterich, Simon-Johannes Kinkelin, and Michael Bron^{*,[a]}

Abstract: Gold nanoparticles were synthesized and supported on carbon, or directly synthesized on carbon according to five different methods reported in literature, aiming at particles < 10 nm. Characterization was done with transmission electron microscopy and thermogravimetric analysis. Although all syntheses yielded particles with an average diameter < 10 nm, the formation of few very large particles, where a relatively large amount of Au is buried, as well as loss during the supporting procedure led to the exclusion of

four of the five tested methods for further studies. The most promising AuNPs supported on carbon were tested for the methanol electrooxidation (MEO) in alkaline media. Four different Au-loadings were realized, and supporting led to moderate particle growth depending on the loading. To compare MEO activity of the samples with different Au-loadings a conversion factor was developed where the MEO activity can be compared in terms of NP size and Au-loading.

Introduction

Gold nanoparticles (AuNPs) are of great interest for a broad variety of technologies, including catalysis, nano-electronics and biomedicine, because of their exceptional chemical stability, catalytic activity and unique size-depending electrical and optical properties.^[1,2] Among all sizes monodisperse sub 10 nm AuNPs are a very fascinating material. Their share of surface atoms is overtaking that of the bulk atoms, and as a consequence the atomic surface coordination decreases which leads to new catalytic properties, reactivity and stability.^[3] For electrocatalytic applications, AuNPs are usually immobilized on a supporting material, for higher stability, practicality and synergetic catalytic effects of the support. Often used supporting materials are conductive carbons, including CNTs,^[4] MWCNTs^[4] and carbon blacks^[5] as well as metal oxides like ZnO,^[6] TiO₂^[7] and SiO₂.^[6]

A large body of literature is available describing the synthesis of monodisperse AuNPs with particle diameters below 10 nm.^[8–12] Supporting these previously synthesized gold nanoparticles is a non-trivial issue. To support AuNP on carbon, the particles usually are stirred with added carbon support followed by drying (50–120 °C, air or argon atmosphere). The dry product is usually treated, depending if/what sort of stabilizing agent is used in the synthesis.^[12,13] These post-treatments are mainly

done for two reasons, first to increase the stability of the catalyst and second to remove surfactants (e.g. the stabilizer) and thus to liberate the gold surface, since any remaining surfactants could hinder surface reactions. Furthermore, some surfactants were shown to modify the selectivity of the catalyst.^[13,14] However, depending on the treatment and supporting material, there is particle growth to be expected,^[15] indicating that this treatment has to be done with great care.

In this study, we evaluate and compare various synthesis routes for sub 10 nm AuNP^[4,8–11] towards applicability of the supported NP in electrocatalysis. A special focus is on the gold utilization during synthesis and supporting procedure and on the resulting electrocatalytic properties. Given the known issues of greenhouse gas emissions due to the burning of fossil fuels and the recent developments in the field of alkaline fuel cells (e.g., use of anion exchange membranes), there is re-growing interest in the electrochemical oxidation of small organic molecules, which may be used in direct alcohol fuel cell, for example.^[16,17] Typical commercial catalysts for the direct alcohol fuel cell are PtNP based catalysts on carbon support, which are showing excellent activities for the MEO.^[18] Because of the poisoning of Pt by CO (by-product of the alcohol oxidation) and also the high price of Pt and the comparably lower activity of Pt based catalysts in alkaline media there is an immense interest in Pt free catalysts.^[18,19] Due to this, the electrocatalytic oxidation of methanol (MEO)^[20] has been chosen as a test reaction in this study.

Results and Discussion

Five different methods reported in literature were used for AuNP synthesis. In methods 1–3, AuNP were preformed using reducing agents and stabilizer, and the preformed AuNP were then transferred onto a carbon support. In methods 4 and 5, the AuNP were directly synthesized on carbon support. All

[a] E. Dieterich, S.-J. Kinkelin, Prof. Dr. M. Bron
Institut für Chemie, Technische Chemie I
Martin-Luther-Universität Halle-Wittenberg
Von-Danckelmann-Platz 4, 06120 Halle (Germany)
E-mail: michael.bron@chemie.uni-halle.de

Supporting information for this article is available on the WWW under
<https://doi.org/10.1002/cnma.202200098>

© 2022 The Authors. ChemNanoMat published by Wiley-VCH GmbH. This is an open access article under the terms of the Creative Commons Attribution Non-Commercial NoDerivs License, which permits use and distribution in any medium, provided the original work is properly cited, the use is non-commercial and no modifications or adaptations are made.

syntheses were aiming at Au particle sizes < 10 nm. As reducing agents NaBH₄ or KBH₄ were used, while 1-dodecanethiol (1-DDT), polyvinylpyrrolidone or no capping agent was applied to control particle growth, depending on the method. Details on the synthesis methods can be found in the experimental part.

STEM and TEM images were recorded to evaluate the size and size distribution of AuNPs after synthesis as well as supported on carbon material. Figure 1 shows TEM images of the synthesized AuNP, while Table 1 presents the statistical evaluation of these images. The TEM images show a distribution of gold particle sizes from 1.1 to 182 nm (Supporting Information (SI) Figure 1f) for method 1 (synthesis according to Jana et al.^[9]). While most Au particles are in the targeted size range of < 10 nm (SI Figure 2a)), still a major loss of gold occurs to particles which are not in the targeted size range (if 1 out of 600 AuNPs is in the range of ~182 nm, the loss is around ~96%_{Au}). While the average particle size agrees with the literature, the standard deviation differs from the reported values. For the synthesized AuNP according to method 1 a color change from light- to dark-red was observed over the next few hours, which indicates a particle growth.^[21] The AuNPs synthesized according to method 2 – Martin et al.^[8] and method 3 – Brust et al.^[10] are well within the targeted size range (1.1–10.9 nm and 0.6–7.5 nm) with an average size and a small standard deviation of 3.8 nm (± 1.0 nm) or 2.3 nm (± 0.6 nm) (SI Figure 2a)). Both results are in close agreement to the literature, and no changes in color were observed afterwards. The AuNPs synthesized according to method 3 are stable for at least eight months (SI Figure 3, 4 and SI Table 2). Their size can be changed by varying the length of the carbon-chain of the stabilizer used during synthesis (SI Figure 5 and SI Table 3). Due to the formation of large Au particles, method 1 was not further considered for Au/C catalyst preparation.

TEM images of Au/C are shown in Figure 2 while Table 2 shows the evaluation of the TEM images and the TG measurements. Au/C synthesized according to method 4 – Marshall et al.^[11] (Figure 2c) and g)) and method 5 – Zhang et al.^[22] (Figure 2d) and h)) shows a broader size range and AuNPs >

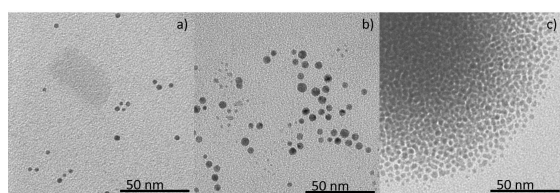


Figure 1. Representative TEM images of AuNPs synthesized according to a) method 1; b) method 2 and c) method 3.

method	Average size (stdv.) in nm	Size range in nm	Particles measured	Reported size in nm
1	3.4 (± 5.8)	1.1–182	1006	3.5 (± 0.7) ^[9]
2	3.8 (± 1.0)	1.1–10.9	3747	4.8 ^[8]
3	2.3 (± 0.6)	0.6–7.5	1800	2.0–2.5 ^[10]

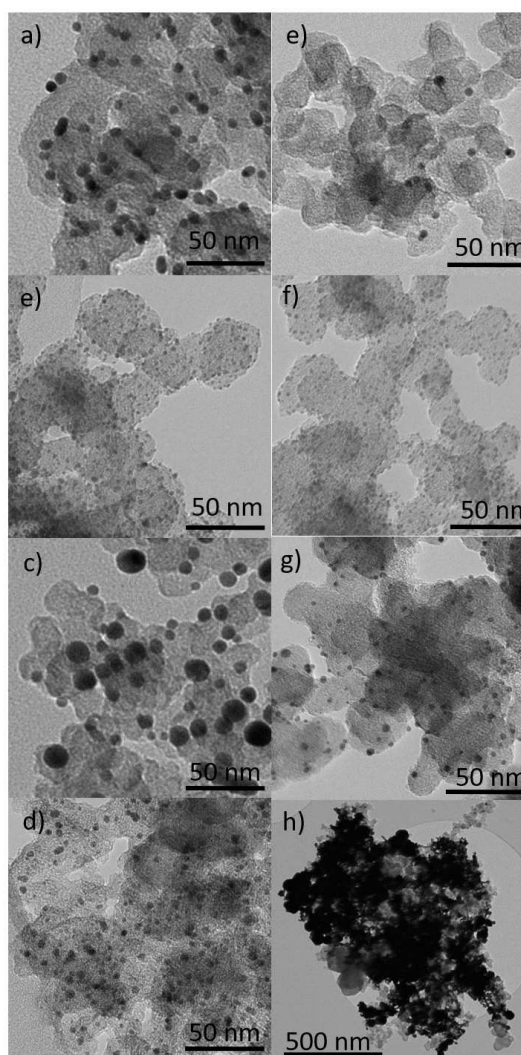


Figure 2. TEM images of the treated Au/C samples synthesised according to a), e) method 2; b), f) method 3; c), g) method 4 and d), h) method 5.

10 nm. Method 5 shows agglomerations of gold up to a few micrometers (Figure 2h)). More than 95% of the particles are in the targeted size range (size distribution for particles < 10 nm SI Figure 2b)), still the particles > 10 nm imply a big loss of gold in particles much larger than the targeted size range.

ARTICLE IN PRESS

A :COMPARATIVE STUDY OF THE SYNTHESIS OF SUB-10 NM CARBON-SUPPORTED GOLD NANOPARTICLES AND THEIR SUITABILITY FOR METHANOL ELECTROOXIDATION IN ALKALINE MEDIA

Table 2. Size, size range and transfer rate of the amount of gold used in the syntheses related to the amount of Au on the supporting material after Au/C sample treatment. Reported sizes in nm for method 4–4.7 nm^[11] and method 5–6.7 nm (size range 2–16 nm)^[22].

Method	Average size (stdv.) in nm	Size range in nm	Particles measured	Transfer rate in % (stdv.)
2	4.3 (± 1.0)	1.1–11.2	761	26 (± 23)
3	3.9 (± 1.3)	0.8–9.2	7053	76 (± 6)
4	4.1 (± 1.6)	0.8–18.1	662	169 (± 79)
5	6.3 (± 21)	1.3–449	646	102

During the supporting process, the mean particle sizes of the AuNPs synthesized according to method 2 and method 3 grew from 3.8 to 4.3 nm respectively 2.3 to 3.9 nm (see Figure 2a), e), b) and f)). Another important aspect is the amount of transferred gold during the synthesis and supporting process, which is determined from the Au-loading on Vulcan XC72 as examined by TG measurement (SI Figure 6 and SI Table 1). In Table 2 the fractions of transferred gold are shown. Transfer rates above 100% for the products according to method 4 and 5 are presumably the result of loss of carbon material during the synthesis. The carbon supported AuNPs show transfer rates between 26 and 76% (method 2 and 3, respectively). None of the synthesized Au/C products show a fully homogenous distribution of the AuNP on the supporting material (Figure 2). Some of the TEM images may suggest a homogenous particle distribution on the supporting material but there are areas on the supporting material without AuNPs, also in TEM images not shown. This is presumably related to inhomogeneous surface properties of the supporting material. To conclude, Au/C synthesized according to method 3 and then supported on Vulcan XC72 and treated as described shows only AuNPs in the targeted size range (i. e., no loss of material buried in large AuNPs) and an average loss of only ~24% during the synthesis and supporting procedure. Therefore, this catalyst was used for all further syntheses and investigations.

After establishing the most suitable preparation procedure for well-defined Au/C electrocatalysts with Au particle size < 10 nm, the Au-loading on Vulcan XC72 has been varied in order to evaluate its influence on the properties of Au/C in the MEO in alkaline electrolyte. Catalysts with four different Au-loadings were prepared. Table 3 shows the particle sizes, standard deviations, size ranges (from TEM, SI Figures 1 and 7), Au-loadings (from TG measurements) and the electrochemical surface area (ECSA) normalized by the total catalyst weight, as detailed in the SI. Around 97% of the AuNPs are < 10 nm and none are > 13 nm (SI Figure 7). As mentioned above, generally the AuNPs don't show a homogenous distribution on the supporting material (compare SI Figure 1c).

As mentioned above, the interest in the electrooxidation of small organic molecules is ongoing given the possibility of establishing CO₂-neutral energy conversion cycles, in case the organic molecules are prepared from renewable resources and converted in e.g. fuel cells. Recent progress in the field of alkaline fuel cells (in particular, progress in alkaline exchange membranes) together with the known electrocatalytic activity of gold in alkaline solution (in comparison to acids, where it is rather inactive) motivated us to investigate the properties of Au/C prepared as mentioned above towards the MEO. The four catalysts prepared with different Au-loadings were investigated towards the MEO using cyclic voltammetry in different electrolyte solutions (0.1 M KOH as base electrolyte, and with addition of 0.5 M, 2 M or 5 M MeOH). Figure 3 shows cyclic voltammograms (CVs) of one of the catalysts in the electrolyte solutions with different MeOH concentrations (Figure 3b)) and all four catalysts in the same solution (5 M MeOH, Figure 3a)). In 0.1 M KOH four potential regions with different contributions of Faradaic currents may be distinguished (SI Figure 8), namely the gold oxidation (Au-ox.) and the carbon corrosion (both in the forward scan, i.e. scan to more positive potentials), the gold reduction (Au-red.) in the backward scan and the OH⁻ desorption. Obviously, the Au-ox. and carbon corrosion are overlapping. In MeOH-containing KOH electrolyte, as expected a different behavior is observed. In the forward scan the MEO is overlapping with the Au-ox., and in the backward scan the Au-red. is overlapping with the MeOH-ox. and probably the oxidation of reaction intermediates.^[12,23–25] The CVs show an increase of the MeOH- and Au-ox. peak current with higher Au-loading and a higher MEO peak current with increasing MeOH concentration in the electrolyte. Also the oxidation peaks in the backward scan are increasing with both, higher Au-loading and higher MeOH concentration in the electrolyte. Interestingly, in the electrolyte solutions with higher MeOH concentration the MEO starts already at potentials below 0 V, i.e. below the potential where Au is oxidized. We assume that OH⁻ adsorption might aid in the MeOH oxidation at less positive potentials. Furthermore, from the CVs it seems that progressing Au-ox.

Table 3. Particle sizes, size ranges and metal amount of Au/C together with the intended Au-loading as well as the electrochemical surface area (ECSA) calculated from the Au reduction peak of the catalysts used in electrocatalytic experiments.

catalyst	Average size (stdv.) in nm	Size range in nm	Amount of Au in wt.% (theoretical wt.%)	ECSA in m ² /g _{cat.}
Au/C-1.7	2.9 (± 1.3)	0.8–9.2	1.7 (2.5)	0.12
Au/C-3.6	3.1 (± 1.0)	1.2–9.0	3.6 (5.0)	0.21
Au/C-8.3	4.4 (± 1.4)	1.1–12.2	8.3 (10.0)	0.64
Au/C-25	5.1 (± 1.7)	1.5–12.3	25.0 (24.0)	2.35

A :COMPARATIVE STUDY OF THE SYNTHESIS OF SUB-10 NM CARBON-SUPPORTED GOLD NANOPARTICLES AND THEIR SUITABILITY FOR METHANOL ELECTROOXIDATION IN ALKALINE MEDIA

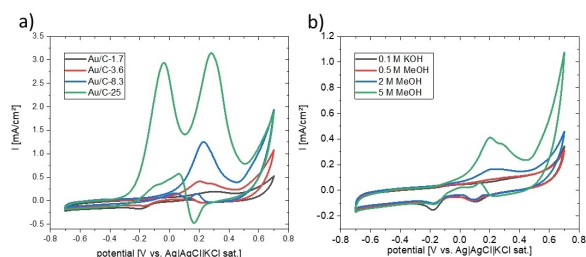


Figure 3. 25th cycle from CVs, a) Au/C catalysts in 5 M MeOH and 0.1 M KOH electrolyte; b) Au/C-3.6 in the four different used electrolyte solutions (0.1 M KOH as well as 0.5 M, 2 M and 5 M MeOH in 0.1 M KOH).

inhibits MeOH-ox., as seen by the decrease in oxidation current above ~0.5 V, and only at very positive potentials the current rises again, which might be an overlap between MeOH-ox. on oxidized Au at high overpotentials and carbon corrosion.

Notably, during the CV measurement of Au/C-25 there is a fifth Faradaic peak building up and reaching a stable level after 15 cycles with a maximum at around -0.05 V (Figure 3a) and SI Figure 9 and 10). In literature, intermediates/products of the MEO reaction which could be oxidized further are formaldehyde, formate and CO.^[26] CV measurements of solutions containing these intermediates did not show peaks at the observed potential for Au/C-25, thus we suspect that accumulation of these intermediates are not responsible for the slow generation of this new oxidation peaks (SI Figure 11). In detail, formate is oxidized around 0.3 V. For the measurement of formaldehyde in the electrolyte there is an oxidation current observed starting very early at -0.47 V and, as literature predicts, a formate peak is observed also, as formate is a known oxidation product of formaldehyde.^[26,27] CVs of CO saturated electrolyte do not show significant additional peaks, as literature suggests.^[28,29] A local pH change was also considered, but considered unlikely since the pH-dependent carbon corrosion at higher potentials seems to be unchanged. CVs under rotation of the electrode however seem to indicate that forced convection leads to a depletion of the responsible species in the vicinity of the surface, as seen by a decrease of the peak with increasing rotation rate at the Au/C-25 catalysts (SI Figure 9b)). Considering possible reaction pathways and intermediates for the MEO^[12,23,30-32] we suggest a change of selectivity with a higher Au-loading, which we assume to result from the smaller particle distances. We can only speculate that a high concentration of intermediates (e.g. formaldehyde),

which is build up locally, leads to solution chemistry and formation of intermediates, which then yield the unexpected CV peak.

It is not an unexpected result that the catalysts with higher Au-loading show higher MEO currents and ECSA. However, to quantitatively compare the different catalysts, we defined a conversion factor (cf) (SI section 1.2). This factor displays the capability to oxidize MeOH (both forward and backward scan) as normalized by the Au-red. electrical charge, which lets us compare the MeOH-ox. activity with regard to particle size and Au-loading. This comparison is valid as long as the MEO mechanism of the different catalysts are similar. Thus, the data for Au/C-25 has to be considered with caution, since the developing peak likely does not stem from initial MeOH-ox. To estimate the activity for MeOH-ox. thus, only the charges from the peak at approx. 0.2-0.3 V were used to calculate the cf of Au/C-25. Figure 4 shows the cf and the particle size in dependence of the Au-loading. For Au/C-1.7, -3.6 and -8.3 it is reasonable to assume the same MEO mechanism from the very same CV behavior. For these catalysts clearly the cf is changing with the Au-loading and is having a maximum for Au/C-3.6, and this behavior is valid for all three different MeOH concentrations used in this study. The electrochemical surface_{ECSA} specific current density shows the same behavior, i.e. is highest for Au/C-3.6, as displayed in Table 4, 5th column. On the other hand, the mass and the surface_{GCE} specific current densities (i.e., related to geometrical surface area) are showing a different

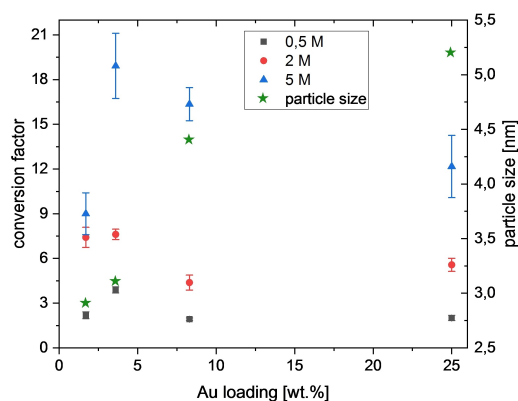


Figure 4. Conversion factor (cf) extracted from CV and particles size vs. the Au-loading for MEO over Au/C catalysts for all three MeOH concentrations used.

Table 4. MEO maximum current (5 M MeOH electrolyte corrected by the corresponding measurement in 0.1 M KOH) normalized by the geometric electrode area (0.1256 cm²), normalized by the amount of gold and by the calculated ECSA, as well as oxidation charge related to amount of gold.

catalyst	surface _{GCE} specific current density in mA/cm ²	mass specific oxidation charge density in mC/mg _{Au}	mass specific current density in mA/mg _{Au}	surface _{ECSA} specific current density in mA/cm ²
Au/C-1.7	0.14	263.42	55.59	0.76
Au/C-3.6	0.50	443.10	92.97	1.59
Au/C-8.3	1.39	439.75	111.27	1.44
Au/C-25	3.83	410.20	102.10	1.09

behavior, which can be explained by the fact, that only the peak currents of the CVs are taken into account, and not the whole oxidation charge. If the oxidation charge is considered (Table 4, 3rd column), again the Au/C-3.6 catalyst shows the best performance. These considerations also emphasize the advantage of the *cf*, which uses all oxidation charge (forward and backward scan) compared to the consideration of only the mass or surface_{GCE} specific peak current densities to compare the catalysts.

Keeping in mind the different particle sizes of these catalysts, this observation might point to a particle size effect in MEO on gold. On the other hand, the differences in average particle sizes between Au/C-1.7 and Au/C-3.6 are small. In literature MEO mass specific oxidation currents have been reported to increase with the Au-loading,^[33] which is in contrast to our results.

We would like to emphasize again that we have carefully chosen a catalyst preparation procedure leading to high Au utilization and low Au losses, which might explain the higher values compared to literature. While the mass specific and the surface_{GCE} specific current densities show different behaviors, the *cf* values indicate a non-monotonous effect of the Au-loading which is supported by the behavior of the surface_{ECSA} specific current and emphasizes the advantage of using the charge instead of the maximum current for catalyst comparison. Furthermore, also with increasing average particle size the *cf* is decreasing. Thus we conclude that for optimum MEO on supported gold nanoparticles, both particle size and loading on the carbon have to be adjusted.

Conclusion

In this study, different synthesis methods reported in literature for the preparation of AuNP and Au/C catalysts are investigated. All synthesis routes yield AuNPs in the average sizes reported in the respective literature. However, for method 1, 4 and 5 a high loss of gold to particles > 10 nm and for method 2 a high loss of gold during the supporting process are observed, rendering these methods inappropriate for fundamental studies in electrocatalysis. The most suitable approach was method 3 (a synthesis procedure according to Brust et al.), with a relatively small Au loss during synthesis and very moderate increase in size during the supporting process (average particle size 2.3 nm, supported 3.9 nm; size range 0.8–12.3 nm). Also the particles show only minor size changes during storage and their size can be manipulated by changing the stabilizing agent, which makes them even more interesting for a wide range of applications.

The mentioned nanoparticles were employed to prepare four Au/C catalysts with different Au-loadings, which led to a moderate, but loading-dependent growth of the nanoparticle sizes. To compare the catalysts towards MEO, a conversion factor (*cf*) was defined, which takes into account the different exposed surface areas of the catalysts. The *cf* for the catalyst with an Au-loading of 3.6 wt. %_{Au} is the highest and suggests that the activity for the MEO from a combination of this Au-loading and particle size is optimal. All four catalysts show

higher current per cm² and current per mg_{Au} peak values for the MeOH-ox. than comparable Au/C catalysts in literature.^[33] Compared to commercial Pt/C catalysts (170 mA/mg_{Pt}, 20 wt.%_{Pt}, ECSA 28 m²/g_{cat.}) the mass specific current of the Pt/C catalysts is higher what could be explained by their much larger ECSA.^[34] Therefore, further studies should investigate how to increase the ECSA of Au/C and take into account possibly present surfactants e.g. stabilizer which could decrease the ECSA.^[35] An unexpected peak was observed for the catalysts with an Au-loading of 25 wt.%_{Au}. Investigations of typical intermediates of the MEO could not clarify the origin of this peak and it probably results from locally high intermediate concentration and small particle distances on the support.

Experimental Section

Chemicals

The following chemicals and materials were used as received: HCl (37%, ROTH), HNO₃ (65%, ROTH), ethanol (abs. HPLC, Th Geyer), DI H₂O (SG water Ultra Clear UV ultrapure water, 0.055 μS*cm⁻¹), HAuCl₄·3 H₂O (ACS 99.99% metal basis, Au 49.0% min, Alfa Aesar), NaBH₄ (99%, Acros Organics), 1-dodecanethiol (> 98%, Sigma Aldrich), potassium iodide (≥ 9.5% ROTH), toluene (> 99.5% for synthesis, ROTH), NaOH (> 99%, ROTH), acetone (99.5% for synthesis, ROTH), n-hexane (> 99% p.a. ACS, ROTH), tetra-n-octylammonium bromide (98 + %, Alfa Aesar), Vulcan XC72 (carbon black, Cabot), polyvinylpyrrolidone K-30 (Sigma Aldrich), NH₄OH (Rotipura, ROTH), KBH₄ (99.98%, ROTIMETIC), methanol (99.98%, ROTH), Nafion 117 (sol. 5%, Sigma Aldrich), potassium formate (≥ 9%, Sigma Aldrich), formaldehyde (37%, ROTH), CO (10.21% in He, Air Liquide).

Instruments and measurements

Instruments used during the synthesis of nanoparticles include a rotary evaporator (Heidolph G3) and a centrifuge (Eppendorf 5804). Transmission electron microscopy (TEM) was performed on a Zeiss, Leo 912 Omega (120 keV, specific point-resolution 0.37 nm) and scanning transmission electron microscopy on a Zeiss GeminiSEM 500 with EDX (Oxford Ultim Max & Oxford Extreme and EBSD, Oxford C-Nano), resolution: 0.5 nm at 15 kV; 0.9 nm at 1 kV, 1.0 nm at 500 V, accelerating voltage: 0.02–30.0 kV, magnification: 50 times to 2,000,000 times, high efficiency InLens secondary detector for ultra-high resolution surface information). For the measurements the sample was suspended in ethanol and drop-casted onto carbon-coated copper grids, followed by drying at room temperature.

Thermogravimetric measurements were done to evaluate Au-loading in the supported catalysts and were performed with a Netzsch STA 449 F1 thermobalance. ~10 mg of sample were placed in a crucible (Al₂O₃) followed by heating (10 K/min) in 20% O₂/Ar up to 1000 °C.

Cyclic voltammetry was carried out using a Metrohm Autolab PGSTAT 128 N. For the measurement a four-neck one-compartment glass cell with three electrodes immersed into 0.1 M KOH electrolyte with/without 0.5 M, 2 M or 5 M MeOH, flushed with N₂ for 20 min, was used. An Ag|AgCl|KCl_{sat.} electrode (Meinsberger) was used as reference electrode, a Pt-net or Au-net as counter electrode and a freshly polished (1 μm, 0.3 μm Al₂O₃ powder and DI H₂O on fleece) catalyst coated glassy carbon electrode (GCE, A = 0.126 cm²)

as working electrode. The working electrode was prepared by dispersing the sample with a loading of 2.7 mg/ml (ratio 977/23 EtOH/Nafion 117) under sonication (Bandelin Sonocool, 75% intensity) for 15 min. Then 3.5 μl were drop casted onto the GCE twice and dried at RT (resulting loading 150 $\mu\text{g cm}^{-2}$). Cyclic voltammetry was performed between -0.7 and 0.7 V vs. Ag|AgCl|KCl_{sat.} (all potentials are given relative to Ag|AgCl|KCl_{sat.}). The following procedure was applied: three CV cycles with a scan rate of 20 mVs⁻¹ were followed by 20 cycles with 500 mVs⁻¹. After repeating this, another three cycles with 20 mVs⁻¹ were recorded. The rotating disc electrode (Radiometer, motor BM-ED1101) measurements were carried out as follows, 15 cycles with 20 mVs⁻¹, followed by 2 cycles at each rpm (rpm in the order 400, 900, 1600, 900 and 400).

Synthesis

Numerous syntheses for sub 10 nm AuNPs are reported in the literature, which provide a large variety of AuNPs with different or no surfactants. A selection of these (Martin et al.,^[8] Jana et al.,^[9] Brust et al.,^[10] Marshall et al.^[11] and Zhang et al.^[12]) was used for this study and the resulting AuNP were supported on Vulcan XC72 carbon black. All glassware was pre-cleaned in aqua regia under stirring for 12 h followed by heating up to 50 C with reflux cooling. Afterwards all glassware was flushed with DI water and boiled in DI water for at least 1 h. All solutions were prepared with DI water or abs. EtOH. All syntheses were performed at least three times, except the synthesis according to Zhang et al.^[12]

The first synthesis, referred to as method 1, was a modified procedure of Jana et al.^[9] for 3.5 nm thiol-capped AuNPs. Briefly 20 ml of 0.25 mmol/l HAuCl₄·3 H₂O were stirred in a 100 ml one-neck flask. 0.6 ml of 0.1 M NaBH₄, freshly prepared, was added dropwise and stirred for 15 min. 20.6 μl of 1-DDT were added and stirred for 1 h. 40 mg potassium iodide and 2 ml toluene were added, followed by 3 min of vigorous shaking. The toluene phase was collected and stored at 4 C.

The second synthesis – method 2 – was performed according to Martin et al.^[8] Two stock solutions, 50 mmol/l HAuCl₄·3 H₂O with the same molar ratio of HCl and 50 mmol/l NaBH₄ with the same molar ratio of NaOH where prepared. 9.5 ml DI water were stirred (350 rpm) in a 50 ml beaker. 100 μl of HAuCl₄ stock solution where added, followed by addition of 425 μl of NaBH₄ stock solution. The dispersion was boiled for 3 min and cooled down to RT in a water bath before it was transferred to a 100 ml one-neck flask. 6.33 ml acetone were added followed by 7.58 ml n-hexane; in between and after the single additions the dispersion was mixed vigorously. The organic phase was collected and stored at 4 C.

The third synthesis, referred to as method 3, was modified after Brust et al.^[10] A solution of 184.5 mg tetraoctylammoniumbromide in 6.75 ml toluene was stirred at 350 rpm. 3.75 ml freshly prepared 0.03 M HAuCl₄·3 H₂O were added dropwise and stirred for 10 min, followed by the addition of 81 μl 1-DDT and then the addition of 3125 μl freshly prepared 0.4 M NaBH₄ within 2 s and then 2 h of stirring to complete the reaction. After decanting the organic phase, the volume was reduced to one tenth by a rotary evaporator (55 C, ~120 mbar), followed by adding 40 ml of EtOH and storing at 4 C for 16 h. The precipitate was separated by centrifugation (5000 rpm, 30 min) and washed with EtOH twice. The product was dispersed in 3 ml toluene, 7 ml of EtOH were added, and the dispersion was stored at 4 C.

The fourth method is according to Marshall et al.^[11] where the AuNPs are directly transferred onto the carbon support. The required amount of Vulcan XC72 (114.2 mg), depending on the loading (here 20 wt. %_{Au}), was suspended in DI water (10 ml H₂O

per 100 mg supporting material) for 5 h in an ultrasonic bath (100 ml one-neck flask). Two stock solutions of 50 mmol/l HAuCl₄·3 H₂O with the same molar ratio of HCl and 50 mmol/l NaBH₄ with the same molar ratio of NaOH were prepared. 28 ml of DI water were mixed with 0.61 ml of the HAuCl₄-stock solution in a 100 ml one-neck flask. 0.83 ml of the freshly prepared NaBH₄-stock solution were added. This particle dispersion was added to the carbon dispersion and stirred for 20 h. The product was filtrated and washed with 100 ml DI water and dried at 60 C overnight.

Method 5 is a modified synthesis according to Zhang et al.^[12] where the AuNPs are synthesized directly on the carbon support. 160.7 mg Vulcan XC72 was filled into a 1 l one-neck flask while 56.7 mg HAuCl₄·3 H₂O where added to a second 1 l one-neck flask. To the latter flask, 300 ml DI water and 1.598 g PVP K-30 followed by another 180 ml DI water were added. The mixture was stirred until the PVP K-30 dissolved well. This Au-solution was added to the carbon support, stirred for 10 min and then suspended in an ultrasonic bath for 1 h. The pH of the dispersion was 3.2. 1 M NH₄OH was added until the pH value reaches 9.3, followed by addition of 25 ml freshly prepared 0.6 M KBH₄ solution. The dispersion was stirred for 24 h, centrifuged (5000 rpm, 90 min) and washed with 80 ml DI water. The washing was repeated three times. After the washing, the product was dried at 60 C for 15 h.

Supporting of AuNP on Vulcan XC72

To support the prepared particles on Vulcan XC72 a method modified after^[36] was used. The required amount of carbon black was dispersed by sonication in n-hexane (20 ml/100 mg n-hexane/carbon black) for 6 h. The respective AuNP suspension was dispersed by sonication for 30 min. Then it was added to the carbon black dispersion, sonicated again for 30 min and stirred overnight. The dispersion was separated by centrifugation (5000 rpm, 30 min) and washed with ethanol, followed by drying at 60 C and ~500 mbar overnight. The product was a black powder, labelled Au/C. All supporting processes were done at least three times for the different AuNP syntheses. The theoretical Au-loading was, if not mentioned otherwise, 20 wt. %_{Au}.

Catalyst treatment

The literature reports different treatment methods for Au/C which aim to increase the stability and remove surfactants from the gold surface.^[16,36–38] In this work, the Au/C catalysts were treated at 300 C with 20% O₂/Ar for 1 h followed by 2 h at 400 C under 15% H₂/Ar atmosphere in a tube-furnace. The total gas flow was 6 l/h with a heating ramp of 10 K/min. Before the heating ramp was started, the quartz glass tube with the quartz glass vessel, in which the sample was placed, was flushed with Argon (6 l/h) for 30 min.

Acknowledgements

We thank Annett Quetschke (Institut für Chemie, Technische Chemie I, Martin-Luther-Universität Halle Wittenberg) for performing TEM and TG measurements and Frank Syrowatka (Interdisziplinäres Zentrum für Materialwissenschaften, Martin-Luther-Universität Halle-Wittenberg) for the STEM measurements. Dr. Matthias Steimecke (Institut für Chemie, Technische Chemie I, Martin-Luther-Universität Halle Wittenberg) is acknowledged for in-depth scientific discussions. Open Access funding enabled and organized by Projekt DEAL.

Conflict of Interest

The authors declare no conflict of interest.

Data Availability Statement

The data that support the findings of this study are available from the corresponding author upon reasonable request.

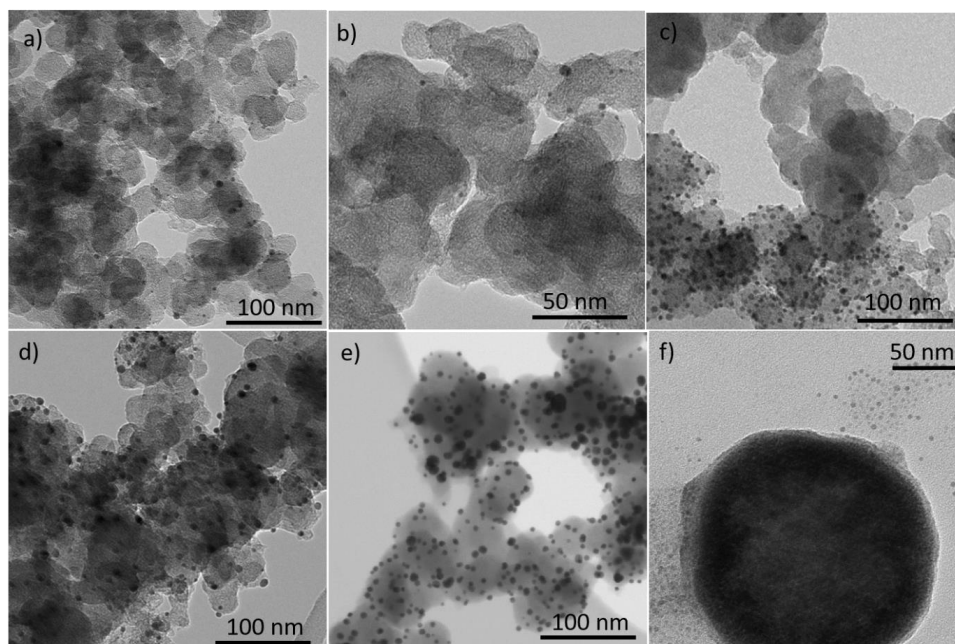
Keywords: electrochemistry · gold nanoparticles · methanol electrooxidation · supported catalysts · synthesis design

- [1] M.-C. Daniel, D. Astruc, *Chem. Rev.* **2004**, *104*, 293–346.
[2] W. Kurashige, Y. Niihori, S. Sharma, Y. Negishi, *Coord. Chem. Rev.* **2016**, *320–321*, 238–250.
[3] J. Piella, N. G. Bastús, V. Puentes, *Chem. Mater.* **2016**, *28*, 1066–1075.
[4] R. Zhang, M. Hummelgård, H. Olin, *Mater. Sci. Eng.* **2009**, *158*, 48–52.
[5] J. Luo, M. M. Maye, N. N. Kariuki, L. Wang, P. Njoki, Y. Lin, M. Schadt, H. R. Naslund, C.-J. Zhong, *Catal. Today* **2005**, *99*, 291–297.
[6] G. Li, D.-E. Jiang, C. Liu, C. Yu, R. Jin, *J. Catal.* **2013**, *306*, 177–183.
[7] A. Primo, A. Corma, H. García, *Phys. Chem. Chem. Phys.* **2011**, *13*, 886–910.
[8] M. N. Martin, J. I. Basham, P. Chando, S.-K. Eah, *Langmuir* **2010**, *26*, 7410–7417.
[9] N. R. Jana, L. Gearheart, C. J. Murphy, *Langmuir* **2001**, *17*, 6782–6786.
[10] M. Brust, M. Walker, D. Bethell, D. J. Schiffrin, R. Whyman, *J. Chem. Soc. Chem. Commun.* **1994**, *0*, 801–802.
[11] A. T. Marshall, V. Golovko, D. Padayachee, *Electrochim. Acta* **2015**, *153*, 370–378.
[12] S. Yan, S. Zhang, Y. Lin, G. Liu, *J. Phys. Chem. C* **2011**, *115*, 6986–6993.
[13] B. Donoeva, P. E. de Jongh, *ChemCatChem* **2018**, *10*, 989–997.
[14] Z. Niu, Y. Li, *Chem. Mater.* **2014**, *26*, 72–83.
[15] L. Prati, A. Villa, *Acc. Chem. Res.* **2014**, *47*, 855–863.
[16] A. S. Aricó, P. Bruce, B. Scrosati, J.-M. Tarascon, W. van Schalkwijk, *Nat. Mater.* **2005**, *4*, 366–377.
[17] J. Hou, Y. Shao, M. W. Ellis, R. B. Moore, B. Yi, *Phys. Chem. Chem. Phys.* **2011**, *13*, 15384–15402.
[18] S. S. Siwal, S. Thakur, Q. B. Zhang, V. K. Thakur, *Mater. Today Chem.* **2019**, *14*, 100182.
[19] Z. Yin, H. Zheng, D. Ma, X. Bao, *J. Phys. Chem. C* **2009**, *113*, 1001–1005.
[20] S. A. C. Carabineiro, *Front. Chem.* **2019**, *7*, 702.
[21] N. G. Bastús, J. Comenge, V. Puentes, *Langmuir* **2011**, *27*, 11098–11105.
[22] K. Zhang, W. Wang, W. Cheng, X. Xing, G. Mo, Q. Cai, Z. Chen, Z. Wu, *J. Phys. Chem. C* **2009**, *114*, 41–49.
[23] K. Shen, C. Jia, B. Cao, H. Xu, J. Wang, L. Zhang, K. Kim, W. Wang, *Electrochim. Acta* **2017**, *256*, 129–138.
[24] R. Banerjee, D. Ghosh, J. Satra, A. B. Ghosh, D. Singha, M. Nandi, P. Biswas, *ACS Omega* **2019**, *4*, 16360–16371.
[25] S. Möller, S. Barwe, J. Masa, D. Wintrich, S. Seisel, H. Baltruschat, W. Schuhmann, *Angew. Chem. Int. Ed. Engl.* **2020**, *59*, 1585–1589.
[26] J. Hernández, J. Solla-Gullón, E. Herrero, A. Aldaz, J. M. Feliu, *Electrochim. Acta* **2006**, *52*, 1662–1669.
[27] M. Avramov-Ivic, R. R. Adzic, A. Bewick, M. Razaq, *J. Electroanal. Chem. Interfacial Electrochem.* **1988**, *240*, 161–169.
[28] M. Haruta, A. Ueda, S. Tsubota, R. M. Torres Sanchez, *Catal. Today* **1996**, *29*, 443–447.
[29] N. Mayet, K. Servat, K. B. Kokoh, T. W. Napporn, *Electrocatalysis* **2021**, *12*, 26–35.
[30] J. Zhang, P. Liu, H. Ma, Y. Ding, *J. Phys. Chem. C* **2007**, *111*, 10382–10388.
[31] A. B. Anderson, H. A. Asiri, *Phys. Chem. Chem. Phys.* **2014**, *16*, 10587–10599.
[32] S. S. Sarmoor, S. J. Hoseini, R. Hashemi Fath, M. Roushani, M. Bahrami, *Appl. Organomet. Chem.* **2018**, *32*, e3979.
[33] S. Yan, S. Zhang, *Int. J. Hydrogen Energy* **2011**, *36*, 13392–13397.
[34] Y. Liu, H. Yang, X. Li, L. Mao, *Mater. Lett.* **2013**, *106*, 287–289.
[35] J. Xian, Q. Hua, Z. Jiang, Y. Ma, W. Huang, *Langmuir* **2012**, *28*, 6736–6741.
[36] J. Luo, M. M. Maye, N. N. Kariuki, L. Wang, P. Njoki, Y. Lin, M. Schadt, H. R. Naslund, C.-J. Zhong, *Catal. Today* **2005**, *99*, 291–297.
[37] K. Sun, T. Cheng, L. Wu, Y. Hu, J. Zhou, A. MacLennan, Z. Jiang, Y. Gao, W. A. Goddard, Z. Wang, *J. Am. Chem. Soc.* **2017**, *139*, 15608–15611.
[38] C. Rogers, W. S. Perkins, G. Veber, T. E. Williams, R. R. Cloke, F. R. Fischer, *J. Am. Chem. Soc.* **2017**, *139*, 4052–4061.

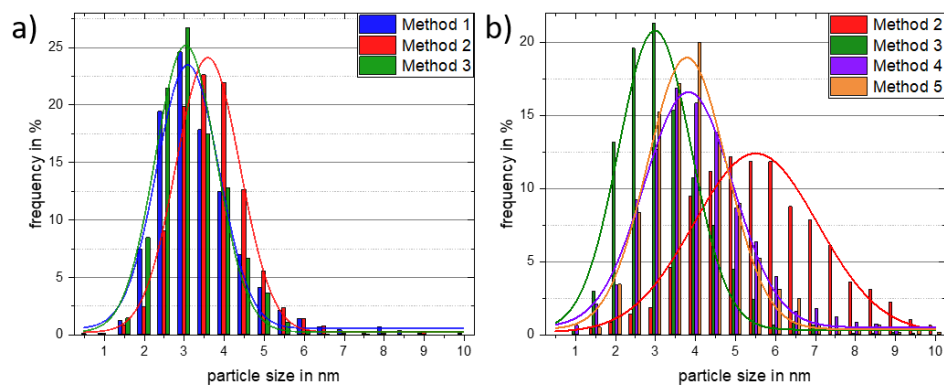
Manuscript received: March 2, 2022
Revised manuscript received: April 7, 2022
Accepted manuscript online: April 8, 2022
Version of record online: May 5, 2022

ARTICLE IN PRESS

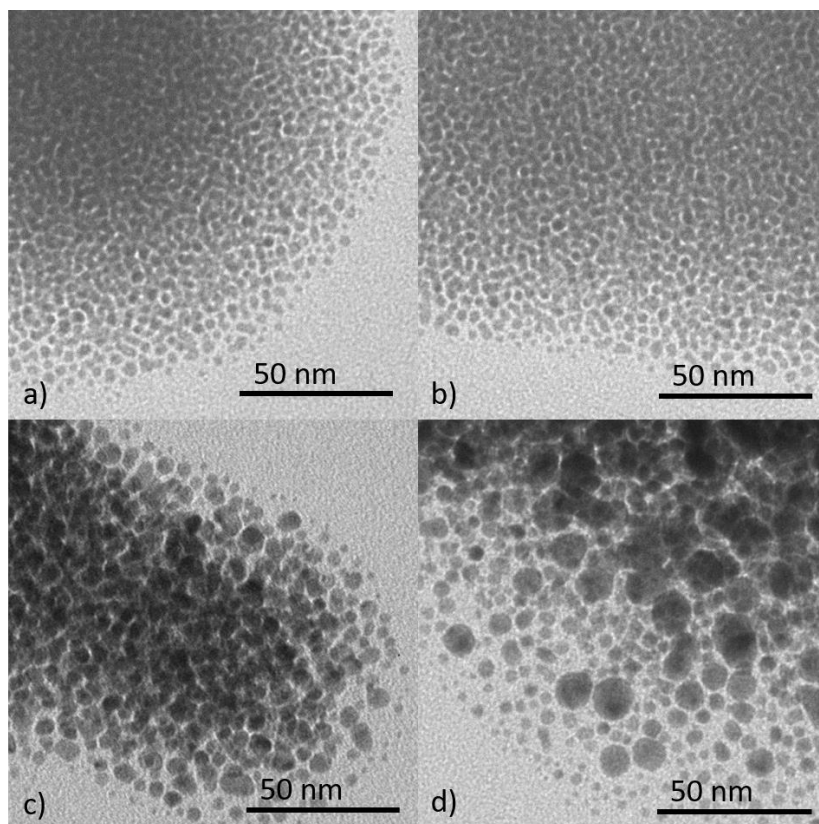
COMPARATIVE STUDY OF THE SYNTHESIS OF SUB-10 NM CARBON-SUPPORTED GOLD NANOPARTICLES AND THEIR SUITABILITY FOR METHANOL ELECTROOXIDATION IN ALKALINE MEDIA



SI Figure 1: TEM images of the catalysts Au/C-1.7 (a), -3.6 (b), -8.3 (c), (d) and -25 (e, f): example of a large AuNP obtained with method 1

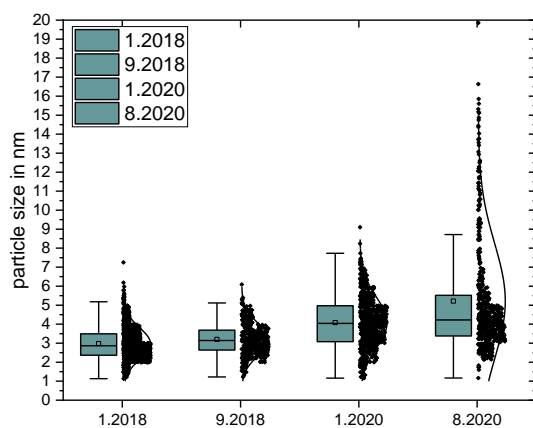


SI Figure 2: Particle size distribution of a) Au particles and b) Au/C catalysts of all different synthesized samples of this study with the corresponding Gaussian curves

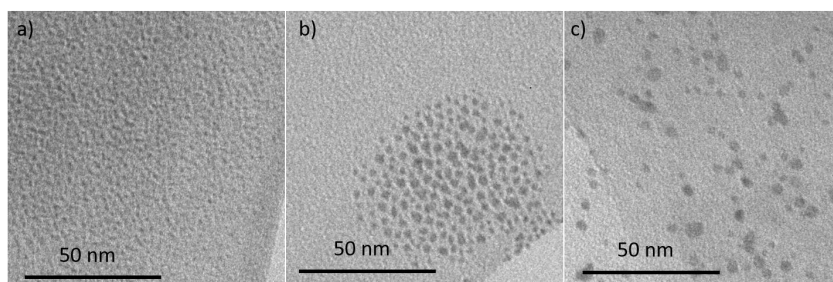


SI Figure 3: TEM images of AuNP according to the synthesis of Brust et al.^[1] after different storage time in a glass flask at room temperature a) freshly prepared, b) after 9 month, c) 24 month, d) 32 month.

ARTICLE: COMPARATIVE STUDY OF THE SYNTHESIS OF SUB-10 NM CARBON-SUPPORTED GOLD NANOPARTICLES AND THEIR SUITABILITY FOR METHANOL ELECTROOXIDATION IN ALKALINE MEDIA

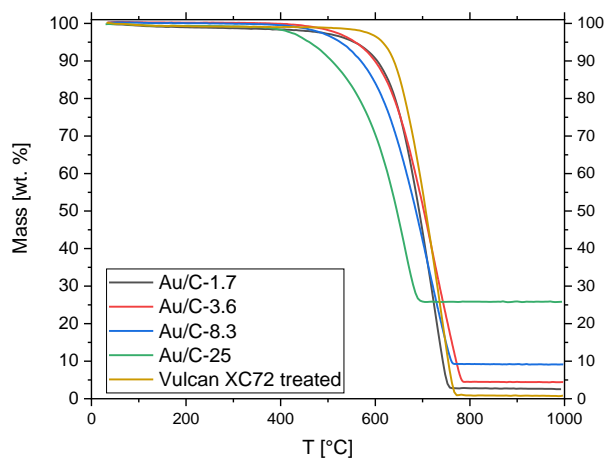


SI Figure 4: AuNP size distribution over the time with whiskers showing 25th or 75th percentile, while the box is 50th percentile. The line is showing the median, the square the average, the dots are measured values.

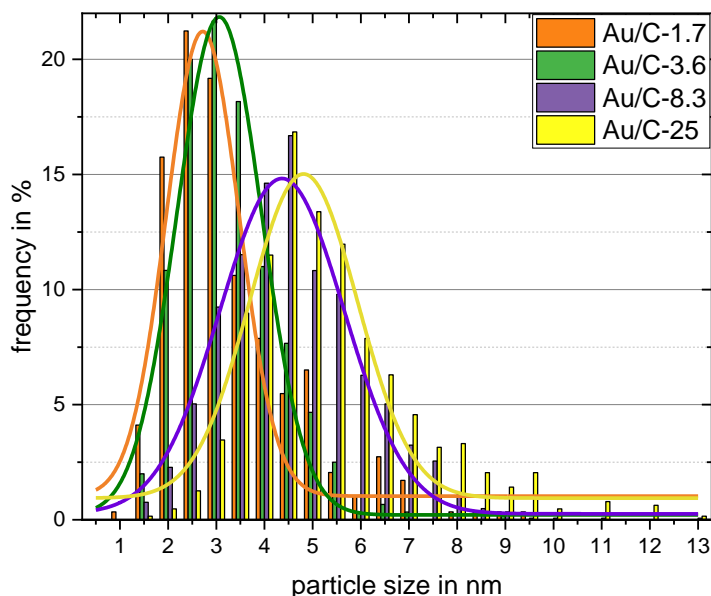


SI Figure 5: AuNP synthesized according to Brust et al.^[1]; size variation by changing the stabilizer a) 1-octadecanethiol, b) 1-dodecanethiol and c) 1-pentethiol

A :COMPARATIVE STUDY OF THE SYNTHESIS OF SUB-10 NM
CARBON-SUPPORTED GOLD NANOPARTICLES AND THEIR SUITABILITY
FOR METHANOL ELECTROOXIDATION IN ALKALINE MEDIA



SI Figure 6: Thermogravimetric measurement of the different samples and of Vulcan XC72 which was treated the same way as the samples



SI Figure 7: Gold particle size distribution of the catalysts Au/C-1.7, -3.6, -8.3 and -25 with the corresponding Gaussian curves

SI Table 1: Results of TG measurement and Au-loading corrected by the solid residue of treated Vulcan XC72.

sample	Solid residue [wt.%]	Calculated Au-loading [wt.%]
Vulcan XC72 treated	0.8	
Au/C-1.7	2.5	1.7
Au/C-3.6	4.4	3.6
Au/C-8.3	9.1	8.3
Au/C-25	25.8	25.0

1.1.1. Size degradation over storage time of AuNPs synthesized according to method 3

SI Table 2: Ageing of AuNP during time, while stored in a glass flask at room temperature.

Date	Average size (stdv.) in nm	Size range in nm	Particles measured
01.2018	2.3 (\pm 0.6)	0.6 – 6.0	1800
09.2018	3.2 (\pm 0.9)	1.2 – 6.1	324
01.2020	4.1 (\pm 1.4)	1.2 – 9.1	677

08.2020 5.2 (\pm 3.0) 1.2 – 20.3 525

1.1.2. Size variation of AuNPs synthesized according to method 3 by changing the stabilizing agent

SI Table 3: AuNP size variation by changing the stabilizing agent.

Stabilizer	Average size (stdv.) in nm	Size range in nm	Particles measured
1-octadecanethiol	1.8 (\pm 0.5)	0.6 – 3.2	1800
1-dodecanethiol	2.3 (\pm 0.6)	0.6 – 6.0	1800
1-pentethiol	4.5 (\pm 3.1)	0.8 – 50.2	1988

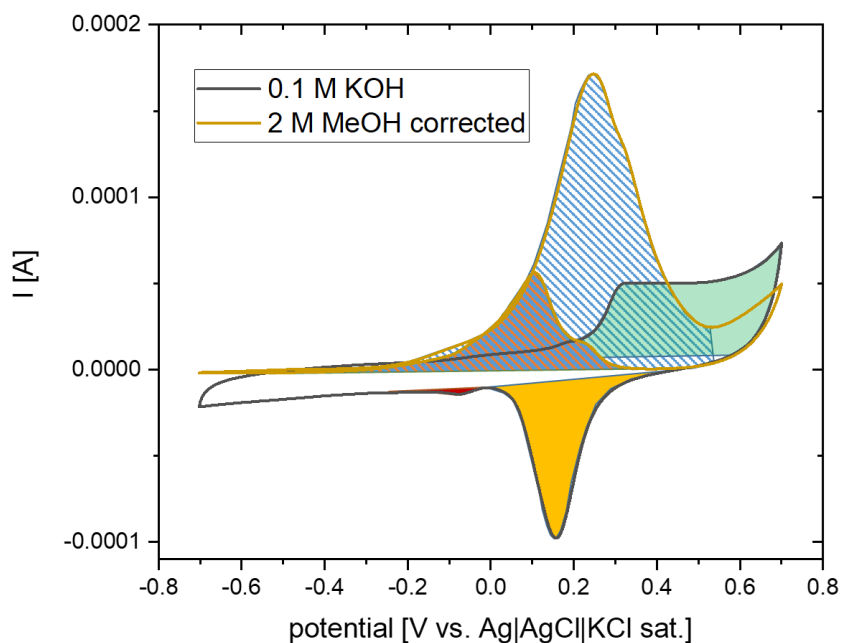
1.1.3. Calculation of the ECSA

The ECSA was calculated according to literature^[2] (also AuNP on Vulcan XC72) using a charge density of 493 $\mu\text{C}\cdot\text{cm}^{-2}$ for the area of the Au-reduction peak (corrected by the corresponding blank measurement in 0.1 M KOH) divided by the scan rate (50 mV/s^{-1}). The charge for Au/C-1.7, -3.6, -8.3 and -25 is 11.5, 19.6, 59.6 and 218.0 μC .

1.2. Conversion factor

The conversion factor (cf) to compare the MEO capability of the different catalysts consist of three different electric charges, by integrating the areas in the CV measurements with KOH as electrolyte and MeOH and KOH as electrolyte corrected by the KOH measurements and divide these by the scan rate (areas in CV respectively in the CV corrected by the KOH measurement SI Figure 8). These three electric charges C_1 (MeOH-oxidation (corrected, forward scan)), C_2 (MeOH-oxidation and oxidation of reaction intermediates (corrected, backward scan)) and C_3 (Au-reduction, backward scan).^{[4][5][6]}

$$cf = \frac{|C_1| + |C_2|}{|C_3|}$$

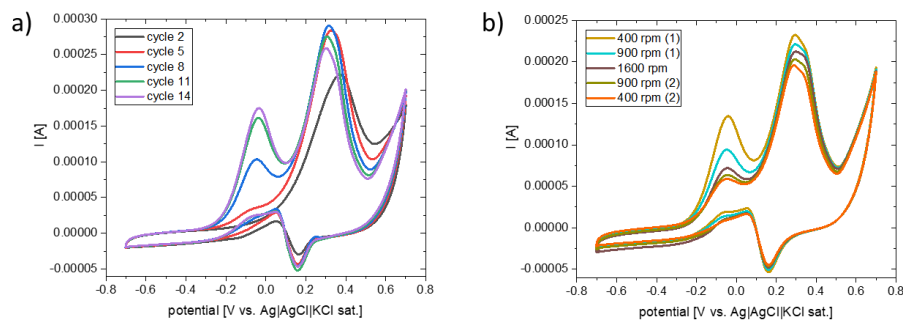


SI Figure 8: Third cycle of CV measurement of Au/C-25 in 0.1 M KOH (grey line) and 2 M MeOH in 0.1 M KOH corrected by the measurement in 0.1 M KOH (yellow line). Blue striped area – MeOH-oxidation, forward scan; red striped area – MeOH-Oxidation and oxidation of reaction intermediates, backward scan; light green area – Au oxidation and carbon corrosion, forward scan; yellow area - Au-reduction, backward scan; red Area – OH-desorption, backward scan.^{[4][5][6]}

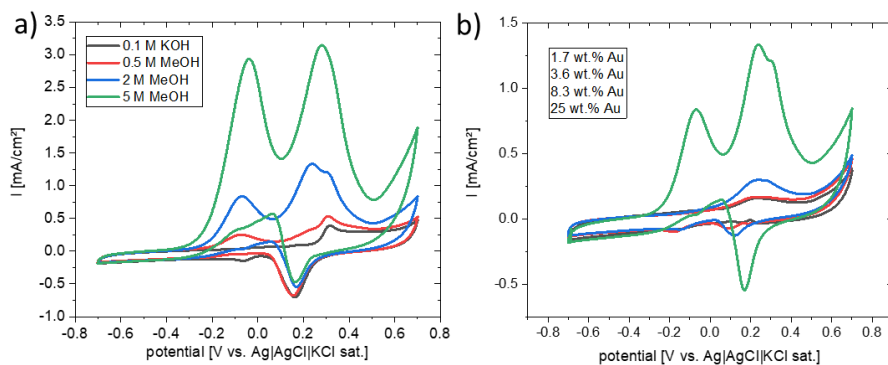
1.3. RDE measurement

SI Figure 9 a) shows the development of the unassigned peak during CVs without rotation. This peak current is decreasing during CVs with rotation, because of convection. The CVs with rotation also do show a decrease of the MeOH-ox. and Au-ox. peak, which can be ascribed to catalyst degradation.^[3]

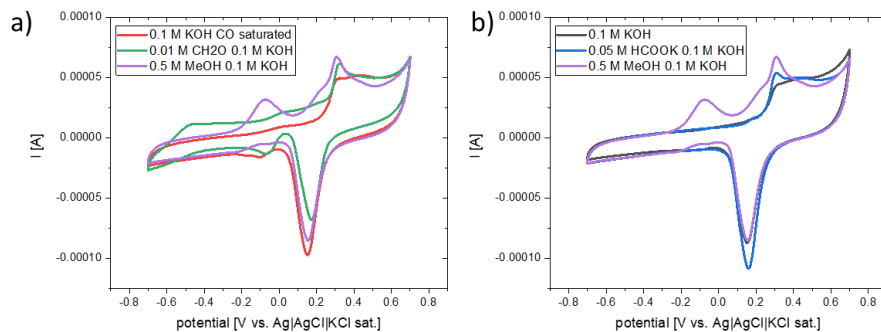
A :COMPARATIVE STUDY OF THE SYNTHESIS OF SUB-10 NM
CARBON-SUPPORTED GOLD NANOPARTICLES AND THEIR SUITABILITY
FOR METHANOL ELECTROOXIDATION IN ALKALINE MEDIA



SI Figure 9: a) CVs of Au/C-25 in 5 M MeOH and 0.1 M KOH electrolyte, b) 2nd CV of RDE measurements (2 CVs at each rpm) after 15 CVs without rotation. Measurements in in order 400, 900, 1600, 900 and 400 rpm.



SI Figure 10: cyclic voltammograms of a) Au/C-25 in different electrolytes and b) the different catalysts with an electrolyte of 2 M MeOH and 0.1 M KOH.



SI Figure 11: CVs with Au/C-25 as catalyst, of measurements with possible reaction intermediates of the MeOH-ox. a) red: 0.1 M KOH, saturated for 20 min with CO; green: 0.1 M KOH and 0.01 M formaldehyde (which is stabilized in solution by 0.001 M MeOH); purple: 0.1 M KOH, 0.5 M MeOH. B) black: 0.1 M KOH, blue 0.1 M KOH and 0.05 M formate, purple 0.1 M KOH and 0.5 M MEOH

2. Literature

- [1] M. Brust, M. Walker, D. Bethell, D. J. Schiffrin, R. Whyman, *J. Chem. Soc., Chem. Commun.* **1994**, 0, 801–802.
- [2] M. Simões, S. Baranton, C. Coutanceau, *Appl. Catal., B* **2010**, 93, 354–362.
- [3] J. L. Bott-Neto, T. S. Martins, S. A. S. Machado, E. A. Ticianelli, *ACS applied materials & interfaces* **2019**, 11, 30810–30818.
- [4] S. Yan, S. Zhang, Y. Lin, G. Liu, *J. Phys. Chem. C* **2011**, 115, 6986–6993.
- [5] K. Shen, C. Jia, B. Cao, H. Xu, J. Wang, L. Zhang, K. Kim, W. Wang, *Electrochimica Acta* **2017**, 256, 129–138.
- [6] R. Banerjee, D. Ghosh, J. Satra, A. B. Ghosh, D. Singha, M. Nandi, P. Biswas, *ACS omega* **2019**, 4, 16360–16371.



Cite this: *Nanoscale Adv.*, 2022, 4, 5154

Quantifying the removal of stabilizing thiolates from gold nanoparticles on different carbon supports and the effect on their electrochemical properties†

Emil Dieterich, Simon-Johannes Kinkelin, Matthias Steimecke and Michael Bron *

Gold nanoparticles <10 nm in size are typically prepared using stabilizing agents, e.g. thiolates. Often standard recipes from literature are used to presumably remove these stabilisers to liberate the surface, e.g. for catalytic or electrocatalytic applications, however the success of these procedures is often not verified. In this work, thiolate-stabilised AuNPs of ca. 2 nm in size were synthesized and supported onto three different carbon supports, resulting in loadings from 15 to 25 wt% Au. These materials were post treated using three different methods in varying gas atmospheres to remove the stabilizing agent and to liberate the surface for electrochemical applications. Using thermogravimetry – mass spectroscopy (TG-MS), the amount of removed stabilizer was determined to be up to 95%. Identical location scanning transmission electron microscopy (il-(S)TEM) measurements revealed moderate particle growth but a stable support during the treatments, the latter was also confirmed by Raman spectroscopy. All treatments significantly improved the electrochemically accessible gold surface. In general, the results presented here point out the importance of quantitatively verifying the success of any catalyst post treatment with the aim of stabilizer removal.

Received 22nd August 2022
Accepted 2nd November 2022

DOI: 10.1039/d2na00561a

rsc.li/nanoscale-advances

Introduction

Supported gold nanoparticles (AuNPs) are of particular interest for a wide range of applications, including catalysis. Factors determining their catalytic properties are, among others, size, shape and dispersion on a support, metal–support-interactions as well as surfactants. Therefore, there is a major interest in tunable and controllable syntheses of supported nanoparticles.^{1–4} For AuNPs below 10 nm the share of surface atoms overtakes the amount of bulk atoms, which results in new optical and electronic properties. A large number of studies addresses the size and shape of AuNPs depending on the chosen synthesis.^{2,4,5} The characteristics of the materials directly depend on the chosen stabilizing agent, the synthesis conditions and the support material.

For the application as (electro)catalysts, the AuNPs are usually immobilized onto support materials like carbon nanotubes,⁶ multi-walled carbon nanotubes,⁶ carbon blacks⁷ and metal oxides like ZnO,⁸ TiO₂⁹ and SiO₂.⁸ Supporting typically results in higher stability, ease of use and synergetic effects with

the support material. AuNP which are synthesized as colloids before their immobilization are usually covered by surfactants which are also referred to as stabilizers. The stabilizer has the crucial role of protecting the colloids against aggregation and growth, because of their higher surface energy. Typical stabilizing agents used in the AuNP synthesis are polyvinyl alcohol (PVA), polyvinylpyrrolidone (PVP), thiolates *etc.*¹⁰ However, it is often unclear to which extent the stabilizing agent is influencing the activity, selectivity and stability of the AuNPs in catalytic reactions. For example, PVA exhibits a shielding effect in the liquid phase glycerol oxidation on Au/TiO₂, where the remaining PVA entails a negative impact on the activity.¹¹ Alkanethiolates are widely used stabilizing agents for various kinds of metals since they form self-assembling monolayers (SAMs) on the metal surfaces, e.g. Au,¹² Ag,¹³ Cu,¹⁴ Pt¹⁵ and Pd.¹⁶ A different surface behavior is observed for Au compared to Pt group metals in the surface binding of thiolate, where the bonding structure on Au is more ordered compared to Pt.^{16,17} For palladium nanoparticles stabilized by alkanethiolates, a Pd⁰ core with a PdS_x shell has been found, which is poisoning the nanoparticles with respect to hydrogenation and dehydrogenation.¹⁶ It is also shown that the d-electron distribution on AuNPs is altered by thiol capping agents and the stabilized Au atoms are depleted in 5d-electrons because of the strong S–Au interaction.¹⁸ Stabilizing agents are thus modifying the electronic structure and are therefore having a great impact on

Institut für Chemie, Technische Chemie I, Martin-Luther-Universität Halle-Wittenberg, Von-Danckelmann-Platz 4, 06120 Halle, Germany. E-mail: michael.bron@chemie.uni-halle.de

† Electronic supplementary information (ESI) available: Additional experimental details, TEM images as well as Raman and electrochemical data. See DOI: <https://doi.org/10.1039/d2na00561a>



activity and selectivity. Furthermore, the stabilizer might react under catalytic conditions, which can damage and change the structure of the catalyst during the reaction, which might result in a change of the catalytic properties.¹⁹ Therefore, the removal of stabilizing agents is of particular interest. However, the removal of any stabilizer does not necessarily imply a fully liberated metal surface.

After surfactant removal, the NPs are typically stabilized by interaction with the support material and by small molecules from the surrounding. These small molecules often are more easy to displace and therefore less critical for the catalytic reaction.¹⁰ During the removal, there is usually a change in shape as well as a growth of the nanoparticles. This growth is affected by the conditions used during stabilizer removal as well as the support material.^{20,21} The removal is a very delicate process and depending on the stabilizer there are different common methods to remove the stabilizer, such as washing with different solvents and acids, UV-ozone irradiation treatment, calcination or heat treatment in different gas atmospheres.^{7,22–25}

Concerning the supporting process of AuNPs stabilized by thiolates, different methods are suggested, which are to choose with caution depending on the chosen metal, since, as already mentioned above, the alkanethiolates-metal surface behavior varies. Commonly, the AuNPs are stirred with the support, followed by a drying step (50–120 °C, air or argon atmosphere). To actively remove the stabilizing thiolates, various treatment processes were reported: (I) annealing for 10 h in air at temperatures between 120 and 185 °C,²⁶ (II) heating in vacuum for 1 h⁸ to overnight²⁷ at 150–180 °C, (III) treating up to 300 °C in N₂²⁸ and (IV) treatment at 300 °C with 20% O₂/N₂ followed by 400 °C with 15% H₂/N₂.²⁹ Depending on the treatment and support material, particle growth is to be expected.⁴

As already mentioned, in addition to the activity, the stability towards a given application is also influenced by the presence or absence of stabilizers or their residues. Typical degradation mechanisms during electrochemical stress are particle growth by Ostwald ripening or agglomeration, dissolution, detachment of particles and loss of electric contact.^{30–32} The stability also depends on the particle size, with smaller particles being less stable. As shown in^{33,34} particles below 5 nm show a significantly lower stability against repeated oxidation and reduction in acid media because of dissolution.

In this work, an in-depth investigation of the effect of different heat treatment processes (300 °C 20% O₂/Ar, 400 °C 15% H₂/Ar, both individually or combined) onto thiolate-protected AuNPs in comparison to untreated AuNPs on different carbon supports is made. In particular, we want to analyze the amount of removed stabilizer determined by TG-MS as well as the influence of treatments onto the morphological characteristics examined by identical location-(S)TEM, Raman spectroscopy and cyclic voltammetry. Furthermore, the stability towards electrochemical stress in alkaline and acidic media is investigated by cyclic voltammetry. This work will demonstrate that care must be taken when removing thiolate capping agents from Au catalysts and that both temperature and gas atmosphere during removal are important.

Methods

Chemicals

The following chemicals and materials were used as received: ethanol (abs. HPLC, Th Geyer), DI H₂O (SG water ultra clear UV ultrapure water, 0.055 μS cm⁻¹), HAuCl₄·3 H₂O (ACS 99.99% metal basis, Au 49.0% min, Alfa Aesar), NaBH₄ (99%, Acros Organics), 1-dodecanethiol (>98%, Sigma Aldrich), toluene (>99.5% for synthesis, ROTH), *n*-hexane (>99% p.a. ACS, ROTH), tetra-*n*-octylammonium bromide (98+%, Alfa Aesar), Vulcan XC72 (carbon black, Cabot), Nafion 117 (sol. 5%, Sigma Aldrich), Baytubes C 150 P (carbon nanotubes, C-purity >95%, number of walls 3–15, Bayer Material Science), Black Pearls 2000 (carbon black, Cabot), argon (99.999%, Air Liquide), oxygen (99.998%, Air Liquide), hydrogen (99.999%, Air Liquide), potassium hydroxide (99.98%, ROTIMETIC, 3N8), perchloric acid (Supra 70%, ROTH), CO₂ (99.995%, Air Liquide).

Instruments and measurements

Instruments used during the synthesis of nanoparticles include a rotary evaporator (Heidolph G3) and a centrifuge (Eppendorf 5804). For the carbon pre-treatment a furnace (Nabatherm RHTH 80-300/18) and for the AuNPs on carbon treatment a tube furnace (Carbolite MTF 12/38/250) were used.

Transmission electron microscopy (TEM) was performed using a Zeiss Leo 912 Omega (120 keV, specific point-resolution 0.37 nm) and a scanning transmission electron microscope (STEM) (Zeiss GeminiSEM 500 with EDX (Oxford Ultim Max & Oxford Extreme and EBSD, Oxford C-Nano), resolution: 0.5 nm at 15 kV; 0.9 nm at 1 kV, 1.0 nm at 500 V, acceleration voltage: 0.02–30.0 kV, magnification: 50 times to 2 000 000 times, high efficiency InLens secondary detector for ultra-high resolution surface information). For the measurements the sample was suspended in ethanol and drop-casted onto carbon-coated copper grids (PLANO GmbH, carbon holey film, 2.05 mm Cu-net 300 mesh), followed by drying at room temperature. For the identical location measurements, the same preparation was used, but instead of the carbon-coated copper grids, carbon-coated gold finder grids (PLANO GmbH, carbon holey film on Au-finder grids, net type H7) were used.

Raman spectroscopy was performed with an InVia Raman spectrometer setup (Renishaw), which is equipped with a microscope with a 100× objective (both Leica), a Cobolt CW DPSS laser (532 nm excitation wavelength), a 1800 l mm⁻¹ grating and a Peltier cooled charge coupled device (CCD) camera detecting the Raman scattering. The Raman spectrometer was calibrated to a silicon reference peak and the signal was adjusted to 520.4 cm⁻¹ before the measurements. For every sample at least three Raman mapping experiments with 42 to 110 measurement points each and a distance of ~1 μm in *x*- and *y*-direction between the measurement points were performed. The spectra were recorded between 800 and 1900 cm⁻¹ with 1.0% laser intensity and 15 s integration time for all CNT samples and the untreated as well as the H₂ and O₂ treated Vulcan samples. All BP2000 and the Vulcan sample with combined treatment were measured with 0.5% laser intensity



and 20 s integration time since these samples were damaged by irradiating with higher intensities.

Thermogravimetric measurements combined with mass spectroscopy analysis (TG-MS) were used to evaluate the gold loading on the supported catalysts and the amount of removed stabilizer. The measurements were performed with a Netzsch STA 449 F1 thermobalance. ~5 mg of sample were placed in a crucible (Al₂O₃) followed by heating (10 K min⁻¹) in 20% O₂/Ar up to 1000 °C. 500 μL of CO₂ were pulsed using a sample loop, at 5 min and 83 min, as an internal reference, and data were normalized to the average area of these peaks to compare the individual measurements. The mass spectrometer (Netzsch QMS 403C Aëolos) was probing the exhaust stream for specific masses (44 g mol⁻¹ (CO₂), 28 g mol⁻¹ (CO), 64 g mol⁻¹ (SO₂), 29 g mol⁻¹ (COH⁺), 45 g mol⁻¹ (COOH⁻), 91 g mol⁻¹ (unknown)³⁵).

The specific surface area (SSA) was determined with a Sorptomatic 1990 (Thermo Finnigan). Before each measurement, the sample was heated under vacuum (10⁻⁵ mbar) at 120 °C for 24 h. The adsorption and desorption isotherms were measured at 77 K using nitrogen as adsorbate at relative pressures p/p_0 of 0.05 to 0.3. The evaluation of the adsorption data was done using the Brunauer-Emmett-Teller (BET) theory.

Cyclic voltammetry was carried out with a Metrohm Autolab PGSTAT 128N potentiostat. A four-neck one-compartment glass cell with three electrodes immersed into 0.1 M KOH or 0.1 M HClO₄ electrolyte solution, flushed with Ar for 20 min, was used. An Ag|AgCl|KCl_{sat.} electrode (Meinsberger Elektroden) served as reference electrode, an Au-mesh (Au-net 99.9%, Goodfellow) as counter electrode and a freshly polished (1 μm, 0.3 μm Al₂O₃ powder and DI H₂O on fleece) catalyst coated glassy carbon electrode (GCE, $A = 0.126 \text{ cm}^2$) as working electrode. The working electrode was prepared by dispersing the sample in EtOH/Nafion 117 solution (ratio v/v 977/23) with a loading of 3 mg ml⁻¹ under sonication (Bandelin Sonocool, 75% intensity) for 5 min. Then 3.14 μL of this suspension were drop-casted onto the GCE four times and dried at room temperature in between (resulting loading was 300 μg cm⁻²). Cyclic voltammetry was performed between 0.3 V and 1.65 V vs. RHE in HClO₄ and 0.05 V to 1.65 V vs. RHE in KOH electrolyte solution. The following procedure was applied: the internal resistance was determined using the current interrupt method, followed by 1000 CV cycles at a scan rate of 50 mV s⁻¹. For the electrochemical degradation measurements on identical location Au-finder grids the identical setup was used but instead of 1000 CVs, 10 CVs were performed. The sample holder for the Au-finder grids is displayed in the ESI, paragraph 1.4.†

Synthesis

All glassware was pre-cleaned with aqua regia, as detailed in the ESI, paragraph 1.1† and for solution preparation DI water was used. All experiments were carried out at least three times to ensure reproducibility.

For AuNP synthesis a modified³⁶ procedure according to Brust *et al.*¹² was used. Briefly, a solution of 184.5 mg tetraoctylammonium bromid (TOAB) in 6.75 ml toluene was prepared followed by dropwise addition of 3.75 ml freshly prepared

0.03 M HAuCl₄·3 H₂O aqueous solution. The dispersion was stirred for 10 min, followed by the addition of 81 μL 1-dodecanethiol (1-DDT). 3125 μL of freshly prepared 0.4 M NaBH₄ aqueous solution was added. The dispersion was stirred until the aqueous phase became clear, and the aqueous phase was decanted to remove excess educts. The organic phase was reduced to a tenth of its volume with a rotary evaporator. Then 40 ml of ethanol was added and the suspension was stored at 4 °C for 16 h. The precipitate was separated by centrifugation (5000 rpm, 30 min) and washed with ethanol twice for removal of excess stabilizing agent. Then the product was dispersed in 3 ml toluene and 7 ml ethanol were added. The suspension was stored at 4 °C.

AuNP were supported onto carbon (Vulcan XC72 as well as Black Pearls 2000 and Baytubes (both pre-treated, see below)), according to a modified method presented in,²⁹ if not mentioned otherwise. The required amount of carbon black was suspended in *n*-hexane (20 ml/80–100 mg *n*-hexane/carbon black) for 5:30 h with the aid of an ultrasonic bath. The AuNP suspension was agitated for 30 min (ultrasonic bath). The latter suspension was then added to the carbon black suspension, sonicated again for 30 min and stirred overnight. The solid was separated by centrifugation (5000 rpm, 30 min), washed with ethanol to remove any remaining impurities from the colloid synthesis and dried at 60 °C and ~500 mbar overnight. The product was a black powder labelled Au/C and the calculated Au-loading was 20 wt% Au.

For the pre-treatment of Baytubes and Black Pearl 2000 the material was placed in a quartz glass vessel in a furnace, which was flushed before (~30 min) and during the treatment with Ar (10 L h⁻¹). Then the support material was heated to 800 °C (5 K min⁻¹) for 1 h to achieve a homogenous starting material.

Catalyst treatments

Different treatment methods are suggested in literatur.^{8,12,26,27} Accordingly, in this work the various samples were treated in a tube-furnace under different conditions. Treatment processes at 300 °C in 20% O₂/Ar for 1 h, 400 °C in 15% H₂/Ar for 1 h, and both treatments combined (the oxygen followed by the hydrogen treatment) were compared with the samples without treatment. The total gas flow was 6 L h⁻¹ with a heating ramp of 10 K min⁻¹. For the treatment a tube-furnace was used with a quartz glass tube (ø 35 mm) and a quartz glass vessel. Before starting the heating ramp, the quartz glass tube containing the sample was flushed with Ar for at least 30 min. For the combined treatment, in between the oxygen and the hydrogen treatment the system was flushed with Ar for 30 min. These treatments were carried out both on the powdery samples as well as on those deposited onto Au finder grids.

Results and discussion

To unravel the influence of the various treatment procedures on the size and distribution of the AuNP and the structure of the support material, transmission electron microscopy (TEM) and scanning transmission electron microscopy (STEM) images



B :QUANTIFYING THE REMOVAL OF STABILIZING THIOLATES FROM GOLD NANOPARTICLES ON DIFFERENT CARBON SUPPORTS AND THE EFFECT ON THEIR ELECTROCHEMICAL PROPERTIES

View Article Online

Nanoscale Advances

Paper

were recorded before and after the treatments. These investigations were carried out on the powder samples but also for Au/Vulcan of samples deposited onto Au-finder grids for identical location-(S)TEM (il-(S)TEM) investigations.

All supported Au samples in this work were prepared with colloidal AuNPs, the synthesis and properties of which are discussed in detail in our previous work (for a representative TEM image and size distribution see ESI Fig. 2†).³⁶ An average size of 1.9 nm (± 0.4 nm) with a size distribution in the range of 0.6–7.5 nm was found. In the present work, besides Vulcan XC72 (“Vulcan”), Baytubes (“CNTs”) and Black Pearls 2000 (“BP2000”) were used as support. A negligible particle growth, if any, is observed during the supporting procedure as can be evaluated from the TEM images in Fig. 1(a), (c), (e) and ESI Fig. 3(a), (c), (i),† as well as the corresponding average particle sizes and standard deviations in Fig. 2(a) (blue bars).

For all samples the average particle sizes and standard deviations after the various treatment processes are shown in Fig. 2(a). Corresponding selected (S)TEM images of the powdery samples after the various treatment procedures are shown in ESI Fig. 3,† while the evaluation of the (S)TEM images and the Au-loading measured by TG-MS are summarized in ESI Table 1.† For a better visualization, the particle size distribution is additionally shown in ESI Fig. 4.† The results clearly indicate particle growth specific for each treatment and support. AuNPs on Vulcan and CNTs show a similar behavior with a significant particle growth that increases in the $O_2^- < H_2^- < O_2 + H_2^-$ -treated sample. In contrast, on BP2000 the particle growth is less pronounced, and also the order of the particle growth changes to $H_2^- < O_2^- < O_2 + H_2^-$ -treatment. This different behavior supposedly is caused by different surface areas and defect structures of the supports.^{20,21,37} While Vulcan and CNT have a similar specific surface area (SSA_{BET}), BP2000 has a significantly higher SSA_{BET} (Vulcan – 217 $m^2 g^{-1}$, CNT – 200 $m^2 g^{-1}$ and BP2000 – 1357 $m^2 g^{-1}$). Despite Vulcan and CNTs are similar in terms of SSA, clearly there is a difference in their

structure, as Vulcan has a greater share of disordered carbon whereas CNTs should possess and increased amount of graphitic surface carbon, albeit certainly with defects. Vulcan and BP2000 show a similar structure in terms of their share of disordered and graphitic structured carbon. Thus, the differences in particle growth likely can be attributed to the different SSA.

Raman measurements indicate only minor changes of the carbon support by the treatment processes as shown in Fig. 2(b) and ESI Fig. 5.† The ratio between the so-called D- and G-band (D/G ratio), which is indicative of the ratio between disordered and graphitic carbon, slightly changes. It seems to be slightly reduced for the O_2^- - and the $O_2 + H_2^-$ -treated samples, which might indicate removal of amorphous/disordered carbon by the oxygen treatment, however these changes are within the error bars of the measurements and should not be over-interpreted.

Besides the general assessment of particle growth of the powdery samples, as discussed above, il-(S)TEM allows for much deeper insight into the local changes. Fig. 1 and 3 display il-(S)TEM images of Au/Vulcan before and after the treatment procedures with a focus on the Au particles (Fig. 1) and on the carbon support (Fig. 3). It can be seen that the particle growth is not homogeneous and that in areas of higher particle density there is obviously an increased growth. Furthermore, larger particles in particular remain intact and only change their position slightly, while many smaller particles disappear. Therefore, we suggest a particle surface mobility during the treatments that leads to agglomeration. This particle mobility increases with decreasing particle size. That would also explain the lower growth of the AuNP on BP2000 support compared to Vulcan and CNTs resulting from a higher particle-to-particle distances because of the higher SSA (see above), although there is a greater particle mobility due to the smaller particles size. No influence of the growth behavior was found whether treating the samples as powder (~ 100 mg) or onto the Au-finder grids.

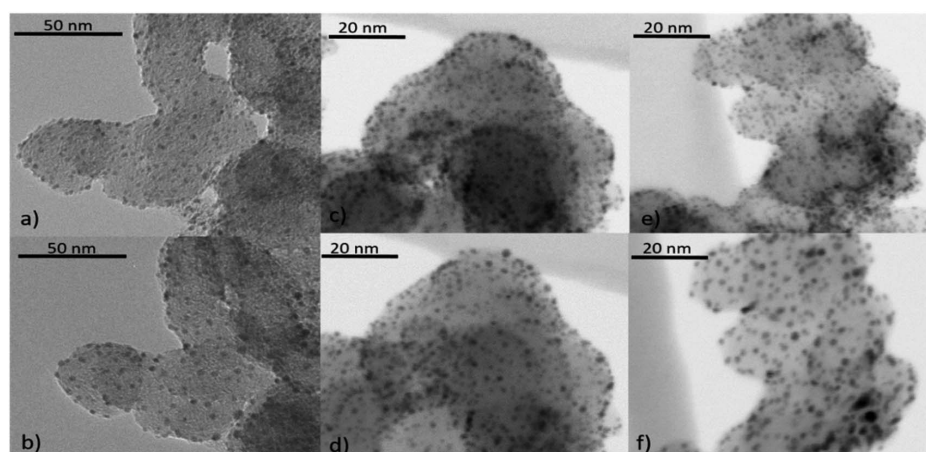


Fig. 1 Identical location (S)TEM images of Au/Vulcan, (a), (c), (e) untreated and (b) O_2^- , (d) H_2^- and (f) $O_2 + H_2^-$ -treated.



B :QUANTIFYING THE REMOVAL OF STABILIZING THIOLATES FROM GOLD NANOPARTICLES ON DIFFERENT CARBON SUPPORTS AND THE EFFECT ON THEIR ELECTROCHEMICAL PROPERTIES

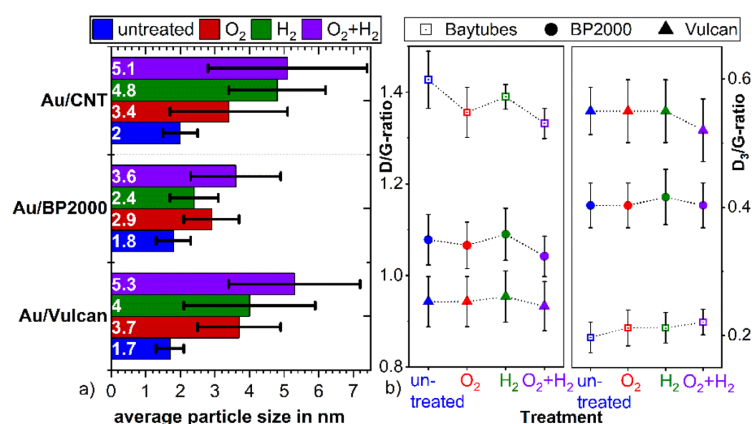


Fig. 2 (a) Particle size (as noted at the base of the bars) and standard deviation depending on the specific treatment of the powder samples, (b) D/G-band intensity ratio and the D₃/G-band intensity ratio of the differently treated samples, as obtained from Raman measurements.

il-(S)TEM has further been used to unravel possible changes which might occur at the support material during heat treatment. Fig. 3 indicates, that there are only minor changes in the support material (Fig. 3(a), (b), (e) and (f), yellow circles) for the O₂- and the O₂ + H₂-treated samples, in accordance with the Raman results. For the H₂-treated samples no changes in the support material are observed at all by il-(S)TEM. However, there are some crystal-like structures of higher density observable (Fig. 3(a) red circles), which are removed by the treatments. Since it is unlikely that these structures are gold particles, because they are removed by the treatments, we assume that they consist of impurities from the carbon support. These structures can be observed in all untreated samples and are

always removed during the treatments. As shown in ESI Fig. 6† we can exclude excess stabilizer as this impurities because of the different appearance in TEM images.

The total amount of stabilizer removed by the different treatments was determined by TG-MS measurements. To ensure the effect of excess stabilizer in the catalysts is as small as possible the products were repeatedly washed with ethanol after the synthesis. ESI Fig. 6† shows the appearance of 1-DDT which is not present in the (S)TEM images of our samples. As already discussed, the stabilizing agents respectively surfactants have a crucial role in determining the catalytic properties of metallic nanoparticles and for most applications there is a need of stabilizer free particles. Fig. 4(a) and (b) present TG

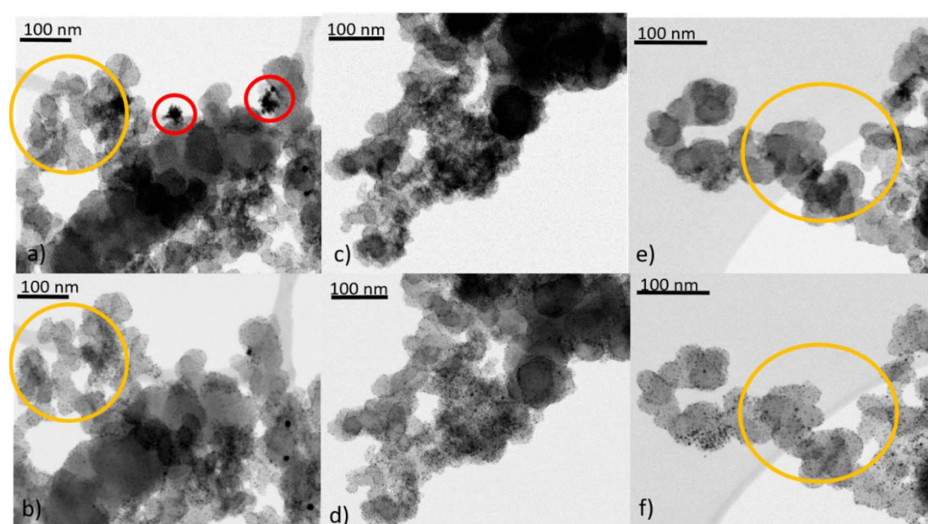


Fig. 3 il-(S)TEM images of Au/Vulcan, top row (a), (c), (e) untreated and (b) O₂-, (d) H₂- and (f) O₂ + H₂-treated. Yellow circles to highlight areas of changes of Vulcan during treatments. Red circles for removal of impurities.



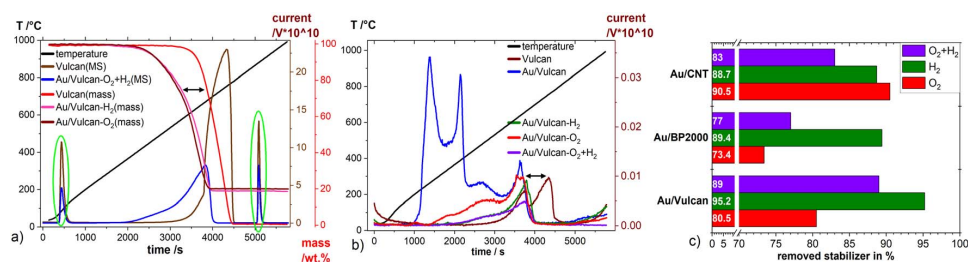


Fig. 4 (a) TG-MS measurements with currents normalized to the CO₂ ($m/z = 44u$) peak area, baseline corrected, (b) SO₂ ($m/z = 64u$) currents multiplied $\times 1000$, green circles in (a) CO₂ injections for normalization, (c) amount (as noted at base of the bars) of removed stabilizer from AuNP by the different treatments (see text).

curves of Vulcan and Au/Vulcan as well as the corresponding MS signals of CO₂ (Fig. 4(a)) and of SO₂ (Fig. 4(b)) of the different treated and untreated samples as well as the bare support material. To compare the un-/treated samples in terms of amount of removed stabilizer, the SO₂ MS-signal was normalized by the area of the CO₂ injection peaks (see Experimental part) and then corrected by the normalized SO₂ MS-signal of the related bare un-/treated support (see also ESI paragraph 1.3†). While the SO₂ quotient of the untreated sample is related to an Au surface fully covered with stabilizing agent plus the sulphur impurities in the support, the SO₂ quotient from the support is directly proportional to the amount of sulphur impurities in the carbon support. The resulting unit-less quotient after correction with by support is therefore proportional to the amount of SO₂ on the Au surface. The normalization towards a standard was necessary due to the fluctuations of the MS signal, which are obvious for the different samples as shown for the CO₂ signal in Fig. 4(a) (green circles).

The SO₂ formation (comp. Fig. 4(b)) of the untreated sample (Au/Vulcan) starts around 200 °C, while it shifts to higher temperatures for the treated samples. It is evident that the main part of the sulfur is removed at higher temperatures (200–400 °C), indicating that treatment processes below 200 °C in air or Argon are not sufficient for stabilizer removal, while temperatures and atmospheres used in this study are (see below). There is also displacement of the decomposition curve from TG ($\sim 90^\circ$ C, (Fig. 4(a) black arrow) as well as for the SO₂ MS signal (Fig. 4(b) black arrow) between the support and the samples, which suggest that the AuNP are catalyzing the thermal carbon oxidation of the support.

Fig. 4(c) summarizes the amount of stabilizer removed from the different Au/C samples by the various treatments. For Au/BP2000 and Au/Vulcan the H₂-treated samples retain the lowest amount, while the O₂- and the O₂ + H₂-treated samples show much higher amounts of remaining stabilizer (or its decomposition/oxidation products). For Au/CNTs a different behavior is observed. Here, the O₂- and the H₂-treated samples retain a comparable low amount, while the combined treatment surprisingly leaves a higher amount of stabilizer in the sample. In contrast to the Au/CNT sample, where these observations cannot be finally clarified, the behavior of Au/Vulcan and Au/BP2000 can be plausibly explained. For Au/BP2000 and Au/

Vulcan the combined treatment is showing a higher amount of remaining stabilizer then the H₂-treatment. We assume that during the O₂-treatment the stabilizer is oxidized to a species that cannot be removed by H₂-treatment; in contrast, 1-DDT is substantially removed by the H₂-treatment.

To further characterize the different carbon-supported Au samples and to analyze the influence of the different treatment procedures towards the surface properties, electrochemical methods, here cyclic voltammetry, in two different electrolyte solutions (0.1 M KOH, 0.1 M HClO₄) were applied. ESI Fig. 7(a)–(e)† show cyclic voltammograms (CVs, Fig. 5(a)) of the samples as well as the Au-mass specific reduction charge (Fig. 5(b)) and the double layer capacity (ESI Fig. 7(f)†). The CVs show Au-oxidation (forward scan ~ 0.8 V in HClO₄, ~ 0.1 V in KOH) which is overlapping with corrosion of the supporting carbon material. The Au-reduction peak (backward scan ~ 0.8 – 0.9 V in HClO₄, ~ -0.02 to 0.1 V in KOH) is proportional to the Au surface and therefore used to determine the impact of the various treatments on the accessible Au surface.³⁶ All samples have in common that the untreated samples display significantly less intense Au redox features in comparison to the treated ones, which is a result of surface blocking by the stabilizing agent, underpinning again the necessity of stabilizer removal. On closer inspection of the CVs, the Au reduction peak of the untreated samples is shifted (~ 60 mV in HClO₄; ~ 100 mV in KOH) to lower potentials in comparison to the treated samples in all cases. The same holds true for the Au-oxidation, which is shifted to higher potentials and inseparably accompanied by carbon oxidation.³⁶ Thus, while blocking the surface, the stabilizer also protects the gold from being oxidized. For a quantitative evaluation of the redox features, the Au-reduction peak was integrated and its charge was normalized to the Au mass loading for all samples (cf. Fig. 5(b)). As mentioned above, a higher reduction charge equivalent to a higher free surface area can be deduced for all samples. However, a noticeable higher mass-specific charge of untreated Au/CNT in comparison to the untreated samples of Au/Vulcan and Au/BP2000 is also apparent. Furthermore, the increase of the mass specific charge of Au/CNT after all treatments is significantly lower than for all other samples, although the change in particle size is comparable to Au/Vulcan (cf. Fig. 3(a)). To understand this issue, it should be recalled that the particles of the untreated



B : QUANTIFYING THE REMOVAL OF STABILIZING THIOLATES FROM GOLD NANOPARTICLES ON DIFFERENT CARBON SUPPORTS AND THE EFFECT ON THEIR ELECTROCHEMICAL PROPERTIES

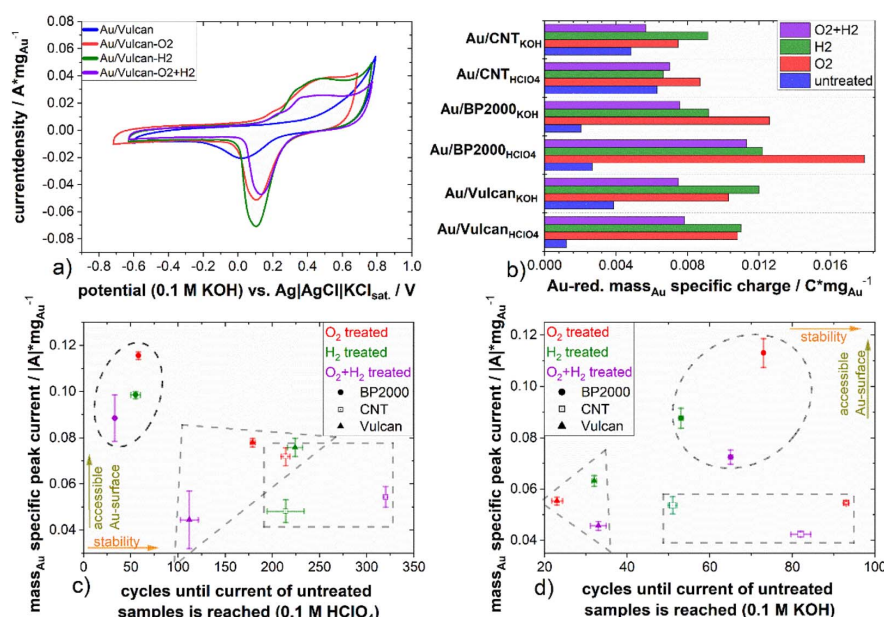


Fig. 5 (a) Cyclic voltammograms (3rd cycle) of the untreated and differently treated AuNP on Vulcan in 0.1 M HClO₄, (b) the Au-reduction peak area normalized by the Au-loading (Au-mass specific charge), (c) and (d) absolute minimum currents of the Au-reduction peaks over the number of cycles until the absolute minimum current of the untreated sample is reached for degradation measurements in (c) 0.1 M HClO₄ and (d) 0.1 M KOH, all evaluated currents were corrected by the capacitive current through baseline correction.

samples are smaller than those of the corresponding treated samples, which in principle should result in larger free surface area (*i.e.* redox features) than the treated ones. The observation that the larger particles show more intense redox features indicates that also for the CNT-supported samples there is a significant effect of the treatment, and for the other samples the removal effect is even more pronounced than suggested by Fig. 5(b). However, a second effect should be considered here, which is a possibly poor electrical contact through the protective stabilizing agent to the support material, which might be different in case of Au/CNT with the more ordered, graphitic support, which could lead to a better contact and thus higher mass specific charge of the untreated sample. However, as already mentioned, the Au-oxidation and -reduction is shifted, which means that a higher potential is needed for the reaction and the Au-reduction charge is smaller, thus probably both effects are responsible.

Comparing the different treatment processes, the samples treated in a single step (only H₂ or O₂) display higher mass specific reduction charge than the samples that underwent the combined treatment, indicating a higher electrochemically available gold surface area.

The double layer capacity (ESI Fig. 7(f)†), which is indicative of the whole catalysts surface area and not just that of the gold, is increasing with all treatments. We assume that the increase by the H₂ treatment is solely due to the removal of stabilizer, which blocks most of the Au and some support surface. For the O₂ treatments, we expect a higher surface functionalization of

the support in addition to the effects we assumed for the H₂ treatments. For the combined treatment, a mixture of the effects can be assumed. The high increase of the double layer capacity of the BP2000 samples after the treatment indicates a particularly high surface functionalization and defect formation in these samples during the treatment as well as the smaller AuNPs with higher Au surface.

With respect to a possible application of these materials in various electrochemical conversion reactions, the stability during potential cycling is of interest. In particular, the influence of the presence of stabilizing material should be addressed. Thus, all samples were exposed to repeated (up to 1000 cycles) electrochemical stress by cyclic voltammetry. The mass specific current of the Au-reduction peak in KOH and HClO₄ was taken for quantitative evaluation of the experiment and is shown for the treated samples at the y-axis in Fig. 5(c) and (d). Selected CVs of the stress cycling can be found in ESI Fig. 8 and 9.† As already mentioned, the untreated samples show the lowest Au-reduction current. Therefore, the treated samples were analyzed in relation to the untreated sample to emphasize the effect of the treatment and the number of cycles that are needed to reach the current of the untreated sample, which was taken as a measure for evaluation. Fig. 5(c) and (d) present at the x-axis the number of cycles which are needed until the Au-reduction current of the treated sample reaches the Au-reduction current of the untreated sample. At the y-axis the mass specific current of all treated samples in HClO₄ and KOH electrolyte, respectively is presented. The measurements in



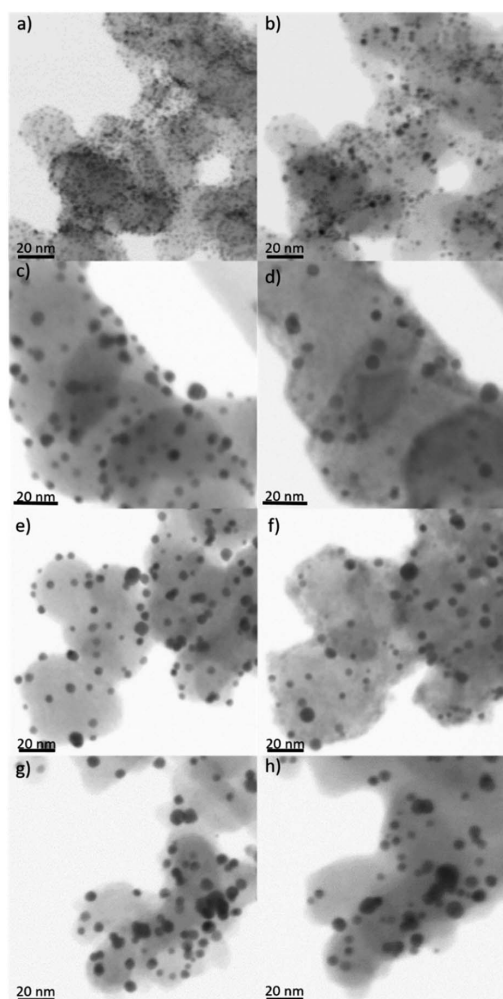


Fig. 6 il-(S)TEM images of Au/Vulcan before being subjected to electrochemical stress in 0.1 M KOH, untreated (a), O₂- (c), H₂- (e) and O₂ + H₂-treated (g) and after subjected to electrochemical stress un- (b), O₂- (d), H₂- (f) and O₂ + H₂-treated (h).

acidic electrolyte indicate a higher cycling stability (up to 320 cycles) compared to the measurements in alkaline electrolyte. This is also supported by ESI Fig. 10,† which shows the mass specific reduction current minimum over the number of cycles. The Au/BP2000 samples show the highest mass specific reduction current while the Au/Vulcan and Au/CNT samples are performing similarly, still in average the Au/CNT samples have the lowest mass specific current, which agrees with the particle size of the treated sample and the initial CVs. Au/CNTs is showing the highest average cyclic stability. The higher stability of Au/CNTs is assumed to be a results of the structural difference of the CNTs compared with BP2000 and Vulcan and also stronger particle-support interaction. Furthermore, it is

apparent that for the untreated samples, there is a strong increase in reduction current during the initial cycles, which might indicate stabilizer removal and surface liberation. However, it must also be stated that there seems to be no straightforward correlation between treatment procedure and stability.

Additionally, il-STEM of the untreated and treated Au/Vulcan sample was performed before and after electrochemical stress to further investigate the electrochemical stability and the degradation mechanism. Fig. 6 shows the il-(S)TEM images of Au/Vulcan untreated and treated before and after electrochemical stress. There is an obvious loss of particles in the il-(S)TEM images and furthermore a growth of the remaining particles. While the growth appears to occur predominantly in areas with larger particles and higher particle density, a greater loss of particles appears in the area of smaller particles (Fig. 6 and ESI Fig. 11–13†). It is also noticeable that there is no apparent carbon loss or drastically changes in the support structure in the il-(S)TEM images (ESI Fig. 12†) nor a change of the double layer capacity during the electrochemical stress (ESI Fig. 8 and 9†).

Conclusions

This study examines typical treatment procedures of thiolate stabilized AuNP on three widely used carbon supports (Vulcan XC72, Baytubes and Black Pearls 2000) towards the amount of removed stabilizer, the particle growth and change of the carbon support during the treatment as well as the electrochemically accessible Au surface and the stability against electrochemical stress. A combination of a treatment with 20% O₂/Ar at 300 °C followed by 15% H₂/Ar at 400 °C is such an often-used treatment in literature. This work, however, sheds light on the processes occurring during such treatment, which are often not considered in literature.

With this treatment at least 77% (Au/CNT) of the stabilizer were removed (77–89%). The single H₂-treatment is removing a higher amount stabilizer (89–95%) while the O₂-treatment leads to a broad variation (73–91% of removed stabilizer) depending on the support material. il-(S)TEM investigations show the influence of treatments and support specific particle growth. The particle growth was more intense for the combined treatment in comparison to the single treatments. The results lead us to the assumption that the support specific growth results mainly from the different SSA of the support material, therefore a higher SSA leads to lower particle growth. The electrochemical investigations show that the gold reduction charge is not direct proportional to the particle size and also there is a shift in the Au oxidation and reduction potential which let us assume that there is poor or no electrical contact between AuNP and support material for the untreated samples. Also there is an increase of the double layer capacity which likely stems from carbon surface functionalization and stabilizer removal of the Au surface. There are only slight changes of the support materials by the various treatments. With il-(S)TEM small changes were observed for the O₂- and the O₂ + H₂-treated sample. This is consistent with the Raman measurements,



which show slightly higher changes after these treatments compared with the H₂ treatment. Also there are negligible specific structural changes observed.

Furthermore, the stability against electrochemical stress was examined, and compared to the untreated samples. The electrochemical stability depends mainly on the electrolyte and the support material. The il-(S)TEM examination of electrochemically stressed Au/Vulcan displays a growth of the particles predominantly in the area of high particle density. Also the loss of NP is mainly restricted to smaller particles. Finally, there is no observable loss of support or change in the double layer capacity.

In conclusion, we were demonstrating that the single treatments used by us are better in terms of less intense particle growth. Furthermore, the single H₂-treatment removed most stabilizer with up to 95% in comparison to the combined treated samples and might be the best choice in removing thiolates from a gold surface. However, all treated samples showed higher electrochemical available surface area. For the particle growth, a dependence of the SSA of the support can be found as well as a particle surface mobility, which is higher for smaller particles. This leads to the specific loss of smaller particles mainly by agglomeration.

Author contributions

E. D. synthesized the catalysts and performed the treatments, conducted the electrochemical measurements, analyzed the TEM, STEM, TG-MS and electrochemical measurements and wrote the draft. S.-J. K. performed parts of the Raman measurements and evaluated them. M. S. contributed with in-depth scientific discussions. The work was supervised by M. B. The draft was proofread by all authors.

Conflicts of interest

There are no conflicts to declare.

Acknowledgements

We thank Annett Quetschke (Institut für Chemie, Technische Chemie I, Martin-Luther-Universität Halle Wittenberg) for performing TEM and TG-MS measurements, Eik Koslowski (Institut für Chemie, Technische Chemie I, Martin-Luther-Universität Halle Wittenberg) for performing Raman measurements and Frank Syrowatka (Interdisziplinäres Zentrum für Materialwissenschaften, Martin-Luther-Universität Halle-Wittenberg) for the STEM measurements. Martin-Luther-University Halle-Wittenberg helped in meeting the publication cost of this article.

References

- 1 D. Astruc, ed. *Nanoparticles and catalysis*, Wiley-VCH, Weinheim, 2008.
- 2 M.-C. Daniel and D. Astruc, *Chem. Rev.*, 2004, **104**, 293–346.

- 3 W. Kurashige, Y. Niihori, S. Sharma and Y. Negishi, *Coord. Chem. Rev.*, 2016, **320–321**, 238–250.
- 4 L. Prati and A. Villa, *Acc. Chem. Res.*, 2014, **47**, 855–863.
- 5 L. Prati and A. Villa, *Gold catalysis. Preparation, characterization, and applications*, Pan Stanford Publishing, Singapore, 2016.
- 6 R. Zhang, M. Hummelgård and H. Olin, *Mater. Sci. Eng.*, 2009, **158**, 48–52.
- 7 J. Luo, M. M. Maye, N. N. Kariuki, L. Wang, P. Njoki, Y. Lin, M. Schadt, H. R. Naslund and C.-J. Zhong, *Catal. Today*, 2005, **99**, 291–297.
- 8 G. Li, D. Jiang, C. Liu, C. Yu and R. Jin, *J. Catal.*, 2013, **306**, 177–183.
- 9 A. Primo, A. Corma and H. García, *Phys. Chem. Chem. Phys.*, 2011, **13**, 886–910.
- 10 Z. Niu and Y. Li, *Chem. Mater.*, 2014, **26**, 72–83.
- 11 A. Villa, Di Wang, G. M. Veith, F. Vindigni and L. Prati, *Catal. Sci. Technol.*, 2013, **3**, 3036.
- 12 M. Brust, M. Walker, D. Bethell, D. J. Schiffrin and R. Whyman, *J. Chem. Soc., Chem. Commun.*, 1994, 801–802.
- 13 M. M. Oliveira, D. Ugarte, D. Zanchet and A. J. G. Zarbin, *J. Colloid Interface Sci.*, 2005, **292**, 429–435.
- 14 T. P. Ang, T. S. A. Wee and W. S. Chin, *J. Phys. Chem. B*, 2004, **108**, 11001–11010.
- 15 T. Laiho, J. Leiro and J. Lukkari, *Appl. Surf. Sci.*, 2003, **212–213**, 525–529.
- 16 G. Corthey, A. A. Rubert, A. L. Picone, G. Casillas, L. J. Giovanetti, J. M. Ramallo-López, E. Zelaya, G. A. Benitez, F. G. Requejo, M. José-Yacamán, R. C. Salvarezza and M. H. Fonticelli, *J. Phys. Chem. C*, 2012, **116**, 9830–9837.
- 17 P. Carro, G. Corthey, A. A. Rubert, G. A. Benitez, M. H. Fonticelli and R. C. Salvarezza, *Langmuir*, 2010, **26**, 14655–14662.
- 18 P. Zhang and T. K. Sham, *Appl. Phys. Lett.*, 2002, **81**, 736–738.
- 19 J. Xian, Q. Hua, Z. Jiang, Y. Ma and W. Huang, *Langmuir*, 2012, **28**, 6736–6741.
- 20 L. Prati, A. Villa, C. E. Chan-Thaw, R. Arrigo, D. Wang and D. S. Su, *Faraday Discuss.*, 2011, **152**, 353–365, discussion 393–413.
- 21 L. Prati, A. Villa, A. R. Lupini and G. M. Veith, *Phys. Chem. Chem. Phys.*, 2012, **14**, 2969–2978.
- 22 S. M. Ansar, F. S. Ameer, W. Hu, S. Zou, C. U. Pittman and D. Zhang, *Nano Lett.*, 2013, **13**, 1226–1229.
- 23 V. Mazumder and S. Sun, *J. Am. Chem. Soc.*, 2009, **131**, 4588–4589.
- 24 N. Naresh, F. G. S. Wasim, B. P. Ladewig and M. Neergat, *J. Mater. Chem. A*, 2013, **1**, 8553.
- 25 J. Wu, J. Zhang, Z. Peng, S. Yang, F. T. Wagner and H. Yang, *J. Am. Chem. Soc.*, 2010, **132**, 4984–4985.
- 26 C. Rogers, W. S. Perkins, G. Veber, T. E. Williams, R. R. Cloke and F. R. Fischer, *J. Am. Chem. Soc.*, 2017, **139**, 4052–4061.
- 27 K. Sun, T. Cheng, L. Wu, Y. Hu, J. Zhou, A. MacLennan, Z. Jiang, Y. Gao, W. A. Goddard and Z. Wang, *J. Am. Chem. Soc.*, 2017, **139**, 15608–15611.
- 28 Z. Zhuang and W. Chen, *J. Colloid Interface Sci.*, 2019, **538**, 699–708.



Paper

- 29 J. Luo, M. M. Maye, N. N. Kariuki, L. Wang, P. Njoki, Y. Lin, M. Schadt, H. R. Naslund and C.-J. Zhong, *Catal. Today*, 2005, **99**, 291–297.
- 30 K. J. Mayrhofer, J. C. Meier, S. J. Ashton, G. K. Wiberg, F. Kraus, M. Hanzlik and M. Arenz, *Electrochem. Commun.*, 2008, **10**, 1144–1147.
- 31 F. J. Perez-Alonso, C. F. Elkjær, S. S. Shim, B. L. Abrams, I. E. Stephens and I. Chorkendorff, *J. Power Sources*, 2011, **196**, 6085–6091.
- 32 Y. Shao-Horn, W. C. Sheng, S. Chen, P. J. Ferreira, E. F. Holby and D. Morgan, *Top. Catal.*, 2007, **46**, 285–305.
- 33 J. T. Steven, V. B. Golovko, B. Johannessen and A. T. Marshall, *Electrochim. Acta*, 2016, **187**, 593–604.
- 34 M. Smiljanić, U. Petek, M. Bele, F. Ruiz-Zepeda, M. Šala, P. Jovanović, M. Gaberšček and N. Hodnik, *J. Phys. Chem. C*, 2021, **125**, 635–647.
- 35 M. Iqbal, J. McLachlan, W. Jia, N. Braid, G. Botton and S. H. Eichhorn, *J. Therm. Anal. Calorim.*, 2009, **96**, 15–20.
- 36 E. Dieterich, S.-J. Kinkelin and M. Bron, *ChemNanoMat*, 2022, **8**, e202200098.
- 37 S. Campisi, C. E. Chan-Thaw, Di Wang, A. Villa and L. Prati, *Catal. Today*, 2016, **278**, 91–96.

Open Access Article. Published on 03 November 2022. Downloaded on 3/16/2023 1:30:28 PM.
This article is licensed under a Creative Commons Attribution-NonCommercial 3.0 Unported Licence.



B :QUANTIFYING THE REMOVAL OF STABILIZING THIOLATES FROM GOLD NANOPARTICLES ON DIFFERENT CARBON SUPPORTS AND THE EFFECT ON THEIR ELECTROCHEMICAL PROPERTIES

Electronic Supplementary Material (ESI) for Nanoscale Advances.
This journal is © The Royal Society of Chemistry 2022

Quantifying the removal of stabilizing thiolates from gold nanoparticles on different carbon supports and the effect on their electrochemical properties

Emil Dieterich, Simon-Johannes Kinkelin, Matthias Steimecke and Michael Bron*

Institut für Chemie, Technische Chemie I

Martin-Luther-Universität Halle-Wittenberg

Von-Danckelmann-Platz 4, 06120 Halle, Germany

E-mail: *michael.bron@chemie.uni-halle.de

Supporting information

1. Additional experimental details

1.1. Glassware cleaning with aqua regia

All glassware was cleaned with aqua regia before use. Flasks were filled with aqua regia, while vessels etc. were submerged in aqua regia and stirred for at least 12 h under reflux. Afterwards the temperature was increased in steps of 5 °C every 20 min up to 50 °C which was held for 1 h. Finally the flasks were filled with DI water, vessels etc. were submerged in DI water and the temperature was increased until boiling and kept there for at least 30 min with reflux cooling.

1.2. Treatment of supporting materials as reference materials for TG-MS

The Vulcan carbon and the pre-treated CNT and BP2000 were treated with 15 % H₂/Ar at 400 °C for 1 h or 20 % O₂/Ar at 300 °C for 1 h or with both treatments combined, in the same way as the Au/C catalysts. Afterwards they were investigated by TG-MS in order to determine the amount of liberated SO₂, which was then used for correcting the results of Au/C.

1.3. TG-MS SO₂ area correction and normalization using CO₂ injections

In order to compare amounts of liberated SO₂ during TG-MS between different measurements, the SO₂ peak areas, as measured with the MS, were normalized to the peak area resulting from CO₂ injections with a fixed amount of CO₂. The mean value of the peak areas of both CO₂ injections was calculated ($\frac{A_{CO_2-1} + A_{CO_2-2}}{2} = A_{CO_2-avg}$) and the SO₂ peak area was divided by the sample specific A_{CO_2-avg} . From the unitless quotient

B :QUANTIFYING THE REMOVAL OF STABILIZING THIOLATES FROM GOLD NANOPARTICLES ON DIFFERENT CARBON SUPPORTS AND THE EFFECT ON THEIR ELECTROCHEMICAL PROPERTIES

$\left(\frac{A_{SO_2\text{-sample in } V*s}}{A_{CO_2\text{-avg.-sample in } V*s}}\right)$ of each sample the quotient of the respective support $\left(\frac{A_{SO_2\text{-support in } V*s}}{A_{CO_2\text{-avg.-support in } V*s}}\right)$ was subtracted. This final quotient for the untreated sample corresponds to 0 % of removed stabilizer. By subtracting the quotient of the other samples from the quotient of the untreated sample the relative amount of removed stabilizer is calculated.

1.4. Sample holder for the Au finder grids for electrochemical measurements

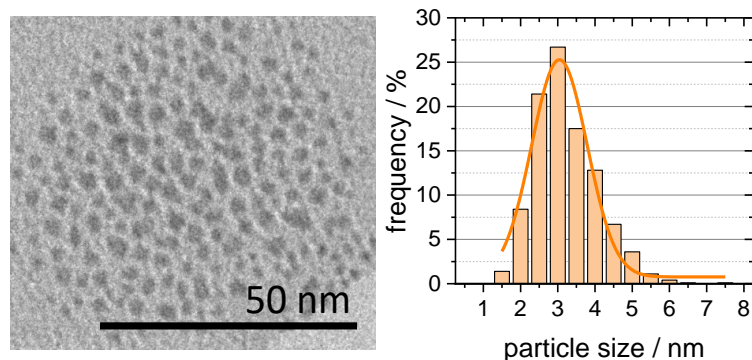
In order to perform electrochemical experiments, the Au finder grids where contacted as shown in SI Figure 1. The Au-finder grid is placed in the middle of the freshly polished glassy carbon electrode embedded in PTFE. Then a custom-made PTFE cap is placed on top of the GCE and pressed down to bring the carbon film of the Au-finder grid in strong contact with the GCE. In this way, the Au-finder grid is contacted over its whole area. The PTFE-embedded electrode may then be screwed to a standard electrode holder and is ready for electrochemical experiments-



SI Figure 1. Representation of the sample holder for the Au-finder grids with a costume made PTFE cap.

B :QUANTIFYING THE REMOVAL OF STABILIZING THIOLATES FROM GOLD NANOPARTICLES ON DIFFERENT CARBON SUPPORTS AND THE EFFECT ON THEIR ELECTROCHEMICAL PROPERTIES

1.5. Additional Figures



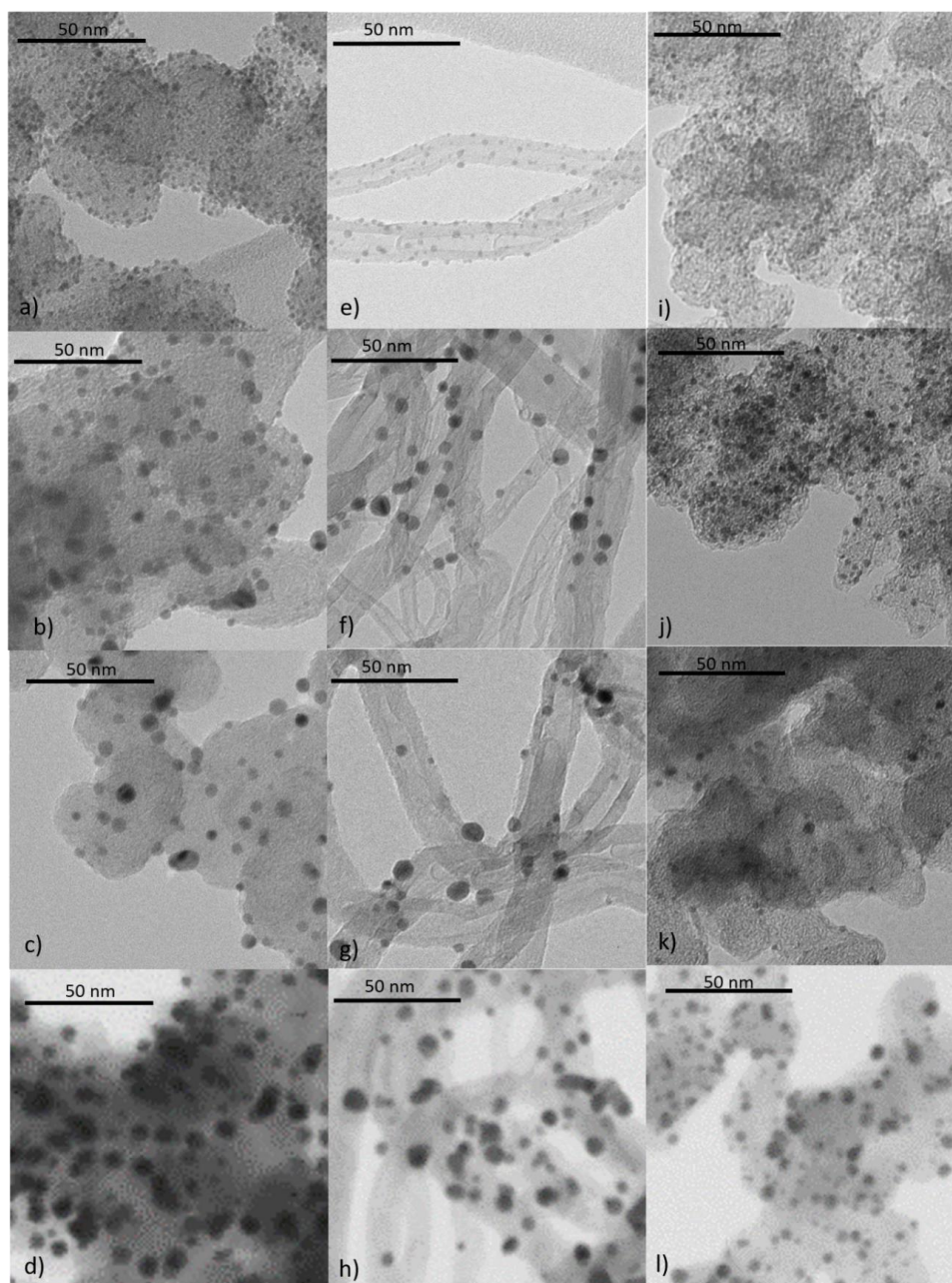
SI Figure 2. TEM image of the colloidal AuNPs and their size distribution (at least 1800 particles evaluated) with a Gaussian curve fitted.

SI Figure 2. shows a TEM image of the as prepared AuNPs (left) and the particle size distribution (right) of the AuNPs. Both represent the initial state of the AuNPs before any further steps (including deposition onto a support) were carried out.

SI Table 1. Size, size range, standard deviation and particles counted for TEM measurements of the treated powder samples, as well as the solid residue of the different carbon materials after the different treatments, for correction of the TG-MS measurements of the metal loading.

Sample	Treatment	Particle size (stdv.) / nm	Size range / nm	Particles measured	Au loading / wt.%	Solid residue of treated support / wt.%
Au-Vulcan	O ₂	3.7 (± 1.2)	1.4–11.0	2375	18.1	1.7
	H ₂	4.0 (± 1.9)	1.9-9.0	3062	17.1	1.4
	O ₂ +H ₂	5.3 (± 1.9)	0.6-12.3	1464	25.0	0.8
	untreated	1.7 (± 0.4)	0.6-3.8	2381	16.8	0.5
Au-CNT	O ₂	3.4 (± 1.7)	1.0-10.6	502	15.5	1.4
	H ₂	4.8 (± 1.4)	1.7-9.4	489	15.0	1.9
	O ₂ +H ₂	5.1 (± 2.3)	1.3-21.2	530	21.1	1.9
	untreated	2.0 (± 0.5)	0.6-3.9	514	14.6	0.8
Au-BP2000	O ₂	2.9 (± 0.8)	1.1-6.3	516	16.7	1.2
	H ₂	2.4 (± 0.7)	0.7-5.6	501	19.9	0.5
	O ₂ +H ₂	3.6 (± 1.2)	1.2-8.5	611	24.9	0.5
	untreated	1.8 (± 0.5)	0.6-3.6	396	17.1	1.8

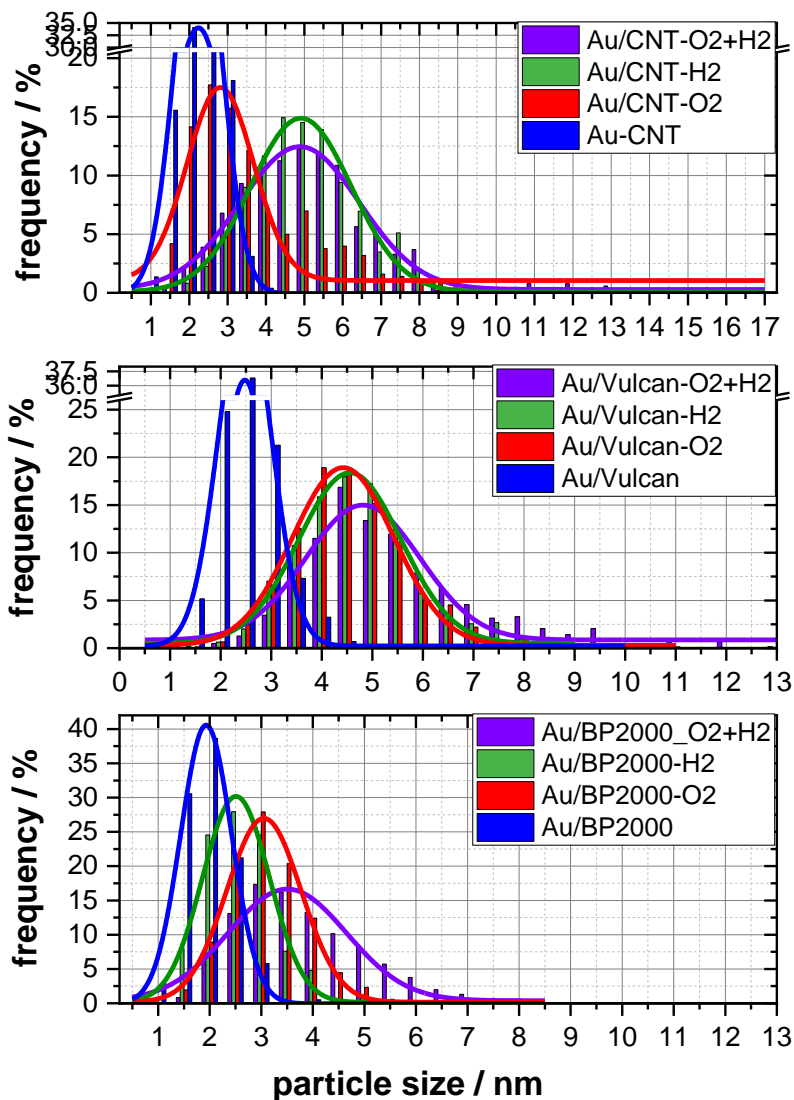
B :QUANTIFYING THE REMOVAL OF STABILIZING THIOLATES FROM GOLD NANOPARTICLES ON DIFFERENT CARBON SUPPORTS AND THE EFFECT ON THEIR ELECTROCHEMICAL PROPERTIES



SI Figure 3. (S)TEM images of AuNP on Vulcan (a-d)), on Baytubes (e-h) and on BP2000 (i-l). Top Row (a, e, i) untreated; b), f), j) 300 °C 20% O₂/Ar treated, c), g), k) 400 °C 15% H₂/Ar; d), h), l) combined treatment).

SI Figure 3 presents (S)TEM images of the untreated and treated powder samples and the respective values are summarized in SI Table 1. The treatment-dependent particle growth, as described in the article is clearly visible.

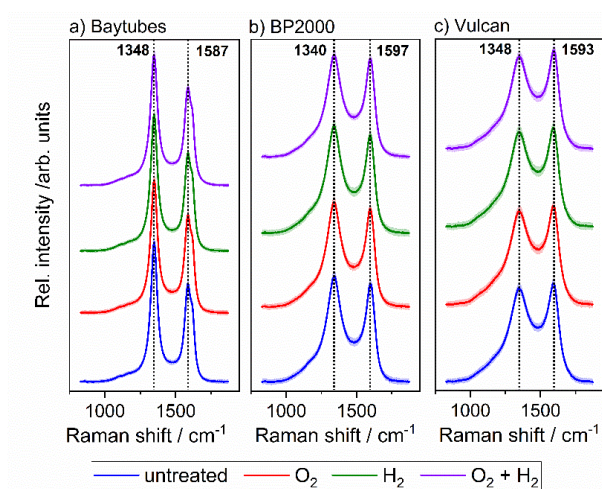
B :QUANTIFYING THE REMOVAL OF STABILIZING THIOLATES FROM GOLD NANOPARTICLES ON DIFFERENT CARBON SUPPORTS AND THE EFFECT ON THEIR ELECTROCHEMICAL PROPERTIES



SI Figure 4. Particle size distribution according to different treatments and supporting materials a) Vulcan, b) CNT and c) BP2000 with the corresponding Gaussian curves fitted.

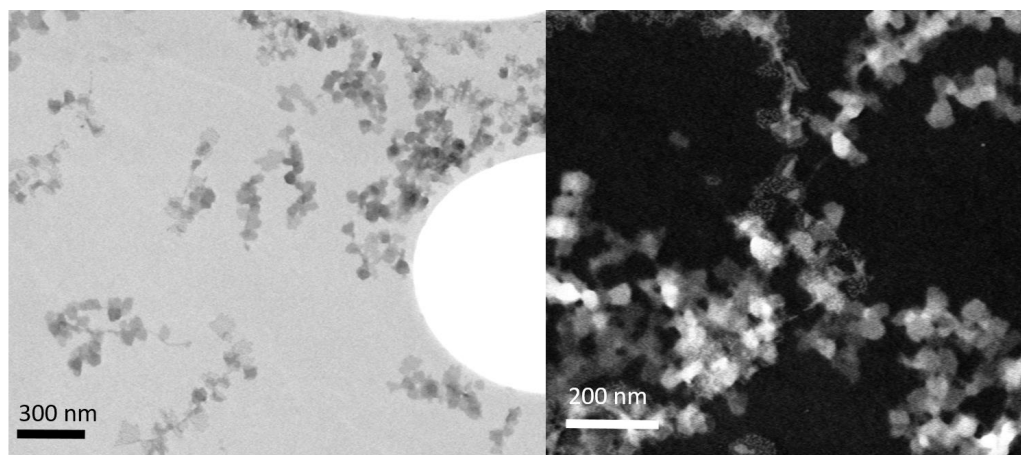
SI Figure 4 presents the particle sizes and size distributions of the different treated Au/C materials, corresponding to the data shown in Figure 3a) in the main article and showing that the AuNP exhibit a Gaussian-type particle size distribution around the average particle size.

B :QUANTIFYING THE REMOVAL OF STABILIZING THIOLATES FROM GOLD NANOPARTICLES ON DIFFERENT CARBON SUPPORTS AND THE EFFECT ON THEIR ELECTROCHEMICAL PROPERTIES



SI Figure 5. Averaged spectra of the Raman mapping measurements of the different treated samples, dotted lines D-Band ($\sim 1345 \text{ cm}^{-1}$) and G-Band ($\sim 1585 \text{ cm}^{-1}$).

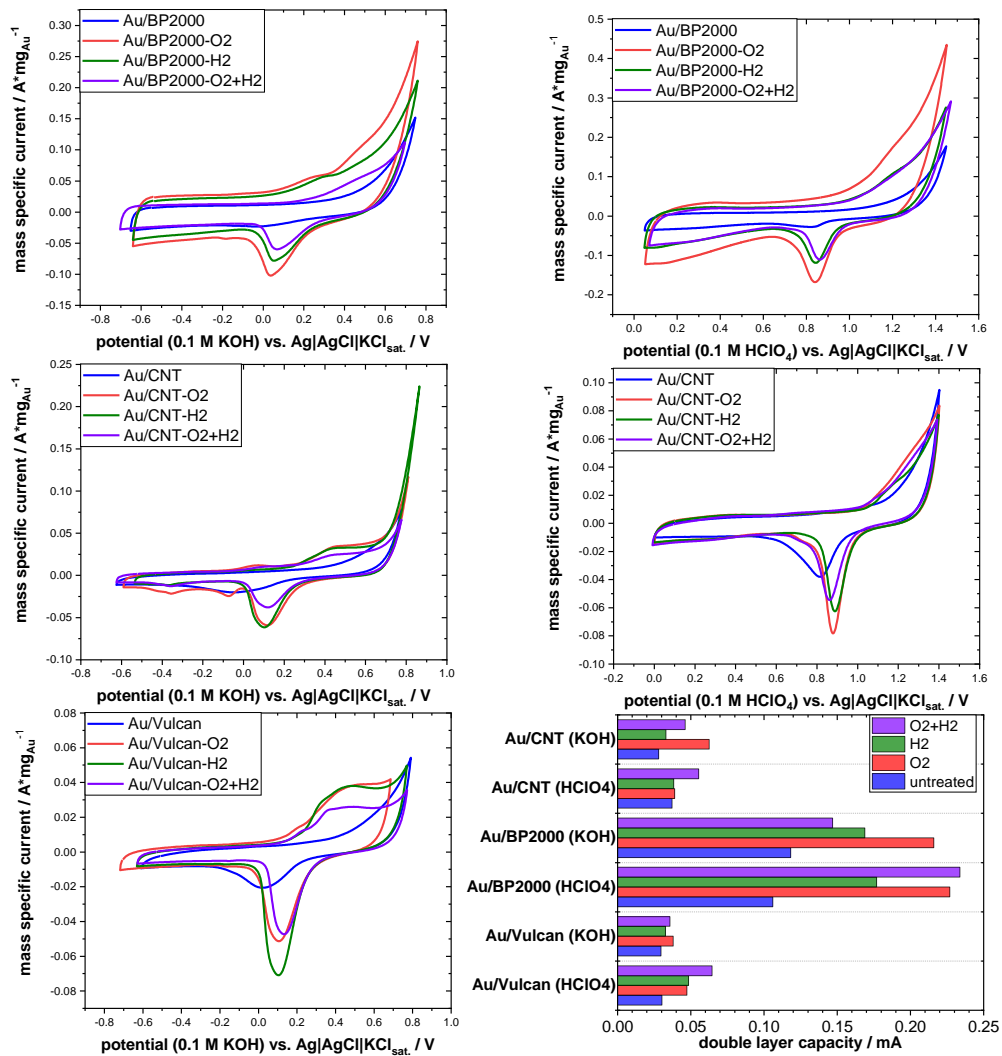
SI Figure 5 presents the results of Raman mapping measurements. These measurements underline the differences in the Raman spectra of the investigated samples, which result from their different structural features, as well as the impact of the treatments onto the carbon materials. The G-Band ($\sim 1585 \text{ cm}^{-1}$) represents the share of graphitic carbon and the D-Band ($\sim 1345 \text{ cm}^{-1}$) indicates the shares of disordered carbon.^{1,2}



SI Figure 6. STEM images of pure 1-dodecanthiol. Left: full STEM detector, right: dark field contrast with only the outer rings of the STEM detector to visualize a higher contrast.

SI Figure 6 presents STEM images of the stabilizing agent 1-dodecanthiol to check if excess stabilizing agent is present in the samples. The dark field contrast image presents a higher contrast for regions of higher electron density. The quite homogeneous contrast shows that there are no materials with high electron density (e.g. metals) involved in the presented samples.

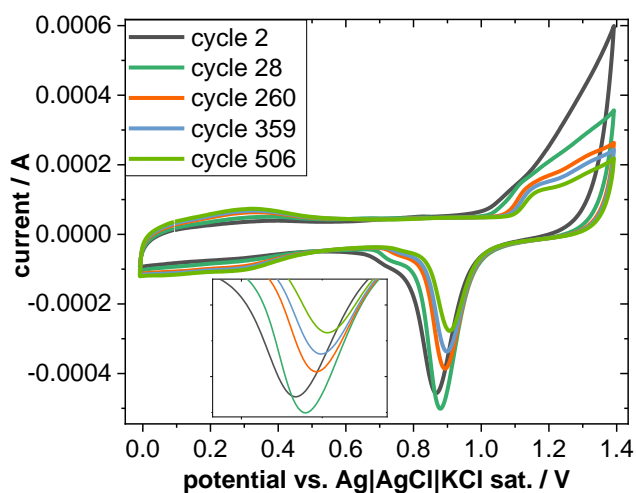
B : QUANTIFYING THE REMOVAL OF STABILIZING THIOLATES FROM GOLD NANOPARTICLES ON DIFFERENT CARBON SUPPORTS AND THE EFFECT ON THEIR ELECTROCHEMICAL PROPERTIES



SI Figure 7. 3rd CV of the different samples in 0.1 M HClO₄ and 0.1 M KOH, respectively, as well as the double layer capacity of all samples in the different electrolytes obtained from the 3rd CV.

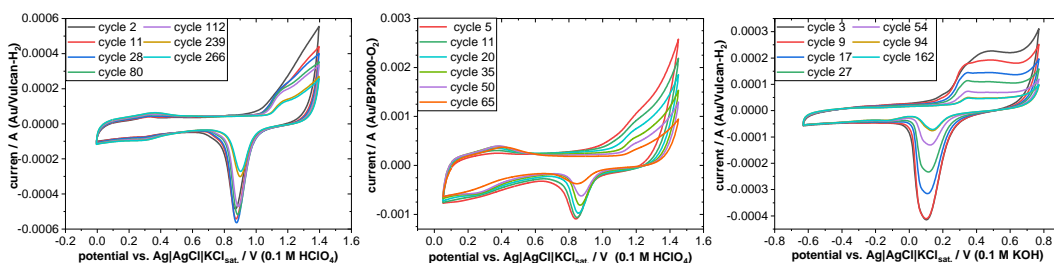
SI Figure 7 presents CVs of all samples, treated and untreated, in 0.1 M KOH and of the BP2000 and the CNT sample in 0.1 M HClO₄ and the double layer capacity of all samples in 0.1 M KOH and 0.1 M HClO₄. The figure clearly demonstrates the different behavior caused by the different support materials and the rather similar behavior of each individual material after the different treatments.

B :QUANTIFYING THE REMOVAL OF STABILIZING THIOLATES FROM GOLD NANOPARTICLES ON DIFFERENT CARBON SUPPORTS AND THE EFFECT ON THEIR ELECTROCHEMICAL PROPERTIES



SI Figure 8. Representative CVs showing a degradation experiment of Au/CNT-O₂+H₂ in 0.1 M HClO₄ with an enlarged view of the Au-reduction peak in the inset.

SI Figure 8 presents selected cycles of a CV measurement of Au/CNTs which were treated with the combined treatment. Initially a current increase can be observed for the Au reduction peak (cycle 2 to 28) followed by a current decrease. Prolonged cycling for 1000 cycles led to the disappearance of the gold redox features (not shown).

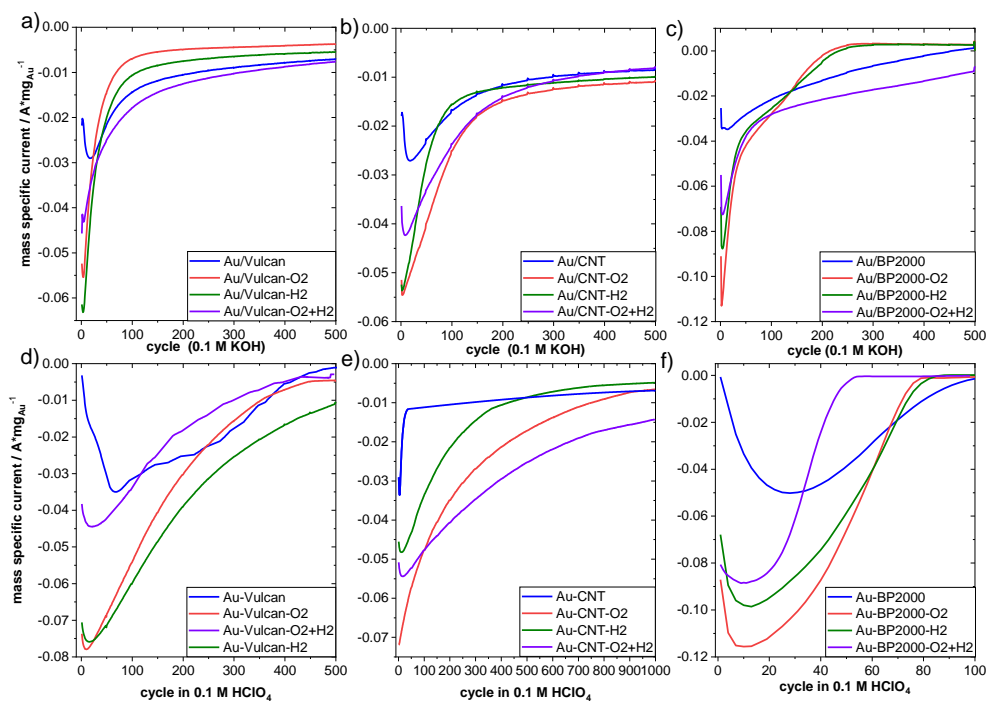


SI Figure 9. Representative CVs of degradation experiments for Au/Vulcan-H₂ in 0.1 M HClO₄ (left), Au/BP2000-O₂ in 0.1 M HClO₄ (middle) and Au/Vucan-H₂ in 0.1 M KOH (right)

SI Figure 9 presents further representative degradation CVs. The comparison between the measurements of Au/Vulcan-H₂ in 0.1 M HClO₄ and 0.1 M KOH (left and right graph in SI Figure 8) underlines that in KOH no additional peaks appear, whereas in 0.1 M HClO₄ a redox peak pair develops between 0.2 and 0.4 V, which is typically attributed to quinone-type redox features of the carbon support. Similar peaks are visible in other measurements in 0.1 M HClO₄ (cf. SI Figure 7 and SI Figure 8, middle). Such quinone-type surface groups at the support (pseudo-capacitive in nature) can be found after chemical oxidation of a bare CNT support as well³.

B : QUANTIFYING THE REMOVAL OF STABILIZING THIOLATES FROM GOLD NANOPARTICLES ON DIFFERENT CARBON SUPPORTS AND THE EFFECT ON THEIR ELECTROCHEMICAL PROPERTIES

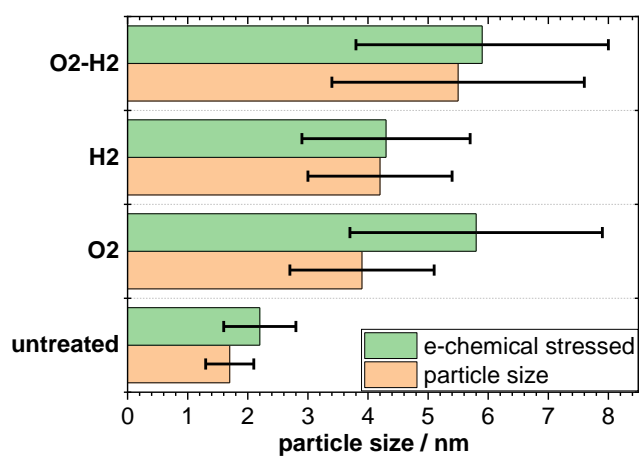
However, since there is no increase in the double layer capacity, one may assume that existing edges and corners are oxidized during the CVs. Considering the lower thermal stability of the carbon support in the presence of AuNPs (see TG-MS results in the main article) an electrocatalytic activity of AuNPs for the carbon oxidation may be proposed.



SI Figure 10. Average (three repeated measurements) Au-mass specific current of the Au-reduction peak over the number of degradation CV cycles.

Si Figure 10 shows the development of the Au-reduction peak minimum with ongoing degradation CVs. A different degradation behavior can be observed for the various samples.

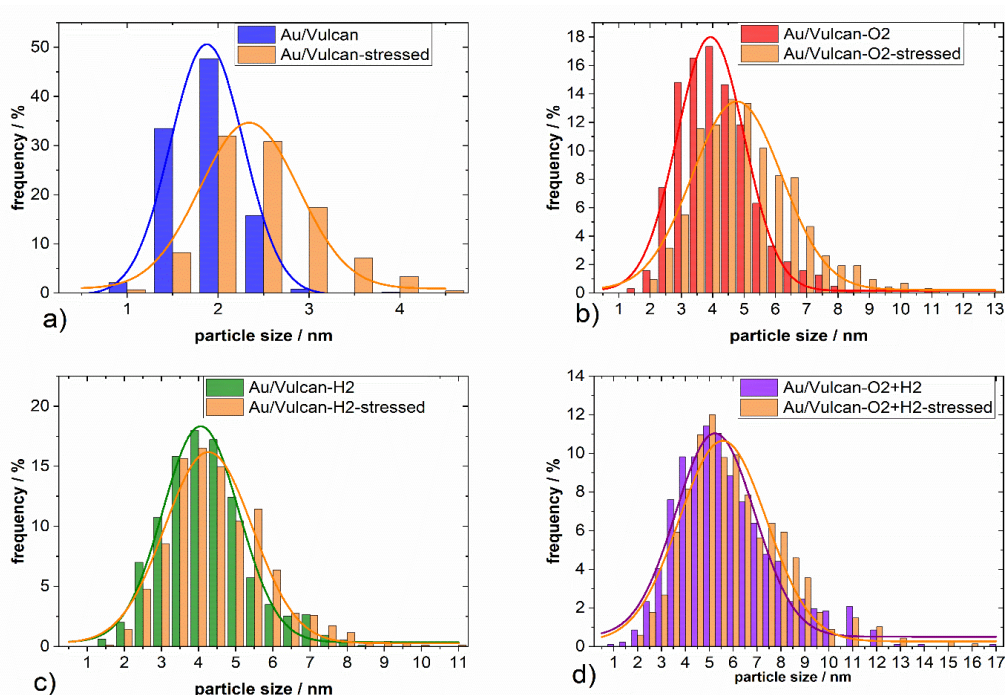
B :QUANTIFYING THE REMOVAL OF STABILIZING THIOLATES FROM GOLD NANOPARTICLES ON DIFFERENT CARBON SUPPORTS AND THE EFFECT ON THEIR ELECTROCHEMICAL PROPERTIES



SI Figure 11. Development of particle sizes and size distributions of the electrochemically stressed samples as obtained from il-(S)TEM investigations

SI Figure 11 displays the particle growth during the electrochemical stress procedure of Auf/C catalysts on the Au-finder grids as well as the standard deviation of the particle sizes, which is increased after electrochemical stress.

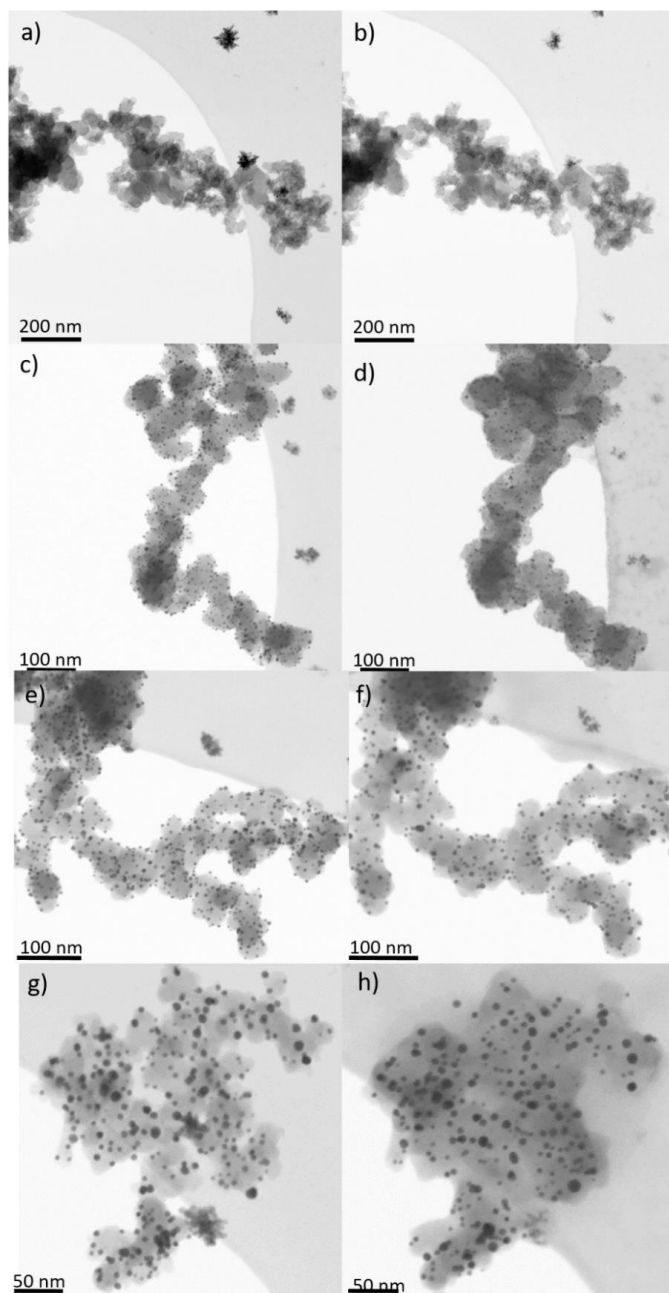
B : QUANTIFYING THE REMOVAL OF STABILIZING THIOLATES FROM GOLD NANOPARTICLES ON DIFFERENT CARBON SUPPORTS AND THE EFFECT ON THEIR ELECTROCHEMICAL PROPERTIES



SI Figure 12. Particle size distribution of untreated a), O₂- b), H₂- c) and O₂+H₂-treated Au/Vulcan before and after electrochemical stress in 0.1 M KOH.

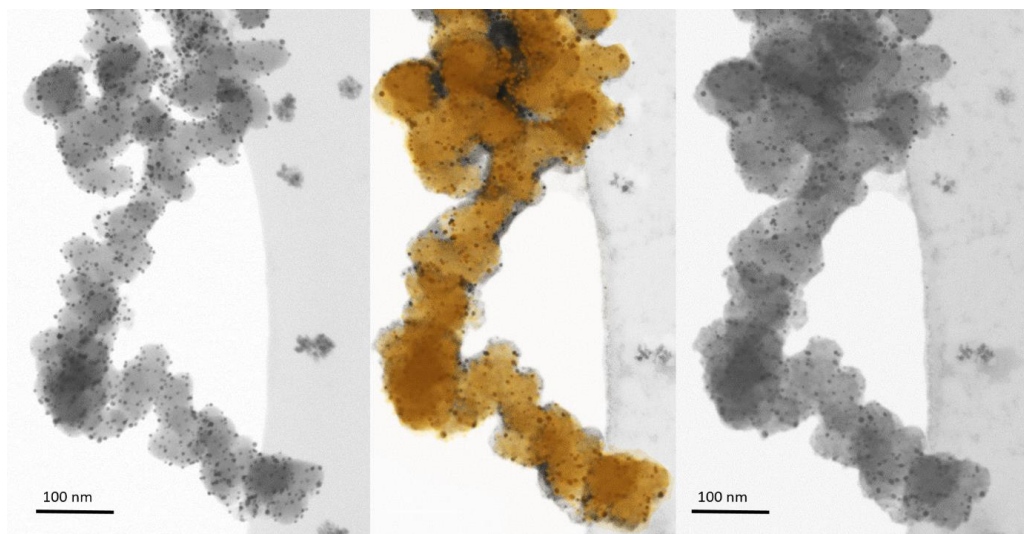
SI Figure 12 shows the particle size distribution of the untreated and treated Au/Vulcan samples before and after electrochemical stress on the Au-finder grids in 0.1 M KOH. While SI Figure 10 intends to provide an easier comparison between the samples, SI Figure 11 gives a more detailed view on the changes of particle sizes and underlines the loss of smaller particles and the wider particle size distribution.

B :QUANTIFYING THE REMOVAL OF STABILIZING THIOLATES FROM GOLD NANOPARTICLES ON DIFFERENT CARBON SUPPORTS AND THE EFFECT ON THEIR ELECTROCHEMICAL PROPERTIES



SI Figure 13. il- (S)TEM images of Au/Vulcan before being subjected to electrochemical stress, un- a), O₂- c), H₂- e) and O₂+H₂- treated g) and after subjection to electrochemical stress un- b), O₂- d), H₂- f) and O₂+H₂-treated h).

SI Figure 13 presents il-(S)TEM images of lower magnification to assess possible changes in the carbon support structure. However very obviously only very minor changes occur to the support during electrochemical stress.



SI Figure 14. STEM images of Au/Vulcan before (left) and after (right) electrochemical stress. The figure in the middle provides an overlay of both images where the sample after electrochemical stress treatment is displayed in orange.

However, interestingly there is kind of a swelling of the carbon support observable (SI Figure 13 and 14). This could be due to KOH from the electrolyte which is remaining after the electrochemical treatment, but also could be a bloat of the carbon structure due to intercalation or defects resulting from the electrochemical carbon oxidation. However, since there is no obvious loss or drastically change nor change of the double layer capacity this should rule out strong support changes or material loss as degradation mechanism.

References

- 1 M. M. Lucchese, F. Stavale, E. M. Ferreira, C. Vilani, M.V.O. Moutinho, R. B. Capaz, C. A. Achete and A. Jorio, *Carbon*, 2010, **48**, 1592–1597.
- 2 A. Sadezky, H. Muckenhuber, H. Grothe, R. Niessner and U. Pöschl, *Carbon*, 2005, **43**, 1731–1742.
- 3 M. Steimecke, S. Rümmler and M. Bron, *Electrochim. Acta*, 2015, **163**, 1–8.

Multimethod Approach to the Low-Overpotential Region of Micro- to Macro-Scale Working Electrodes of Sub-10 nm Gold Nanoparticles in the CO₂ Reduction Reaction

Emil Dieterich, Lukas Herrmann, Olga Dzhyginas, Lukas Binnenböse, Matthias Steimecke, Simon-Johannes Kinkelin, and Michael Bron*

Cite This: <https://doi.org/10.1021/acs.analchem.3c02338>

Read Online

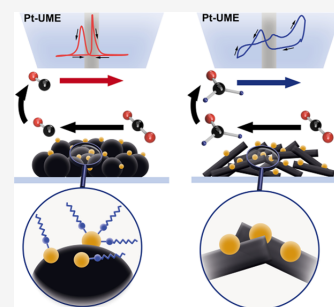
ACCESS |

Metrics & More

Article Recommendations

Supporting Information

ABSTRACT: The electrochemical carbon dioxide reduction reaction (CO₂RR) over carbon-supported gold nanoparticles (AuNP) was investigated using a broad variety of (electro)analytical methods, including linear sweep voltammetry with a rotating disk electrode (LSV-RDE), sample-generation tip-collection mode of scanning electrochemical microscopy (SG/TC-SECM), as well as full cell tests with highly sensitive online gas chromatography (GC). In contrast to most other studies, this work focuses on the low-overpotential region (0 to -0.4 V vs RHE) where initial product formation is already detected and addresses micro- to macro-sized electrodes. The sub-10 nm AuNPs supported on three different carbon supports (CNTs and carbon blacks) were pretreated in H₂/Ar to remove the stabilizer used during AuNP synthesis. LSV-RDE points toward different CO₂RR mechanisms at the samples, additionally confirmed by the SG/TC-SECM and full cell tests with online GC. Besides H₂ and CO, the AuNP supported on carbon nanotubes showed significant evolution of H₂CO in contrast to the other two samples, which was additionally confirmed by accumulating the product during chronoamperometric RDE experiments followed by mass spectroscopic analysis. Surface analysis indicated a complete removal of residual thiolate stabilizer molecules exclusively at the AuNPs supported on carbon nanotubes, which may result in a change in the adsorption geometry or reaction mechanism at this sample. The results demonstrate the effectiveness of the combination of these multiple methods to investigate the CO₂RR in the low-overpotential region.



Downloaded via MARTIN LUTHER UNIV HALLE WITT on November 1, 2023 at 19:16:01 (UTC).
See <https://pubs.acs.org/sharingguidelines> for options on how to legitimately share published articles.

To counteract global warming, it is of paramount importance to avoid further increase of the CO₂ level in the atmosphere, which may be achieved by reducing CO₂ emissions and/or using CO₂ as a source for the production of valuable compounds.^{1,2} Many different approaches for the recycling of CO₂ have been reported, and among them, the electrochemical CO₂ reduction reaction (CO₂RR) is a largely emission-free and highly potent method, as long as the energy is supplied by renewable sources.³

Currently, the economic feasibility of the electrochemical CO₂RR is challenged by its high overpotentials, low energy efficiency, and/or poor selectivity.⁴ Typically, transition-metal catalysts used for CO₂RR are separated into three groups, based on their main reduction product, which is CO (Au, Ag, Zn), HCOO⁻ (Pb, Cd, Sn...), or CH₄, C₂₊ (mainly Cu). In aqueous solutions, additionally, the competing hydrogen evolution reaction (HER) has to be considered, which is prioritized on, e.g., Pt, Ti, and Fe, but also occurs at the CO, HCOO⁻, and CH₄ or C₂₊ selective catalysts.⁵ Although there is particular interest in the direct production of methane or higher hydrocarbons by the CO₂RR, the poor selectivity and high overpotentials are major challenges. Here, copper catalysts are the main focus, for which numerous studies are

available.⁶⁻⁸ Alternatively, there is a significant interest in the highly selective production of HCOO⁻, H₂CO, or well-defined mixtures of CO/H₂ for synthesis gas processes.^{2,9}

One of the materials with the highest selectivity and lowest overpotential for CO formation during CO₂RR is gold, where the CO formation starts at potentials between -0.2 and -0.4 V vs RHE depending on the morphology of the Au catalyst.^{10,11} Besides CO, Au catalysts form other products like HCOO⁻ and CH₃OH but with very low faradaic efficiency (< 2%) and/or high overpotentials (HCOO⁻ -0.4 V and CH₃OH -0.96 V vs RHE).^{10,12,11} Gold nanoparticles (AuNPs) show size-dependent activity and selectivity in the composition of the CO/H₂ product gas. Zhu et al.¹³ investigated the size effect of AuNP from 4 to 10 nm where smaller AuNPs showed higher activity for the HER, while

Received: May 30, 2023

Revised: September 26, 2023

Accepted: October 13, 2023

larger ones were more selective to CO formation. The highest activity toward CO formation was found for 7.7 nm AuNPs. These findings were supported by density functional theory (DFT) calculations, which showed increased activity of corners for the HER, while edges and planes are more active for the adsorption of CO₂. Wang et al.¹⁴ investigated 4–6 nm AuNPs supported on heteroatom-doped CNTs, starting from –0.3 V vs RHE. Only N-doped CNTs exhibited inherent CO₂RR activity. The activity of AuNP on N-doped and S-doped CNTs increased, and the overpotential decreased. Still, the only products found were CO and H₂. While HCOO[–] and CH₃OH were found at structured gold catalysts, AuNP supported on different carbon materials (e.g., commercial carbon blacks,^{13,15,16} reduced graphene oxide,¹⁷ multiwalled carbon nanotubes,¹⁸ or graphene nanoribbons¹⁹) only produced CO and H₂.

Reliable and accurate analysis of the product composition is an essential aspect of CO₂RR research given such a diverse array of possible products. CO₂RR catalyst characterization is often performed by linear sweep voltammetry (LSV) as well as GC for gaseous and ¹H NMR or HPLC for liquid or dissolved product determination. While LSV is usually performed from 0 to –0.8 V to –1.2 V vs RHE, it is unselective toward the formed products. On the other hand, gas-phase analysis by GC typically starts at potentials below –0.4 V vs RHE. The same holds true for the other approaches to analyze gaseous and liquid products,^{10,13,15,16,19} which is likely due to the small product amounts formed in the low-overpotential region and the resulting increased analytical effort when using GC and ¹H NMR or HPLC. Additionally, this region might be considered of less practical importance, and as a consequence, product analysis of this low-overpotential region is often missing. However, CO₂ reduction to CO, H₂CO, HCOOH, CH₃OH, and CH₄ is, according to calculations, already possible in the potential range from +0.2 to –0.3 V vs SHE (SHE at 1 atm, 25 °C calculated to standard Gibbs energies of the reactants in the reaction),²⁰ and a thorough understanding of the CO₂RR requires analysis of this potential region, too. In a recent work, we showed that the sample-generation tip-collection mode of scanning electrochemical microscopy (SG/TC-SECM) overcomes this potential gap and allows for a fast *in situ* evaluation of the products formed during CO₂RR in the low-overpotential region.²¹ Particularly for the analysis of small product amounts, the high sensitivity of the SECM is a great benefit. Furthermore, the local pH can be assessed during the reaction, which has a significant impact on selectivities,^{22,23} making SECM especially beneficial for a fast *in situ* analysis in this potential region. Still, in the literature, SECM is usually applied at potentials below –0.4 V vs RHE.^{12,22–24} The low-overpotential region of 0 to –0.4 V vs RHE is a potential region little noticed.

The aim of this work is to unravel the CO₂RR over three different carbon-supported (carbon blacks and CNTs) gold nanoparticles (AuNPs), namely, Au-BP2000, Au-Vulcan, and Au-CNT, in the low-overpotential region using a broad variety of (electro)analytical methods including LSV-RDE, *in situ* SECM, and full cell tests with online GC as well as chronoamperometric RDE experiments combined with *ex situ* mass spectroscopy (MS), and to bridge the gap to more practical potential values.

EXPERIMENTAL SECTION

The electrochemical measurements were carried out using a potentiostat (Metrohm Autolab PGSTAT 128N) in a three-electrode setup employing a reference electrode (RE, Ag/AgCl KCl_{sat}, Meinsberger Elektroden), a counter electrode (CE, Au mesh 99.9%, Goodfellow), and a working electrode (WE, sample-coated glassy carbon disc electrode (GCE), HTW GmbH, A = 0.126 cm²). For WE preparation, the GCE was polished (1 μm, 0.3 μm Al₂O₃ powder, and DI H₂O on polishing fleece) and the sample was dispersed (3 mg mL^{–1}, EtOH/Nafion 117 solution) in an ultrasonic bath (Bandelin Sonocool, 75% intensity) for 5 min assisted by repeated manual shaking every minute. Then, 3.14 μL was drop-cast onto the GCE four times and left to dry in between the casts (catalyst loading 300 μg cm^{–2}). The electrodes were submerged into the electrolyte (0.5 M KHCO₃) in a four-necked glass cell, which was purged (20 min) and then further overflowed with the respective gas (Ar or CO₂).

The procedure for the initial electrochemical analysis consists of linear sweep voltammetry (LSV) employing the WE described above as a rotating disc electrode (RDE). Before and after LSV, cyclic voltammetry (CV) was carried out to monitor possible changes of the catalyst during the CO₂RR. The internal resistance was determined by electrochemical impedance spectroscopy (EIS). The WE was rotated to avoid any diffusion limitation. In detail, the procedure consists of 20 CVs with a scan rate (SR) of 500 mV s^{–1}, 0.1–1.35 V vs RHE, followed by two times two CVs from 0.1 to 1.6 V vs RHE with SRs of 200 and 20 mV s^{–1} and then the LSV (SR 5 mV s^{–1}, 0.8 to –0.4 V vs RHE) with the rotating electrode (900 rpm, Radiometer, motor BM-EDI101). Afterward, another two times two CVs (SR 2 × 20, 2 × 200 mV s^{–1}, 0.1–1.6 V vs RHE) and then the EIS (0.4 V, 50 kHz–0.1 Hz, amplitude 5 mV, peak to peak) were recorded with the stationary electrode. This procedure was carried out first in Ar-purged electrolyte (0.5 M KHCO₃, pH ~ 8.35) and directly afterward in a second cell, except for the 20 CVs with 500 mV s^{–1}, with the CO₂-purged electrolyte (pH ~ 7.35) with the identical catalyst film.

The same setup as that for the LSV-RDE experiments was also used during potentiostatic chronoamperometric RDE experiments but with a higher catalyst loading to increase conversion. The sample suspensions were prepared with 6 mg mL^{–1}, and a catalyst loading of 600 μg cm^{–2} was pipetted onto the GCE. 20 mL of 0.5 M KHCO₃ was saturated with CO₂. During the potentiostatic chronoamperometric RDE, a constant flow of CO₂ was allowed to pass over the electrolyte and a potential of –0.3 V vs RHE was held for 3:30 h for each sample. Afterward, 40 μL of the electrolyte was transferred into an Al₂O₃ crucible and analyzed in a TG-MS (thermo balance, Netzsch Jupiter STA 449 F1 coupled with a mass spectrometer, Netzsch QMS 403C Aeolos). For the analysis, a temperature of 35 °C was held for 15 min, which was then raised to 90 °C at 5 K min^{–1} and held for 20 min. Ar was used as the carrier gas to the MS. The exhaust stream was analyzed for *m/z* 28 (CO or N₂), 30 (CH₂O), 32 (CH₃OH), 45 (HCOO[–]), and 46 (HCOOH).

Scanning electrochemical microscopy (SECM) was performed with a commercial setup (Sensolytics, Bochum) equipped with a positioning system, a bipotentiostat (Autolab PGSTAT 128N), and a home-built cell. Samples (see below) were drop-cast onto an ITO electrode (indium-doped tin oxide on quartz glass, PGO GmbH, Iserlohn, 2 × 2 cm², 20 Ω cm^{–1},

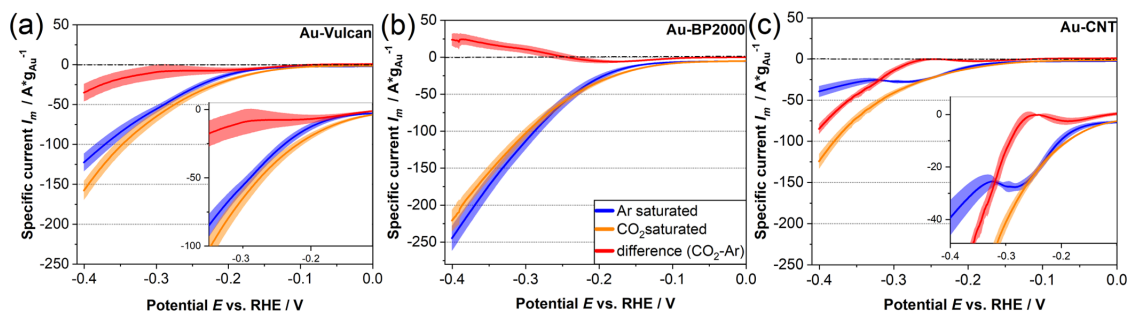


Figure 1. LSV-RDE measurements in CO₂ and Ar-saturated electrolyte solutions (0.5 M KHCO₃, RT) and the difference between these two measurements for (a) Au-Vulcan, (b) Au-BP2000, and (c) Au-CNT; the color code in (b) is valid for all diagrams.

precleaned in acetone for 30 min in an ultrasonic bath), which was used as the working electrode (substrate). A Pt microelectrode (UME, 10 μm (diameter) platinum wire in glass, RG \sim 30, Sensolytics, Bochum) served as the additional working electrode. The UME was polished before use with 1 and 0.3 μm alumina polishing paper. An Ag|AgCl|KCl_{sat.} as a reference electrode and a Pt wire (Goodfellow) as a counter electrode were mounted into the cell, which was filled with 0.5 M KHCO₃ and continuously saturated with CO₂. Prior to the measurements, the UME was lowered down onto a blank region of the ITO, then lifted up for 10 μm , and positioned above the sample spot. Three consecutive CVs were carried out at the UME (SR 20 mV s⁻¹, from -0.6 to 0.9 V vs Ag|AgCl|KCl_{sat.}) at each substrate potential, which was lowered from 0 to -0.9 or -1.1 V vs Ag|AgCl|KCl_{sat.} in 50 mV steps. Catalyst suspensions with 3 mg mL⁻¹ were prepared with EtOH/Nafion (49:1, V/V) in the case of Au-Vulcan and Au-CNT or with EtOH/water/Nafion mixtures (310:10:13.3, V/V) for Au-BP2000 and drop-cast onto a confined circular area of the ITO ($A = 0.196 \text{ cm}^2$) with a resulting loading of 153 $\mu\text{g cm}^{-2}$ (Au-CNT and Au-Vulcan) or 77 $\mu\text{g cm}^{-2}$ (Au-BP2000).

For reference measurements of possible CO₂RR products, the very same SECM setup and procedure at the UME was used. However, the UME did not approach the surface. The electrolyte containing various amounts of a single product molecule was purged with the respective gas (CO₂ or Ar) as during the SECM measurements, and again, three consecutive CVs were recorded in the electrolyte solution with and without the respective reference substances.

For the online gas chromatographic measurements (GC, Nexis 2030, Shimadzu, barrier ion discharge detector, Carboxen-1010-Plot, sample loop 500 μL), an in-house-built two-compartment cell (PVC cell, Viton seals) with gas inlet and outlet was used (see Figure S1). Each compartment provides a volume of $\sim 45 \text{ cm}^3$ (40 mL of electrolyte, 5 mL headspace). A graphite plate covered with the respective sample (6.25 cm², 400 $\mu\text{g cm}^{-2}$ loading) served as the working electrode prepared by drop casting from the respective sample suspension (4 mg mL⁻¹, EtOH/Nafion, 977:23, V/V). Furthermore, a Ag|AgCl|KCl_{sat.} electrode was placed in the compartment of the working electrode, whereas a Ni mesh (99.5%, RECEMAT BV) served as the counter electrode in the other compartment (see the SI for details on the electrochemical procedure). A Nafion 115 membrane (Dupont, 1 cm², soaked in 0.5 M H₂SO₄ overnight and rinsed with DI H₂O afterward) separated the two compartments. Initially, the

electrolyte was intensely purged with CO₂ for 40 min. During the experiments, the electrolyte was continuously purged from the bottom of the cell with 0.2 l h⁻¹ of CO₂ as a carrier gas and to ensure full saturation. The exhaust stream of the working electrode compartment was connected to the GC by PTFE tubing.

All measurements (LSV-RDE, SECM, and GC cell tests) were carried out at least three times to ensure reproducibility. All potentials were calculated to the reversible hydrogen electrode (RHE) (646 mV vs Ag|AgCl|KCl_{sat.} in CO₂-saturated and 705 mV in Ar-saturated 0.5 M KHCO₃).

Further information regarding used chemicals, standard instruments and measurements, synthesis of the catalysts,^{25,26} and catalyst characterization using standard procedures are given in the SI.

RESULTS AND DISCUSSION

Catalysts. AuNPs on carbon nanotubes (Baytubes (CNTs)) and carbon blacks (Vulcan XC72 (Vulcan) and Black Pearls 2000 (BP2000)) were used to study the low-overpotential region in the CO₂RR over gold. The synthesis of the catalysts including the removal of the thiol-based stabilizer used during nanoparticle synthesis has been described in our previous works.^{25,26} Thiol-stabilized NPs were chosen instead of, for example, citrate-stabilized ones due to the fact that our mentioned previous work showed that these NPs can be supported onto carbon materials with minor particle growth compared to a broad particle size distribution as well as particle growth observed with other NPs. The average particle size of Au supported on Vulcan and Au on CNT was between 4 and 4.9 nm (stdv. 1.4–1.9 nm), while the AuNPs on BP2000 were smaller (2.4–2.7 nm, stdv. 0.7–1 nm). The Au loadings were determined to be 15–24 wt % (Table S1). These three supports were chosen because of their structural similarities and differences, allowing us to unravel possible support influences in the low- and high-overpotential regions. Vulcan and CNTs have comparable specific surface areas (SSA_{BET}) of 254 and 232 m² g⁻¹ but significant differences in their carbon structure, while BP2000 has a structure comparable to that of Vulcan but a much larger SSA_{BET} (1385 m² g⁻¹). Similarities of the structure of the carbon supports are evident in the Raman analysis.²⁶ The catalysts are analyzed by XPS for their surface structure and by TG-MS for the amount of stabilizing agent removed.²⁶ The TG-MS analysis showed that for Au-Vulcan 2.9%, for Au-BP2000 5.4%, and for Au-CNT 8.2% of the stabilizing agent remained in the bulk of the sample (Figure S4).

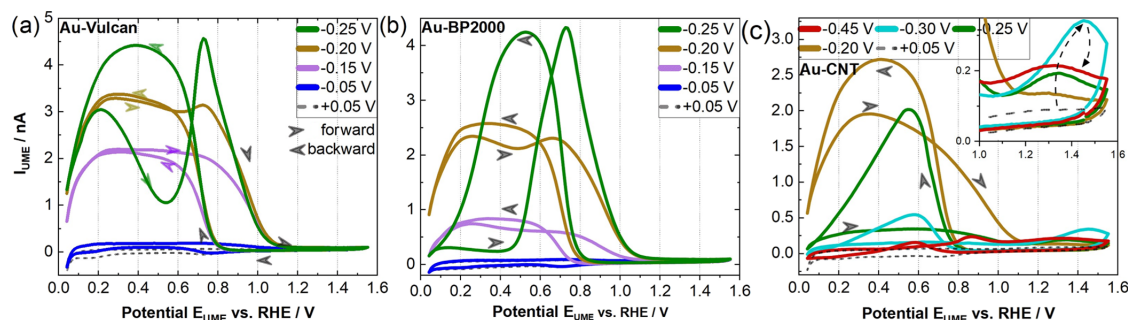


Figure 2. CVs of the UME at different substrate potentials of (a) Au-Vulcan, (b) Au-BP2000, and (c) Au-CNT; arrows indicate the scan direction of CVs, Au-CNT inset arrows indicate the potential-dependent behavior of the oxidation peak at ~ 1.35 V_{UME} vs RHE. The color code in all diagrams corresponds to the substrate potential of the sample ($E_{\text{substrate}}$), as assigned, while the diagrams show the CV response of the UME in close proximity to the substrate. All measurements were made in CO₂-saturated 0.5 M KHCO₃ at RT.

However, to further understand the differences observed during SECM analysis (see below), it turned out to be necessary to evaluate the influence of the surface chemistry of the Au/carbon catalysts on their electrochemical behavior. Thus, a more detailed XPS surface analysis was carried out, which has been discussed in detail in the SI. In short, Au-CNT has the smallest diversity in surface structure, with no remaining thiols, and the highest amount of Au–C bonds, followed by Au-Vulcan, which is close to Au-CNT in terms of the Au surface structure and fwhm but has the highest amount of remaining sulfur. In the case of Au-BP2000, the highest share of surface-bound, adsorbed thiols, disorder of the surface facets, and the highest fwhm were found. These surface structure findings correlate with the different particle sizes.

LSV-RDE. Figure 1 shows LSV-RDE measurements in Ar-purged (LSV_{Ar}) and in CO₂-saturated (LSV_{CO₂}) solutions as well as the difference between both. As a simplification, it is assumed that in Ar-saturated electrolyte, the HER is the only reaction taking place, while in the CO₂-saturated solution, the HER and the CO₂RR are taking place simultaneously. The difference between both measurements would then be showing the minimum current related to the CO₂RR. However, this is only valid in the case where CO₂ in the electrolyte does not influence the HER. Still, it has to be taken into account that the HER and the CO₂RR are competing reactions, and the HER may be suppressed by the presence of CO₂. For this reason, LSV measurements have to be discussed with caution and leave a lot of room for interpretations.²⁷

There was no CO₂RR activity observed for the bare carbon supports in the investigated potential region (Figure S11). In the case of Au-Vulcan (Figure 1a), the appearance of the LSVs corresponds to those in the literature,^{17,28} where LSV_{CO₂} shows an increase of the current compared to LSV_{Ar}. Thus, the difference plot presents reduction currents, and the catalyst is active for the CO₂RR. The difference plot shows a local maximum at -0.26 V, which might indicate a change of the activity/selectivity of the CO₂RR and/or the HER or an earlier onset potential of LSV_{CO₂}. Thereafter, the slope in the difference plot increases, indicating a higher activity for the CO₂RR. For Au-BP2000 (Figure 1b), the difference plot shows positive currents, which presumably indicates a suppression of the HER by the CO₂RR. This is supported by the higher increase of the LSV_{Ar} slope compared to the LSV_{CO₂} slope, which results in higher currents of LSV_{Ar}

starting at -0.24 V. Thus, from these LSVs, no conclusion is possible whether the CO₂RR is taking place or not. For Au-CNT (Figure 1c), a unique behavior is observed. While the LSV_{CO₂} shows the expected progression, the LSV_{Ar} shows a local minimum of the reduction current at -0.32 V. This may indicate a change in the HER reaction path.²⁹ The LSV_{CO₂} shows more negative currents than the LSV_{Ar}, which results from the higher activity toward CO₂RR. As a consequence, the difference plot of Au-CNT shows a local minimum at -0.25 V, which probably results from the earlier onset of the LSV_{CO₂}, a first stronger increase of the slope of the LSV_{Ar} or a change of the activity of the CO₂RR/HER.

All measurements show a current increase in the low-overpotential region for the CO₂-saturated electrolyte compared with the Ar-saturated electrolyte. This is likely due to CO₂RR but could also point to a more positive HER onset potential in the CO₂-saturated electrolyte, resulting from CO₂RR, pH effects, and/or adsorbates influencing the overpotential of the HER. Au-BP2000 shows the highest mass specific currents, while those of Au-Vulcan and Au-CNT are comparable. This is probably a result of the higher electrochemical surface area (ECSA) of Au-BP2000 because of the smaller particle size of the AuNP on the BP2000 support. The ECSA was calculated³⁰ by integration of the charge from the Au reduction peak area and is 31.6 m² g⁻¹ for Au-CNT, 35.8 m² g⁻¹ for Au-Vulcan, and 40.5 m² g⁻¹ for Au-BP2000 (Figure S3).

A different behavior of the Au-carbon catalysts toward CO₂RR depending on the supporting material and the particle size is obvious. Comparing Au-Vulcan and Au-BP2000, the progression of the LSVs is similar, but the smaller NPs of Au-BP2000 show a higher Au-specific current in the Ar-saturated electrolyte. This is in agreement with the literature that smaller AuNPs have an increased HER activity.¹³

Scanning Electrochemical Microscopy. Given the difficulties in doubtlessly assigning observed currents in LSV to specific reactions, SECM experiments were conducted, where an ultramicroelectrode (UME) is positioned close to the Au-carbon catalyst to provide insights into product formation during CO₂RR. A CV is recorded at the UME, while the Au-carbon sample is kept at a defined potential, and the UME CV features correspond to products released from the sample during CO₂RR. Figure 2 shows the UME responses when the Au-carbon catalysts are polarized to low overpotentials

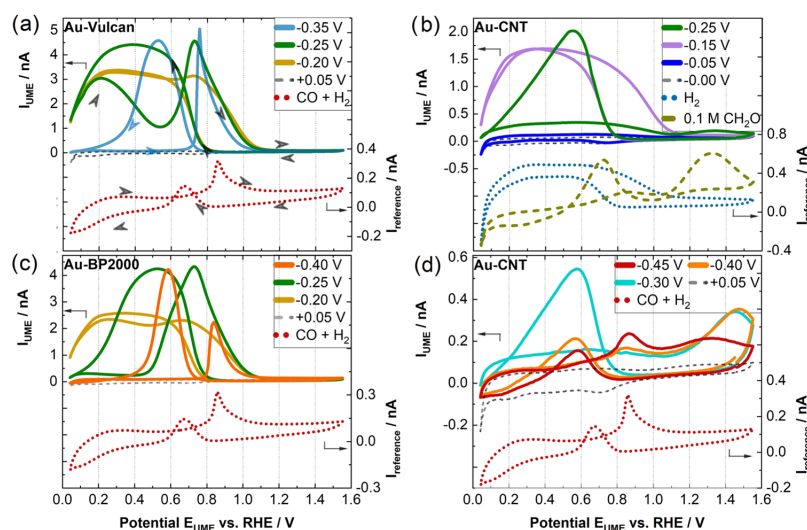


Figure 3. CVs of the UME in close proximity to the three substrates (vs RHE) for (a) Au-Vulcan, (c) Au-BP2000, (b, d) Au-CNT (substrate potentials as indicated) combined with plots of CVs of reference molecules (CO + H₂, H₂, and formaldehyde) in the lower part of the diagrams. The arrows in part a indicate the scan direction. All measurements in CO₂-saturated 0.5 M KHCO₃ at RT.

(between 0.05 and -0.25 or 0.05 – 0.45 V in the case of Au-CNT). For 0.05 V, the CVs show typical Pt features of the UME (Figure S12), with the Pt H_{upd} region and PtO formation and reduction. Details are given in our previous work.²¹ With more negative substrate potentials, there is an increase in the UME current between 0.15 and 0.8 or 1.05 V (depending on the scan direction), which is only observed below the potential of PtO formation at the Pt UME.³¹ This strong current increase is attributed to the hydrogen oxidation reaction (HOR) at the UME (see Figure S12 and below for attribution of certain current features at the UME to specific products). Thus, the hydrogen evolution reaction (HER) takes place at the substrate, starting from $E_{\text{substrate}} = -0.004$ V, and is clearly present at -0.05 V for all samples (for a detailed comparison, see Figure S12a–c). The HER remains dominant at all samples with a further decrease of the substrate potential, reaching 2 – 4.5 nA at the maximum UME current. However, at $E_{\text{substrate}} = -0.2$ V, a well-defined shoulder is observed in the forward scan at 0.75 V in the CV of the UME for Au-Vulcan and Au-BP2000. For Au-CNT, the results are different (Figure 2c). Here, a dominant oxidation peak can be found at 0.55 V in the backward scan, whereas a second oxidation peak is shifted to 1.35 V at the UME. This peak becomes more pronounced at $E_{\text{substrate}} = -0.3$ V and shifts up to 1.45 V in the CV of the UME. This finding indicates a completely different product formation at Au-CNT in contrast to the other two catalysts in the studied potential region. In order to allow for an assignment of the UME CV response in close distance to the substrates, UME CVs of reference molecules, which are expected as CO₂RR products from the literature (H₂, CO, HCOO[−], CH₃OH) as well as further molecules, were recorded with various concentrations or gas mixtures in the very same setup. All of the measurements are summarized in Figure S13, and selected results are jointly presented for comparison in Figure 3 together with the UME CVs of all samples at relevant substrate potentials. In the cases of Au-Vulcan and Au-BP2000 (Figure 3a,c), the CVs from reference measurements with both

carbon monoxide and hydrogen seem to reflect the shape of the CVs recorded close to the samples. While formate, which can be found at copper structures,²¹ also shows this type of double peak behavior (Figure S13d), the onset potentials and peak positions are in closer agreement to the reference CV of a mixture of CO + H₂ (Figure 3a,c, red dotted curve). While pure CO (Cf. Figure S12e) only shows a single oxidation peak in the forward scan at ~ 0.25 V, the additional presence of hydrogen gives rise to another oxidation peak in the backward scan. This can be explained by the formed PtO at high potentials at the Pt UME, which is reduced at 0.75 V to Pt. At this point, hydrogen molecules can be easily oxidized at the Pt UME, while the adsorption of CO molecules starts in parallel and blocks further hydrogen oxidation reaction (HOR). In the following forward scan, the CO is oxidized again, which proceeds parallel to the PtO formation.³¹ For decreasing substrate potentials, the current is decreasing because of the reduction of the ITO electrode (starting at around $E_{\text{substrate}} = -0.35$ V).²¹ Nevertheless, the peak positions are significant and present.

As said before, Au-CNT shows a deviating UME response. The assignment (Figure 3b,d) of the UME response shows hydrogen (blue, dotted line) present at $E_{\text{substrate}} = -0.15$ V. The additional oxidation peak at the UME at high potentials (~ 1.35 V), which further shifts to a higher potential (~ 1.45 V) with a decreased substrate potential, can be assigned to formaldehyde reference measurements (Figure 3b, dark yellow, dashed-dotted line). The formaldehyde evolution is present until $E_{\text{substrate}} = -0.4$ V and diminishes at -0.45 V. In parallel, the double peak behavior with an oxidation peak at 0.85 V in the forward and another in the backward scan at 0.55 V becomes evident as observed for the other two samples and is also assigned to the CO + H₂ gas evolved from the sample. However, the maximum current of both peaks is lower, indicating a lower amount of evolved molecules. As a first summary, at all samples at $E_{\text{substrate}} = -0.45$ V, the coevolution of hydrogen and carbon monoxide is observed; however, in the

case of Au-CNT, in a potential window from -0.25 to -0.40 V, the unique evolution of formaldehyde can be found.

We assume that this difference in selectivity results from the AuNPs and their interaction with support and stabilizer residuals; however, pH changes may affect the product formation, too. Here, *in situ* SECM measurements are also able to provide additional insights. Note that the lower vertex of the CV at the UME is set to 0.05 V, thus slightly passing the region where hydrogen evolution (HER) is starting (cf. Figure S12a–c). The onset of HER currents can be seen as a pH reference since the HER is pH-sensitive. This bending of the curves is found at all samples until $E_{\text{substrate}} = -0.25$ V, which allows the conclusion of very little pH change until here. Unfortunately, this internal pH sensor does not work in case CO is present in significant amounts (see Figure S13e) and is blocking the Pt surface of the UME. However, both oxidation peaks observed at a decreased substrate potential at all samples as well as in the reference mixture of H₂ + CO are only slightly affected until $E_{\text{substrate}} = -0.45$ V. In particular, the onset potential of the oxidation peak in the backward scan (~ 0.8 V) is unchanged in all measurements. Again, this is linked to the pH-sensitive reduction of PtO/Pt, which was already used for SECM pH determination in another work.²² Employing SECM with pH-sensitive Au microelectrodes, Monteiro et al. found a potential region between -0.25 and -0.4 V, where the pH does not significantly increase and the buffer system HCO₃⁻/CO₂ seems to act fast enough.²³ Comparing our reference measurements in CO₂ and Ar-saturated electrolyte (Figure S13 c-h) at $\text{pH}_{\text{CO}_2} \sim 7.35$ compared to $\text{pH}_{\text{Ar}} \sim 8.35$ indeed indicates that minor pH changes would alter the appearance of the CV. Consequently, the absence of such changes in the *in situ* SECM measurements confirms that local pH changes are of minor influence on the results in the low-overpotential region, which is the focus of investigation in this work.

Potentiostatic Chronoamperometry with Ex Situ Mass Spectrometry. To further support the findings from *in situ* SECM, potentiostatic chronoamperometry with a rotating disc electrode was performed at -0.3 V for 3:30 h to accumulate the evolved products within the electrolyte. Initial ¹H- and ¹³C-NMR measurements did not show any product formation, presumably due to the very small concentrations. Thus, a small sample of the electrolyte was transferred into the gas phase by heating and analyzed by mass spectroscopy (MS), detecting a signal of 30 (*m/z*). This experiment was performed for all samples, as well as the blank electrolyte, which was later subtracted from all sample measurements. Furthermore, 10 mM formaldehyde was added to a blank electrolyte and measured in the same way. In contrast to the other samples, only in the case of Au-CNT a signal corresponding to formaldehyde was detected (Figure S14). Lim et al.³² showed that in RDE experiments the local pH is close to the pH of the bulk electrolyte. The formation of formaldehyde during both RDE experiments and SECM underlines that pH changes have a minor influence on the product selectivity in the low-overpotential region.

Full Cell Tests with Online GC. To further quantify the major gaseous products of the CO₂RR at Au-carbon and to extend the measurements from microscale electrodes to larger sizes, all catalysts were analyzed in a full cell test stand (cf. Figure S1a) using a GC with a highly sensitive barrier ion discharge (BID) detector (for H₂ and CO calibration, see Figure S2). In contrast to other works, we additionally focus on

the low-overpotential region for further insights into the results from LSV-RDE and *in situ* SECM. The results of this low-overpotential region are presented in Figure 4. The onset of

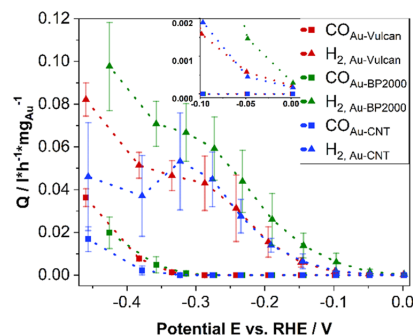


Figure 4. Product volume flow of CO and H₂ in the low-overpotential region during full cell tests, as obtained by online GC, plotted against the *iR*-corrected potential. Inset shows the potential region of the onset of H₂ detection. All measurements were performed in CO₂-saturated 0.5 M KHCO₃ at RT.

the HER is -0.05 V, which is in accordance with the strong currents measured at the UME during the SECM experiments. Au-BP2000 shows the highest HER rate, which agrees with the results of the LSV-RDE. The HER rate increases exponentially until -0.27 V, where the slope of the curve decreases for all three catalysts until -0.4 V. In contrast to the other two catalysts, there is a local decrease of the HER for Au-CNT at around -0.38 V, which is the most negative potential found for formaldehyde evolution by SECM. Note also that no significant CO evolution is observed in this region, while the current in LSV experiments was increasing. This behavior is likely caused by a change of the reaction path, where hydrogen is consumed by another reaction, i.e., formaldehyde formation. In cases of Au-Vulcan and Au-BP2000, the HER slope decrease occurs at the onset of CO formation, pointing to a competition between these two reactions, or the decrease might be a result of minor pH effects.

The CO evolution onset is around -0.33 V for Au-Vulcan and Au-BP2000 and -0.38 V for Au-CNT. Due to the small product amounts and low currents, it is not justified to calculate faradaic efficiencies (FEs) in this potential region due to large statistical errors. The comparison of the online GC with the SECM onset potentials represents the high sensitivity of CO detection by the Pt UME of SECM, which can already detect CO at -0.2 V for Au-BP2000 and Au-Vulcan. The volume solubility of CO is around 1.25 times that of H₂ in H₂O (CO 0.022 mL_{CO} mL_{H₂O}⁻¹, H₂ 0.018 mL_{H₂} mL_{H₂O}⁻¹),³³ which might lead to a delay of the first potential where CO is found in GC. To counteract this possible delay, the potential hold time was set to 45 min.

To allow for a comparison of our catalysts with the literature, we extended the full cell-GC investigations to more negative potentials, which are typically investigated in the literature. The potential thus was further decreased to -0.87 V, and the results are presented in Figure 5a. The hydrogen production steadily increased, and the HER rate showed the strongest increase on Au-CNT, while for the other two catalysts, the increase was more or less similar. This again points to the different behaviors of the Au-CNT catalyst. The

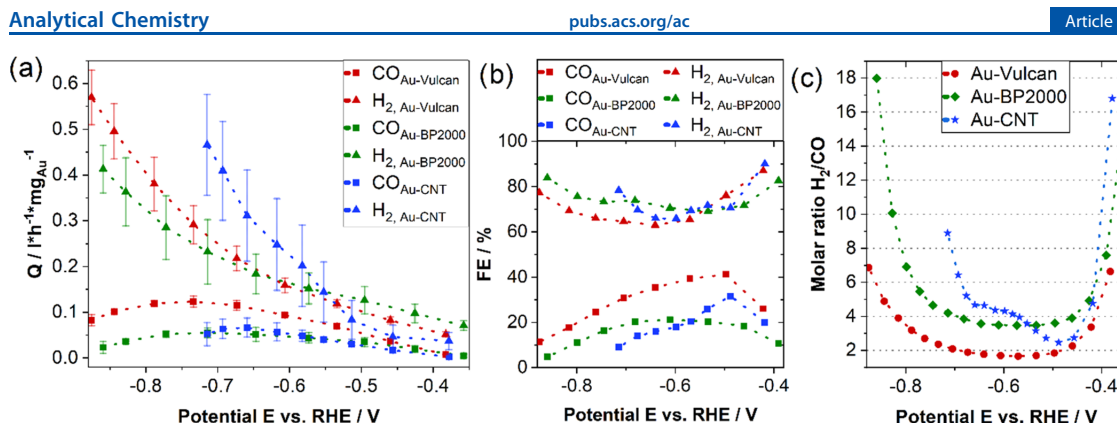


Figure 5. (a) Product formation rate of H₂ and CO, normalized to the Au loading, as obtained from online GC during full cell tests; (b) faradaic efficiency for H₂ and CO for Au-Vulcan, Au-CNT, and Au-BP2000; and (c) molar ratio of H₂/CO, plotted against the *iR*-corrected potential. All measurements were performed in CO₂-saturated 0.5 M KHCO₃ at RT.

CO flow rate is the highest at -0.73 V for Au-Vulcan, -0.71 V for Au-BP2000, and -0.66 V for Au-CNT (Figure 5a). The highest faradaic efficiency toward CO (FE_{CO}, Figure 5b) for Au-Vulcan and Au-BP2000 is found at -0.5 V and for Au-BP2000 at -0.6 V. In the case of Au-Vulcan, a FE_{CO} of $\sim 40\%$ is the highest for all three catalysts. The FE_{CO} values are in close range to those of the literature, with 4 nm AuNPs on the carbon support, which shows a maximum FE_{CO} of $\sim 60\%$ at -0.9 V and also $\sim 40\%$ at -0.5 V.¹³ For Au-CNT, the FE_{CO} at -0.4 V agrees with the literature¹⁴ of $\sim 20\%$. Differently, in the literature, the FE_{CO} increases strongly with further potential decrease, while the FE_{CO} here decreased below -0.5 V. We assume this decrease was as a result of particle degradation, e.g., by electrochemical stress.²⁶ The total FE does not always match 100%, which can be explained by the low selectivity toward side reactions of nongaseous products or parasitic reactions, which are probably higher for Au-CNT, as indicated by the lower total FE and the difference in selectivity. Although gold is highly selective for CO formation, it is also obvious that the HER rate of the investigated catalysts is significant. The molar ratio of H₂/CO in dependence of the potential is presented in Figure 5c, showing that the molar ratio is adjustable by the catalyst and the applied potential in a precise range. From an application point of view, a particular interest lies in molar ratios of 2 (methanol synthesis gas) or 3 (methane synthesis).

The unexpected finding of formaldehyde in the low-overpotential region, as observed for the first time with SECM and confirmed by *ex situ* MS, might deserve some discussion at this point. As known from the literature (see the SI for details regarding the literature on the CO₂RR mechanism), *COOH and *OCOH are presumably the adsorbates relevant for CO formation as product/intermediate, while *CO would further lead to CH₃OH. Furthermore, both forms of adsorbed *OCHO already contain one hydrogen bound to the carbon atom and might be reduced further to CH₂O (+H₂O) with three more protons and electrons. Calculations showed that a methanol forming mechanism on Au undercoordinated surfaces proceeds via desorbed CH₂O as an intermediate.¹⁰ The desorption of CH₂O is energetically favored compared to its bonding to the surface; however, its formation was experimentally not observed yet. One reason for this might be the self-condensation to C₂ products according

to the aldol and/or Cannizzaro reaction in strong acidic or base media, which again emphasizes the importance of the pH for the reaction mechanism.^{29,34,35} Thus, the differences between the three catalysts of this study presumably stem from changes of the adsorption geometry of intermediates, which may be explained on the basis of the detailed analysis of surface chemistry: no remaining sulfur residuals of the stabilizer were found on the surface of Au-CNT by XPS, while, on the other hand, such sulfur residuals were detected for all three samples by TG-MS. These, at first sight, contradicting findings may be explained by differences in the binding of thiolate traces to the catalyst surfaces. CNTs with their different surface structures might interact with the aliphatic groups of the stabilizer,³⁶ thus avoiding interaction of S with the AuNP. Indeed, the XPS measurements show that in Au-CNT, the AuNPs are free from thiolates or other sulfur species, while on the carbon black (Au-Vulcan, Au-BP2000) supported samples, Au-S bonds were detected. As mentioned earlier, small amounts of stabilizer cannot be neglected since traces of surfactants may block certain surface sites, with a direct influence on the activity and selectivity.^{37,27} Thus, we conclude that while in Au-BP2000 and Au-Vulcan the undercoordinated sites, which might form formaldehyde, are blocked by sulfur, these surface sites are available on Au-CNTs. At this point of our investigation, we cannot, however, fully rule out that sulfur doping of the support occurs instead, which also might influence catalytic properties. However, since the amount of sulfur found is extremely low, we postulate that a direct blocking of certain active sites is much more likely compared to an indirect effect via doping of the support. Additionally, as detailed in the SI, the sulfur binding energies found by us do not fit with those found for S-doped carbons. Furthermore, while in the high-overpotential region changes in pH and/or secondary reactions might impede formaldehyde detection, our particular focus on the low-overpotential region allowed us to prove formaldehyde formation with two independent techniques for the first time.

In general, a consistent picture of the CO₂RR over carbon-supported AuNP is obtained, regardless of the size of the applied electrodes, which ranges from micro (SECM, μ -dot) over medium (LSV-RDE, 0.13 cm²) to macro (test stand, 6.5 cm²). The multiple methods approach allowed comprehensive insights into the CO₂RR regions in terms of formed products

and the local pH, in particular, in the low-overpotential region, the dynamic current response over the applied potential region on medium-sized electrodes, and online product analysis of gaseous products for larger electrodes.

CONCLUSIONS

Three different Au-carbon catalysts were investigated toward their structural properties as well as their electrochemical and CO₂RR characteristics with a particular focus on the low-overpotential region using a range of (electro)analytical techniques. The catalysts were prepared by depositing thiol-stabilized gold nanoparticles onto the supports, followed by a heat treatment step to remove the stabilizer. No stabilizing agent was found on the surface of Au-CNT in contrast to that on Au-Vulcan and Au-BP2000. Furthermore, the Au surface structure of Au-CNT is less diverse than that of Au-Vulcan and Au-BP2000. LSV-RDE shows a local maximum for the difference CO₂RR plot for Au-CNT, which is known in the literature to indicate a change in the adsorption geometry.²⁹ Using SECM, we found H₂ and CO as products in CO₂RR over Au-Vulcan and Au-BP2000, with onsets of -0.004 and -0.2 V, respectively. For Au-CNT, a unique behavior was found by SECM, with formaldehyde and H₂ evolution in the potential range of -0.25 to -0.4 V, while for more negative potentials, also H₂+CO was found. Since there is no shift of the HER as well as the CO oxidation on the UME, which are both known to be pH-sensitive,²² strong local pH changes during CO₂RR can be excluded as causes for the differences. Chronoamperometric RDE experiments coupled with *ex situ* MS confirmed formaldehyde formation. The study was complemented using macroscopic electrodes in a GC-coupled electrochemical cell. The decrease in the HER production rate, as observed with GC, supports a change in the mechanism. Additionally, the outstanding detection limit for local CO detection by SECM helps more precisely determine the onset potentials for specific products formed.

In general, a consistent picture of the CO₂RR over AuNP was obtained: in the range from -0.25 to -0.4 V, the CO₂RR mechanism on Au-CNT is different from the mechanism on Au-Vulcan and Au-BP2000 because of a different H/CO₂ adsorption geometry and formaldehyde is produced to a significant amount, compared with Au-Vulcan and Au-BP2000, where CO is a major product in this potential range. The HER however is taking place in both cases. We consider this unique finding of formaldehyde formation important since usually in other works it is not detected, with arguments based on a direct subsequent reaction of the formaldehyde.^{29,34,35} Therefore, we propose that on Au-CNT, CO₂ is adsorbed as *COOH and/or *OCOH and then further hydrogenated to formaldehyde if the Au surface is free from sulfur impurities, while the smallest remaining impurities from the stabilizer block certain sites at the catalyst surface and lead to CO+H₂ as a product. Furthermore, we clearly show that the low-overpotential region is of particular interest for the mechanism discussion and cannot be neglected, as most of the published work does.

ASSOCIATED CONTENT

Supporting Information

The Supporting Information is available free of charge at <https://pubs.acs.org/doi/10.1021/acs.analchem.3c02338>.

Short overview of the literature regarding the CO₂RR mechanism; experimental details such as cleaning procedures, catalyst characterization, and the full cell test stand setup; deeper insight into the XPS analysis; overview and detailed scans and the corresponding fits of the XPS measurements and the applied fitting parameters; detailed list of the evaluated fits, before and after treatment; LSV-RDE measurements of the bare support in comparison with the selected LSV-RDE curves of the catalysts; SECM measurements of the initial hydrogen oxidation currents determined by SECM with Pt UME and SECM reference measurements, where the electrolyte was enriched with different amounts of methanol, oxalic acid, formaldehyde, potassium formate, CO, H₂, and CO+H₂; and MS results of the electrolyte analysis after prolonged potentiostatic chronoamperometry RDE experiments (PDF)

AUTHOR INFORMATION

Corresponding Author

Michael Bron – Institut für Chemie, Technische Chemie I, Martin-Luther-Universität Halle-Wittenberg, 06120 Halle, Germany; orcid.org/0000-0002-3965-5691; Email: michael.bron@chemie.uni-halle.de

Authors

Emil Dieterich – Institut für Chemie, Technische Chemie I, Martin-Luther-Universität Halle-Wittenberg, 06120 Halle, Germany

Lukas Herrmann – Institut für Chemie, Technische Chemie I, Martin-Luther-Universität Halle-Wittenberg, 06120 Halle, Germany; orcid.org/0000-0003-3463-5496

Olga Dzhyginas – Institut für Chemie, Technische Chemie I, Martin-Luther-Universität Halle-Wittenberg, 06120 Halle, Germany

Lukas Binnenböse – Institut für Chemie, Technische Chemie I, Martin-Luther-Universität Halle-Wittenberg, 06120 Halle, Germany

Matthias Steimecke – Institut für Chemie, Technische Chemie I, Martin-Luther-Universität Halle-Wittenberg, 06120 Halle, Germany; orcid.org/0000-0002-9726-4074

Simon-Johannes Kinkelin – Institut für Chemie, Technische Chemie I, Martin-Luther-Universität Halle-Wittenberg, 06120 Halle, Germany; orcid.org/0000-0001-6624-4209

Complete contact information is available at: <https://pubs.acs.org/doi/10.1021/acs.analchem.3c02338>

Author Contributions

The manuscript was written by E.D. All authors have given approval to the final version of the manuscript. E.D. analyzed the S/TEM, TG-MS, XPS, and some of the electrochemical measurements. E.D. conducted the potentiostatic chronoamperometry RDE, L.H. conducted the LSV-RDE, O.D. conducted the SECM under supervision of M.S., and L.B. under supervision of E.D. performed the online GC test stand measurements. S.-J.K. and M.S. contributed with in-depth scientific discussion. The work was supervised by M.B.

Notes

The authors declare no competing financial interest.

H

<https://doi.org/10.1021/acs.analchem.3c02338>
Anal. Chem. XXXX, XXX, XXX–XXX

ACKNOWLEDGMENTS

The authors thank Annett Quetschke (Institut für Chemie, Technische Chemie I, Martin-Luther-Universität Halle-Wittenberg) for performing TEM and TG-MS measurements, Eik Koslowski (Institut für Chemie, Technische Chemie I, Martin-Luther-Universität Halle-Wittenberg) for performing XPS and Raman measurements, Frank Syrowatka (Interdisziplinäres Zentrum für Materialwissenschaften, Martin-Luther-Universität Halle-Wittenberg) for the STEM measurements, and Jonas Jacobs (Institut für Chemie, Anorganische Chemie, Martin-Luther-Universität Halle-Wittenberg) for in-depth scientific discussions.

REFERENCES

- (1) Ait Ahsaine, H.; Zbair, M.; BaQais, A.; Arab, M. *Catalysts* **2022**, *12*, 450.
- (2) Hoang, V. C.; Gomes, V. G.; Kornienko, N. *Nano Energy* **2020**, *78*, No. 105311.
- (3) Whipple, D. T.; Kenis, P. J. A. *J. Phys. Chem. Lett.* **2010**, *1*, 3451.
- (4) Liu, X.; Xiao, J.; Peng, H.; Hong, X.; Chan, K.; Nørskov, J. K. *Nat. Commun.* **2017**, *8*, No. 15438.
- (5) Bagger, A.; Ju, W.; Varela, A. S.; Strasser, P.; Rossmeisl, J. *ChemPhysChem* **2017**, *18*, 3266.
- (6) Gattrell, M.; Gupta, N.; Co, A. J. *Electroanal. Chem.* **2006**, *594*, 1.
- (7) Vickers, J. W.; Alfonso, D.; Kauffman, D. R. *Energy Technol.* **2017**, *5*, 775.
- (8) Zhang, L.; Zhao, Z.-J.; Gong, J. *Angew. Chem.* **2017**, *129*, 11482–11511.
- (9) Seh, Z. W.; Kibsgaard, J.; Dickens, C. F.; Chorkendorff, I.; Nørskov, J. K.; Jaramillo, T. F. *Science* **2017**, *355*, No. aad4998.
- (10) Cave, E. R.; Montoya, J. H.; Kuhl, K. P.; Abram, D. N.; Hatsukade, T.; Shi, C.; Hahn, C.; Nørskov, J. K.; Jaramillo, T. F. *Phys. Chem. Chem. Phys.* **2017**, *19*, 15856.
- (11) Chen, Y.; Li, C. W.; Kanan, M. W. *J. Am. Chem. Soc.* **2012**, *134*, 19969.
- (12) Sreekanth, N.; Phani, K. L. *Chem. Commun.* **2014**, *50*, 11143.
- (13) Zhu, W.; Michalsky, R.; Metin, Ö.; Lv, H.; Guo, S.; Wright, C. J.; Sun, X.; Peterson, A. A.; Sun, S. *J. Am. Chem. Soc.* **2013**, *135*, 16833.
- (14) Wang, A.; Zhu, Y.; Sun, J.; Hu, S.; Zhang, X.; Niu, D. *Appl. Surf. Sci.* **2023**, *635*, 157692.
- (15) Trindell, J. A.; Clausmeyer, J.; Crooks, R. M. *J. Am. Chem. Soc.* **2017**, *139*, 16161.
- (16) Nursanto, E. B.; Jeon, H. S.; Kim, C.; Jee, M. S.; Koh, J. H.; Hwang, Y. J.; Min, B. K. *Catal. Today* **2016**, *260*, 107.
- (17) Zhao, Y.; Wang, C.; Liu, Y.; MacFarlane, D. R.; Wallace, G. G. *Adv. Energy Mater.* **2018**, *8*, No. 1801400.
- (18) Verma, S.; Hamasaki, Y.; Kim, C.; Huang, W.; Lu, S.; Jhong, H.-R. M.; Gewirth, A. A.; Fujigaya, T.; Nakashima, N.; Kenis, P. J. A. *ACS Energy Lett.* **2017**, *193*–198.
- (19) Rogers, C.; Perkins, W. S.; Veber, G.; Williams, T. E.; Cloke, R. R.; Fischer, F. R. *J. Am. Chem. Soc.* **2017**, *139*, 4052.
- (20) Liu, A.; Gao, M.; Ren, X.; Meng, F.; Yang, Y.; Gao, L.; Yang, Q.; Ma, T. *J. Mater. Chem. A* **2020**, *8*, 3541.
- (21) Steimecke, M.; Araújo-Cordero, A. M.; Dieterich, E.; Bron, M. *ChemElectroChem* **2022**, *9*, No. e202101221.
- (22) Dieckhöfer, S.; Öhl, D.; Junqueira, J. R. C.; Quast, T.; Turek, T.; Schuhmann, W. *Chem. – Eur. J.* **2021**, *27*, No. 5906.
- (23) Monteiro, M. C. O.; Mirabal, A.; Jacobse, L.; Doblhoff-Dier, K.; Barton, S. C.; Koper, M. T. M. *JACS Au* **2021**, *1*, 1915.
- (24) Monteiro, M. C. O.; Dieckhöfer, S.; Bobrowski, T.; Quast, T.; Pavesi, D.; Koper, M. T. M.; Schuhmann, W. *Chem. Sci.* **2021**, *12*, 15682.
- (25) Dieterich, E.; Kinkelin, S.-J.; Bron, M. *ChemNanoMat* **2022**, *8*, No. e202200098.
- (26) Dieterich, E.; Kinkelin, S.-J.; Steimecke, M.; Bron, M. *Nanoscale Adv.* **2022**, *4*, 5154.
- (27) Cai, X.; Li, G.; Hu, W.; Zhu, Y. *ACS Catal.* **2022**, *12*, 10638.
- (28) Goyal, A.; Marcandalli, G.; Mints, V. A.; Koper, M. T. M. *J. Am. Chem. Soc.* **2020**, *142*, 4154.
- (29) Calvino, K. U. D.; Alherz, A. W.; Yap, K. M. K.; Laursen, A. B.; Hwang, S.; Bare, Z. J. L.; Clifford, Z.; Musgrave, C. B.; Dismukes, G. C. *J. Am. Chem. Soc.* **2021**, *143*, 21275.
- (30) Habrioux, A.; Sibert, E.; Servat, K.; Vogel, W.; Kokoh, K. B.; Alonso-Vante, N. *J. Phys. Chem. B* **2007**, *111*, 10329.
- (31) Prass, S.; St-Pierre, J.; Klingele, M.; Friedrich, K. A.; Zamel, N. *Electrocatalysis* **2021**, *12*, 45.
- (32) Lim, C.; Harrington, D. A.; Marshall, A. T. *Electrochim. Acta* **2017**, *238*, 56.
- (33) Wiesenburger, D. A.; Guinasso, N. L. *J. Chem. Eng. Data* **1979**, *24*, 356.
- (34) Birdja, Y. Y.; Koper, M. T. M. *J. Am. Chem. Soc.* **2017**, *139*, 2030.
- (35) Zhou, Y.; Yeo, B. S. *J. Mater. Chem. A* **2020**, *8*, 23162.
- (36) Inkpen, M. S.; Liu, Z.-F.; Li, H.; Campos, L. M.; Neaton, J. B.; Venkataraman, L. *Nat. Chem.* **2019**, *11*, 351.
- (37) Kim, B.; Seong, H.; Song, J. T.; Kwak, K.; Song, H.; Tan, Y. C.; Park, G.; Lee, D.; Oh, J. *ACS Energy Lett.* **2020**, *5*, 749.

Supporting information

Multimethod approach to the low overpotential region of micro- to macro-scale working electrodes of sub-10 nm gold nanoparticles in the CO₂ reduction reaction

*Emil Dieterich, Lukas Herrmann, Olga Dzhyginas, Lukas Binnenböse, Matthias Steimecke, Simon-Johannes Kinkelin, and Michael Bron**

Institut für Chemie, Technische Chemie I
Martin-Luther-Universität Halle-Wittenberg
Von-Danckelmann-Platz 4, 06120 Halle, Germany
E-mail: michael.bron@chemie.uni-halle.de

OVERVIEW ON RELEVANT LITERATURE REGARDING THE ELECTROCHEMICAL CO₂RR MECHANISM

Various mechanisms have been proposed for the CO₂RR depending on different models of adsorption of CO₂, which in turn depend on the catalysts material and morphology, as well as on the local pH, mass transport as well as type and concentration of the electrolyte.^{1,2,3,4,5,6,7,8,9} One may distinguish between concerted proton-electron transfer (CPET) and direct adsorption. The CPET adsorption is further divided into five possible adsorption mechanisms.⁵ For the direct adsorption (*CO₂*), high overpotentials are calculated by DFT which in turn means that CPET is favored in the low overpotential region.¹⁰ The five predicted adsorption species are *OCHO, *HCOO, *COOH and *OCOH where in case of *OCHO one or both O and for *OCOH both the O and C are bound to the electrode surface.⁵ For CO₂RR on Au, stronger adsorption favors CO formation, while weaker binding favors formate as intermediate^{7,11} and CO preferentially desorbs from Au¹. Therefore, *COOH and *OCOH are presumably the adsorbates for CO formation as

product or intermediate, whereas *CO as intermediate for further methanol formation is calculated, however, selectivity is below 1 %, which may result from the facile desorption of *CO from Au surface.¹ Calculations of *CO as first intermediate on Au show a minimum energy pathway with H₂CO as desorbed intermediate which is then further reduced to CH₃OH. This presumably results from a changed desorption mechanism of H₂/CO, which also inhibits the *CO desorption.¹ While both types of *OCHO adsorbates are already binding one hydrogen to the carbon atom and can further be hydrogenated, these adsorbates are rare on Au because of its oxophobic character.^{4,5,7}

ADDITIONAL EXPERIMENTAL DETAILS

Chemicals. The following chemicals and materials were used as received: ethanol (abs. HPLC, Th Geyer), DI H₂O (SG water Ultra Clear UV ultrapure water, 0.055 μS cm⁻¹), HAuCl₄ • 3 H₂O (ACS 99.99 % metal basis, Au 49.0 % min, Alfa Aesar), NaBH₄ (99 %, Acros Organics), 1-dodocanethiol (1-DDT) (> 98 %, Sigma Aldrich), toluene (> 99.5 % for synthesis, ROTH), n-hexane (> 99 % p.a. ACS, ROTH), tetra-n-octylammonium bromide (TOAB) (98+ %, Alfa Aesar), Vulcan XC72 (carbon black, Cabot), Nafion 117 (sol. 5 %, Sigma Aldrich), Baytubes C 150 P (carbon nanotubes, C-purity > 95 %, Number of walls 3-15, Bayer MaterialScience), Black Pearls 2000 (carbon black, Cabot), Ar (99,999 %, Air Liquide), CO₂ (99,995 %, Air Liquide), HCl (37%, ROTH), HNO₃ (65%, ROTH), KHCO₃ (> 99.5 %, ROTH), CO (10.34 % in He, Air Liquide), H₂ (99.999 %, Air Liquide), KHCO₃ (99 %, Sigma Aldrich), CH₂O (16 % (w/v) methanol free, Thermo Fischer™), C₂H₂O₄ (99 % anhydrous, Sigma Aldrich), CH₃OH (> 99.98 % ultra LC-MS, ROTH), graphite foil (GF-175, Graphite Materials GmbH), Nafion Membrane (DuPont Nafion 115 membrane) and Ni-mesh (Goodfellow 99.0 %).

Instruments and measurements. All glassware was cleaned with aqua regia. For this purpose, all glassware was kept in aqua regia for at least 12 h under stirring and reflux. Afterwards the temperature was increased every 20 min for 5 K up to a final temperature 50 °C, which was held for 1 h. Thereafter all parts were cleaned with boiling DI water for at least 30 min under reflux.

For the catalyst synthesis a rotary evaporator (Heidolph G3) and a centrifuge (Eppendorf 5804) were used. The Baytubes carbon nanotubes and Black Pearl 2000 support were pre-treated (800 °C, Ar-atmosphere, 1 h, 5 K min⁻¹) in a furnace (Nabertherm RHTH 80-300/18) and the AuNP on carbon support were treated with H₂ (15 % H₂/Ar, 6 l h⁻¹, 400 °C, 1 h, 10 K min⁻¹) in a tube furnace (Carbolite MTF 12/38/250).

The scale calibration from Ag|AgCl|KCl_{sat.} to RHE was measured by using a multi-meter and a RHE (Gaskatel) and the used Ag|AgCl|KCl_{sat.} electrode in the corresponding electrolyte saturated with CO₂ or Ar. For CO₂ saturated and for Ar saturated 0.5 M KHCO₃ -646 mV respectively -704 mV was measured. This was confirmed by calculation using the pH of the corresponding electrolyte solution (7.35 for CO₂ purged and 8.35 for Ar purged 0.5 M KHCO₃) with $E_{RHE} = E_{Ag|AgCl|KCl_{sat.}} + E^0_{Ag|AgCl|KCl_{sat.}} + 0.0591 \cdot pH$ where $E^0_{Ag|AgCl|KCl_{sat.}} = 0.197$ V at 25 °C.¹²

Synthesis of the catalysts. The AuNP were prepared by a modified synthesis^{13,14} according to Brust et al.¹⁵. Briefly, three stock solutions of 0.05 M TOAB in toluene, 0.03 M HAuCl₄ • 3 H₂O and 0.4 M NaBH₄ in DI H₂O were prepared. The molar ratio of the metal/stabilizing agent (1-DDT)/phase transfer agent (TOAB)/reduction agent (NaBH₄) was 1/3/3/10. 3.75 ml of Au stock solution was added to 6.75 ml of the TOAB solution. After 10 min of stirring, 81 µl of 1-DDT was introduced. Then 12.5 ml of the freshly prepared NaBH₄ stock solution was added, followed by stirring until the aqueous phase became clear. The organic phase was extracted by decanting and

reduced to one tenth of its volume and 40 ml abs. EtOH were added, followed by storage at 4 °C for 16 h. The precipitate was separated and washed with abs. EtOH twice. The product was dispersed in 3 ml toluene and 7 ml abs. EtOH.

The AuNP were supported onto the respective carbon support (Vulcan XC72, Black Pearls and Baytubes) by a modified method^{13,14} according to.¹⁶ A suspension of the supporting material was prepared in n-hexane (20 ml/80 mg) by ultrasonication for 6 h. The AuNP were redispersed by ultrasonication for 30 min. and the AuNP suspension was added to the suspension of the carbon support and sonicated for further 30 min, followed by stirring overnight. The liquid phase was removed by centrifugation and the precipitate was washed with abs. EtOH. Finally, the product was dried at 60 °C and ~500 mbar overnight.

The dried Au/support samples were post treated according to a previously published method¹⁴. The sample was placed in a tube furnace in a quartz glass vessel. The tube furnace was purged with Ar for 30 min, followed by heat treatment in 15 % H_2/Ar ($6 l h^{-1}$) at 400 °C ($10 K min^{-1}$) for 1 h. The atmosphere was changed to Ar before cooling down, after holding 400 °C for 1 h.

Catalyst characterization. Au particle sizes were determined from micrographs recorded with a scanning transmission electron microscope (Zeiss GeminiSEM 500 with EDX, Oxford Ultim Max & Oxford Extreme and EBSD, Oxford C-Nanoresolution: 0.5 nm at 15 kV; 0.9 nm at 1 kV, 1.0 nm at 500 V, accelerating voltage: 0.02-30.0 kV, magnification: 50 times to 2,000,000 times, high efficiency Inlens secondary detector for ultra-high resolution surface information) and a transmission electron microscope (Zeiss, Leo 912 Omega, 120 keV, specific point-resolution 0.37 nm). The samples were prepared by suspending < 1 mg in EtOH and drop casting on carbon coated copper grids (PLANO GmbH, carbon hole film 2.05 mm Cu-net 300 mesh) and drying at

room temperature. The amount of gold on the support was determined by thermogravimetric measurements (Netzsch STA 449 F1). ~5 mg of the sample were placed in an Al₂O₃ crucible followed by heating (10 K min⁻¹) in 20 % O₂/Ar up to 1000 °C. The specific surface areas (SSA_{BET}) of the supporting materials were determined with a Sorptomatic 1990 (Thermo Finnigan). Before the measurements, the samples were heated under vacuum (10⁻⁵ mbar) at 120 °C for 24 h. Adsorption and desorption isotherms were measured using nitrogen as adsorbate (77 K, relative pressure p/p_0 0.05 to 0.3), followed by evaluation of the adsorption data by Brunauer-Emmett-Teller (BET) theory. Surface characterization of the samples was carried out by X-ray photoelectron spectroscopy (XPS) with a DAR 400 (Omicron) with an Al K_α line (250 W, 1486 eV). Overview scans were performed with 200 eV pass energy, 5 sweeps, 1 eV steps, detail scans with 30 eV pass energy, 10 sweeps and 0.1 eV steps. The spectra were analyzed with CasaXPS.

FULL CELL TESTS WITH GAS CHROMATOGRAPHY

The on-line GC CO₂RR measurements were carried out as follows. Initially, 2 CVs (0.1 V to 1.6 V vs. RHE, 500 mV•s⁻¹, all further potentials in this document are vs. RHE) were applied, followed by holding the WE at 0 V for 10 min. Then again 2 CVs were applied, followed by holding the CO₂RR potential under investigation for 3200 s. After 600 s and 2700 s a sample was injected from the exhaust gas stream into the GC. This procedure was carried out in the potential region 0 V... -0.4 V. In this potential region, the long duration of 3200 s was necessary to obtain a constant product composition in the gas stream (low rate of product formation). At more negative potentials (-0.45 V ... -1.2 V) 2 CVs were recorded followed by a potential hold for 1200 s followed again by holding at 0 V for 1200 s. After the first 1200 s the GC was recorded.

The potentials were changed in 50 mV steps from 0 to -1.2 V. Before the measurements, the internal resistance was determined, and potentials were iR -corrected.

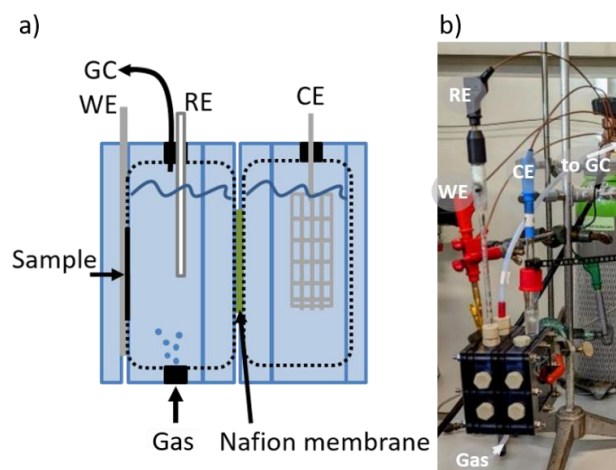


Figure S1. a) Scheme of the in-house build two compartment electrochemical cell coupled with a GC, b) photograph of the cell with connected electrodes and PTFE tube for gas supply and connection to the GC. RE - $Ag|AgCl|KCl_{sat.}$, WE – graphite plate with sample and CE – Ni-mesh.

The Faradaic efficiency was calculated using $FE = (Q_{theo.} / Q_{measured}) \cdot 100$, whereby $Q_{theo.}$ is the average current over time multiplied by the time to load the GC sample loop with the corresponding flow rate, while $Q_{measured} = n \cdot F \cdot z$ (n amount of product measured by GC, F faradaic constant, z charge transferred for the corresponding product - for CO and H_2 it is 2) was calculated using the results of the GC measurements.

For the determination of the amount of product the GC was calibrated for CO and H_2 . For H_2 calibration, H_2 and CO_2 were mixed by mass flow controllers to yield 4.39 % H_2 in CO_2 . Defined volumes of this mixture were injected to the GC with a syringe. This was repeated three times for each volume. The chromatograms of different volumes of H_2/CO_2 -mixtures are shown in Fig. S2a.

Using the integrated peak area, a calibration curve was calculated (Fig. S2c). For CO the same procedure was repeated, using a mixture containing 1.03 % CO in CO_2 . The chromatograms are shown in Fig. S2b) and a calibration curve was calculated (Fig. S2d). Using these the calibration curves, the amounts of products were calculated under the assumption of an ideal gas.

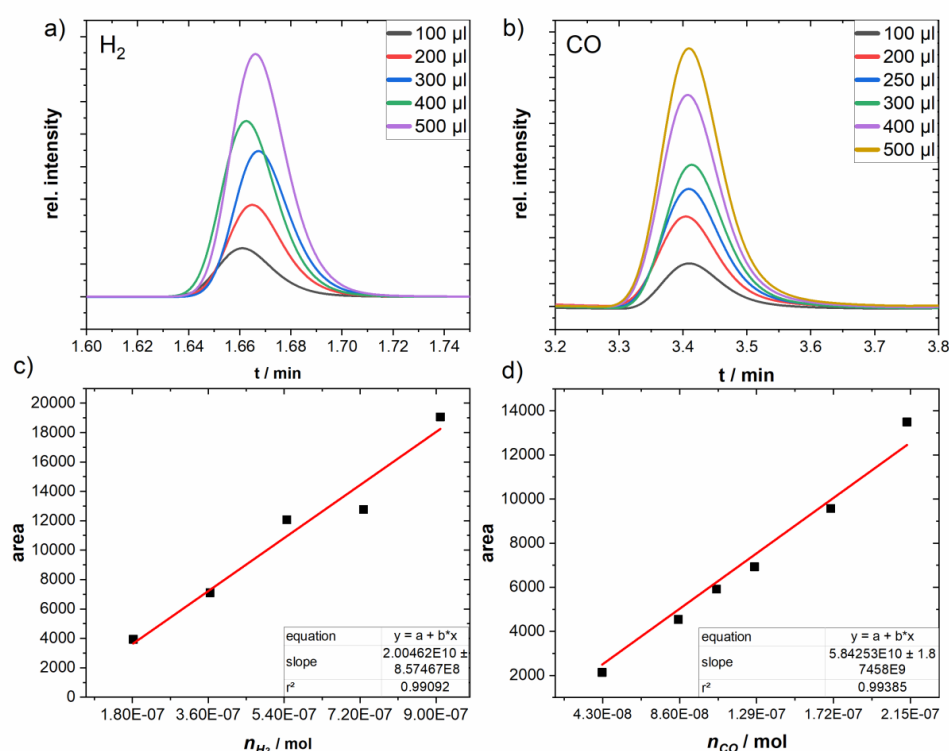


Figure S2. Exemplary calibration chromatograms of a) H_2 and b) CO of different volumes injected by a syringe with 4.39 % H_2 respectively 1.03 % CO in CO_2 . In c) and d) the calculated calibration curves are shown.

CATALYSTS

The following Tab. S1 summarizes relevant parameters of the used catalysts. The particle size was analyzed by STEM, the Au loading by TG and the ECSA was calculated¹⁷ from the CV in 0.5 M KHCO₃ purged with CO₂ before the LSV_{CO2} measurement (see Fig. S3). For more information about catalyst synthesis and treatment see our previous work.^{13,14}

Table S1. Average particle size, size range, standard deviation, Au loading of the catalysts and calculated ECSA. The Au loading is corrected by the solid residue of the support, which was determined from TG measurements of the corresponding supporting material that was also treated under the same conditions as the catalyst.

Catalyst	Average NP size / nm (stdv.)	NP size range / nm	Number of NP analyzed	Au loading / wt.%	ECSA / m ² g ⁻¹
Au-Vulcan(1)	4.0 (± 1.9)	1.9-9.0	3062	17.1	35.8
Au-Vulcan(2)	4.8 (±1.6)	1.4-11.2	588	14.8	
Au-BP2000(1)	2.4 (± 0.7)	0.7-5.6	501	19.9	40.5
Au-BP2000(2)	2.7 (± 1.0)	1.1-14.3	636	23.5	
Au-CNT(1)	4.8 (± 1.4)	1.7-9.4	489	15.0	31.6
Au-CNT(2)	4.9 (± 1.4)	2.0-9.7	590	18.9	

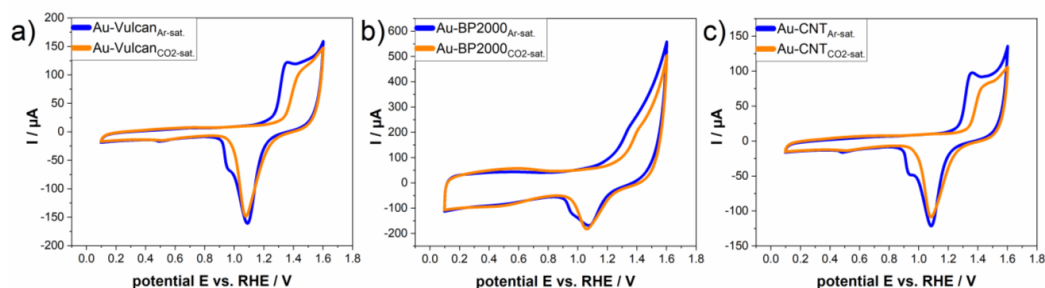


Figure S3. Cyclic voltammograms of a) Au-Vulcan, b) Au-BP2000 and c) Au-CNT in 0.5 M KHCO₃ Ar or CO₂ saturated, with 50 mV•s⁻¹, which were used for the ECSA calculation.

The ECSA was calculated with a charge density of 493 µC•cm⁻² as used literature¹⁷ for AuNP on Vulcan XC 72 with an upper limit of 0.25 V vs. MSE in 0.1 M NaOH (pH 13, $E_{RHE} = E_{MSE} + E_{MSE}^0 + 0.0591 \cdot \text{pH}$ where $E_{MSE}^0 = 0.615$ V resulting in an upper limit of 1.633 V vs. RHE) in the corresponding CVs. The charge density per µg_{Au} of the reduction peak (A•V•g_{Au}⁻¹) corrected by a blank measurement was divided by the scan rate (20 mV•s⁻¹) and further divided by the charge density.

TG-MS MEASUREMENTS FOR RESIDUAL STABILIZING AGENT

Following the procedure described in¹⁴ all samples were analyzed for remaining stabilizing agent. The results are presented in Fig. S4 where Au-Vulcan showed the least remaining stabilizer in the sample, but the highest standard deviation (2.9 % ± 3.6 %) followed by AuBP2000 (5.4 % ± 1.3 %) and Au-CNT (8.2 % ± 0.2 %).

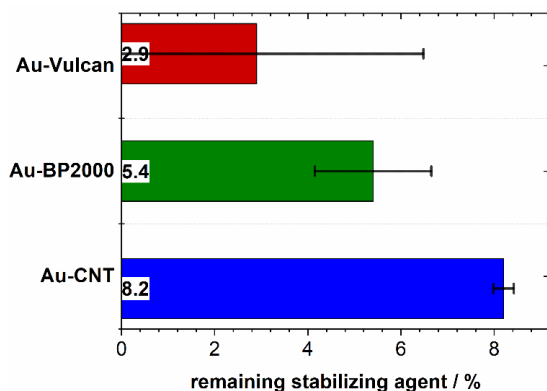


Figure S4. Amount of remaining stabilizer from TG-MS analysis for Au-Vulcan, Au-BP2000 and Au-CNT.¹⁴

XPS ANALYSIS

To analyze the surface composition of the catalysts and to unravel the effect of the post treatment onto the stabilizing agent and the catalysts, XPS measurements were carried out. Overview scans as well as detail scans for Au 4f, S 2p, C 1s and O 1s were recorded of the sample before and after the post treatment and fitted according to literature to provide insight into the structure and assembly of the surfaces. Spectra can be found below in Fig. S6 (overview) and Fig. S7-S10 (detail scans) All fitting parameters are listed in Tab. S3.

Fig. S5a, b and c show detail scans of the S 2p region with insets showing exemplary STEM images of the related catalysts, while Fig. S5d presents the sulphur content, the share of the different Au species from the Au 4f fits and the full width half max (FWHM) of these fits. Additionally, in Fig. S6, the overview scans and the detail scans of all three catalysts before and after the post treatment are shown in order to unravel any influence on the surface structure during the removal of stabilizing agent by hydrogen treatment. The results of the XPS analysis are

summarized in Tab. S2, while all fitting parameters are summarized in Tab. S3. For signals related to the carbon support only negligible changes can be observed by XPS (cf. before and after post treatment Fig. S6, S7 and S8). The O 1s detail scans (Fig. S8) show, that about 90 % of the oxygen is bound the support and the amount of oxygen directly bound to Au is negligible. For the S 2p detail scan (Fig. S9, Tab. S2) the removal of the stabilizing agent is confirmed by the reduced Sulphur content in the XP spectra recorded after the post treatment compared to those before. The data is also establishing that there is no Sulphur in Au-CNT left, while traces are remaining in Au-Vulcan and Au-BP2000. Furthermore, S-doping of the carbon material should be ruled out, as the binding energies for Au-BP2000 and Au-Vulcan don't fit with the suitable binding energies for S doped carbon. Specially for Au-CNT there should not be any S-doping, as there is no Sulfur found by XPS.¹⁸ The fits of these spectra have to be taken with some caution due to low signal intensity. However, they indicate that > 60 % of the remaining sulfur is bound as RS-H and only minor parts are directly bound to gold. The Au detail scan (Fig. S10) shows an increase of the Au-C bond by the post treatment which reasonably indicates stabilizer removal and direct attachment of AuNP to the support. Also the fits of the Au 4f detail scan show a clear course, where Au(0) and Au-C have the highest share in Au-CNT and Au^{δ+} the smallest. Au^{δ+} presents electrically disconnected AuNP and thiol bound to Au.^{19,20} Furthermore Au-CNT displays the lowest FWHM, whereby the broadness of the FWHM is related to crystal field splitting and surface defects.²¹ The high amounts of RS-H bond in the S 2p signal show that the remaining stabilizing agent is not directly bound to the Au surface in the form of RS-Au, as often assumed by literature^{22,23,24}. Most likely the thiolate is partly bound to the support by interactions of the aliphatic group of the thiolate with the support or by adsorptive bonds between the thiolate-group to the gold surface.² The remaining share of directly Au-bound thiolates is very small but may

have influences that cannot be neglected. Small amounts of surfactant may specifically block certain facets, kinks or edges and may have a direct influence on the electrochemical activity/selectivity in the CO_2RR .^{3,25} The smallest share of $Au^{\delta+}$ for Au-CNT further promotes the absence of thiol species directly bound to Au in Au-CNT. These findings suggest that Au-CNT has the smallest amount of low coordinated Au atoms and diversity in surface structure.

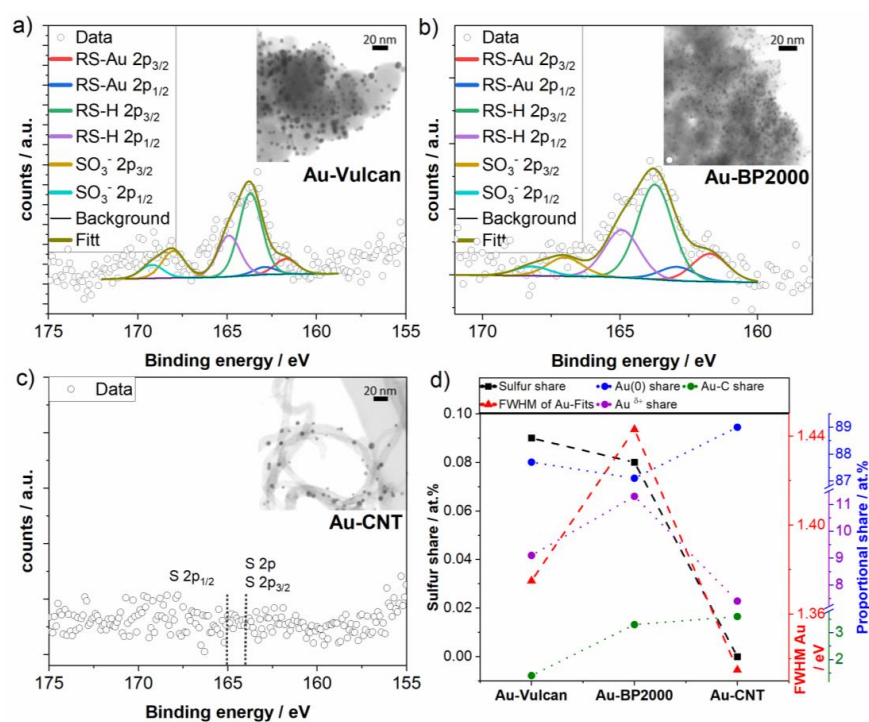


Figure S5. XPS S 2p detail scan of a) Au-Vulcan, b) Au-BP2000 and c) Au-CNT with insets of STEM images and d) comparison of the sulfur content of the samples, the FWHM of the Au 2p fits and the amounts of the different Au species, lines are only inserted to guide the eye.

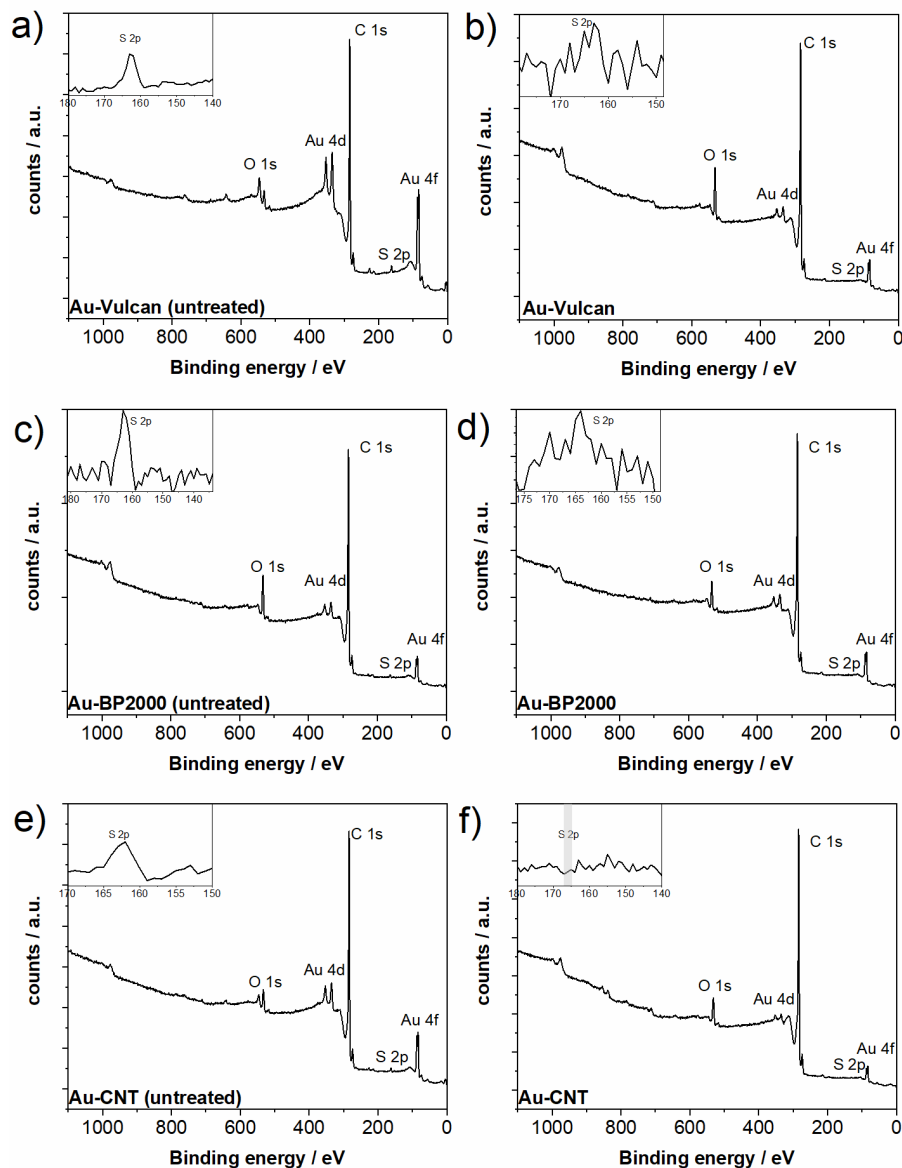


Figure S6. XPS overview scans with an inset of the S 2p region for a) Au-Vulcan (untreated), b) Au-Vulcan, c) Au-BP2000 (untreated), d) Au-BP2000, e) Au-CNT (untreated) and f) Au-CNT. The C 1s signal was fitted and is at 284.0 eV for all samples.

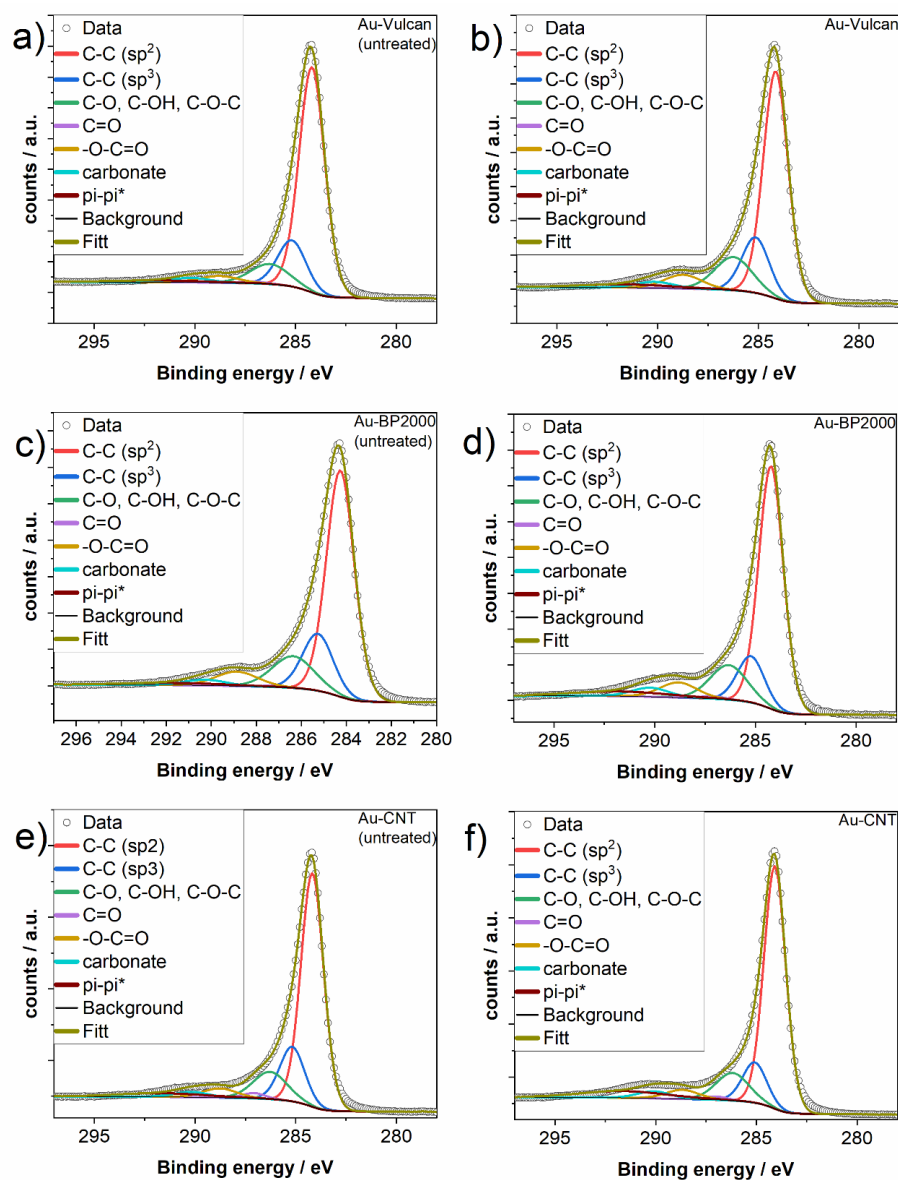


Figure S7. C 1s XPS detail scan for a) Au-Vulcan (untreated), b) Au-Vulcan, c) Au-BP2000 (untreated), d) Au-BP2000, e) Au-CNT (untreated) and f) Au-CNT.

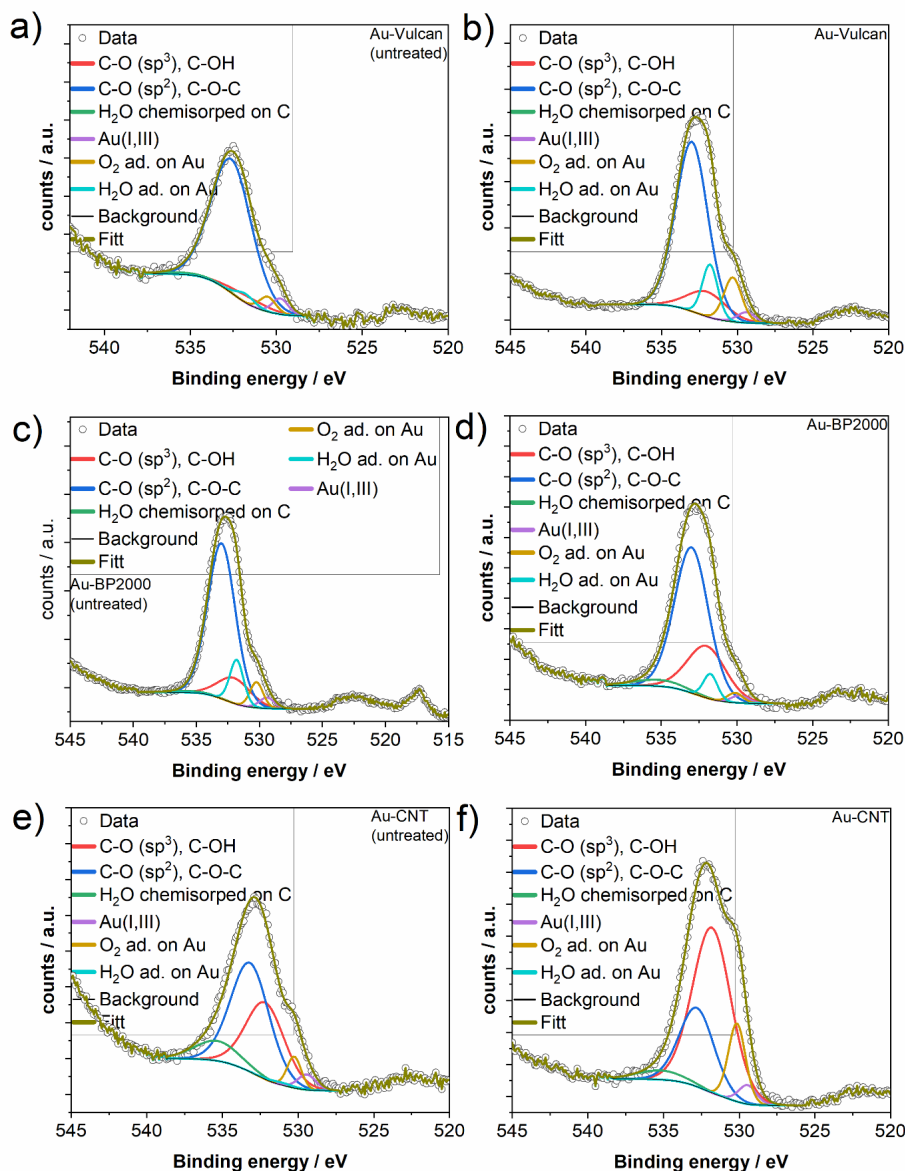


Figure S8. O 1s XPS detail scan for a) Au-Vulcan (untreated), b) Au-Vulcan, c) Au-BP2000 (untreated), d) Au-BP2000, e) Au-CNT (untreated) and f) Au-CNT.

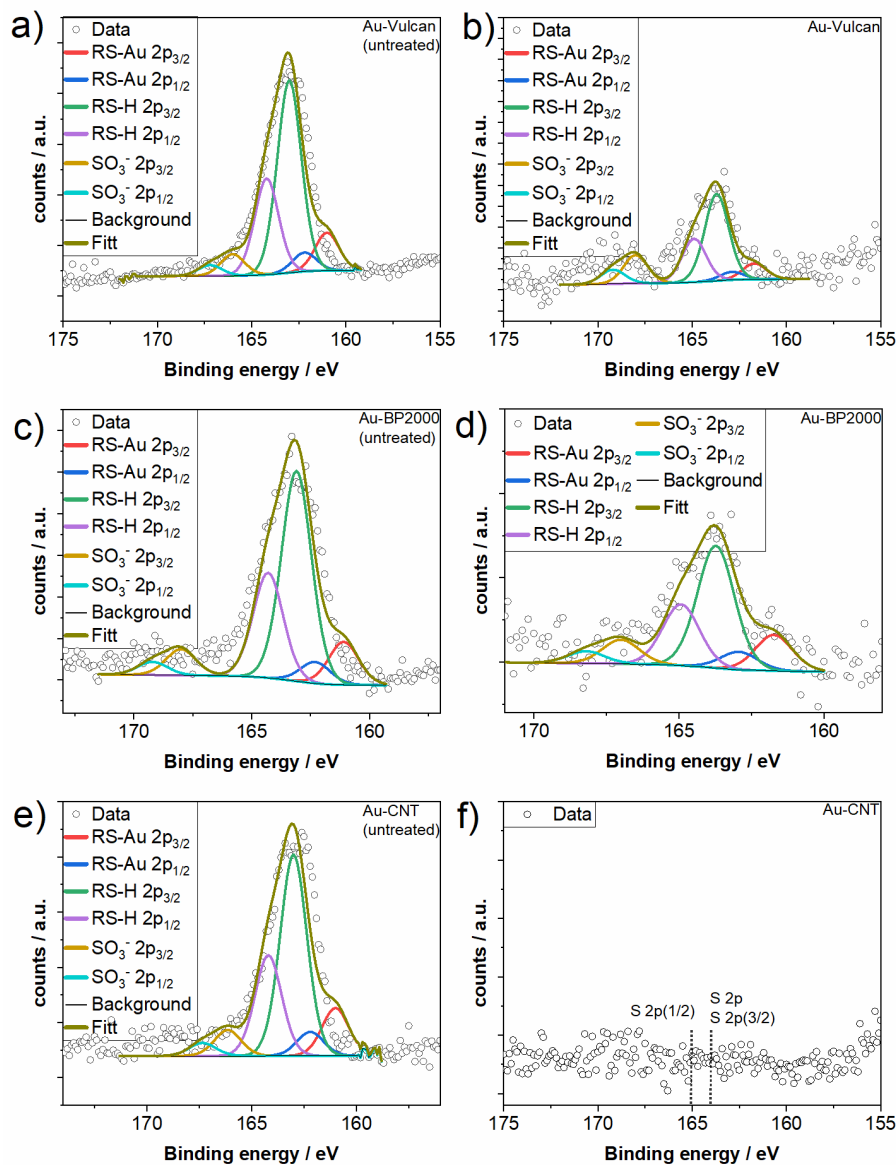


Figure S9. S 2p XPS detail scan for a) Au-Vulcan (untreated), b) Au-Vulcan, c) Au-BP2000 (untreated), d) Au-BP2000, e) Au-CNT (untreated) and f) Au-CNT.

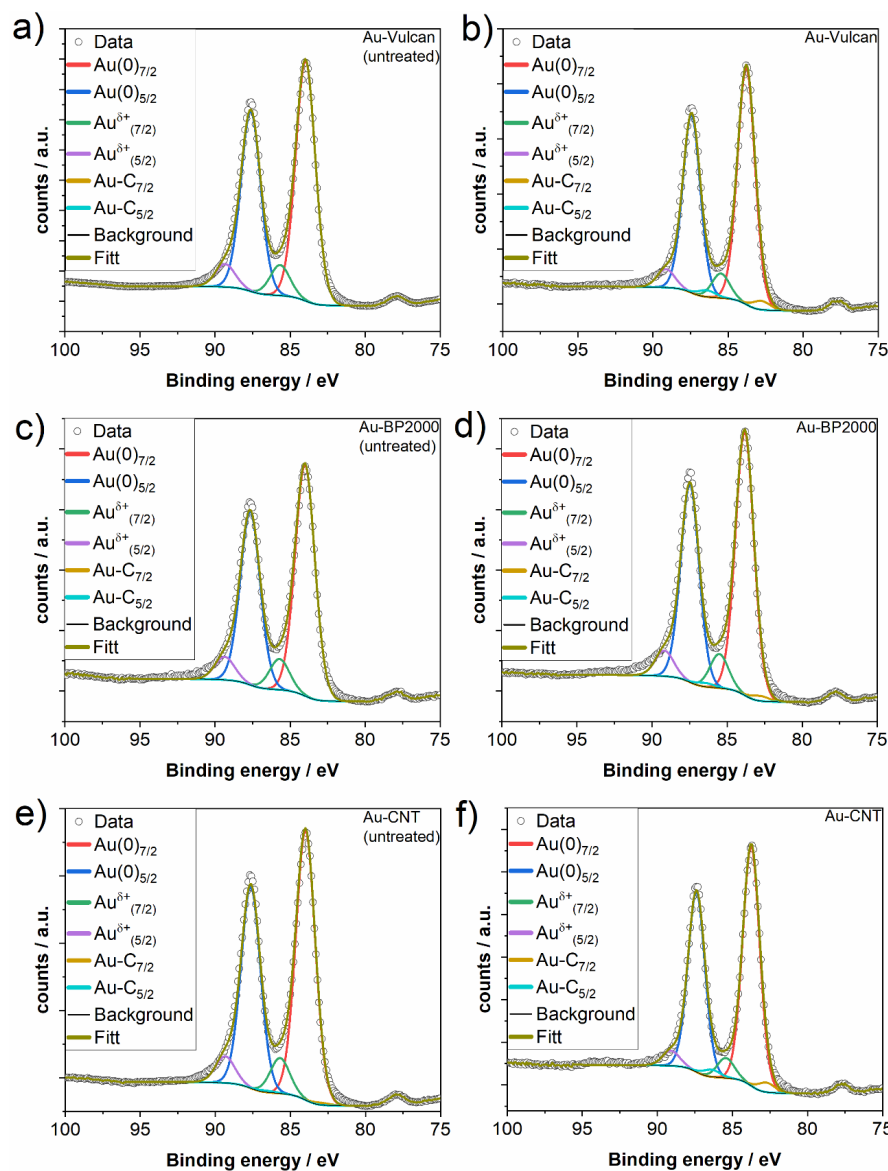


Figure S10. Au 4f XPS detail scan for a) Au-Vulcan (untreated), b) Au-Vulcan, c) Au-BP2000 (untreated), d) Au-BP2000, e) Au-CNT (untreated) and f) Au-CNT.

Table S2. Composition of the different samples according to the XPS overview scans of the final samples as well as the samples before the post (surfactant removal) treatment (LOD: limit of detection).

Sample	C / at. %	O / at. %	S / at. %	Au / at. %
Au-BP2000 (untreated)	91.7	6.7	0.6	1.1
Au-BP2000	94.9	4.0	0.08	1.1
Au-CNT (untreated)	93.8	3.6	0.8	1.8
Au-CNT	94.9	4.5	< LOD	0.6
Au-Vulcan (untreated)	91.8	2.7	1.7	3.9
Au-Vulcan	91.4	7.6	0.09	0.9

Table S3. Fitting parameters (binding energy, full width at half maximum (FWHM), spin orbit split and area distribution for spin orbit split) for the different species fitted in the O 1s, S 2p, C 1s and Au 4f detail scans of the XPS analysis.

Detail scan	species	Binding energy / eV	FWHM / eV
O 1s ^{26,27,20,28}	C-O (sp3), C-OH	532.1 (± 0.1)	2.9 (± 0.3)
	C-O (sp2), C-O-C	532.9 (± 0.3)	2.8 (± 0.3)
	Chemisorbed H ₂ O	535.4 (±0.2)	3.8 (± 0.3)
	Au(I,III)	529.6 (± 0.2)	1.3 (± 0.2)
	O ₂ adsorbed on Au	530.3 (± 0.2)	1.3 (± 0.2)
	H ₂ O adsorbed on Au	531.5 (± 0.4)	1.5 (± 0.4)
S 2p ^{19,29,22}	RS-Au	161.4 (± 0.3)	1.5 (± 0.1)
Spin orbit split 1.2 eV	RS-H	163.4 (± 0.4)	1.5 (± 0.1)
	SO ₃ ⁻	167.1 (± 0.9)	1.5 (± 0.1)
Area distribution 3/2 to 1/2 is 2 to 1			
Au 4f ^{20,28,23,24,30}	Au(0)	83.7 (± 0.1)	1.3 (± 0.1)
Spin orbit split 3.65 eV	Au ^{δ+}	85.4 (± 0.1)	1.3 (± 0.1)
	Au-C	82.7 (± 0.1)	1.3 (± 0.1)
Area distribution 7/2 to 5/2 is 4 to 3			
C 1s ^{26,27,31}	C-C (sp2)	284.0 (± 0.1)	1.3 (± 0.2)
	C-C (sp3)	285.2 (± 0.1)	1.4 (± 0.2)
	C-O, C-OH, C-O-C	286.3 (± 0.1)	2.0 (± 0.2)
	C=O	287.1 (± 0.1)	1.3 (± 0.2)
	-O-C=O	288.8 (± 0.1)	2.0 (± 0.2)
	Carbonate	290.2 (± 0.1)	2.0 (± 0.2)
	Pi-pi*	291.7 (± 0.1)	5.2 (± 0.2)

Table S4. FWHM and area% of the results of the detail scan fits of the XPS measurements, two lines for S 2p and Au 4f for the spin split.

	Au-BP2000 un-treated		Au-BP2000		Au-Vulcan un-treated		Au-Vulcan		Au-CNT un-treated		Au-CNT	
O 1s	FWHM/eV	%	FWHM/eV	%	FWHM/eV	%	FWHM/eV	%	FWHM/eV	%	FWHM/eV	%
C-O (sp ³), C-OH	3.0	13.0	3.0	25.3	2.7	4.5	3.0	11.7	3.0	33.5	3.0	56.7
C-O (sp ²), C-O-C	2.6	68.4	2.7	62.6	2.8	83.8	2.5	66.4	3.0	47.5	2.7	24.3
chemisorbed H ₂ O	4.0	1.0	4.0	4.1	3.8	1.5	4.0	0.0	3.5	10.2	3.7	3.9
Au(I,III)	1.4	2.6	1.3	1.6	1.1	3.9	1.4	2.3	1.4	3.1	1.4	3.0
O ₂ adsorbed on Au	1.2	5.3	1.2	1.9	1.1	3.8	1.4	9.6	1.1	5.1	1.3	12.0
H ₂ O adsorbed on Au	1.3	9.7	1.1	4.5	1.3	2.5	1.2	10.0	1.9	0.7	1.0	0.1
S 2p												
RS-Au	1.5	7.8	1.5	9.9	1.5	7.6	1.5	6.1	1.5	8.8	1.5	0.0
	1.5	7.6	1.5	9.7	1.5	7.4	1.5	6.0	1.5	8.6	1.5	0.0
RS-H	1.5	38.1	1.5	33.9	1.5	38.6	1.5	33.5	1.5	37.0	1.5	0.0
	1.5	37.3	1.5	33.2	1.5	37.8	1.5	32.8	1.5	36.2	1.5	0.0
SO ₃ -	1.5	4.7	1.5	6.7	1.5	4.3	1.5	10.9	1.5	4.8	1.5	0.0
	1.5	4.6	1.5	6.5	1.5	4.2	1.5	10.7	1.5	4.7	1.5	0.0

Table S5. FWHM and area% of the results of the detail scan fits of the XPS measurements, two lines for S 2p and Au 4f for the spin split.

	Au- BP2000 untreated	Au- BP2000	Au- Vulcan untreated	Au- Vulcan	Au- CNT untreated	Au- CNT					
C1s	FWHM / eV	FWHM / eV	FWHM / eV	FWHM / eV	FWHM / eV	FWHM / eV					
	%	%	%	%	%	%					
C-C (sp ²)	1.5	60.0	1.4	60.2	1.5	67.8	59.6	62.0	1.3	63.3	
C-C (sp ³)	1.6	16.7	1.6	12.7	1.7	15.3	16.1	16.0	1.4	11.6	
C-O, C-OH, C-O-C	2.2	12.6	2.2	12.9	2.3	9.1	2.2	13.1	1.9	10.8	
C=O	1.5	0.4	1.4	0.6	1.5	0.6	1.5	0.0	1.4	1.3	0.9
...O-C=O carbonate	2.2	5.7	2.3	5.6	2.3	3.1	2.2	5.4	3.7	1.9	3.6
pi-pi*	5.8	2.3	5.8	4.7	6.0	2.0	5.8	3.4	3.9	5.1	7.0
Au4f											
Au(0)	1.6	45.2	1.4	44.6	1.5	45.4	1.4	44.9	1.5	44.9	45.7
	1.6	43.1	1.4	42.5	1.5	43.3	1.4	42.8	1.5	42.8	43.4
A ^{δ+}	1.6	6.0	1.4	5.8	1.5	5.8	1.4	4.6	1.5	5.9	3.8
	1.6	5.7	1.4	5.5	1.5	5.5	1.4	4.4	1.5	5.6	3.6
Au-C	1.6	0.0	1.4	0.9	1.5	0.0	1.4	1.7	1.5	0.4	1.8
	1.6	0.0	1.4	0.8	1.5	0.0	1.4	1.6	1.5	0.3	1.7

LSV-RDE

Fig. S11 shows LSV-RDE measurements of the bare support and of the three catalysts in Ar and CO_2 saturated 0.5 M $KHCO_3$. These measurements demonstrate that the bare support is not active for the CO_2RR as well as the HER, in the potential region investigated.

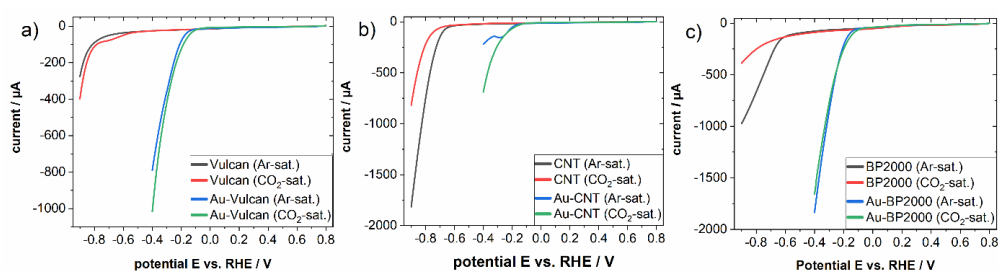


Figure S11. LSV-RDE measurements of the supports and of the samples in Ar- and CO_2 -saturated 0.5 M $KHCO_3$, a) Vulcan and Au-Vulcan, b) CNT and Au-CNT, c) BP2000 and Au-BP2000, purge gas as indicated.

SECM

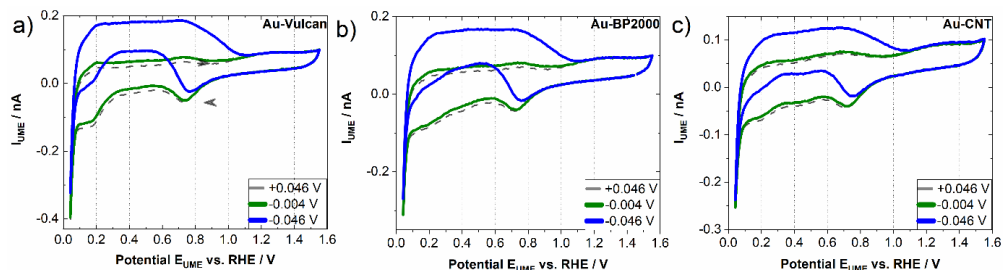


Figure S12. CVs of the microelectrode during SECM measurements over a) Au-Vulcan, b) Au-BP2000 and c) Au-CNT, at substrate potentials as indicated in the inset.

Fig. S12 presents CVs of the microelectrode during SECM measurements of the three catalysts to show the small but specific HOR currents of around 10 pA at the microelectrode, starting from substrate potentials of -0.004 V vs. RHE. As can be seen, these currents are small but not

negligible. This experiment further underlines the high sensitivity of the SECM for H₂ with a Pt UME, since smallest traces can be observed.

Further CVs were recorded at the UME at more negative substrate potentials to detect any products formed by CO₂RR at the underlying substrate. To correlate the obtained CVs with specific products, reference measurements of literature-known CO₂RR products in different concentrations were recorded, and are displayed in Fig. S13. To clarify deviations due to small pH changes, the measurements were carried in CO₂ and Ar saturated 0.5 M KHCO₃. The measurements show specific differences between CO₂ or Ar saturated electrolyte, which allows to estimate pH effects. The pH dependency of the HER is evident. In CO₂ saturated electrolyte the HER appears at around 0.1 V, in Ar saturated electrolyte the HER is not visible, since it is shifted to slightly more negative potentials. On the other hand, the reference CV of dissolved oxalic acid (Fig. S13b) shows the opposite behavior, as the concentration of the 0.25 M C₂H₂O₄, 0.5 M KHCO₃ decreases the pH and the HER is shifted to potentials of around 0.25 V. In Fig. S13i an SECM measurement the CO₂RR of Au-Vulcan in Ar purged electrolyte is shown. It is evident that HCO₃⁻ is a negligible source for CO₂RR.

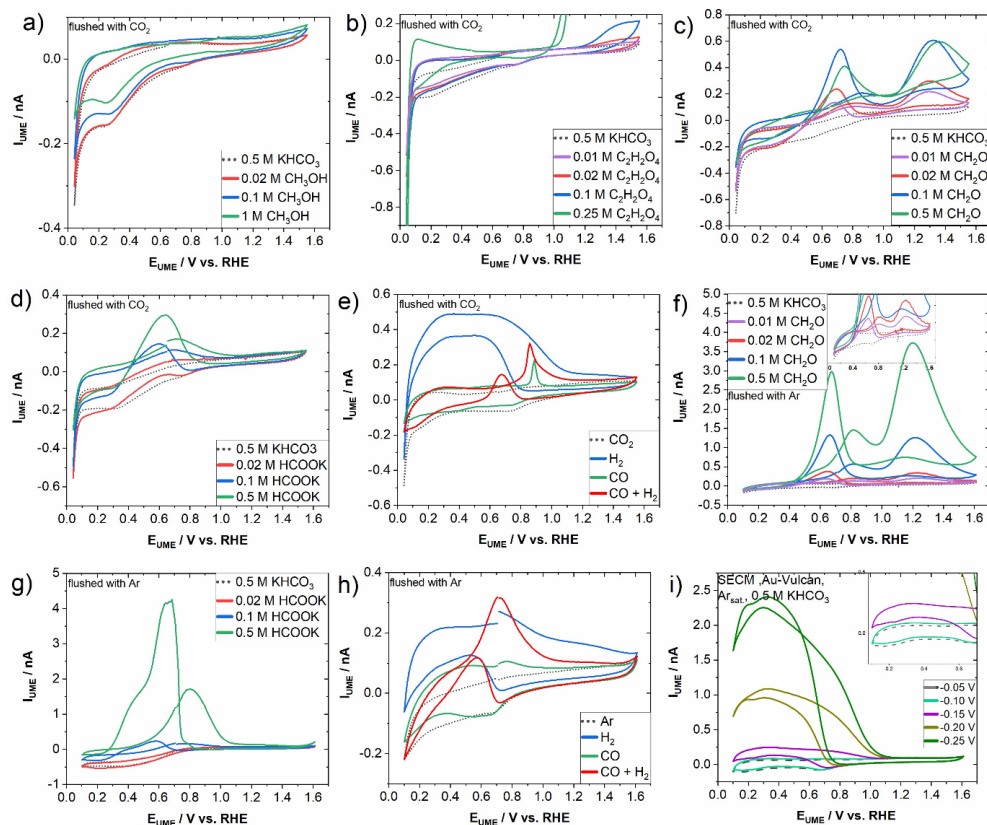


Figure S13. CV reference measurements at a Pt UME ($10 \mu\text{m}$) of possible CO_2RR products at various concentrations in CO_2 or Ar saturated 0.5 M KHCO_3 for the identification of CO_2RR products by SECM, of a) methanol (sat. gas: CO_2), b) oxalic acid (CO_2) pH (4.5) corrected x-axis (460 mV), c) formaldehyde (CO_2), d) potassium formate (CO_2), e) CO , H_2 and $CO + H_2$ (CO_2), f) formaldehyde (Ar) g) potassium formate (Ar) and h) CO , H_2 and $CO + H_2$ (Ar) and i) an SECM (SG/TC) measurement of Au-Vulcan in 0.5 M KHCO_3 (Ar saturated).

POTENTIOSTATIC CHRONOAMPEROMETRY RDE EXPERIMENTS

To validate the unexpected SECM-finding of formaldehyde formation during CO_2RR over Au-CNT, an additional experiment with a standard three electrode setup was conducted, where an

RDE was used to avoid diffusion limitation. Furthermore, local pH changes are drastically reduced by the improved mass transport.³² Samples of the electrolyte were taken after prolonged CO₂RR and investigated in a TG-MS setup. Fig. S14 displays the MS signals obtained after heating up the electrolyte. A signal of $m/z = 30$ (CH₂O) was found for the electrolyte from CO₂RR over Au-CNT, while none was observed for Au-BP2000 and Au-Vulcan. The figure also shows the reference measurements with a certain amount of CH₂O added to 0.5 M KHCO₃. Additionally, the signals $m/z = 32$ (CH₃OH) and 45/46 (HCOO⁻/HCOOH) were investigated without any positive result.

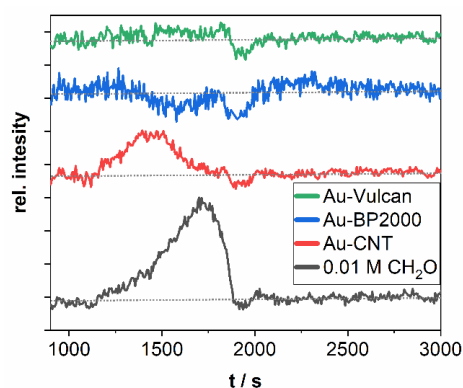


Figure S14. MS signal of $m/z = 30$ g•mol⁻¹ of the TG-MS measurement of 0.5 M KHCO₃ electrolyte samples of Au-Vulcan, Au-BP2000 and Au-Vulcan recovered after potentiostatic RDE experiments at -0.3 V and a reference measurement of 0.01 M CH₂O, 0.5 M KHCO₃. All measurements were normalized to the area of a 500 μ l CO₂ injection as described in our previous work.¹⁴

References

(1) Cave, E. R.; Montoya, J. H.; Kuhl, K. P.; Abram, D. N.; Hatsukade, T.; Shi, C.; Hahn, C.; Nørskov, J. K.; Jaramillo, T. F. Electrochemical CO₂ reduction on Au surfaces: mechanistic

aspects regarding the formation of major and minor products. *Phys. Chem. Chem. Phys.* **2017**, DOI: 10.1039/c7cp02855e.

(2) Inkpen, M. S.; Liu, Z.-F.; Li, H.; Campos, L. M.; Neaton, J. B.; Venkataraman, L. Non-chemisorbed gold-sulfur binding prevails in self-assembled monolayers. *Nat. Chem.* **2019**, DOI: 10.1038/s41557-019-0216-y.

(3) Kim, B.; Seong, H.; Song, J. T.; Kwak, K.; Song, H.; Tan, Y. C.; Park, G.; Lee, D.; Oh, J. Over a 15.9% Solar-to-CO Conversion from Dilute CO₂ Streams Catalyzed by Gold Nanoclusters Exhibiting a High CO₂ Binding Affinity. *ACS Energy Lett.* **2020**, DOI: 10.1021/acsenergylett.9b02511.

(4) Calvinho, K. U. D.; Alherz, A. W.; Yap, K. M. K.; Laursen, A. B.; Hwang, S.; Bare, Z. J. L.; Clifford, Z.; Musgrave, C. B.; Dismukes, G. C. Surface Hydrides on Fe₂P Electrocatalyst Reduce CO₂ at Low Overpotential: Steering Selectivity to Ethylene Glycol. *J. Am. Chem. Soc.* **2021**, DOI: 10.1021/jacs.1c03428.

(5) Birdja, Y. Y.; Pérez-Gallent, E.; Figueiredo, M. C.; Göttle, A. J.; Calle-Vallejo, F.; Koper, M. T. M. Advances and challenges in understanding the electrocatalytic conversion of carbon dioxide to fuels. *Nat. Energy* **2019**, DOI: 10.1038/s41560-019-0450-y.

(6) Rybacki, M.; Nagarajan, A. V.; Mpourmpakis, G. Ligand removal energetics control CO₂ electroreduction selectivity on atomically precise, ligated alloy nanoclusters. *Environ. Sci.: Nano* **2022**, DOI: 10.1039/D2EN00157H.

(7) Yang, D.; Pei, W.; Zhou, S.; Zhao, J.; Ding, W.; Zhu, Y. Controllable Conversion of CO₂ on Non-Metallic Gold Clusters. *Angew. Chem., Int. Ed.* **2020**, DOI: 10.1002/anie.201913635.

(8) Alfonso, D. R.; Kauffman, D.; Matranga, C. Active sites of ligand-protected Au₂₅ nanoparticle catalysts for CO₂ electroreduction to CO. *J. Chem. Phys.* **2016**, DOI: 10.1063/1.4948792.

(9) Birdja, Y. Y.; Koper, M. T. M. The Importance of Cannizzaro-Type Reactions during Electrocatalytic Reduction of Carbon Dioxide. *J. Am. Chem. Soc.* **2017**, DOI: 10.1021/jacs.6b12008.

(10) Lu, Q.; Eid, K.; Li, W.; Abdullah, A. M.; Xu, G.; Varma, R. S. Engineering graphitic carbon nitride (g-C₃N₄) for catalytic reduction of CO₂ to fuels and chemicals: strategy and mechanism. *Green Chem.* **2021**, DOI: 10.1039/D1GC01303C.

(11) Cheng, M.-J.; Clark, E. L.; Pham, H. H.; Bell, A. T.; Head-Gordon, M. Quantum Mechanical Screening of Single-Atom Bimetallic Alloys for the Selective Reduction of CO₂ to C₁ Hydrocarbons. *ACS Catal.* **2016**, DOI: 10.1021/acscatal.6b01393.

(12) Zhang, W.; Huang, C.; Xiao, Q.; Yu, L.; Shuai, L.; An, P.; Zhang, J.; Qiu, M.; Ren, Z.; Yu, Y. Atypical Oxygen-Bearing Copper Boosts Ethylene Selectivity toward Electrocatalytic CO₂ Reduction. *J. Am. Chem. Soc.* **2020**, DOI: 10.1021/jacs.0c01562.

(13) Dieterich, E.; Kinkelin, S.-J.; Bron, M. Comparative Study of the Synthesis of sub-10 nm Carbon-Supported Gold Nanoparticles and their Suitability for Methanol Electrooxidation in Alkaline Media. *ChemNanoMat* **2022**, DOI: 10.1002/cnma.202200098.

(14) Dieterich, E.; Kinkelin, S.-J.; Steimecke, M.; Bron, M. Quantifying the removal of stabilizing thiolates from gold nanoparticles on different carbon supports and the effect on their electrochemical properties. *Nanoscale Adv.* **2022**, DOI: 10.1039/d2na00561a.

(15) Brust, M.; Walker, M.; Bethell, D.; Schiffrin, D. J.; Whyman, R. Synthesis of thiol-derivatised gold nanoparticles in a two-phase Liquid–Liquid system. *J. Chem. Soc., Chem. Commun.* **1994**, DOI: 10.1039/C39940000801.

(16) Luo, J.; Maye, M. M.; Kariuki, N. N.; Wang, L.; Njoki, P.; Lin, Y.; Schadt, M.; Naslund, H. R.; Zhong, C.-J. Electrocatalytic oxidation of methanol. *Catal. Today* **2005**, DOI: 10.1016/j.cattod.2004.10.013.

(17) Habrioux, A.; Sibert, E.; Servat, K.; Vogel, W.; Kokoh, K. B.; Alonso-Vante, N. Activity of platinum-gold alloys for glucose electrooxidation in biofuel cells. *J. Phys. Chem. B* **2007**, DOI: 10.1021/jp0720183.

(18) Wang, A.; Zhu, Y.; Sun, J.; Hu, S.; Zhang, X.; Niu, D. The nature of interaction between Au and heteroatoms-doped carbon nanotubes: Size and electronic effects on CO₂ electroreduction. *Appl. Surf. Sci.* **2023**, DOI: 10.1016/j.apsusc.2023.157692.

(19) Carlini, L.; Fasolato, C.; Postorino, P.; Fratoddi, I.; Venditti, I.; Testa, G.; Battocchio, C. Comparison between silver and gold nanoparticles stabilized with negatively charged hydrophilic thiols: SR-XPS and SERS as probes for structural differences and similarities. *Colloids Surf., A* **2017**, DOI: 10.1016/j.colsurfa.2017.05.045.

(20) Klyushin, A. Y.; Rocha, T. C. R.; Hävecker, M.; Knop-Gericke, A.; Schlögl, R. A near ambient pressure XPS study of Au oxidation. *Phys. Chem. Chem. Phys.* **2014**, DOI: 10.1039/c4cp00308j.

(21) Caprile, L.; Cossaro, A.; Falletta, E.; Della Pina, C.; Cavalleri, O.; Rolandi, R.; Terreni, S.; Ferrando, R.; Rossi, M.; Floreano, L.; Canepa, M. Interaction of L-cysteine with naked gold

nanoparticles supported on HOPG: a high resolution XPS investigation. *Nanoscale* **2012**, DOI: 10.1039/c2nr32741d.

(22) Laiho, T.; Leiro, J.; Lukkari, J. XPS study of irradiation damage and different metal–sulfur bonds in dodecanethiol monolayers on gold and platinum surfaces. *Appl. Surf. Sci.* **2003**, DOI: 10.1016/S0169-4332(03)00462-8.

(23) Higuchi, E.; Okada, K.; Chiku, M.; Inoue, H. Electrocatalytic Activity for Oxygen Reduction Reaction of Au Core/Pt Shell Nanoparticle-Loaded Carbon Black Catalyst with Different Core Sizes. *Electrochim. Acta* **2015**, DOI: 10.1016/j.electacta.2015.03.079.

(24) Joseph, Y.; Besnard, I.; Rosenberger, M.; Guse, B.; Nothofer, H.-G.; Wessels, J. M.; Wild, U.; Knop-Gericke, A.; Su, D.; Schlögl, R.; Yasuda, A.; Vossmeier, T. Self-Assembled Gold Nanoparticle/Alkanedithiol Films: Preparation, Electron Microscopy, XPS-Analysis, Charge Transport, and Vapor-Sensing Properties. *J. Phys. Chem. B* **2003**, DOI: 10.1021/jp030439o.

(25) Cai, X.; Li, G.; Hu, W.; Zhu, Y. Catalytic Conversion of CO₂ over Atomically Precise Gold-Based Cluster Catalysts. *ACS Catal.* **2022**, DOI: 10.1021/acscatal.2c02595.

(26) Datsyuk, V.; Kalyva, M.; Papagelis, K.; Parthenios, J.; Tasis, D.; Siokou, A.; Kallitsis, I.; Galiotis, C. Chemical oxidation of multiwalled carbon nanotubes. *Carbon* **2008**, DOI: 10.1016/j.carbon.2008.02.012.

(27) Hueso, J. L.; Espinós, J. P.; Caballero, A.; Cotrino, J.; González-Elipé, A. R. XPS investigation of the reaction of carbon with NO, O₂, N₂ and H₂O plasmas. *Carbon* **2007**, DOI: 10.1016/j.carbon.2006.07.021.

(28) Zhidkov, I. S.; Kurmaev, E. Z.; Cholakh, S. O.; Fazio, E.; D'Urso, L. XPS study of interactions between linear carbon chains and colloidal Au nanoparticles. *Mendeleev Commun.* **2020**, DOI: 10.1016/j.mencom.2020.05.007.

(29) Heister, K.; Zharnikov, M.; Grunze, M.; Johansson, L. S. O.; Ulman, A. Characterization of X-ray Induced Damage in Alkanethiolate Monolayers by High-Resolution Photoelectron Spectroscopy. *Langmuir* **2001**, DOI: 10.1021/la001101d.

(30) Radnik, J.; Mohr, C.; Claus, P. On the origin of binding energy shifts of core levels of supported gold nanoparticles and dependence of pretreatment and material synthesis. *Phys. Chem. Chem. Phys.* **2003**, DOI: 10.1039/b207290d.

(31) Puziy, A. M.; Poddubnaya, O. I.; Ziatdinov, A. M. On the chemical structure of phosphorus compounds in phosphoric acid-activated carbon. *Appl. Surf. Sci.* **2006**, DOI: 10.1016/j.apsusc.2005.10.044.

(32) Lim, C.; Harrington, D. A.; Marshall, A. T. Effects of mass transfer on the electrocatalytic CO₂ reduction on Cu. *Electrochim. Acta* **2017**, DOI: 10.1016/j.electacta.2017.04.017.